Characterization of Residual Stress and Plastic Strain in Austenitic Stainless Steel 316L(N) Weldments

Thesis

DOCTORAL THESIS

The Open University

Characterization of Residual Stress and Plastic Strain in Austenitic Stainless Steel 316L(N) Weldments

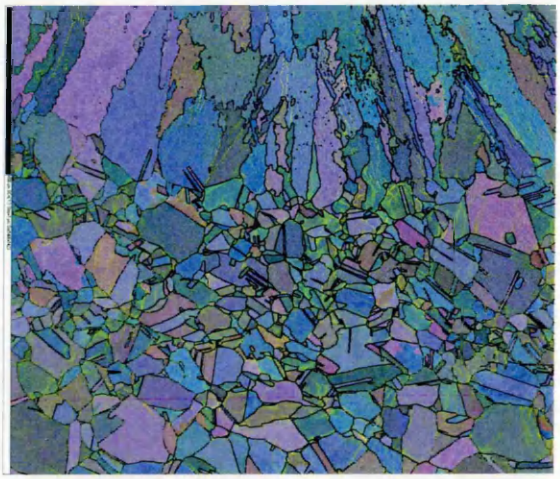

2 pass weld EBSD Map

500μm

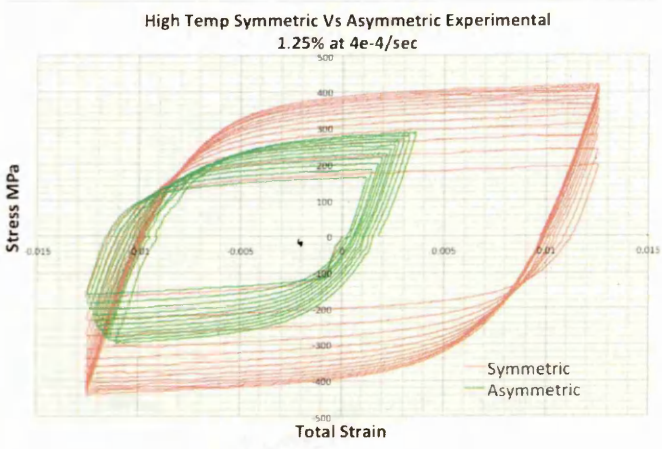

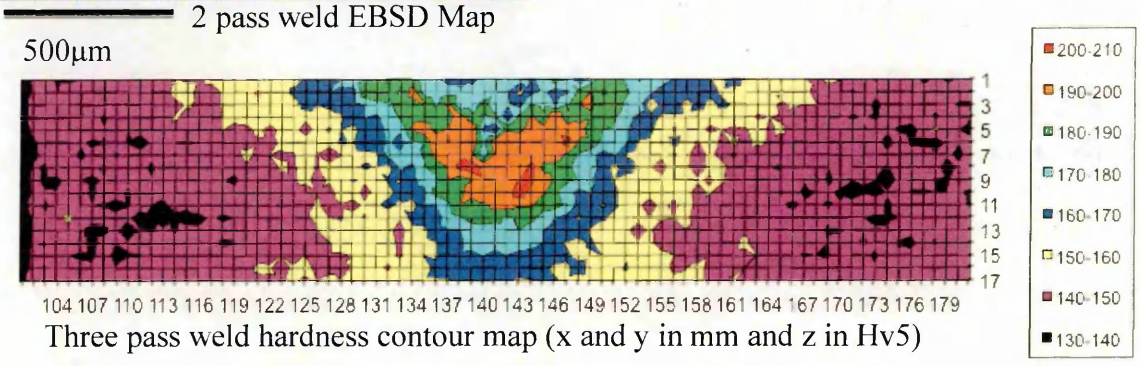

Three pass weld hardness contour map (x and y in mm and z in Hv5)

Shanmukha Rao Moturu

September 2015

Submitted to the Department of Engineering and Innovation, The Open University for the Degree of Doctor of Philosophy

DATE of SUBMISSION: 10 Sep 2015
DATE of AWARD: 22 Dec 2015

ProQuest LLC.
789 East Eisenhower Parkway
P.O. Box 1346
Ann Arbor, MI 48106 – 1346

ABSTRACT

Fusion welding processes commonly involve the localized input of intense heat, melting of dissimilar materials and the deposition of molten filler metal. The surrounding material undergoes complex thermo-mechanical cycles involving elastic and plastic deformation. This processing history creates large residual stress in and around the weld bead, which can be particularly detrimental in reducing the lifetime of fabricated structures, increasing their susceptibility to stress corrosion, fatigue and creep crack growth as well as reducing the fracture load. It is very important to have a proper knowledge of the residual stress distribution in and around the weld region of structured components because knowing this allows their fitness to be assessed and the service life of critical components to be predicted. Characterizing weld residual stress fields either by measurement or finite element simulation is not straightforward because of the strain field complexity, inhomogeneity of the microstructure and the complex geometry of structural weldments.

The residual stress distribution in a slot weld benchmark sample made from AISI 316L(N) austenitic stainless steel was analysed using the neutron diffraction at pulsed source. The presence of crevices and hydrogen containing super glue in the stress-free cuboids are some of the main issues effecting the neutron residual stress measurements. A residual stress of 400-450MPa was observed in first pass weld metal and in the HAZ of a three pass welded plate.

The strain hardening behaviour of AISI 316L(N) steel around the slot weld was studied taking account of the asymmetric cyclic deformation and the typical strain rates experienced; inferences are drawn regarding how such effects should be modelled in finite element weld residual stress computations. The solution annealed material was tested under symmetric and asymmetric cyclic loading at both room and 550°C. During

asymmetric cyclic loading, the 316L (N) material at room and high temperature was less strain hardened than in the same number of cycles of symmetric cyclic loading. At room temperature; the 316L (N) material deformed at fast strain rate showed higher strain hardening than at the slow strain rate. However, at high temperature (550°C); the 316L (N) material deformed at slow strain rate showed higher strain hardening than at the fast strain rate due to dynamic strain ageing. A mixed hardening model was to predict the strain hardening of the 316L (N) material at room and high temperature (550°C). However, the published mixed hardening parameters were unsuccessful in predicting the strain hardening of the symmetric cyclic deformation at high temperature.

Finally, the accumulated cyclic plastic strain resulting from the addition of each weld bead was studied using Electron Backscatter Diffraction (EBSD) and hardness measurements. The EBSD metrics showed a gradual increase of plastic strain and equivalent yield stress from the parent zone (approximately 0.02) to the fusion boundary (approximately 0.05-0.09). Although, in strain controlled cyclic loading, none of the EBSD metrics used were capable of assessing the plastic strain, below 58% cumulative plastic strain path. The quantified plastic strain (from the EBSD) and hardness analysis of the parent material indicates that the material deformed plastically. The EBSD derived plastic strain and equivalent yield stress correlate well with hardness, finite element prediction and von Mises equivalent residual stress.

ACKNOWLEDGEMENT

This doctoral thesis could not be possible without the technical and moral support of numerous people in the department. I would like to thank my supervisors Prof. Peter John Bouchard, Dr. Shirley Northover, Dr. Joe Kelleher and Dr. Jon James for their invaluable guidance and constant encouragement during my studies. I am grateful to Dr. Satheesh Krishnamurthy; Dr Mahesh Anand and Dr Abita Shyorotra Chimpri for their moral support during the hard times of my life. I would also like to express my deepest gratitude to Dr. Susan Storer for helping to review and edit the thesis.

I am indebted to the NeT consortium and the Open University for the financial support and the provision of the benchmark samples. I am also thankful to Prof. Mike Smith, the late Ann Smith and Dr. Ondrej Muransky for their very useful technical discussions and sharing the data during this project. I am also thankful to beamline scientists of the ENGIN-X (ISIS) and VULCAN (SNS) instruments for their valuable guidance and training during my experimental work.

I am indebted to the support given by staff in our department: Stan Hiller, Paul Courtnage ("Courtney"), Pete Ledgard, Gordon Imlach, Ian Norman, Dr. Colin Gagg, Charlie Snelling and Heather Davies. Without their expertise and help, this work would not have been a success. I would also like to thank my friends in the Engineering and Innovation department: Dr. Abdul Khader Syed, Avishek Dey, Jose Rodolpho Leo, Yeli Traore, Shah Karim, Jino Matthews, David Githinji, Jeferson Oliveira, Gerardo, Yadunandan Das, Abdullah-al-Mamun, Rahul Unnikrishnan, Safaa Lebjioui, Paheli Ghosh, Dr. Murat Ozgun Acar, Dr. Asim Zeybek and Dr. Sanjooram Paddea who have withstood everything I have thrown at them for the last few years and I will always be indebted to them. I have enjoyed every minute of the last four years we spent in Milton Keynes.

I would like say a heartfelt thanks to my beloved parents Mr and Mrs Durga Prasad Moturu, Geetha Vani Moturu, my wife, Mrs Suneetha Koganti and my son Jeswant Sai Moturu and my beloved brother, Mr. Phaneendra Babu and his family. Special thanks to Mr Suresh Kakarla and his family for there support in achieving my goals. Finally, I am grateful to Mr. Noel Ward, Mrs. Marian Ward, Miss. Collette Ward and Mr. Nicholas Ward and his wife for their support and considering me as a family member. Without their constant support and love, it was quite impossible for me to finish the thesis on time.

I am dedicating this work and all my future success to my family members with whom I will spend the rest of my life.

PREFACE

This thesis is submitted for the degree of Doctor of Philosophy of The Open University, United Kingdom. The work described in this thesis was carried out in the Department of Engineering and Innovation, Faculty of Mathematics, Computing and Technology, between October 2010 and October 2015, under the supervision of Prof. Peter John Bouchard, Dr. Shirley Northover, Dr. Joe Kelleher and Dr. Jon James.

It is entirely the work of the author except where clearly referenced. None of this work has been submitted for a degree or other qualification at this or any other university. Some of the results of this work have been reported to Europen Network on Neutorn Techniques Standardization for Structural Integrity (NeT) as listed below:

1. Shanmukha Rao Moturu, J.James and P.J.Bouchard. NeT TG4 Project: Residual stress measurement using the SNS VULCAN neutron diffractometer, OU/MatsEng/033, December 2012.
2. Shanmukha Rao Moturu and P.J.Bouchard. NeT TG4 Project: Residual stress measurement using the ENGIN-X neutron diffractometer at ISIS facility, OU/MatsEng/045, November 2013.

Shanmukha Rao Moturu

October 2015

TABLE OF CONTENTS

NOMENCLATURE

τ	Shear stress
σ_0	Initial yield surface
σ_i	Achieved yield surface
θ	Diffraction angle
λ	Wavelength of incident beam
a_0 or d_0	Stress free lattice parameter
a or d	Measured lattice parameter
ν	Velocity of neutron
L	Total flight path
t	Time of Flight
ε	Strain
$\mu\varepsilon$	Micro strain
E	Young's modulus
υ	Poisson's ratio

ABBREVIATIONS

TIG	Tungsten Inert Gas
DCEN	Direct Current Electrode Negative
DCEP	Direct Current Electrode Positive
AC	Alternating Current
HAZ	Heat Affected Zone
FZ	Fusion Zone
SAZ	Strain Affected Zone
SCC	Stress Corrosion Cracking
DSA	Dynamic Strain Ageing
SNS	Spallation Neutron Source
TOF	Time Of Flight
NeT	Neutron Techniques Standardization for Structural Integrity
TG	Task Group
FE	Finite Element

ND	Neutron Diffraction
EDM	Electro Discharge Machining
EBSD	Electron Backscatter Diffraction
SEM	Scanning Electron Microscope
CCD	Charge Couple Device
GND	Geometrically Necessary Dislocation
KAM	Kernel Average Misorientation
LABf	Low Angle Boundary fraction
$AMIS_a$	Overall Average Intragrain Misorientation
SSGB	Solidified Sub Grain Boundary
SGB	Solidified Grain Boundary
SScanSS	Strain Scanning Simulation Software
HV	Vickers Hardness Test

CHAPTER 1. INTRODUCTION

1.1 Background

Stainless steels are widely used in power generating plants, the pharmaceutical industry and transport due to their high corrosion resistance, long service life, toughness, strength and ability to operate at elevated temperatures [1]. Depending on the application and required material properties, different types of steels are used in nuclear power plants, as illustrated in Figure 1.1. The material of interest here is an austenitic stainless steel of type AISI 316L, used in the primary loop system of pressurized water reactors. Due to the complex architecture of a power plant, stainless steels are welded together with similar or dissimilar metals to form components and systems. Welding is a process used for both fabrication and repair of metal parts, where the parts are joined permanently by creating interatomic bonds into an almost homogeneous unit [2]. Welding is a widely used joining process in many industrial sectors, due to its wide applicability and cost effectiveness [3].

However, welding processes and plastically deforming the structural components causes the development of residual stresses (as described in Chapter 2). The magnitude of these residual stresses can reach, or exceed, the yield stress of the material. These stresses can be detrimental in increasing susceptibility to stress corrosion, fatigue and creep degradation, thus potentially reducing the lifetime of a fabricated structure [4]. Thick section ferritic weldments are usually post-weld heat treated (PWHT), which relieves the residual stresses to some extent [5], but austenitic stainless steel weldments are usually left in the as-welded state to avoid introducing any unwanted microstructural changes associated with heat treatment. Weld repairs, for example, in stainless steel structures of light water reactors are susceptible to stress corrosion cracking, and creep damage in high

temperature environments [6–10]. Problems can also arise because the joining material has different material properties to the base material, such as grain size, chemical composition and mechanical properties. During plant operation a structural component is subjected to external stress. This additional stress is added to any existing residual stress within the component, increasing the incidence of degradation and potential failure of the part during service [11]. The failure of critical structural components during service, such as a primary loop pipe malfunction in a pressurized water reactor, may lead to severe unacceptable environmental pollution. Accurate information on the distribution of residual stress in welded structural components allows industries to assess their fitness for service and judge the remaining safe lifetime [12].

1.2 Purpose of this study

The purpose of this research is to understand to what extent modern measurement techniques can be used to characterise and quantify the state of stress and strain in an austenitic stainless steel benchmark weldment. The measurement techniques used include time of flight neutron diffraction for residual stress, strain and texture; EBSD for quantifying plastic strain and yield stress and texture; hardness mapping for plastic strain hardening, and cyclic testing for determine the stress-strain response of material under weld thermal loading.

In order to assess the integrity of a component for safety critical applications assessment by numerical simulation is often needed. Where weld residual stresses play a critical role, experimental validation of weld residual stress predictions may be required. Characterising weld residual stress fields either by experimental measurement or by finite element simulation is not straightforward, owing to the complex nature of the stress and strain fields, the inhomogeneous microstructure and the complex geometry of structural

weldments. Different members of an international round robin consortium [13–15] have investigated the residual stress distributions in benchmark weld components using a variety of experimental methods and numerical simulations [16–20]. Various numerical simulations are compared with each other and with diverse experimental data. The experimental and numerical results have shown substantial scatter, as evidenced in the work of Smith *et al* [16,21]. Estimation of a component's fitness for service and lifetime, based upon significantly scattered data is undesirable because of the resultant uncertainty concerning the component's reliability. In this thesis, the residual stress distribution in a three pass benchmark weld has been characterised in order to identify the issues affecting the reliability of residual stress measurements performed using neutron diffraction.

Material surrounding a deposited weld bead undergoes cyclic deformation at different strain ranges and strain rates depending on how far a section of material is from heat source. Finite element (FE) simulation is often used to model weld thermal cyclic loading and to predict the evolution of stress and strain in weldments. However, the accuracy of weld simulation predictions is reliant on the accuracy of the input material properties and the assumptions made for the simulation. For instance, the following points play a key role in the accurate prediction of weld residual stress and plastic strain.

1. Usually in FE weld simulation, the input material properties such as yield stress and rate of strain hardening are derived from uniaxial symmetric cyclic loading tests (tensile-compression)[21–25]. However, in reality the material experiences asymmetric cyclic loading during welding.
2. The FE input material properties used are often derived from measurement made over a fixed strain range. However, the rate of strain hardening of austenitic stainless steel (316L), at different strain ranges, varies significantly.

3. Similarly, most of FE weld simulations previously reported do not consider the effect of strain rate on the strain hardening of material at both room and high temperature. However with increasing strain rate, the rate of strain hardening of austenitic stainless steel material changes significantly [26–29].

For this thesis, strain hardening resulting from symmetric cyclic deformation and asymmetric cyclic deformation of solution annealed AISI 316L parent material, at both room and high temperatures, was examined. The effect of strain range and strain rate on strain hardening, again for symmetric and asymmetric cyclic deformation was also examined.

During welding, regions of material in and around the vicinity of the weld bead experience different strain ranges and strain rates, depending on how far they are from the heat source. Due to differences in the temperature gradient, the material deform plastically to different extents across the thickness of weldment. The heat-affected zone (HAZ), near the fusion boundary, deforms the most due to its proximity to the weld torch. It is well known that heavily deformed austenitic stainless steel is more susceptible to stress corrosion cracking than undeformed material [30,31]. Information on the accumulated plastic strain around a weld is thus important when assessing a component's fitness for service and its lifetime. Finite Element (FE) simulations are often used to predict the plastic strain in welded samples. However, validating the predicted plastic strain experimentally is challenging due to the limitation of experimental techniques available. Electron backscatter diffraction (EBSD) is an established technique increasingly being used for the quantification of plastic strain [32,33] in strained samples.

This thesis, investigates the possibility of using EBSD for the quantification of the accumulated plastic strain resulting from sequential weld bead deposits, through the thickness of a welded benchmark sample. The results are compared with hardness testing

and finite element predictions. In addition, this research explores the limitations of different EBSD misorientation metrics that can be used when quantifying the accumulated plastic strain due to symmetric and asymmetric cyclic deformation of solution annealed austenitic stainless steel AISI 316L.

1.3 Structure of thesis

Chapter 2 reviews the background literature relevant to this thesis. The topics covered include; austenitic stainless steel (316L), weld thermal analysis, the effect of weld parameters on microstructure, the relationship between the temperature distribution and the magnitude of residual stress, plastic deformation, dynamic strain ageing, cyclic deformation, residual stress, neutron diffraction methods for measuring residual stress and EBSD for assessing the accumulated plastic strain due to welding and strain controlled cyclic deformation.

Chapter 3 includes details of the specimens used for this research work, the benchmark sample design, the design of tensile and cyclic loading samples and details of heat treatment, grain size and texture. Also covered are the mechanical and physical properties of the material used for finite element simulations.

Chapter 4 provides details of the neutron diffraction experiments undertaken at two facilities and the post processing of the collected data. The results, taken at different depths in the benchmark specimen, are examined with respect to their positions relative to the weld deposit. The neutron diffraction results are presented and compared.

Chapter 5 describes, with the choice of experimental parameters, the experimental setup for fixed strain range cyclic deformation test at both room and high temperature, and details of the finite element simulation models and their validation. The chapter

concludes by describing the effects of strain rate and the different cyclic deformation conditions on the strain hardening of the material.

Chapter 6 describes the different experimental setups for the tensile tests performed at room and high temperature, hardness tests, EBSD measurements and the EBSD strain and stress calibration from the tensile test data. Finally quantified EBSD strain and stress results are described and compared with hardness measurements and the finite element predictions. Similarly EBSD derived yield stress results are compared with von Mises equivalent yield stress.

Chapter 7 presents a general discussion of the investigations carried out and Chapter 8 draws conclusions and provides suggestions for further work.

1.4 Figures

Figure 1.1 Different materials used in pressurized water reactor [6]

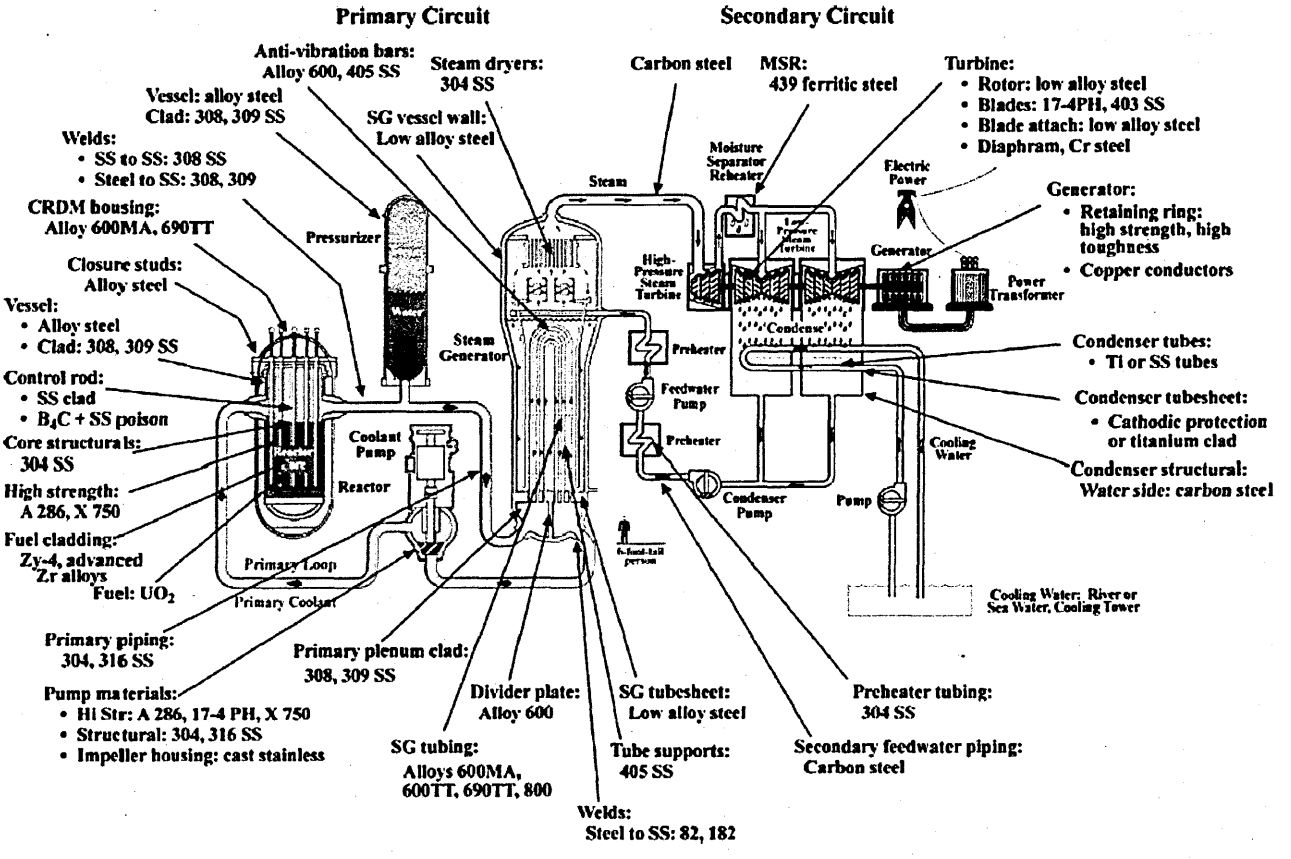

CHAPTER 2. LITERATURE REVIEW

This chapter is divided into two parts; part one gives basic information on AISI type 316L austenitic stainless steel, tungsten inert gas welding and the temperature distributions plastic deformation mechanisms and residual stresses resulting from it. Part two, reviews the experimental techniques available for characterizing residual stress and plastic strain, and evaluates previous studies around welds in AISI type 316L steel. The chapter concludes with the unanswered research questions revealed by this literature review.

2.1 Introduction

In power plant applications, austenitic stainless steels are used because of the stability of their tough, ductile austenitic phase which exists between room temperature and the melting point, and because they are easily weldable. Tungsten Inert Gas (TIG) welding provides precise control of heat input and can produce very clean and high quality welded joints [3,34]. For this reason it is extensively used in the nuclear industries to join heat sensitive components, thin gauge metal and pipes [34]. This research study investigated automatic tungsten inert gas welded plates of AISI 316L(N) to analyse the residual stress and plastic strain due to welding. The desirable features of this austenitic stainless steel are, its resistance to corrosion, good creep resistance, ductility, formability and toughness [8,35]. The chemical composition of austenitic stainless steel 316L(N) is provided in Table 2.1. As specified in the table, the chromium forms a thin passive layer of chromium oxide on the surface of the steel to prevent corrosion and oxidation at elevated temperatures [36] and nickel prevents the formation of ferrite [36].

Manganese prevents solidification cracking or sulphur embrittlement by forming the stable MnS phase [37]. Silicon is added to de-oxidise the material during melting. Molybdenum is included for additional corrosion resistance, specifically to prevent pitting and crevice corrosion [36]. The low carbon content prevents the formation of carbides during welding and hence reduces inter-granular corrosion [8,38].The stacking fault energy [39] is influenced by the alloying elements [40,41]. The addition of nickel in austenitic stainless steel increases the stacking fault energy. Based on a particular nickel content, chromium, cobalt and manganese decrease the stacking fault energy. The stacking fault energy affects the motion of dislocations and activation of cross slip. As a result of this material gets more strain hardened during mechanical deformation as described in section 2.2.

2.2 Welding: Thermal History and Microstructure Effects

TIG welding is a fusion welding process. Electric current is used to generate heat to produce an electric arc between a tungsten electrode and the workpiece, thus melting the edges of two components to be joined. The consumable filler wire, placed close to the tip of the electrode melts to fill the gaps during the welding process. Droplets of molten material form, and the filler and work-piece are mixed to create a weld pool, which solidifies and forms a bond between the two components [3]. The tungsten electrode is most commonly operated in the direct current electrode negative (DCEN) mode with the tungsten electrode connected to the negative terminal of a power supply. With this polarity approximately 60% of the power is concentrated at the work end of the arc, providing deep penetration and a narrow weld area. Previous research has found that during TIG welding, the temperature distribution from the heat source plays a significant role in the development of plastic deformation and residual stresses [34].

2.2.1 Temperature distribution of a moving heat source

In 1940, Rosenthal published an analytical heat distribution model representing steady state autogenous welding [42]. Whilst finite element based thermal analysis of welding is now commonplace, the Rosenthal model provides useful insights [43]. The model assumes that a point heat source moves at uniform velocity, along the surface of a semi-infinite plate. It uses a rectangular coordinate system whose origin coincides with the heat source. Phase transformations and heat loss from the surface of the plate are ignored, and the thermal properties are taken as independent of temperature. The Rosenthal heat flow equation for the steady state temperature distribution is given as;

$$\frac{2\pi(T-T_0)kr}{Q} = \exp\left(\frac{-v(r-x)}{2\alpha}\right) \qquad 2.1$$

Where T is the final temperature, T_0 the initial temperature, k the thermal conductivity, Q the heat transferred from the heat source to the workpiece, v is the source velocity, α the thermal diffusivity, and r the radial distance from the origin. The temperature distribution, in a plane perpendicular to the heat source, is determined by the radial distance *r* from the centre of the heat source. The temperature distribution at any radius from the heat source can be calculated from equation 2.1. For example, Chen *et al.* [44] have analysed numerically the effect of heat input, velocity of welding, thickness of the plate and distance from the heat source on a temperature vs time profile. Mahapatra et al.[45] have analysed the effects of the welding parameters on temperature distributions using three-dimensional numerical analysis. Experimentally measured temperature distributions from the heat source, using an array of thermocouples, during the welding process have been found to produce similar results [46]. In all analyses, the heating and cooling rates vary with the distance from the heat source. Most fusion welding processes involve deposition of molten filler material alongside the melting part of the work piece

material close to the heat source. The volume in which the material has been heated up to its melting point during welding is called the fusion zone [3]. Material adjacent to the fusion zone that has been metallurgically affected (in a away detectable metallographically) by weld thermal transients is known as the "heat affected zone" (HAZ). Beyond the HAZ is a "strain affected zone" (SAZ) that has undergone cyclic yielding [3], and compressive yield. Further away the elastic zone (where deformation could be accommodated without any plastic deformation). These zones are indicated in Figure 2.1 showing one of the stainless steel weldments studied in this thesis. The weld thermal cycles determine the metallurgical state of the material surrounding the heat source [45,47]. The weld parameters and number of weld bead depositions will significantly affect the development of microstructure, the area of fusion boundary, grain size in HAZ and degree of plastic deformation [48–50].

Even though 316L materials are readily weldable due to their low carbon content, they commonly suffer from stress corrosion cracking (SCC) due to the welding process. The magnitude of the plastic strains in the welded material has a significant effect on the SCC growth [31]. The SCC can be minimized effectively by optimizing the weld parameters (travel speed, arc voltage etc.) and by using parent material as filler wire [51,52]. However, local plastic deformation remains in the material due to the localized heat input, and the non-uniform deformation arising from multi pass welding [53]. Numerous studies have been carried out to help predict plastic deformation and residual stress (refer section 2.5.2) in welds using finite elements models [17,19,46,54,55]. However the magnitude and distribution of the plastic strain and residual stress depends on the weld parameters and sequence etc. Easterling [34] has qualitatively described the development of residual stress and plastic strain as a function of temperature, as shown in Figure 2.2. During welding, as the temperature increases, material close to the heat source initially expands, while the

material away from the heat source restrained from expansion due to lower temperature. As a result of this, compressive stresses are generated during heating as shown schematically in Figure 2.2 (i.e. 1 to 2). With further increase of temperature, the flow resistance of the material near heat source decreases and the material becomes softer. This results in the decline of the compressive stresses with increasing temperature and considerable plastic strain may occur, as seen in Figure 2.2 (i.e. 2 to 3 and 4). However, during cooling the material near the heat source contract, while the material away from the heat source restrain the contract, as result of this tensile stress and strain are generated with decreasing temperature as seen in Figure 2.2 (i.e. point 4-6).

Paradowska *et al.*[56] analysed the effect of heat input on the residual stress distribution in low carbon steel repair weld, using the neutron diffraction technique. The highest stresses were noted in the middle of the weld bead. However, the work failed to show clearly the effect of the heat input on the residual stress distribution. Muransky *et al.* [57] have numerically analysed the distribution of residual stress and plastic strain through the thickness of a weld repair plate during multi-pass welding. Both numerical and neutron diffraction analyses have exhibited peak longitudinal and transverse residual stresses in the HAZ of the austenitic stainless steel. Murugan *et al.* [58] analysed the effect of heat input, the geometry of the plate and the number of weld passes on the residual stress distribution, in two different butt weld materials. However, with an increasing number of weld deposits, the magnitude of the residual stress was found to decrease in the bottom of the weld plate (i.e. root weld), whilst on the top weld cap of the butt weld plate it increased. Jiang *et al.* [9] have analysed the effect of multiple weld repairs on microstructure, hardness and residual stress in clad plate. Neutron diffraction results in clad repair weld plate demonstrated a decrease in the residual stresses from the HAZ to the weld cap, and from the HAZ to the parent material. Similarly, hardness test results in

clad repair weld plate have shown higher hardness values at the interface between the weld metal and the base metal. Based on the residual stress, hardness test and microstructure of repair clad plate, Jiang *et al.*, recommends that the clad plate should not be repaired more than 2 times.

Most of the numerical studies in austenitic stainless steel weldments [55,59–66] have not considered the influence of the dynamic strain ageing effect on plastic deformation. Before describing the effects of dynamic strain ageing, it is appropriate to review some basics of cyclic deformation, dynamic strain ageing and its mechanism as associated with welding.

2.3 Monotonic and Cyclic Deformation in 316L(N)-Mechanism and Effects

The plastic deformation of 316L (N) can be described with the help of Figure 2.3. When the applied stress exceeds the yield stress, the deformation stop being elastic and the material is permanently deformed, this is known as plastic deformation.

2.3.1 Mechanism of plastic deformation

When a metal is stressed above its yield point, energy is consumed in generating or moving dislocations. During deformation, the motion of dislocations allows some parts of the crystal to slide across another part of the structure as shown in Figure 2.4. The planes on which sliding occurs are called slip planes. Slip displacement usually occurs along the close packed planes, where the energy required for dislocation motion is minimized. The direction in which the slip occurs is called slip direction. In f.c.c structures, slip normally occurs on planes of the type {111} and where the principal slip

direction is along <110>. The combination of slip plane and slip direction is called a slip system.

The plastic deformation of each material varies depending on its crystal structure. The crystal structure of austenitic stainless steels is a face-centred cubic (fcc), a highly symmetric structure, with 12 equivalent slip systems. This means that austenitic stainless steel deforms more easily than other crystal structures, such as body-centred cubic (bcc) crystal with fewer possible slip systems. The shear stress (refer Figure 2.5) required to move a dislocation is given by [67]

$$\tau = \frac{F}{A} \cos\phi . \cos\lambda \quad 2.2$$

Where the area of the slip plane is A/cos Φ and the force acting in the slip plane in the slip direction is Fcos λ. The resolved shear stress is at maximum when both λ and Φ are at 45°, and tend to become zero when either λ or Φ are at 90°.

If the angle between slip direction and direction of applied load (i.e. λ) is less than 45°, as the deformation of the material begins, λ decreases. Hence, according to equation 2.2, the resolved stress decreases as well. In order to deform the material plastically, the force needed to be increased and maintained, so that the shear stress is always higher than critical shear stress for continued plastic deformation. This phenomenon is known as geometrical hardening [39]. During plastic deformation, the increasing number of defects in the material will impede the flow of dislocations. As a result, additional stress is necessary for the continuation of plastic deformation. This phenomenon is called work hardening or strain hardening.

2.3.2 Work hardening

As deformation of the material proceeds, the material gets harder and stronger. At one point the material reaches a state where further deformation of material leads to failure.

At this stage the tensile strength and hardness of the material are at their maxima. The material's degree of work hardening depends on the density of defects, such as vacancies, interstitials or dislocations (edge, screw or mixed) and on the stacking fault energy [39]. The work of Frank-Reed [39] and Orowan [68] on dislocation loop mechanisms has explained the work hardening of material due to interactions between dislocation and defects. Haojie *et al.* [69] have analysed numerically the work hardening of material due to interaction between screw dislocations and different stacking faults. An excellent review on the stages of strain hardening in monotonic deformation has been given by Kock *et al* [70]. Both Cottrell [71] and Hirth [72] have demonstrated the formation of immobile dislocations due to the interaction of dislocations on the primary slip plane, with ones on the conjugate slip plane.

There are two basic types of dislocation movement that take place; conservative movement (i.e. glide) or non-conservative movement (i.e. climb). In non-conservative movements, activated at high temperature, dislocations move out of their slip plane. At low temperature, the plastic deformation of material mainly occurs by conservative motions. At elevated temperatures, the mobility of the dislocation is high and dislocations can take a new slip plane by cross slip.

Depending on a dislocation's sign and direction, another dislocation moving on the same slip will annihilate, repel it or form a sessile dislocation [39,73]. Sessile dislocations act as strong obstacles for moving dislocations. If the interacting dislocations move on different slip systems, after interaction they will develop jogs or kinks [39]. A jog is a sharp break in the dislocation line moving it out of slip plane, whilst a kink is a sharp break in the dislocation line which remains in the same slip plane [39]. Jogs are also formed by the intersection of two screw dislocations, and play an important role in plastic deformation.

Jogs in screw dislocations can only move, by slip, along the dislocation's line and the only way a screw dislocation can move to a new slip plane, along with a jog, is by climb.

The presence of edge dislocations in a crystal induces compressive stress around an extra half plane of atoms, and tensile stress below the extra half plane, as shown in Figure 2.6. Similarly, shear stresses are induced around screw dislocations. The presence of stress around dislocations will attract defects such as interstitial or substitutional solute atoms, and redistribute them to lower the energy around the dislocations. As a result, an atmosphere builds up around the dislocation, which is known as the Cottrell atmosphere [67,74]. Once an atmosphere has formed, the dislocation can only move by breaking free from the atmosphere or by dragging the atmosphere along with it. In both cases, the metal becomes work hardened due to the restriction of dislocation movement. As a result of this discontinuous motion of dislocations, stress-strain curves at high temperature show serrated flow. This phenomenon is called dynamic strain ageing [75].

2.3.3 Dynamic strain ageing (DSA)

DSA occurs due to interactions between moving dislocations and solute atoms, either interstitial or substitutional [75,76], when solute atoms gain enough velocity to keep up with the moving dislocations and form a Cottrell atmosphere. DSA increases the material's work hardening rate and the ultimate tensile strength, whilst reducing its ductility [77]. One important effect of DSA is negative strain rate sensitivity. The most important variables affecting DSA are the temperature and strain rate [78].In the DSA regime, if, during sample deformation at a given temperature and strain rate, the flow stress decreases with increasing strain rate, this is called negative strain rate sensitivity.

Solute drag, lattice friction and the concentration of the diffusing solutes, all contribute to DSA, as illustrated by Figure 2.7 re-constructed from the work of Blanc and Strudel

[79]. As seen in Figure 2.7, with increasing dislocation velocity, the lattice solute drag force increases friction (see curves 1 and 2), while the effect of dislocation velocity on the nearby concentration of the diffusing solutes is in the opposite direction (see curve 3). The overall result of the contributions of curves 1, 2 and 3, is curve 4. At dislocation velocities below V_M, the dislocation is in the drag zone. In this regime, the velocities of the dislocation and diffusing solute are approximately equal and form a Cottrell atmosphere around the dislocations. With increasing dislocation velocity, a critical force, F_M, is achieved and the dislocation enters the instability zone, where it accelerates enough to break away from the solute atmospheres. With further increases in dislocation velocity, to V_3, the lattice friction forces and dislocation interactions become dominant, and the friction regime begins. This results in a decrease of the dislocation velocity of V_m and an unstable zone is reached. Consequently, the dislocations re-enter the drag regime at V_1. This cycle of drag, instability and friction velocity causes the stress-strain curve to be serrated. Depending on the temperature, the carbon, nitrogen or chromium atoms may be responsible for DSA [80,81].

The formation of Cottrell atmosphere requires long-distance diffusion of solute atoms and therefore occurs only at high temperatures or after long term annealing. Before Cottrell atmospheres form, the solute atoms can reduce their energy by merely changing their position within the unit cell. However, the positions of the solute atoms change only when the unit cell is distorted. Ordering of solute atoms, arising from their occupying preferred positions along certain directions, is called the Snoek order [82]. As a result of Snoek order, an ordered atmosphere (called a Snoek atmosphere) may develop around the dislocation before the formation of the Cottrell atmosphere. The formation of a Snoek atmosphere around a dislocation, impedes its motion, and in order to move the dislocation, a higher yield stress is required [83,84].

In addition to Snoek ordering, the Suzuki effect also contributes to the serration of flow stress. A perfect dislocation in a closed packed structure can split into two partial dislocations, with an enclosed ribbon of stacking fault. As a result, the energy of the dislocation decreases and a stacking fault is formed [82]. As described earlier (section 2.1), alloying elements can decrease the energy of stacking faults in austenitic stainless steel [40,41]. In this case, the local chemical potential difference between a faulted region (for example, between partial dislocations) and the surrounding fcc matrix will provide a driving force for preferential segregation of solute atoms to stacking faults. This Suzuki segregation, resulting from the concentration dependence of the stacking fault energy, lowers the stacking fault energy, causing the fault to become wider and reducing the energy of the crystal.. An additional stress is then required to break the dislocation away from its Suzuki atmosphere, which leads to a yield drop.

The mechanism of DSA has also been explained by an alternative theory. In the DSA zone the solute atoms restrain the motion of the dislocations. In order to maintain the strain rate, additional dislocations are generated [85]. As a result the material gets more work hardened.

2.3.4 Cyclic loading

When a material is subjected to defined number of repetitive tension to compression or compression to tensile cycles, it is called cyclic loading. During cyclic deformation, the dislocation density has been found to increase during the initial forward deformation and decrease during the initial reverse deformation [73], due to the interaction and annihilation of dislocations. Nevertheless, further reverse deformation leads to an increase in dislocation density. A reduction of the yield stress of pre-strained material on reverse loading, is known as the Bauschinger effect [86]. With further cycles of deformation,

the dislocation density frequency increases, resulting in a cyclic hardening response. However, a material's hardness during cyclic deformation depends strongly on the orientation of its grains, the stacking fault energy, any short range order and the active slip 'modes' [87].

The relationship between slip mode and the type of dislocation structure (e.g. tangles, persistent slip bands, cell etc.) formed during the cyclic deformation was first explained by Feltner and Laird [88,89]. Wavy slip mode implies that cross slip can occur easily and that the cyclic stress-strain behaviour is history independent. In the planar slip mode, cross slip is difficult and the material cyclic behaviour is history dependent [90,91].

Austenitic stainless steel 316L has a low stacking fault energy [92], so partial dislocations are widely spaced. Wide stacking faults between partials impede the motion of dislocations and reduce the activation of cross slip. Slip on secondary slip planes is also inhibited in the early stages of deformation. As the deformation proceeds and the density of dislocations increases, activation of the secondary slip increases the interaction of dislocation with defects, and leads to the formation of sessile dislocation and jogs. These sessile dislocations will restrict further dislocation motion and assist the formation of dislocation tangles. At one point cyclic hardening and cyclic softening occur simultaneously [88,89,93]. Hardening is due to the formation of hard structures within the crystal pattern, such as dislocation walls, whilst the softening is due to activation of cross slip, the formation of channels (low dislocation density), and depending on the strain amplitude, activation of persistent slip bands [27,94–99]. After many cycles, the effects of active persistent slip bands and the formation of channels may surpass the hardening effect, leading to cyclic softening and the formation of a stable cellular structure of dislocations.

The DSA temperature range for austenitic stainless steel 316L is reported to be between 300°C-650°C [78,100,101]. Ivanchenko's [102] thesis has analysed the dynamic strain ageing effect on the work hardening of tensile deformed austenitic stainless steels and Ni-base alloys. The DSA for the austenitic stainless steel AISI 316 and Ni base alloys 600 and 690 materials was observed in the temperature range of 200°C-650°C at strain rate from 10^{-6} to 10^{-3} per second. With increasing nitrogen content, the amplitude of the flow stress pulses decreases. This is due to nitrogen atoms accumulation on dislocations or due to formation of multiple Luders bands structures. At 400°C long-range planarity dislocation microstructure; at 288°C short range planarity dislocation microstructure and at 200°C cellular dislocation microstructure was observed in 316NG austenitic stainless steel. Calmunger's [103] thesis has analysed the effects of DSA on the mechanical properties and microstructural development in austenitic alloys. At elevated temperatures the ductility of austenitic alloys increased at slow strain rate in comparison to the austenitic alloys deformed at higher strain rate. However, in aged austenitic alloys, the ductility of materials decreased at slow strain rate due to formation of precipitates in the grain boundaries. During plastic deformation, the stresses are concentrated around precipitates, as result of this intergranular fracture develops. Pham [101] has analysed the effects of DSA on the cyclic deformation response and dislocation microstructure. The DSA becomes less active during the first two cyclic response stage (i.e. hardening and softening stage). This is due to different short range interactions between dislocations and solute atoms. However, the serration becomes more significant after the cyclic softening phase (i.e. secondary cyclic hardening). Pham have shown the serration length is greater for reverse loading transients from tensile peak stress than for during reverse loading transients from compressive peak stress. This is due to vacancy mobility is promoted during reverse loading transients from compressive peak stress and suppressed during reverse loading

transient from tensile peak stress. In DSA regime, the presence of vacancy in crystal structure significantly effects the strain hardening of the material. Gerland *et al.*[104,105] have shown the effect of DSA on the dislocation structure and the fatigue behaviour of 316L at temperatures between 20°C and 600°C. Gerland's study showed a new dislocation structure called corduroy structure, which are formed in vacuum cyclic deformation of 316L material. The corduroy structure is responsible for secondary strain hardening of 316L material at temperature range 200-500°C. The corduroy structure is composed of alternative black (dislocations loops, debris and cavities) and white bands (channels). At 400°C, the formation of corduroy structure is high. The DSA of this material is due the interaction of corduroy structure and planar slip with solute atoms (C and N solute atoms). Similarly, Hong *et al* [78,100,106] have analysed the effect of DSA on slip mode initiation and propagation of multiple cracks, the mechanism of DSA with respect to temperature and strain rate. Hong's studies showed, austenitic stainless steel AISI 316L material experience DSA only at specific temperature range and strain rates, i.e. between 250°C -550°C at a strain rate of 10^{-4} per second; between 250°C -600°C at strain rate of 10^{-3} per second and between 250°C -650°C at strain rate of 10^{-2} per second. In DSA regime, the material gets more strain hardening due to the change in mechanism of plastic deformation, i.e. switching from wavy slip to planar slip mode. The fatigue resistance of austenitic stainless steels AISI 316L was reduced in the regime of DSA. Srinivasan *et al* [107] have studied the effect of DSA on the cyclic stress response and fatigue life of solution annealed and prior cold worked 316L(N) samples. The solution annealed austenitic stainless steel AISI 316L(N) exhibited DSA at 873K. At slow strain rate, Srinivasan noticed post cold worked austenitic stainless steel exhibited higher fatigue endurance as compared to solution annealed material. At temperature range 673-873K, the fatigue life of the solution annealed material was decreased. This is due to, in DSA

regime, higher stress concentration taking place at dislocation pile-up. Which would account for increased crack growth rates and hence reduction in the fatigue life. Samuel [80] has reviewed sample ageing effects on the appearance and disappearance of DSA, at temperatures between 300°C and 650°C due to carbide formation. At low temperature region i.e. 250°C-350°C, the diffusion of interstitial solute to dislocation is main responsible for activation of DSA in 316 material, while at high temperature range i.e. 400°C-650°C, the substitutional solutes like Cr is responsible for activation of DSA in 316L material. The serrations are most distinct in aged material at 650°C. However at one point the serrated flow suddenly ends in aged material at 650°C due to formation of precipitation and resulting decrease of solute concentration by ageing.

The cyclic hardening and softening of a material at different temperatures can be analysed numerically at the macro-scale using an appropriate elastic-plastic constitutive material model. A material's response to cyclic deformation can be described by a hardening 'rule' which describes the behaviour and development of the yield surface. Depending on the type of rule, the model will determine how the yield point changes with the accumulation of plastic strain; this is illustrated in Figure 2.8. The types of rules include isotropic hardening, kinematic hardening, mixed hardening and distortional hardening [108].

2.3.5 FE Elastic plastic constitutive material models

In finite element modelling, isotropic, kinematic and mixed hardening models are known as single surface models. These simple models only consider the change of the yield surface, resulting from plastic strain accumulation. The loading surface defines the boundary of the current elastic region, as seen in Figure 2.8(a). As the stress point moves beyond the boundary of the elastic region, plastic strains are produced on the current loading surface, changing its original configuration (as defined by the hardening rule).

An isotropic hardening model defines the change in size of the yield surface. This model has been widely used in the literature to represent the cyclic stress-strain behaviour of materials [108]. When a uniaxial test specimen is subjected to tensile deformation beyond the yield stress, as shown in Figure 2.8(a), plastic strain is introduced in the material. The maximum stress achieved during tensile deformation determines a new yield limit that is mirrored in compression loading. If the stress is further increased in compression, additional yielding and material hardening will occur, and this further increases the yield strength. Similar behaviour will occur in the next application of tension. An isotropic hardening model is usually assumed for cases where the load is monotonically increased. However, this model does not account for the Bauschinger effect and therefore does not represent cyclic loading very well [108].

The isotropic hardening component defines the variation in cyclic stress hardening, which in turn gives the yield surface size, σ^0, as a function of the equivalent plastic strain ε^{-pl}. It is derived by [108]

$$\sigma^0 = \sigma :_0 + Q_\infty \left(1 - e^{-b\varepsilon^{-pl}}\right) \qquad 2.3$$

Where $\sigma :_0$ is the size of the yield stress at zero equivalent plastic strain, obtained from the first cycle (refer Figure 2.8 (c)). Q_∞ is the maximum change in the size of the yield surface, which can be calculated as the difference between the asymptotic material response and $\sigma :_0$ (refer Figure 2.8 (c)). b is the rate at which the size of the yield surface changes as the material plastically deforms. The size of the yield surface in the i^{th} cycle, σ_i^0 can be evaluated from [108]

$$\sigma_i^0 = \frac{(\sigma_i^t - \sigma_i^c)}{2} \qquad 2.4$$

Where σ_i^t is the peak tensile stress in the plastic range and σ_i^c is the minimum compressive stress in the elastic range as in Figure 2.8 (a).

Similarly, the equivalent plastic strain of the i[th] cycle can be obtained using the following equation [108]

$$\varepsilon^{-pl} = \frac{1}{2}(4_i - 3)\Delta\varepsilon^{-pl} \qquad 2.5$$

Where $\Delta\varepsilon^{-pl}$ is the plastic strain range of cyclic deformation and the i[th] cycle. From Q_{∞}, $\sigma :_0$ and data pair $\sigma_i^0, \varepsilon^{-pl}$ the rate at which the size of the yield surface changes b can be evaluated thus [108]

$$b = \frac{\left(1-\frac{\sigma^0-\sigma:_0}{Q_\infty}\right)}{\varepsilon^{-pl}} \qquad 2.6$$

A kinematic hardening model deals with translation of the yield surface in stress space; see Figure 2.8(b). In this model, the equivalent stress defining the yield surface, σ_i, remains constant and equal to the equivalent stress, σ_0, which defined the yield surface at zero plastic strain, as seen in Figure 2.8(b). Therefore, when a test specimen is uni-axially loaded beyond the yield limit and unloaded into compression, the new compression yield limit is smaller in magnitude than the yield point in tension. In the kinematic hardening model, the elastic range is fixed at twice the initial yield stress value, and never increases.

The kinematic hardening law is given by [108]

$$\dot{\alpha} = \sum_i C_i \frac{1}{\sigma_0}(\sigma - \alpha)\dot{\varepsilon}^{-pl} \quad 2.7$$

Where C_i is the initial kinematic hardening modulus and $\dot{\alpha}$ is the deviatoric part of the kinematic hardening tensor α, which is also known as the back stress tensor. Both parameters C_i can be evaluated from stabilized cyclic test data, as shown in Figure 2.8 (b), σ is stress tensor, σ^0 is the equivalent stress defining the size of the yield surface and $\dot{\varepsilon}^{-pl}$ the equivalent plastic strain rate.

A mixed hardening model can represent both the size changes of the yield surface and its translation through the stress-strain space. A Lamaitre-Chaboche hardening model [109] is widely used, where the evolution of the yield surface is formulated by combining two components; the isotropic hardening component and a non-linear kinematic hardening component. Its implementation in the ABAQUS finite element code can be found in the user manual [110].

The mixed hardening model describes the translation of the yield surface in the stress space using the back stress $\dot{\alpha}$, which is expressed as [24,108]

$$\dot{\alpha} = C_i \frac{1}{\sigma^0}(\sigma - \alpha)\dot{\varepsilon}^{pl} - \gamma_i \alpha \dot{\varepsilon}^{pl} \qquad 2.8$$

Where Ci are the initial kinematic hardening moduli and γi determine the rate at which the kinematic hardening moduli decrease with increasing plastic deformation. C_i and γi are material parameters which are calibrated from monotonic or cyclic test data and $\dot{\varepsilon}^{pl}$ is equivalent plastic strain or plastic path length. σ is the stress tensor,σ^0 is the equivalent stress defining the size of the yield surface. The data pair α_i and $\varepsilon_i^{-\rho l}$ can be calculated from the following equations [108]

$$\varepsilon_i^{pl} = \varepsilon_i - \frac{\sigma_i}{E} - \varepsilon_p^0 \qquad 2.9$$

$$\alpha_i = \sigma_i - \frac{(\sigma_1 + \sigma_2)}{2} \qquad 2.10$$

$$\sigma_s = \frac{\sigma_1 + \sigma_2}{2} \qquad 2.11$$

Where σ_s is the stabilized size of the yield surface. Using data pair α_i and $\varepsilon^{-\rho l}$ calculated from equations 2.9 and 2.10, the non-liner kinematic hardening parameters are defined using equation 2.8.

A mixed hardening model has been used widely to simulate the cyclic hardening in weld simulations due to its accuracy in reproducing cyclic strain-controlled tests, thermo-

mechanical fatigue and in predicting residual stress [21,24,57,111]. In this research study, this mixed hardening model was used for predicting cyclic stress-strain curves. Further detail on previous work using this model to predict cyclic deformation is discussed in section 2.5.3.

2.4 Residual Stresses Measurements Around Welds in 316L(N)

Residual stresses are the stresses which remain in a material in the absence of any external force. Figure 2.9 shows various processes that can generate residual stresses at the macroscopic and microscopic levels [7,112]. In multi-pass welding, the residual stress distribution is affected by different aspects of the welding process, such as the number of passes, the heat generated during welding, the depth and the width of the weld bead [56,113,114]. The presence of tensile residual stresses at a welded joint can reduce the lifetime of the material by increasing its susceptibility to stress corrosion cracking, fatigue and creep growth [4]. Macro stresses are classified as type I residual stress, they are introduced by fabrication processes such as welding or machining. They self-equilibrate over the length scale of the specimen and they can be described by continuum mechanics [7]. Type II residual stresses are inter-granular stresses and typically self-equilibrate between grains or phases. Type III residual stresses are intra-granular stresses that self-equilibrate over a few interatomic distances, and are associated with point defects and dislocations. This thesis is concerned with the type I residual stresses, introduced by welding.

There are a wide range of mechanical and physical techniques developed to measure residual strains or stresses in components and structures [112,115–117]. The strain sensitivity and the spatial resolution of the various strain analysis techniques are represented in

Figure 2.10. Residual stress measurement techniques are broadly classified into two categories: destructive and non-destructive. Destructive methods include hole drilling; the slitting method, the contour method, FIB milling etc., and the non-destructive methods includes X-ray diffraction, neutron diffraction, ultrasonic, Raman spectroscopy etc. In this research study, type 1 residual stresses developed due to the welding process were measured using neutron diffraction. The reasons for choosing neutron diffraction were:

1. The test specimen could not be destroyed as it is part of an international round robin, the NeT project (section 2.5.2).
2. Neutrons have sufficient penetration to measure strains and stresses to the depth required.
3. The wavelength of the neutrons is of the order of the inter-planar spacing. As a result of this, a diffraction angle (2θ) close to 90° enables the user to use a square geometry gauge volume. This allowed measurement in three orthogonal directions (unlike synchrotron diffraction).

2.4.1 Principle of neutron measurements of residual stress:

The crystalline lattice of the material acts as an atomic strain gauge. The spacing, '*d*', between atoms in the crystalline lattice varies depending on the applied stress, as shown in Figure 2.11. The increase or decrease of lattice spacing can be determined from the angular shift (Δ2θ) in the diffracted neutron beam, as defined by Bragg's law;

$$\lambda = 2dsin\theta \qquad 2.12$$

Where, λ is the wavelength of incident beam, θ is the angle of diffracted beam as shown in Figure 2.11, and d is the inter-planar spacing of the measured direction defined by the Q-vector. The d spacing for a particular lattice reflection can be determined if the

wavelength of the incident beam and the angular position of the diffracted peak are known [112,118,119]. Two types of neutron source (continuous and spallation) are available for residual stress measurement [117]. The main differences between spallation and reactor sources are summarized in Table 2.2. In this study, spallation neutron diffraction was used to measure strain in three-pass welded austenitic stainless steel.

2.4.2 Neutron diffraction instruments

The ENGIN-X diffractometer at the ISIS spallation source (Oxford, UK) and the VULCAN diffractometer at the Spallation Neutron Source (SNS), Oakridge, USA were used in the present research. At these facilities accelerated 'bunches' of high-energy protons from a synchrotron ring collide with a heavy atomic target to generate neutrons in sharp pulses. The neutrons pass through a moderator to achieve thermal equilibrium and are guided to the experimental instruments. The layouts of the ENGIN-X instrument at ISIS and VULCAN instrument at SNS are shown in Figure 2.12. The detectors on each instrument are fixed at 90° to the incident neutron beam. The sample is placed with the scattering vector (Q-vector) bisecting the incident and diffracted neutron beams. The main advantages of a spallation neutron source over a reactor source are:

1. A single pulse of neutrons generated in a spallation process has higher neutron intensity.
2. A 'white' beam with different neutron wavelengths enables various families of lattice reflections to be measured simultaneously.

The velocity (v) of a neutron is defined by

$$v = L/t \qquad 2.13$$

Where L is the total flight path (from the moderator to the detector) and t is time of flight (TOF). However, according to de-Broglie wave theory, the wavelength 'λ' is inversely proportional to the velocity.

$$\lambda = \hbar/mv \qquad 2.14$$

Where m is mass of neutron, $\hbar$ is is Planck's constant. combining equation 2.14 and equation 2.13 gives

$$\lambda = (\hbar t)/mL \qquad 2.15$$

Substituting equation, 2.15 into the Bragg equation 2.12 gives the TOF in microseconds.

$$t = mL2dsin\theta/h \qquad 2.16$$

Therefore, at a constant diffraction angle θ, the variable d is directly proportional to the variable t [120]. Hence, the most energetic neutrons arrive at the specimen first and the least energetic neutrons reach it last. In a spallation source the intensity of peaks is plotted as a function of time of flight (TOF) as shown in Figure 2.13. To conclude, in a spallation source the values of two variables in the Bragg equation are already known; the angle (θ=90°) and the wavelength (λ); therefore the third unknown variable, 'd', can be measured. Further details about the ENGIN-X and VULCAN instruments are available in published literature [121–127].

2.5 Evaluation of Residual Elastic Strain and Stress Using Neutron Diffraction

When a crystalline material is loaded, its inter-atomic spacing will change, depending on the applied load. The difference in the inter-atomic spacing can be measured using

neutron diffraction. To measure the strain, the *d* spacing in both strain free material and strained material is required, then the elastic strain can be calculated as; [63,64,73]

$$\varepsilon = ((d - d_0))/d_0 \quad 2.17$$

Where d_0 is the unstrained lattice parameter and d is strained lattice parameter. By calculating the strain values for each direction using equation *2.17*, stress, σ, can be determined using the following equation [129];

$$\sigma_{xx} = [\{E/((1+\upsilon) * (1-2\upsilon))\} * \{(1-\upsilon)\,\varepsilon_{xx} - \upsilon(\varepsilon_{yy} - \varepsilon_{zz}\}] \quad 2.18$$

Where, σ_{xx} is stress in the *x*-direction of the sample (say along the weld), E is the Young's modulus of the bulk material and υ is Poisson's ratio.

2.5.1 Issues affecting strain/stress measurement using neutron diffraction

In this section, important issues affecting the reliability of strain measurement using neutron diffraction are described.

Stress free lattice parameter (a_0): from equation *2.17* it is clear that the unstrained lattice parameter, a_0 also known as the stress-free lattice parameter, plays a key role in evaluating residual strain [128,130–132]. Small variations introduced by differences in chemical composition, inter-granular strains and thermal history can lead to large uncertainties in a_0 due to variations in intensity and/or peak broadening [10,108]. In welded samples, the non-uniform thermo-mechanical history introduces variations in grain size, texture and degree of plastic deformation, which can shift the diffracted peaks. Due to non-homogeneity in the sample, a number of stress free reference values are required to properly interpret the measured strain [130]. A lot of underpinning research work was performed in establishing the standards for residual stress measurement using neutron diffraction [118,135]. The recommendations for selecting and determining the stress-free lattice parameters are available in the literature [135,136].

Many practitioners have used combs, matchsticks, or cylindrical pins and cubes, or cuboids for stress free lattice parameter measurements [137–140]. However, in extracting a 'stress free' sample, the relaxation of macroscopic stress significantly affects the inter-granular stress state [140]. Another effect has been noted in combs, where the comb teeth have been reported to retain macro stress[141]. For weldments, the gradual changes in the stress free lattice spacing resulting from the non-uniform thermal history, and the associated variation in microstructure, necessitates the extraction of stress-free samples from many different locations across a weldment [130].

Gauge Volume effect: The spatial resolution of neutron diffraction measurements depends on the gauge volume chosen [142–146]. The geometrical dimension of the gauge volume depends upon the incident neutron beam and collimator dimensions. As described earlier, the nominal gauge volume for both the ENGIN-X and VULCAN diffractometers is a perfect cuboid [117]. The centroid is defined by the intersection of the incident and the diffracted neutron beams. However, in reality, the neutron beam is divergent, which changes the shape and size of the true gauge volume [147,148]. This is known as the instrumental gauge volume, as shown in Figure 2.14. The centroid of the instrumental gauge volume is the intensity-weighted centre of this volume. The instrumental gauge volume and the nominal gauge volume are properties of the diffractometer itself.

The sampling gauge volume is the volume from which measurements are obtained, and it is part of instrumental gauge volume [149,150]. The sampling gauge volume is strongly affected by its geometrical location within the sample, as well as by material characteristics such as texture, cold work, neutron beam absorption etc. [129,142,150,151]. The centroids of the instrumental gauge volume and sampling gauge volume are identical when completely immersed in a non-neutron absorbing material. However, the sampling gauge volume is affected by partial filling of the instrument gauge volume, attenuation of

neutrons within the sample and the wavelength distribution across the incident beam [145,151–153]. The centroid of the sampling gauge volume is the weighted centre of the gauge volume after accounting for these effects [150].

The nominal gauge volume can most closely be achieved by positioning the slit close to the sample, minimizing the divergence of the neutron beam. However, partial gauge volume immersion, as shown in Figure 2.15, introduces a systematic shift in the diffracted peak, known as a pseudo strain. In TOF, the pseudo strain can be given by [150]

$$\frac{\delta t}{t} = \frac{\delta d}{d} + \frac{\delta l \sin\theta}{l \sin\theta} \qquad 2.19$$

Where t is time of flight, θ is the diffraction angle and l is the total distance travelled by neutrons from the moderator to the detector. From equation *2.9*, it is clear that the shift in a peak is due to the contribution of lattice strain and the variation of '$l\sin\theta$'. The term '$l\sin\theta$' in equation *2.19* represents a weighted average of '$l\sin\theta$' over the whole gauge volume. Pseudo strain also occur when analysing strain in highly absorbing material (such as boron or hydrogen).

Creek *et al.* [154] investigated the effect of pseudo strain on measurement by pulsed neutron sources but did not consider the effect of the incident beam divergence. Creek modelling showed incomplete filling of the gauge volume will generate pseudo strain of 1000με in comparison to the resolution of instruments used to measure such strain (50 με). Suzuki *et al.* [142] have proposed a new analytical model, which can be used to simulate different effects of pseudo-strains. Using spallation source, Suzuki investigated the effect of neutron attenuation, surface effects and a strain distribution on pseudo strains generation. In completed filled gauge volume, the pseudo strains are developed due to change in neutron-weighted center of gravity (ncog) position and it increased with an increase in the size of the gauge volume. Typical pseudo strain distributions due to the

surface effect were noticed through the surface strain measurement regardless of gauge size. Pseudo strains developed due to neutron attenuation and/or the surface-effect exhibited a wavelength dependence associated with a wavelength dependence of the neutron divergence in the super mirror guide tube. Wang *et al* [151,155] have analysed the issues contributing to the pseudo strain: variation of the wavelength across the incident beam, an asymmetric clipping of the diffracted peak profile and lateral displacement of the gauge volume relative to the detector. In Wang's experimental investigation, the error in strain measurement due to wavelength dependent attenuation were within ±50με. The small shift observed due to attenuation in the incident beam can be minimised by placing the sample in preferable place in the diffracted beam. Whilst Hsu *et al.* [153] investigated the multiple scattering and wavelength dependent attenuation effects in steel plates. Hus's systematic investigation has summarised the Bragg edge location between 1.4Å and 3.0Å for a number of common metals. The neutron attenuation coefficient for polycrystalline materials decreases suddenly for certain neutron wavelengths, this effect is known as Bragg edges. Hsu's investigation recommends, if the strain measurements are located at depth of material then one should avoid using neutron wavelength within $\Delta\lambda/\lambda =$ 0.02Å of the Bragg edge. This is because lower order Bragg edges tend to have a bigger discontinuity in total cross section.

Grain Size Effects:

In neutron diffraction, uncertainties in a residual stress measurement depend on the number of grains diffracted [156,157] and the number of grains diffracting depends on the gauge volume size chosen. Therefore, for a given gauge volume, the uncertainties in residual stress are lower for a fine grained sample than in a sample with a large grain size, due to the former's larger number of diffracting grains[129,158].

In polycrystalline material, inhomogeneous plastic deformation due to welding can lead to the development of large inter-granular residual strains [129]. In grains, which are orientated favourably in the loading direction, slip systems will activate and those grains will deform plastically, due to the higher resolved stress. Upon unloading, the size of the plastically deformed grains remains largely unchanged, which hinders the elastic recovery of the non-deformed grains. As a result, elastic strain is locked into the non-deformed grains upon unloading [140]. These elastic strains, in different sets of *hkl* planes, are measured by neutron diffraction [159–161].

The slit positions close to the specimen can cause 'clipping' of the diffracted peaks, shifting their apparent position. These can introduce an error in the determined strain. Webster *et al* [151] demonstrated that this effect was more severe in coarse grained materials. The same paper also demonstrated that an uneven distribution of large grains in the sampling volume can also shift the diffraction peak position on the detectors. Neov *et al* [162] analysed the residual stress in an SS347 grade welded stainless steel specimen. The tensile strain measurements were affected significantly by the grain size of the plate, by twice the real strains measured in the plate. However, by rocking the sample, more grains were diffracted within a given gauge volume, which led to more realistic strain distributions being measured.

2.5.2 Weld residual stress NeT-benchmark

Several different international consortium activities have been undertaken on the prediction and characterization of weld residual stress and distortion of welded samples [13,14,163,164]. One such group is the European Network on Neutron Techniques Standardization for Structural Integrity (NeT)[15]. The main objective of this group was to define recommendations for the prediction and measurement of welding residual stress.

Residual stress measurements using different techniques on benchmark weldments, under well controlled conditions, have been performed by members of this round robin network [16] in order to assess and improve the reliability of residual stress measurements. The measurement techniques applied include neutron diffraction, synchrotron x-ray diffraction, the contour method, deep hole drilling and incremental surface hole drilling. In parallel, round robin finite element analysis residual stress simulations have been performed and compared with the results from the above stress measurements. Several benchmarks have been defined, each managed by a different task group (TG). For example TG1 tackled a single pass weld TIG bead deposited on the surface of the austenitic stainless steel 316L (180×120×17 mm^3) [16,46,61,66,157,165–168].

TG4 is investigating residual stress developed around a three-pass slot weld in a 316 austenitic stainless steel plate (194×150×18 mm^3). The specimen geometry is representative of a weld repair. Several numerical and a few measurements studies have been published related to the NeT TG4 round robin [21,22,24,57,111,139]. The present research is based upon the NeT TG4 benchmark weldment.

2.5.3 Previous NeT TG4 benchmark studies

The distribution of residual stress introduced into a welded austenitic stainless steel component depends on its geometry, the welding parameters and the welding sequence [113,114,169,170]. Benchmark samples are valuable in that they allow analysts to evaluate and improve the accuracy of residual stress measurement and weld modelling [171]. Details of the NeT TG4 benchmark weldment's design and manufacture are given in Chapter 3. The residual stress measurement protocol [172] recommended by the NeT consortium for TG4 analysis is described in Chapter 4.

The first experimental residual stress characterization of a NeT-TG4 weldment was performed at the beamline ID15a of the European Synchrotron Radiation Facility (ESRF)

[139] see Figure 2.16. This experiment has analysed both macro strains and intergranular strains (along line BD only, refer section 4.2.1, Chapter 4) in weldments. The measured lattice parameters for top weld, bottom weld and parent stress free cuboids during this experiment were 3.59653 Å, 3.59716 Å and 0.359752 Å respectively. The differences between the values are due to the slightly different chemical compositions of the filler wire and the parent material. Along plane D (refer to Figure 3.3) the maximum longitudinal residual stress was observed in the HAZ, while the maximum transverse stress, was observed in the first and second weld beads. However, along plane B (refer to Figure 3.3) the maximum transverse stress was noticed in the HAZ, not in the weld bead as observed in Plane D. The residual stresses measurement at the bottom of the plate exhibited stress of ±200 MPa at the centre and ends of plane D and B respectively. The uncertainties recorded during this experiment are ±50 MPa [21]. The longitudinal and transverse stresses in the weld plate are remarkably well self-balanced. However, the severe weld cyclic deformation significantly affected the inter-granular stress analyses along line BD due to the weak diffracted peak intensity and broadening. The same benchmark weld plate 3-1A analysed at ESRF, was later analysed at different reactor sources as summarized in Table 2.3. Muransky [111] has analysed the residual stresses in 3-1A using both neutron diffraction source and finite element (FE) analysis. The FE analysis of weld residual stress was performed using two methods; 3D moving heat source (MHS) and block dumped (BD). The complex 3D stresses using MHS were in better agreement with neutron diffraction results than those analysed using the BD method. However, both methods estimated the longitudinal and normal residual stresses over by 100 MPa or 750 με, in comparison to neutron diffraction results. Later in 2012 Muransky *et al.* [57] compared neutron diffraction results from ESRF with MHS FE predictions. The predicted residual stress distribution and plastic deformation levels were

analysed as a function of weld temperature. However, the effect of DSA on plastic deformation of the material was not considered in the analysis. There is a large discrepancy between the predicted and measured residual stresses in the weld metal. This results from the non-availability of accurate weld metal mechanical properties, which are used as the input database in weld simulation. In later work of Muransky *et al.* [22], improved modelling has minimized the difference between predicted and measured residual stress. However, the papers [22,57] have not explained the possible reasons for the difference between the other neutron diffraction and those from ESRF. Smith *et al.* [21] have presented measurement of the residual stress along line BD of 3-1A weldment (refer to Chapter 4, section 4.2.1), made at different neutron diffraction sources as summarized in Table 2.3. The mean of the measured residual stresses was compared with the predicted stresses. All the diffraction results have shown an average peak residual stress of 400MPa along the weld direction and an average peak residual stress of 250MPa along the transverse direction. However, the paper did not describe the possible reason for the substantial scatter in the results as shown in Figure 2.16.

Smith *et al.* [24] found that the most accurate predictions of weld residual stresses were achieved using a mixed isotropic-kinematic material constitutive model (refer section 2.3.5). However, the accuracy of the prediction depends on the constitutive model selected and the material data used to fit the model parameters [171,173]. The general constitutive model behaviour and its accuracy were validated by comparing the simulated symmetric cyclic loading results with experimental symmetric cyclic loading at room and high temperature [171]. In the present study, the mixed hardening material constitutive model was used to predict the stress-strain curve of cyclic loading. Due to the complexity of austenitic stainless steel welds, the following assumptions were used to simplify the mixed hardening constitutive model.

1. The isotropic hardening parameter Q_∞, the maximum change in the yield surface size, and b, the rate at which the size of the yield surface changes, were defined from a single strain range. These parameters were then applied to all strain ranges, at room and high temperature.
2. Isotropic hardening b, and kinematic hardening γ_i parameters are considered constant at both room and high temperatures. Hence, in the mixed hardening model, only C_i and Q_∞ will vary with temperature and strain range.

As described in section 2.3.4, the amount of cyclic hardening increases with the strain range experienced [27,28,86,101,106,174–177]. Therefore, a representative strain range was chosen, based on the cyclic deformation experienced by the weld (±1.5% and ±2.5% at strain rate 4×10^{-4}/sec [16,63]). Limited cyclic deformation data was available from the NeT consortium. Smith *et al.*[21,24], Joostne *et al.*[178] and Muransky *et al.* [22,57,111] have used a mixed hardening model and a pure kinematic hardening model to predict the weld cyclic deformation. Smith *et al* [21,24] reported that the mixed isotropic-kinematic hardening model, with two kinematic hardening parameters (C_i and γ_i), has predicted the weld cyclic deformation of material with high accuracy [16,21]. The required material input data for the weld cyclic loading simulations was derived from the second cycle of isothermal strain-controlled symmetric cyclic testing of samples of the base metal and weld metal [21]. However, Joostne *et al.* [178] has reported that, at high temperature, the stress strain prediction from a mixed hardening model underestimates the experimental cyclic loading results.

Dewees *et al.* [179] has used a linear kinematic hardening model for predicting cyclic hardening. In his model, the parameters are evaluated from the saturated or stabilized cycles. A stabilized cycle means that the stress does not change, with cycling at a fixed strain range. The cyclic hardening predicted, using this saturated cyclic loading, agrees

well with experimental results both at room and high temperatures. This model is a much simpler approach than when fitting mixed hardening behaviour. Joostne *et al.* [178] has shown that this model, too, under predicts the stresses. In all the numerical analyses described so far, the effect of strain rate on the strain hardening of the material was not considered in either welding or cyclic deformation simulations.

2.6 Plastic Strain Measurement Around Welds in 316L

Various experimental methods such as hardness measurements, neutron diffraction and electron backscatter diffraction (EBSD) provide indirect measures of the degree of plastic strain in deformed sample.

Hardness measurement can be used to assess the plastic strain in a material [182,183]. Hardness is determined by measuring the material's resistance to plastic deformation and this often shows a good correlation with the level of plastic deformation of a material [182,184]. However, a poor surface finish can lead to incorrect indentation measurement, and microstructure variations and heterogeneous deformation etc in the sample will limit the accuracy of the hardness measurements. So, hardness testing is usually used for assessing plastic strain at the macro level of a material.

In neutron diffraction, the width of a diffracted peak increases when a material has undergone plastic strain. This broadening can be measured using the full width at half maximum (FWHM) of the peak [129,185]. The FWHM can be measured using a single peak fitting routine. However, peak broadening can also arise from a non-uniform chemical composition [132] and it is difficult to differentiate between the peak broadening effects of plastic deformation and those due to non-uniform chemical segregation developed during the fabrication process.

The electron backscatter diffraction technique (EBSD) has specific advantages over the other techniques, such as the submicron scale spatial resolution, providing a direct measure of the grain size and shape, phase identification, revealing crystallographic orientations and correlations between various measures of the local misorientations induced in the material, and plastic deformation [33]. In this study, the EBSD technique was used for evaluating the plastic strain distributions resulting from welding.

2.6.1 Electron Backscatter Diffraction (EBSD)

EBSD is used to analyse the microstructure of a crystalline material. Within an SEM chamber, the interaction of the electron beam with atoms near the specimen surface produces backscattered electrons as well as other types of scattering. Backscattered electrons fall on a phosphor screen to form a pattern as shown in Figure 2.17. The phosphor screen is placed closed to the sample to increase collection of the backscattered electron (BE) signal. Tilting the sample, which allows more scattered electron to escape from the surface, due to the shallower electron penetration, [186] also increases the BE signal. Typically the sample is tilted by 70° for EBSD. Below this angle the signal to noise ratio is lower, while above 70° the large intensity gradient across the phosphor screen make it difficult to obtain high quality patterns [187]. Electrons satisfying the Bragg's condition (equation 2.14) are diffracted back from the specimen surface, forming patterns on the phosphor screen, as shown in Figure 2.18 [177]. These lines are known as Kikuchi lines or bands. They arise from high angle diffraction cones from each set of planes [186]. In EBSD the Bragg angle 'θ_B' is small, so the cone segments appear as straight lines and the centreline of the Kikuchi bands represents the trace of an atomic plane. The intersections between Kikuchi bands can be used to calculate a grain's orientation in the material [186].

2.6.2 Instrumental factors in EBSD

In order to build up an orientation map, the SEM electron beam is positioned sequentially on the surface of the material specimen at a grid of points separated by a uniform interval (step size), chosen by the user. At each step, the electrons diffracted from the surface of the sample form a pattern on the phosphor screen. These patterns are recorded using a charge coupled device (CCD) camera and transferred to a computer. The EBSD online acquisition software receives the image and detects the position of the bands using a Hough transformation [188]. Based on the space group of the material, as input by the user from a materials database, theoretically calculated patterns [188] from different predefined orientations are compared with the experimental one to find the closest match. The reliability of indexing is assessed through a pattern misfit parameter known as the mean angular deviation (MAD) [189]. A low MAD value indicates a good match to the theoretically calculated patterns and shows that the measured orientations are reliable [189].

The quality of Kikuchi patterns depends on the exposure time; accelerating voltage, step size, data binning, probe current and the working distance. A long acquisition time for each point gives a high signal/noise ratio and generates good quality Kikuchi-patterns, but leads to exposure times that are not suitable for in-situ experiments. Higher beam currents also give more intense patterns.

The accelerating voltage controls the wavelength of the incident electrons, and so the angular separation of the Kikuchi bands. At higher accelerating voltages narrower Kikuchi bands are formed on the phosphor screen. For narrow bands, the centrelines can be located very accurately. However, increasing the acceleration voltage increases the electron energy, and so the electrons penetrate deeper into the specimen, degrading the spatial resolution. On other hand, reducing the accelerating voltage decreases the penetration depth but the intensity of the Kikuchi patterns decreases [186]. This problem can

be minimised by increasing the number of frames averaged, but this increases the acquisition time, per point.

The angular resolution of an EBSD system defines the smallest identifiable orientation difference between pixels of a grain orientation map. During orientation mapping, poor angular resolution results in "orientation noise" in the acquired data. The angular resolution depends on both the quality of the Kikuchi patterns and on the resolution of the CCD. The resolution of the CCD is controlled by the number of pixels the camera is recording. At higher pixel rates, finer displacements in the Kikuchi patterns can be recorded, allowing accurate orientation measurement, but the acquisition time increases and more memory is needed to store the data [190]. The sensitivity of the CCD camera can be changed through pixel binning. Binning effectively increases the pixel area and reduces the angular resolution. The quality of the Kikuchi pattern and the precise indexing of the Kikuchi pattern are very important in defining local orientations for EBSD data analysis.

2.6.3 EBSD data analysis

The EBSD data recorded from each point contains information on the phase orientation, Kikuchi pattern quality, and its position in the image space. Where there is no orientation information available, the points are known as zero solutions. On well prepared samples, these occur most commonly in severely deformed areas, or where Kikuchi patterns overlap at sub-grain and grain boundaries. This section explains how local plastic strain can be assessed from an EBSD grain orientation map using post-processing software. There are two methods by which localised plastic strain, resulting from dislocations interactions and pile-ups, can be evaluated using EBSD

Method 1 is based on the quality of the EBSD map (image quality maps).

Method 2 is based on the degree of intra-granular misorientation shown on the map [32,191].

The image quality map is based on the quality of the diffracted pattern [32]. Strained regions in the microstructure give poorer patterns than unstrained regions. This is due to diffracted patterns are superposition from each individual subgrain[32]. However, the image quality is also affected due to poor sample preparation and the camera settings, thus preventing reliable quantitative measurement of strain. Further information on the image quality method is available in a publication by Wright *et al.* [32]. In this study, quantitative analysis of misorientations is adopted for evaluating local plastic strain.

2.6.4 Quantitative analysis of misorientation

During plastic deformation the material generates and accumulates dislocations which can be divided into two classes: statistically stored dislocations (SSDs) and geometrically necessary dislocations (GNDs) 32,188. The Burgers vectors of the statistically stored dislocations sum to zero, whilst the sum is non-zero for geometrically necessary dislocations. SSDs are accumulated by the statistical trapping of dislocation during plastic deformation. Hence they are randomly distributed and have no geometrical consequence. The diffraction patterns from the SSDs are degraded due to local perturbations of diffraction lattice planes leading to incoherent scattering, while, the accumulation of GNDs is a result of strain gradient fields due to geometrical constraints of crystal lattice. During plastic deformation GNDs are formed in order to preserve the lattice continuity through accommodating lattice misorientations.

In this research study, the following metrics have been used to quantify the plastic strain from these lattice rotations: Kernel average misorientation (KAM), Low Angle Boundary fraction (LABf) and Average Intragrain Misorientation (AMIS)[32,192].

2.6.4.1 Kernel average misorientation (KAM)

This metric is used to measure the local lattice deformations by considering the misorientations between each measurement point and all the points within a small 'kernel' about that point, but including only those misorientations of less than 2° (refer toFigure 2.19). The measured KAM from each point (for example using a kernel area of 3×3 measurement points) within the deformed crystal lattice can be presented as a frequency distribution. The frequency distribution of KAM data can be fitted using a lognormal distribution [193]. The mean of this lognormal probability distribution has recently been used to investigate the plastic strain in a deformed sample of 316H steel [194].

2.6.4.2 Low angle boundary fraction (LABf)

In this metric [32] the misorientation between adjacent points is measured, concentrating on the angular misorientation range between 2° and 15°, which are taken to constitute a low angle boundary. If the misorientation angle between two adjacent points is greater than 15°, they are expected to be separated by high angle grain boundary. The low angle boundary fraction is calculated by taking the ratio of the length of low angle boundaries to the length of low angle boundary and length of high angle boundaries [192].

2.6.4.3 Average intragrain misorientation (AMIS)

AMIS considers the relative misorientation of all points within a grain. For each grain this metric computes an average misorientation from the misorientations between each measurement point within a grain, and the mean grain orientation. The $AMIS_a$ is an overall average of the average intra grain misorientations from a constituent EBSD grain map, using the following equation [194].

$$AMIS_a = \frac{1}{m}\sum_{j=1}^{m} I_j \qquad 2.20$$

Where 'm' is the total number of grains in an EBSD map, and 'I' represents the AMIS value of each individual grain being measured.

2.7 Welding plastic strain analysis using EBSD

The welding process introduces non-uniform plastic strain into a component. For the TG4 benchmark, this has been predicted by NeT consortium members, using numerical simulation [22,57]. Experimental results from this research study are contributing to the NeT consortium database. For the first time, weld plastic strain is quantified and compared using EBSD and hardness measurements. In addition, very few studies have been published on evaluation of accumulated weld plastic strain using EBSD. The different methods available for strain analysis using EBSD were described earlier, and further information is available in the literature [32,195].

2.7.1 Previous studies on weld plastic strain analysis using EBSD

Table 2.4 summarised the work done so far in quantifying the plastic strain in welded sample using EBSD. Saukkonen *et al.* [196] both characterized the weld microstructure and quantified the plastic strain in a prototype, boiling water reactor, pipe weld made of AISI 304 stainless steel. The plastic strain was quantified by comparing the weld intra-grain misorientations with the calibrated misorientation vs strain curve measured from defined tensile deformed samples. The highest levels of plastic strain (10-20%) were detected in the HAZ of the weld pipe. However, some parameters, which play an important role in determining the plastic strain, such as the temperature of the calibration tests, the weld filler metal and the limiting misorientation angles used for the calibration curve, were missing in this report.

Saez Maderuelo *et al.* [197] have characterized the plastic strain distribution in nickel alloy 600, welded with weld metal 182, using the KAM metric and a metric similar to AMIS. The plastic strain in the HAZ of alloy 600, with two different thermal treatments has been estimated at between 8% and 10% strain, but the strains evaluated from the same sample varied significantly from one metric to another.

Hou *et al.* [198] have analysed the plastic strain in the heat affected zone of a welded joint, between alloy 690TT and alloy 52, using the metric grain average misorientation (GAM) which is similar to $AMIS_a$. Using a GAM calibration curve evaluated from a series of specimens of the alloy 690 base metal tensile deformed at room temperature, the plastic strain increased from 15% at the weld top to 17% at the weld root, and 20% in the HAZ close to the fusion boundary. For all samples, lower strains were measured in the weld alloy 52 than in the HAZ.

Ming *et al.* [199] has quantitatively estimated the strain across dissimilar metal welds between SA508 and 309L, and between 308L and 316L, using KAM. The analysis indicated the dissimilar metal HAZ has a higher plastic strain than the weld metal.

The local deformation in 316GN welded pipe and alloy 600 base metal welded with alloy 82 have also been evaluated using KAM [31,200].

Despite the different weld parameters, number of weld deposits, the weld filler wires, step sizes and different EBSD metrics used, all the published results so far have indicated the peak strain is around the HAZ. This is due to cyclic deformation of the HAZ during the multi weld processes, as described earlier. However, all the calibrated misorientation metrics calibrations were obtained from room temperature tensile tests, while the deformation processes in welded samples takes place at high temperature, so the obtained absolute values of the plastic strain will be questionable [188].

2.7.2 Previous studies on cyclic accumulated strain analysis using EBSD

As described earlier, the cyclic deformation of a material can lead to complex dislocation structures, and very few studies have quantified the accumulated plastic strain induced by cyclic deformation of material in isotropic conditions (such as uniform temperature, deformation etc.) using EBSD. Kamaya [201] has quantified the degree of inter granular misorientation developed due to the strain controlled cyclic deformation of 316 samples. The tensile sample deformed significantly more, and exhibited less fluctuation in crystal orientation inside the grain, in comparison to cyclically deformed sample. Local misorientations formed as a result of cyclic deformation were confined to clusters inside some grains, whereas they developed throughout the tensile samples. The degree of local misorientation increased with the strain amplitude. However, the paper did not account for the effects of poor sample preparation, or the process of EBSD data cleaning. Poor sample preparation will affect the quality of EBSD diffraction patterns and hence the raw

data [187,189,202]. Kamaya *et al.* [203] have investigated cyclic deformation with another metric; modified crystal deformation (MCD). The KAM analysis showed more data fluctuation in the fatigued sample than the MCD analysis, because KAM evaluated the local misorientation at each point, whereas MCD evaluated the misorientation across the whole grain.

2.8 Conclusion

There are many publications in the literature characterising weld residual stress distribution in austenitic stainless steel using neutron diffraction. However, variations in weld parameters (such as heat input), the sequence of weld deposits, geometry (such as pipe, plate, weld bead, etc.) produces highly scattered results. In structures whose structural integrity is of critical importance, such as primary pipe components in a nuclear power plant, a thorough and accurate assessment of the weld residual stress distribution state is essential. The experimental research carried out in this study presents the first attempts to identify all the issues affecting the reliability of residual stress characterization in the NeT-TG4 weldment. New residual stress measurements were taken at two spallation reactor sources, using the ENIGN-X and VULCAN neutron diffractometers. The measured weld residual stresses are compared with published results for the same benchmark sample (ID 3-1A) as was measured by the members of the NeT consortium.

Localized weld thermal cycles lead to non-uniform deformation of material through the thickness of the specimen. EBSD is a very promising technique in terms of assessing localized deformation at high spatial resolution. Most published results have analysed selective locations of multi-pass weld specimens using KAM and AMISa. All published results have quantified the accumulated plastic strain due to multi-pass welding, using room temperature based misorientation calibration curves. However, in real welding the

deformation takes place at high temperature. Therefore, the accuracy of such results is questionable, because the dislocation interaction mechanisms at high temperature are different from those at room temperature. The second objective of the present research is to demonstrate whether EBSD can quantify accumulated plastic strain resulting from one, two and three pass weld deposits in 316L steel using different EBSD metrics.

Finite element computational methods are increasingly being used for the prediction of residual stresses in welded engineering structures. However, the precision of numerical simulations is dependent on the accuracy of the material database and the assumptions applied to simplify the complexity of non-linear analyses. Incorrect assumptions will affect the reliability of the predicted residual stress values. One common assumption is to ignore the strain rate. But the yield stress and the rate of cyclic hardening/softening of the material vary significantly at different strain rates. At room temperature, a high strain rate increases material hardening compared to a material deformed at a slow strain rate. In contrast, at high temperatures (450°C - 650°C), the reverse is true because of DSA. This means that, the weld-cooling rate (which determines the material's strain rate) can affect the material deformation properties. Ignoring this effect may introduce significant error in predicted residual stress values. The results of this study will be used to investigate the magnitude of the possible error arising from ignoring the strain rate effects. A further source of error is that the input parameters for hardening models are usually evaluated from symmetric (tensile-compressive) cyclic deformation testing. However, in reality material cyclic deformation during welding is asymmetric (predominantly compressive). From the literature review, it is clear that the same material subjected to different symmetric cyclic deformation amplitudes will harden by different amounts. However, there have been no previous studies investigating strain controlled asymmetric cyclic deformation. The third objective of the present research is to examine how material

deforms under asymmetric and symmetric strain controlled conditions, at different strain rates and temperatures and how this may affect predicted stresses and strains around welds.

2.9 Tables

Table 2.1 Chemical composition of austenitic stainless steel AISI 316L (N)

Material	C	Si	Mn	P	S	Cr	Mo	Ni	Others
316L(N)	0.030	0.75	2.0	0.045	0.030	16.0/18.0	2.0/3.0	10.0/14.0	N 0.1/0.16

Table 2.2 Differences between reactor sources and spallation sources

Reactor Source	Spallation Source
Monochromatic wave length Continuous neutrons Only one grain family can be analysed (selected by user) Mobile neutron detectors	Polychromatic wave length Pulsed neutrons Multiple grain families can be analysed Neutron detectors fixed at 90°

Table 2.3 Residual stress measurements of 3-1A benchmark have taken place at different sources

S. No	Instrument	Source	316L Benchmark ID
1	European Synchrotron Radiation Facility (ESRF)	Synchrotron	3-1A , 1-1A
2	Australian National Nuclear Research and Development Organisation (ANSTO)	Reactor	3-1A , 2-1A
3	Forschungs Neutronenquelle Heinz Maier Leibnitz (FRM-II)	Reactor	3-1A, 1-1A
4	Helmholtz Zentrum Berlin (HZB-E3)	Reactor	3-1A
5	Institut Laue-Langevin (ILL)	Reactor	1-1A
6	Paul Scherrer Institut (PSI)	Reactor	1-1A

Table 2.4 Plastic strain analysis welded samples using EBSD

S.No	Material	EBSD Metrics	Quantified Plastic Strain	Location	Direction of analysis with respective to weld bead
1	AISI 304 [196]	AMISa	10-20%	HAZ	Perpendicular
2	Nickel alloy 600 [197]	KAM, AMISa	8% and 10%	HAZ	Perpendicular
3	Alloy 690TT and alloy 52 [198]	AMIS	15% at weld top and 17% at the weld root	HAZ	Perpendicular
4	Dissimilar metal [199]	KAM	-	HAZ	Perpendicular

2.10 Figures

Figure 2.1 Different zones in the weld sample

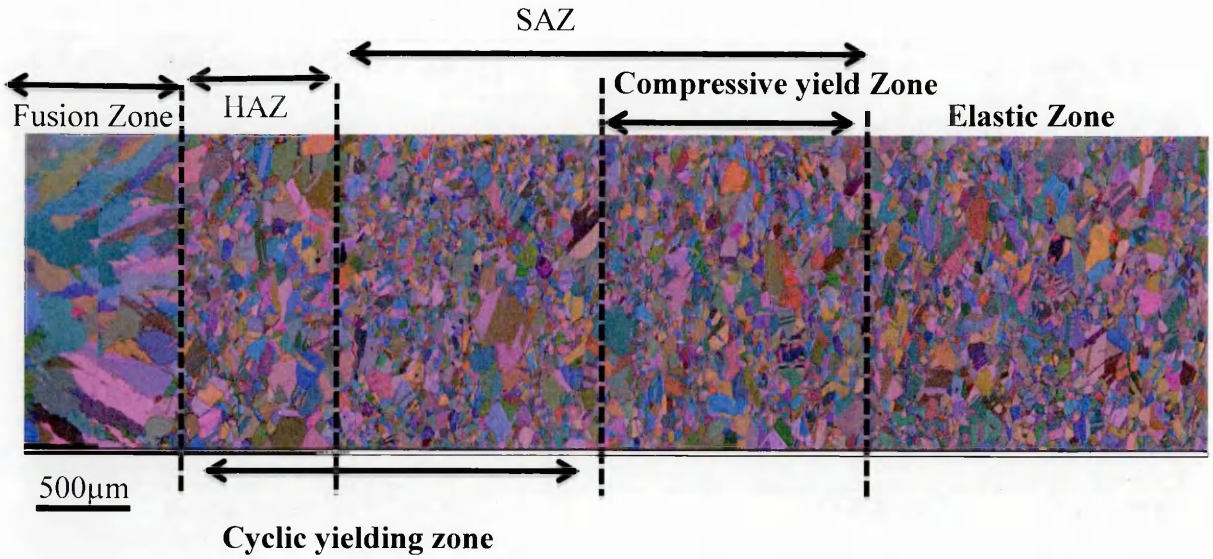

Figure 2.2 Schematic illustration of stress temperature and strain temperature variations during welding [34]

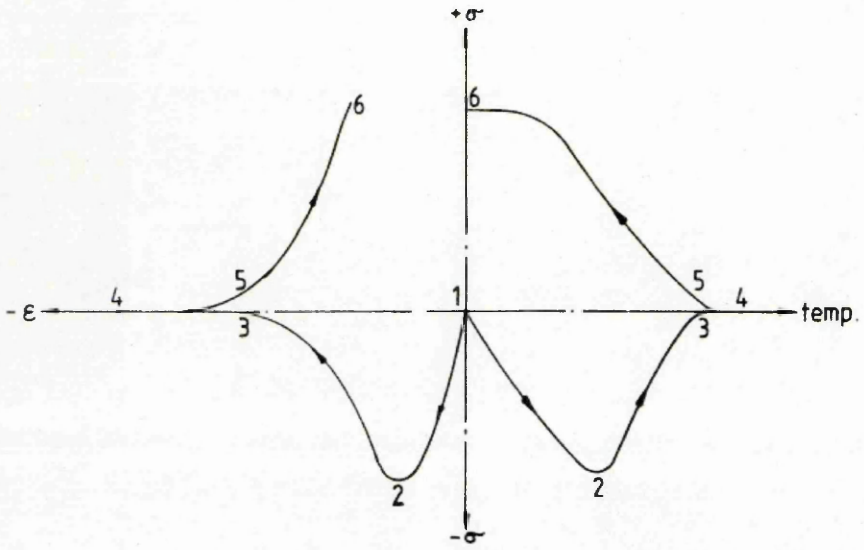

Figure 2.3 Tensile stress vs. strain curve

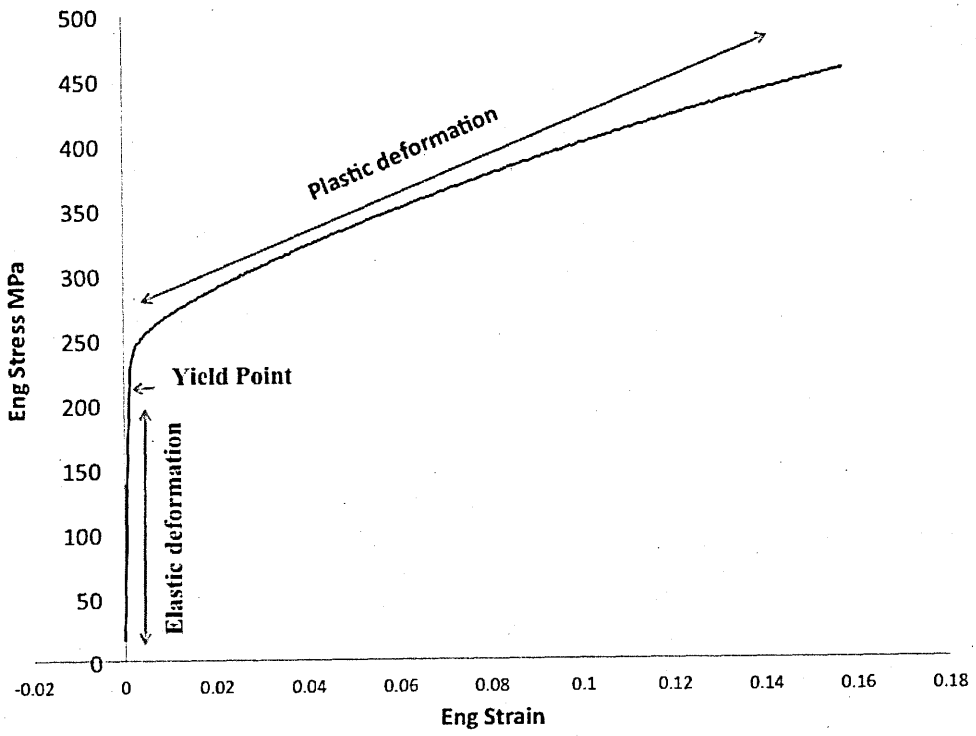

Figure 2.4 Schematic illustration of slip in a single crystal (a) before slip (b) after slip

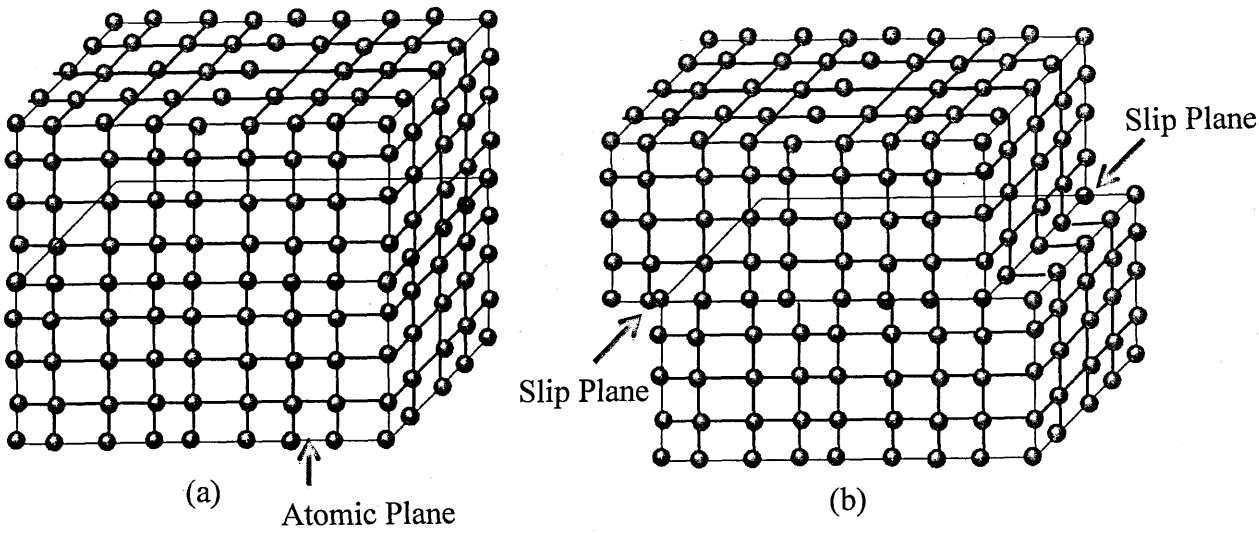

Figure 2.5 Relationship between tensile stress and resolved shear stress during loading of a single crystal

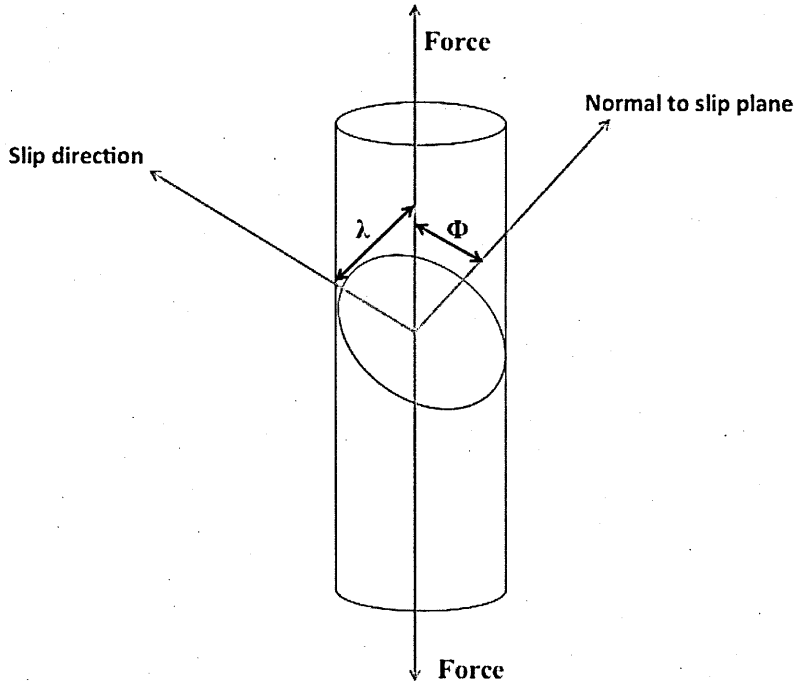

Figure 2.6 Edge dislocation

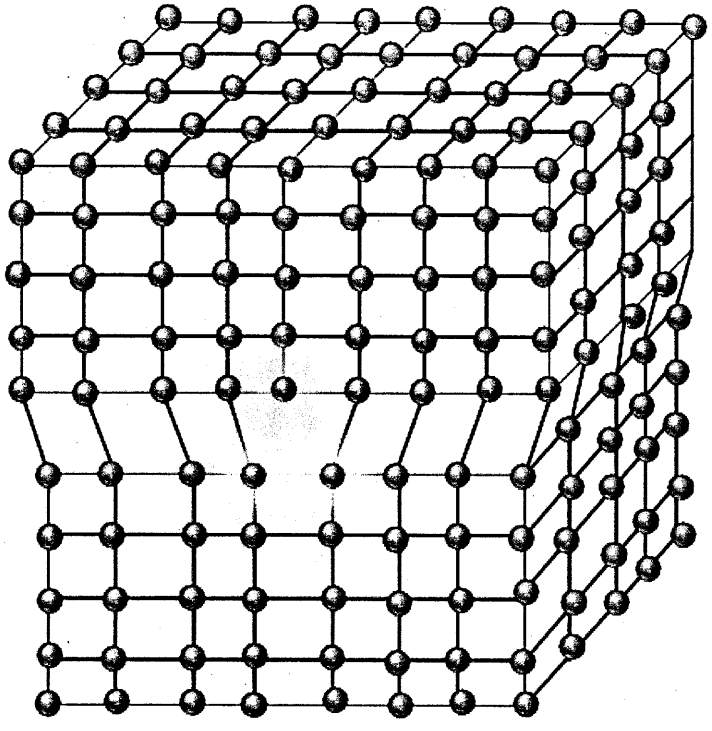

Figure 2.7 Force vs. velocity diagram for a mobile dislocation during DSA [79]

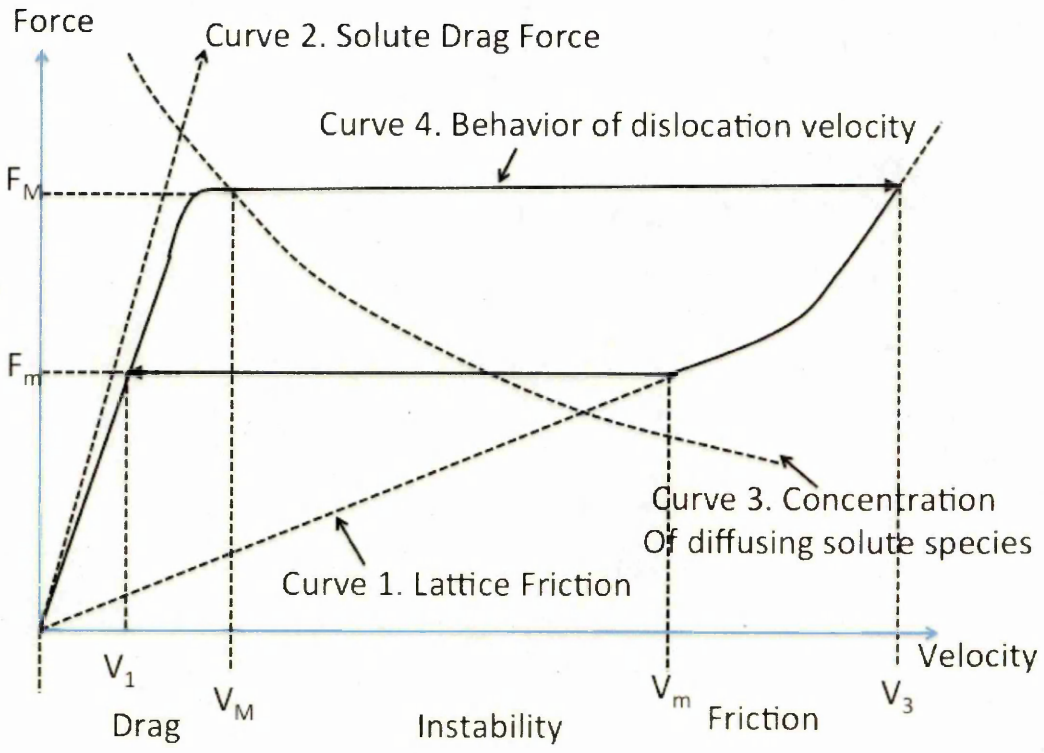

Figure 2.8 (a) Schematic of material response with isotropic hardening model (b) Schematic of material kinematic hardening model

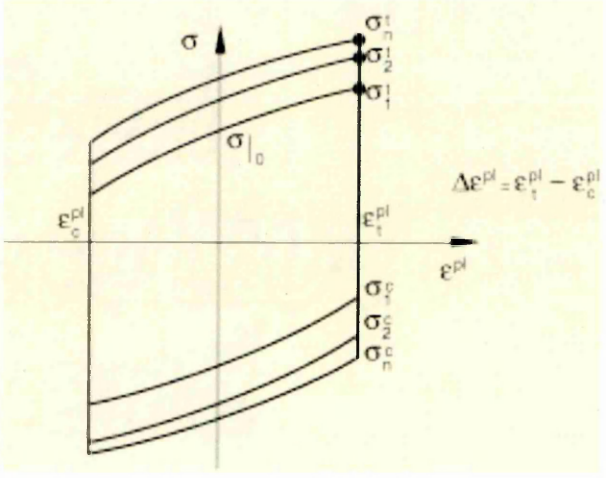

(a)

1. Elastic region
2. Plastic strain region

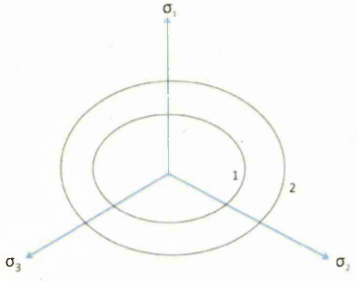

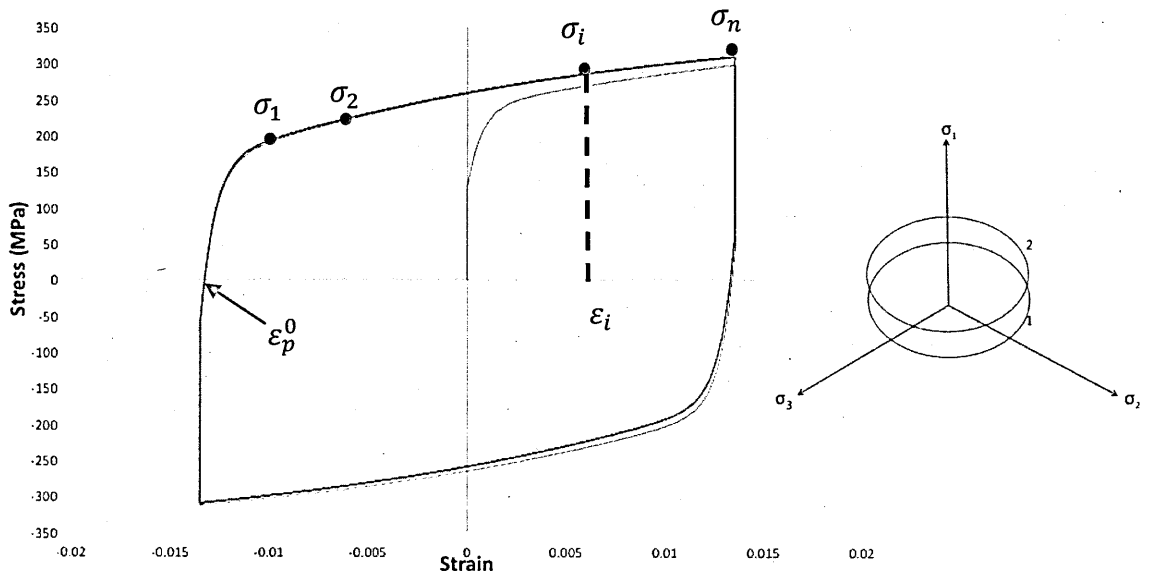
σ_n
σ_i
σ_1
σ_2
ε_p^0
ε_i
Stress (MPa)
Strain
350
300
250
200
150
100
50
0
-50
-100
-150
-200
-250
-300
-350
-0.02
-0.015
-0.01
-0.005
0
0.005
0.01
0.015
0.02
σ1
σ2
σ3
1
2

(b)

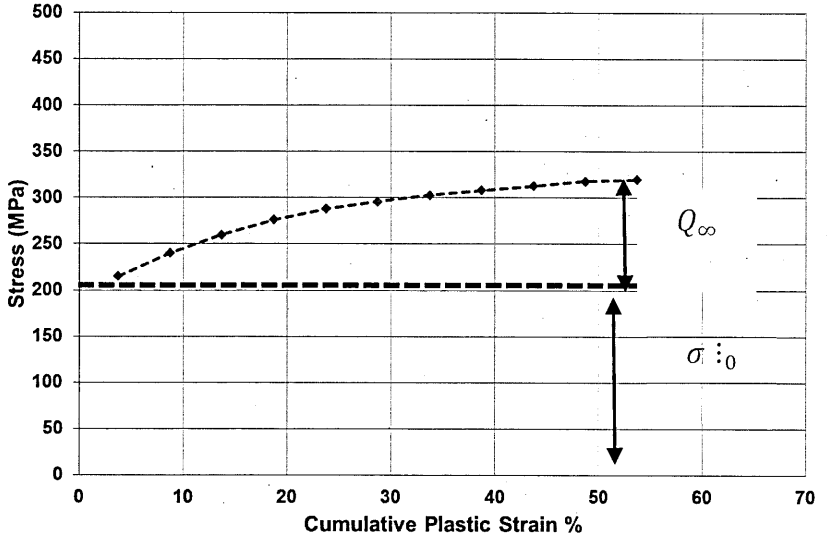
Q_∞
σ_0
Stress (MPa)
Cumulative Plastic Strain %
500
450
400
350
300
250
200
150
100
50
0
0
10
20
30
40
50
60
70

(c)

Figure 2.9 Macro and micro residual stress developed from misfits [7]

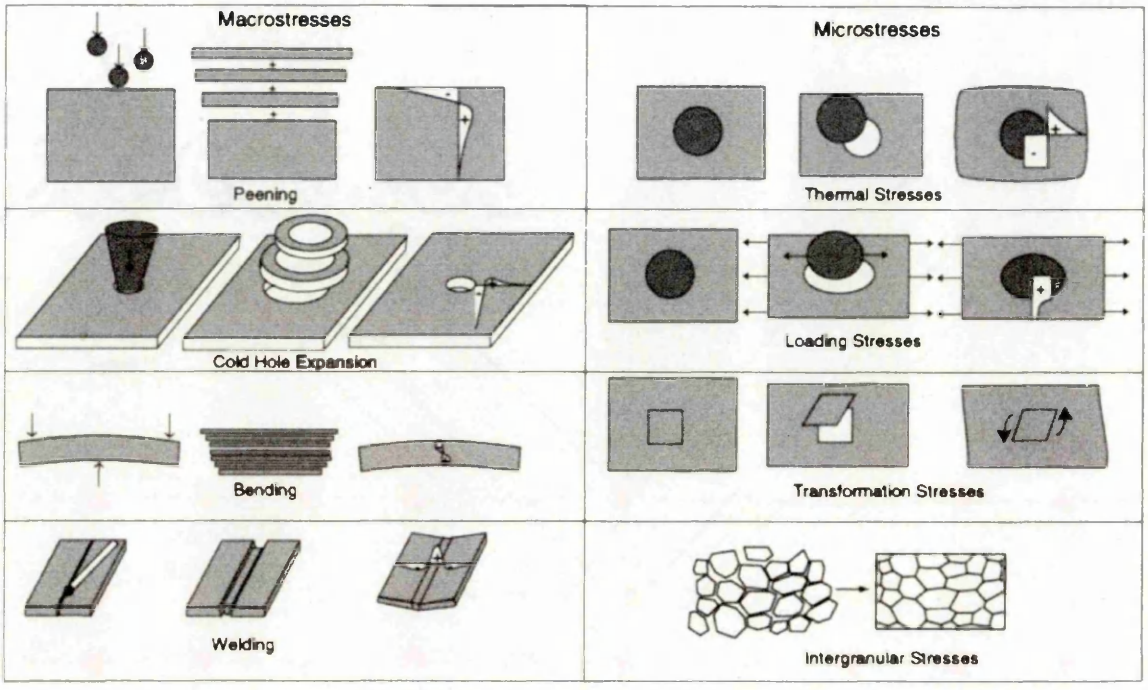

Figure 2.10 Penetration and spatial resolution of different strain analysis techniques

188

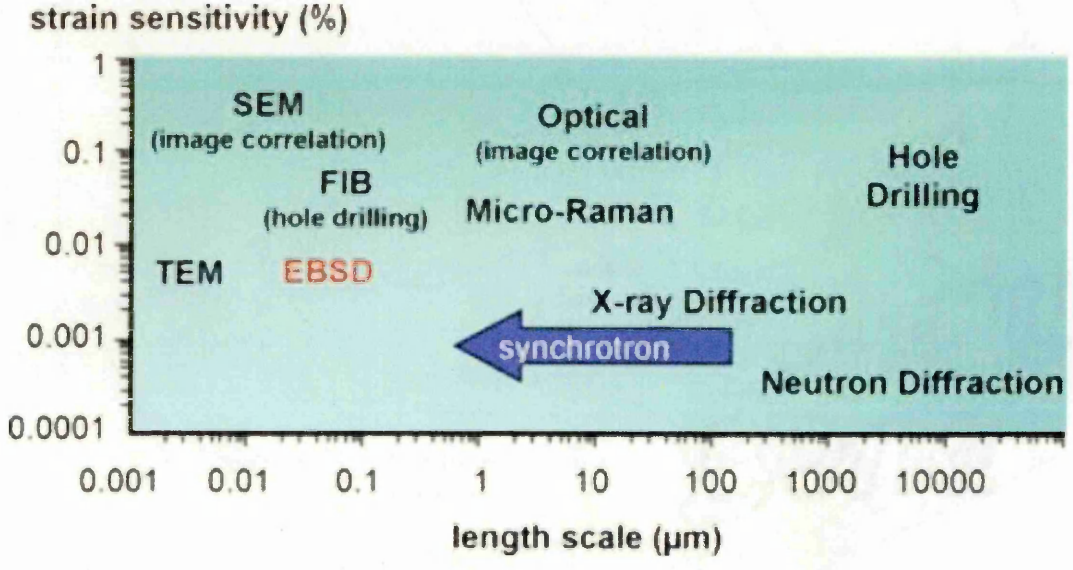

Figure 2.11 Schematic representation of diffraction in unstrained and strained lattice parameter

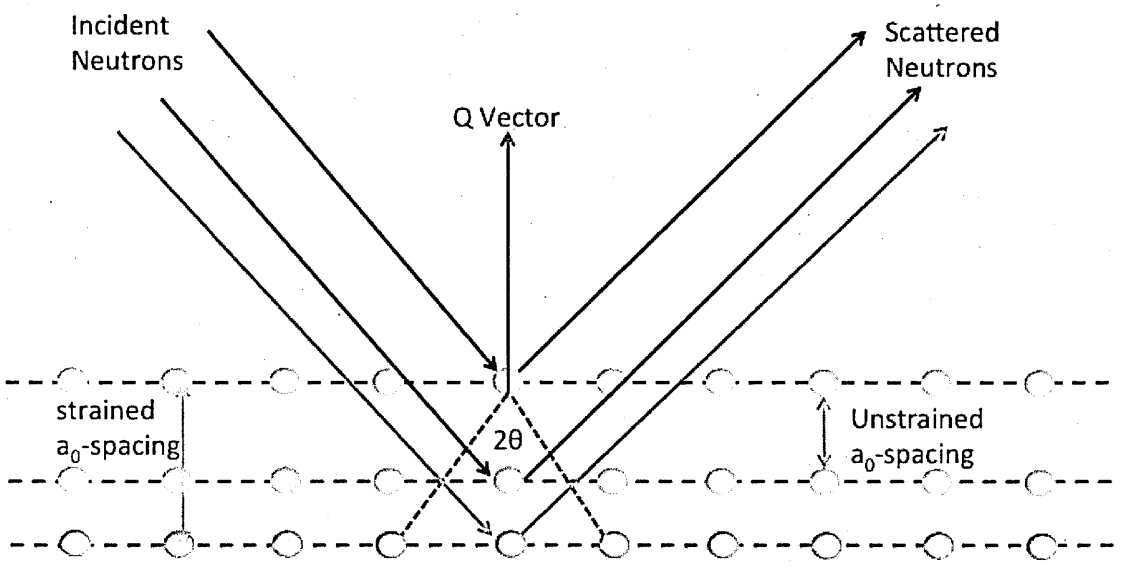

Figure 2.12 Instrument layout (a) VULCAN-SNS [125] (b) ENGIN-X ISIS [121]

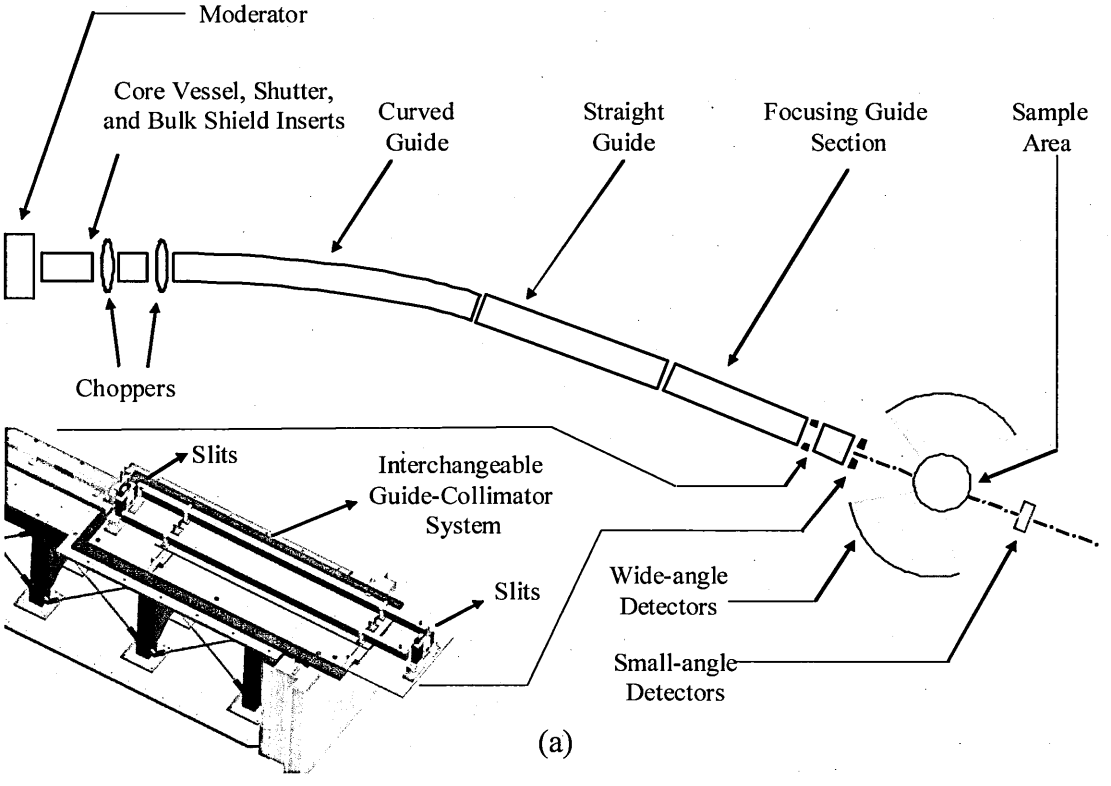

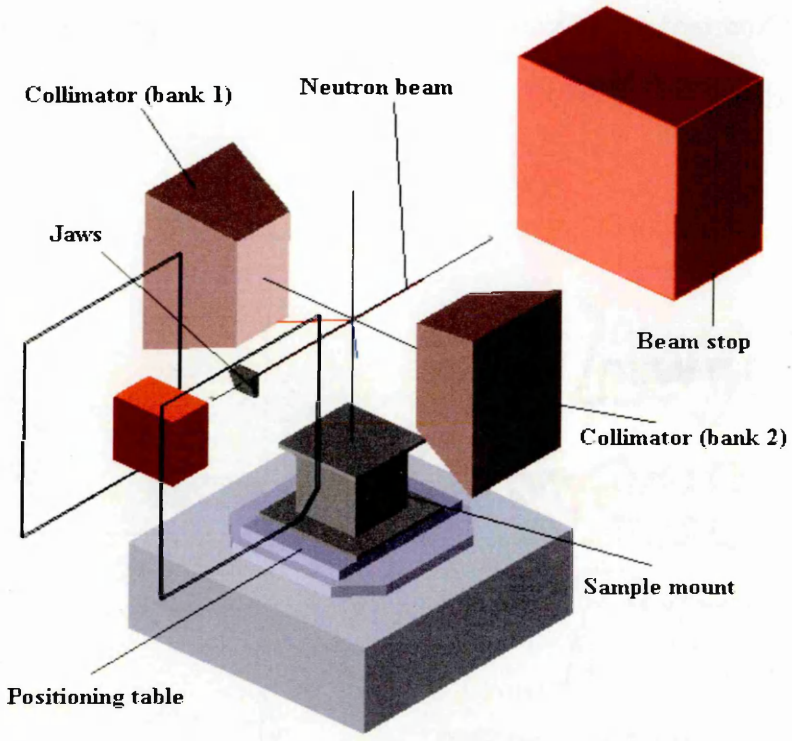

(b)

Figure 2.13 Intensity vs TOF from spallation neutron diffraction for 316L (N) material

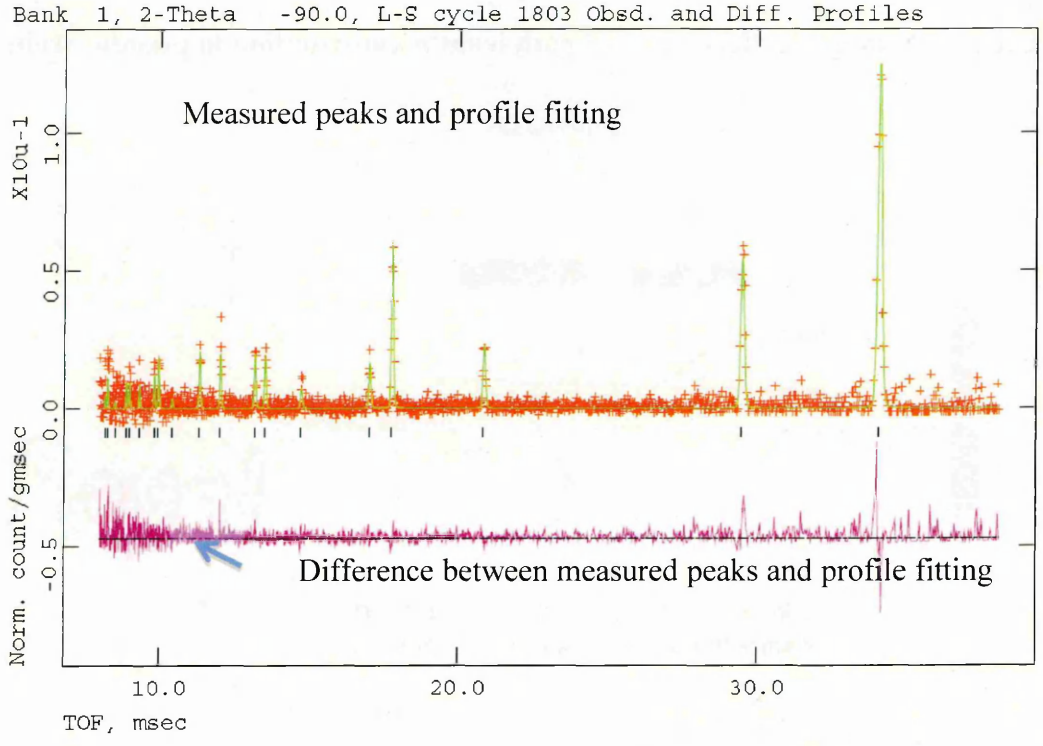

Figure 2.14 (a) Nominal gauge volume and (b) instrumental gauge volume during neutron diffraction

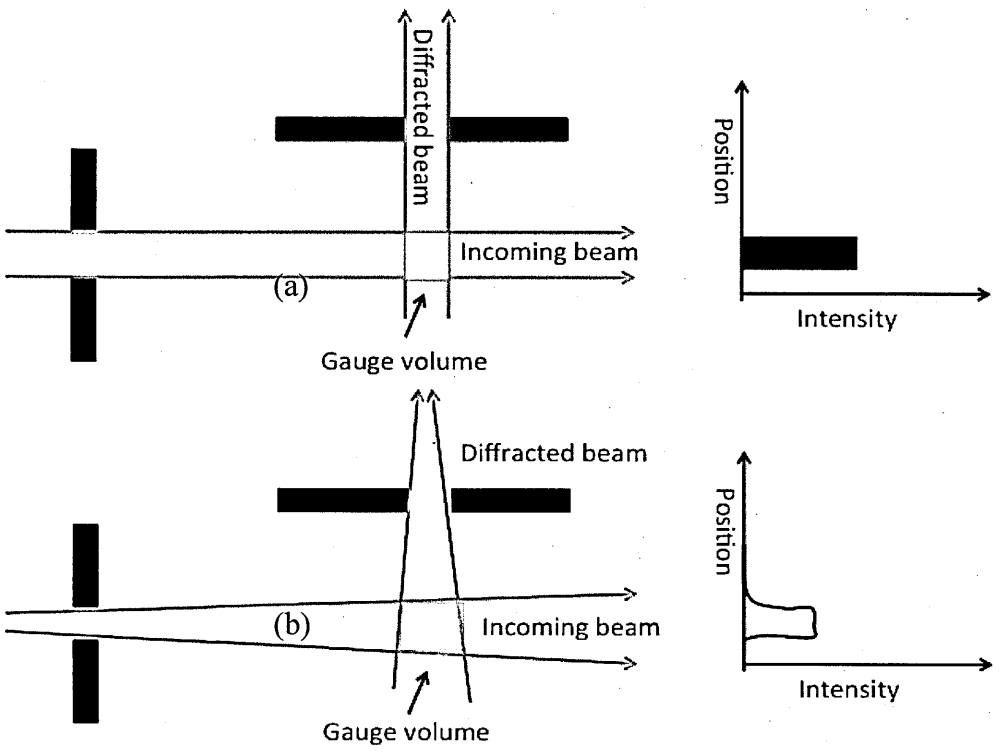

Figure 2.15 Schematic illustration of path lengths contribution to pseudo strain [117]

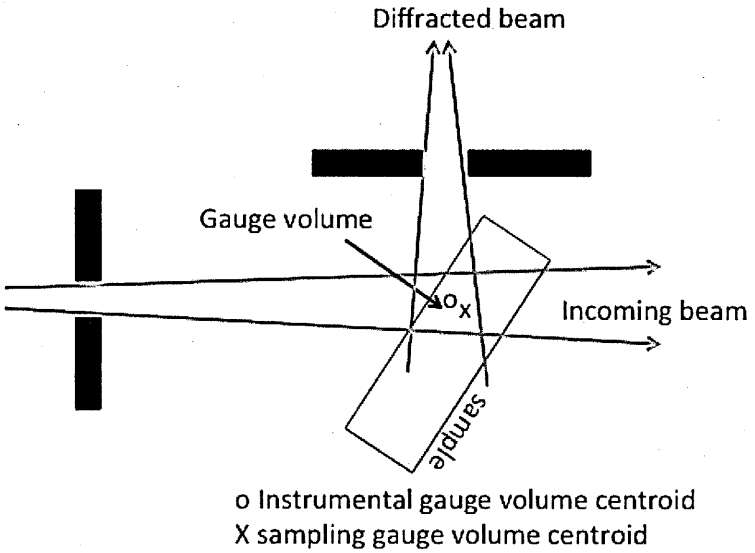

Figure 2.16 Residual stress measurements through thickness of benchmark three pass weld plates ID 3-1A and ID 1-1A [21]

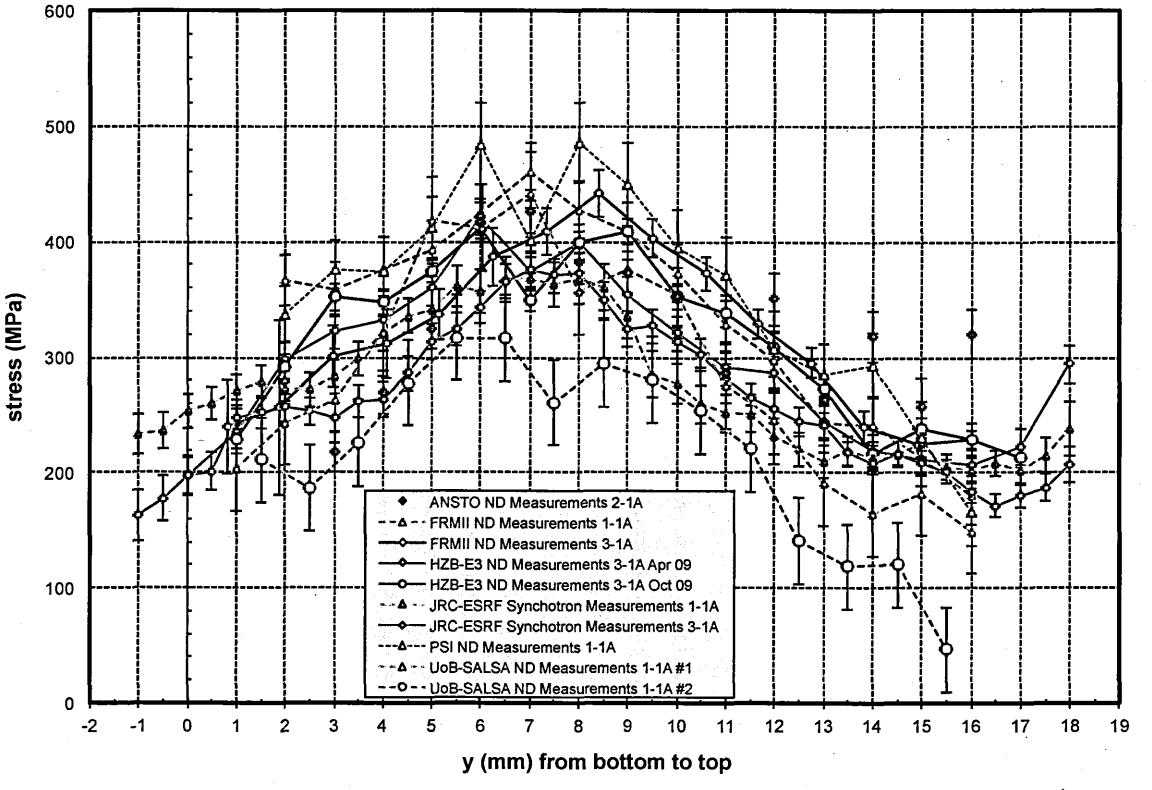

Figure 2.17 Backscattered electrons forming plane traces on phosphor screen [204]

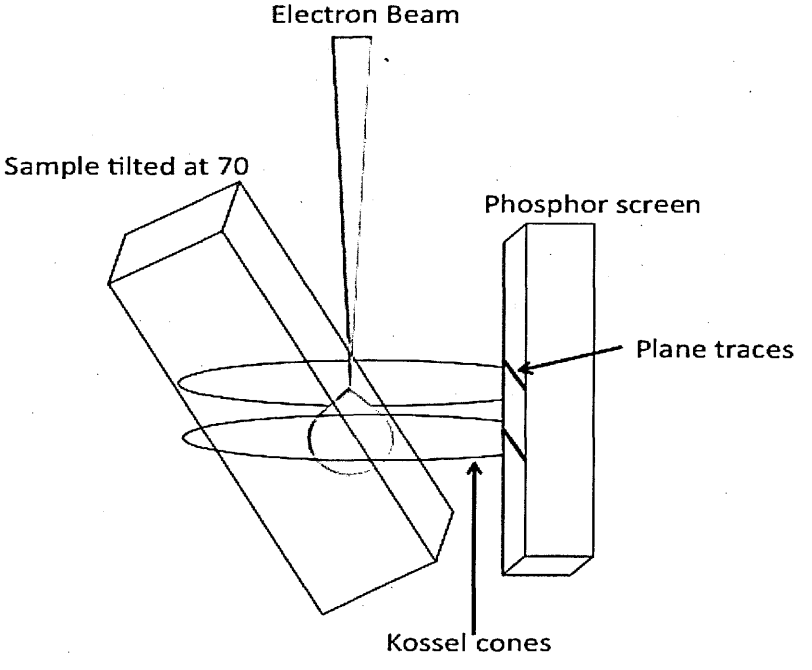

Figure 2.18 Kikuchi pattern from diffracted electrons incident on a phosphor screen for material 316L (N) at 20kV

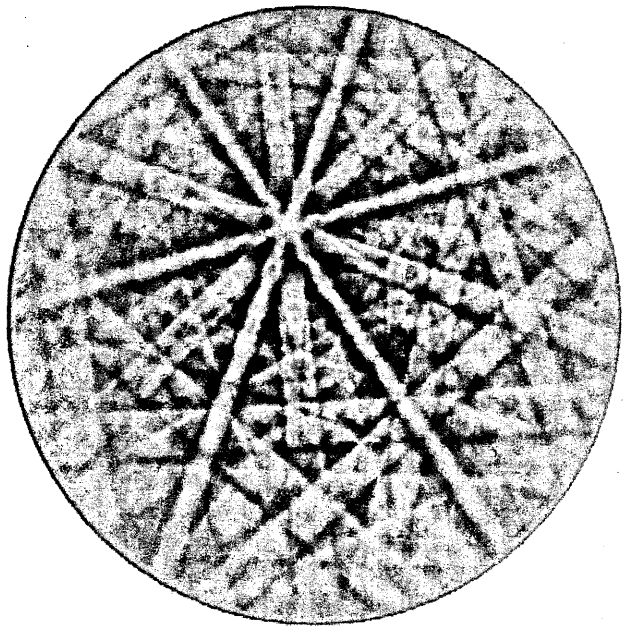

Figure 2.19 Schematic diagram for EBSD metric analysis (a) KAM and (b) AMISa

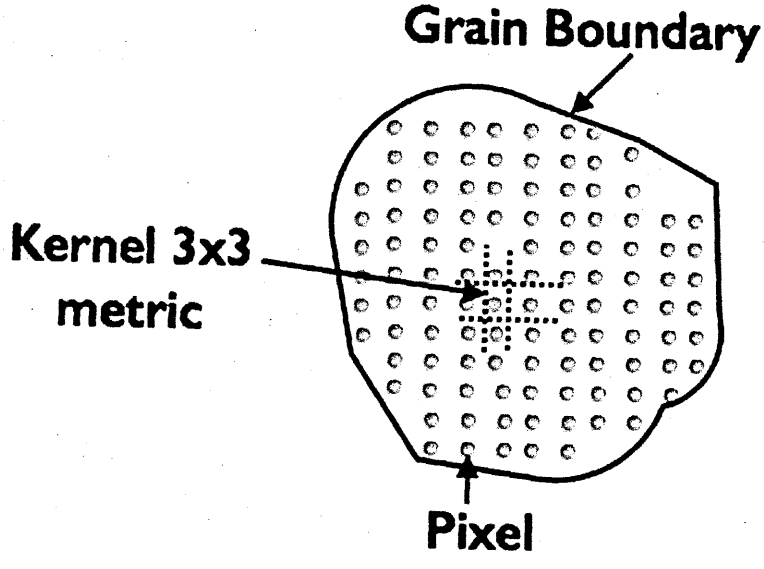

(a)

Step 1: Calculate average orientation of grain

Step 2: The misorientation between the average orientation of grain and the orientation of each pixel is evaluated

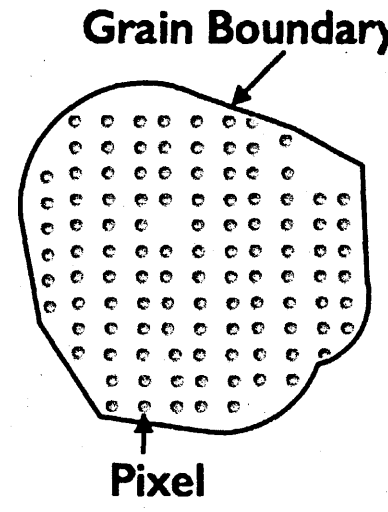

(b)

CHAPTER 3. BENCHMARK WELDMENT DESIGN AND MATERIAL CHARACTERIZATION

This chapter gives detailed background information on the design, manufacture and material characterization of welded test specimens used for the research presented in this thesis. The work has been integrated with residual stress round robin studies of the NeT task group 4 (TG4), see sections 2.5.2 and 2.5.3, on a three pass slot weld in a stainless steel plate. Two of these TG4 benchmark specimens were made available to the author for neutron diffraction measurements. In addition, a quantity of parent material plate was supplied (refer to section 3.4 and Chapter 5) and three special slotted specimens were received, comprising one, two and three pass welds (refer to section 3.3). These were prepared for the plastic strain studies, using EBSD, presented in Chapter 6.

3.1 Introduction

Allocation of the AISI-316L benchmark plate, for determining the evolution of residual stresses using neutron diffraction, is summarized in Figure 3.1 [205,206]. The chemical composition, tensile properties, grain structure and the heat treatment test certificate of `manufacture, stress relief heat treatment and weld parameters are described in section 3.2 below. In total four welded samples were allocated for non-destructive experiments, and were circulated to all groups within task group 4, for weld residual stress measurements using neutron and/or synchrotron X-ray diffraction. In this research project, a single three pass weld plate (ID 3-1A) was used to measure the residual stress field using neutron diffraction at spallation facilities. The principles of neutron diffraction at time of flight sources have been given in Chapter 2, section 2.4.1. Details of the

experiments carried out so far by other members of the NeT consortium have been described, in Chapter 2, section 2.5.3 [172]. This research project contributes towards filling gaps noticed in the literature, by analyzing the following:

1. Residual stress measurements using two different spallation neutron diffraction (ND) sources for the first time.
2. The quantification of the accumulated plastic strain resulting from three sequentially deposited weld passes using electron backscattered diffraction (EBSD) and a hardness testing method.
3. Welding stress-strain studies using symmetric and asymmetric cyclic loading, including the effect of strain rate on strain hardening.

The evolution of residual stress and the accumulated plastic strain during welding has been discussed in Chapter 2 as well as the basic working principles of neutron diffraction, EBSD and Finite Element based weld simulation techniques.

3.2 Manufacturing of TG4 Benchmark Specimens

All of the TG4 test specimens were made from a large piece of AISI type 316L austenitic stainless steel plate (2650 × 2500 × 60 mm), as shown in Figure 3.2(a). Initially, ten blocks (each 250 × 650 × 60 mm) were cut from the raw work piece using water jet cutting. The blocks were further divided into four (Figure 3.2(b)) plates, each of which was machined again to final size (194 × 150 × 18 mm) ready for welding (Figure 3.3 (a) Benchmark specimen dimensions (b) Benchmark specimen dimensions and slot configuration (a)). A weld groove (80 mm long, 6 mm deep) was then milled in the centre of each prepared plate, as seen in Figure 3.3(b). The root of the slot had a radius of 4 mm, which blended with the walls to make an angle of 20° to the plane of the weld centreline,

as shown in Figure 3.3(b) [206,207]. The plates were marked with a co-ordinate system (+/- z and +/- x) and an identification number, as shown in Figure 3.3(a), prior to the welding, as specified in flowchart Figure 3.1. The z coordinate axis was positioned on the top surface along the centreline of the weld groove, and the x coordinate axis was marked at the mid-length position, across the groove.

3.2.1 Stress relief heat treatment

Manufacturing processes such as casting, hot rolling, and machining can lead to residual stresses being introduced into material. In order to eliminate these residual stresses or reduce them to an acceptable level, the material can be annealed using an appropriate heat treatment process. For the TG4 project, each specimen was wrapped in heat treatment foil prior to solution heat treatment at 1050°C in a furnace, for approximately one hour. The plates were then left to cool in the furnace until they reached a temperature of 300° C and then removed for natural cool down to room temperature [206,207].

3.2.2 Three pass weld AISI-316L (N) plate

Figure 3.4 shows an image of the automated pulse Tungsten Inert Gas (TIG) welding machine employed for welding the plates. A summary of the welding parameters is provided in Table 3.1 [206,207]. The feed wire (0.9 mm diameter) AWS A5.0-93 (ER316L) was used to weld the plates. The chemical composition of the filler wire is provided in Table 3.2. During the welding process, the machined base plate (194 x 150 x 18 mm) was left unclamped whilst on the welding table. The second and third weld passes were deposited directly on top of the preceding pass at a travel speed of 76.2 mm/min. The inter pass temperature for both second and third passes was 50°C (±10°C). A total of

seven welded plates were made in this way and labelled 1-1a, 2-1a, 3-1a, 1-1b, 2-1b and 3-1b.

3.2.3 Stress free cuboids extraction

'Stress free' specimens of both parent 316L(N) and weld material are required for neutron diffraction[130] measurements of the unstressed lattice parameters used in the calculation of strain (and hence stress) at each measurement point within the weld plate sample. NeT TG4 allocated two weld plates (ID 1-2B and 2-1B, shown in Figure 3.5(a, b)) and one parent plate (ID 1-1A, in Figure 3.5 (c)) for stress free reference specimen extraction. Table 3.3 lists the stress-free cuboids extracted from each plate. After machining the weld slot, plate ID 1-2B (Figure 3.5 (a)) was not heat treated before the weld deposits were made, whilst plates ID 2-1B (Figure 3.5 (b)) and 1-1A (Figure 3.5 (c)) were solution heat treated before the weld deposits.

Plate ID 1-2B was milled with five-weld grooves (each 80 mm long and 6 mm deep) as shown in Figure 3.5 (a), one slot for a single pass, one slot for the first and second passes, and the third slot for a three-pass weld. The remaining two grooves were left untouched. Each weld groove was separated from the next by a distance of 30mm, measured from the center of each groove. After welding, a transverse slice incorporating the three filled slots, was extracted by electro discharge machining (EDM), as shown in Figure 3.6. The slice was approximately 4 mm wide and 60 mm in length at the mid length position.

From the extracted slices (i.e. along the weld direction as shown in Figure 3.6), a further four 23 × 4 × 3 mm prisms of weld metal were extracted from the top weld metal and bottom of the weld. Each of these prisms was further cut into four cuboids 5 × 4 × 3 mm using EDM. Then each set of four cuboids of weld material were glued together to create larger 'stress free' samples 5 × 8 × 6 mm. Using wire EDM, parent material 'stress

free' cuboids (5 × 4 × 3 mm) were extracted from the + x, - z corner of plate ID 1-1A (Figure 3.5 (c)) and assembled using a similar procedure to that described above. The 5 mm dimension was parallel to the welding direction, the 4 mm dimension parallel to the transverse direction and the 3 mm dimension parallel to the normal direction. The three sets of assembled stress free cuboids (upper weld, bottom weld and parent) were color coded red, green and black respectively and are summarized in Table 3.3.

3.3 Material for Strain Controlled Cyclic Tests

A raw piece of the remaining parent austenitic stainless steel (600 × 50 × 62 mm) was supplied by the NeT TG4 group for the present research (refer to Figure 3.1). This material was specifically for the analysis of weldment cyclic deformation. The rationale for this analysis is described in Chapter 2, section 2.3.4. The supplied work piece was heat-treated using a similar process to that described in section 3.2.1. A thin sample (3 × 50 × 62 mm) was extracted using wire EDM, to enable identification of the rolling direction in the 316L (N) block, using optical micrograph analysis. The rolling plane is identified, in Figure 3.7(a).

3.3.1 Design of strain controlled test specimens

Low cycle fatigue test specimens for the strain controlled cyclic tests were extracted from the block of parent austenitic stainless steel. These specimens were designed following guidelines contained in British Standard (BS) 7270 (1990) [208]. Using wire EDM, cylindrical samples were extracted with their axes parallel to plane D, see Figure 3.7(b), i.e. along the weld direction. A test specimen designed without shoulders, for cyclic loading is shown in Figure 3.8. This shape of sample was originally selected for this research due to the limited availability of the material. However, following cyclic loading, steps were seen on the stress vs. strain cyclic loop, as illustrated in Figure 3.9.

This was due to the backlash between the sample and the collet, which resulted in formation of steps with the load train, and (ii) the length of the M12 thread was longer than required. Therefore, during initial loading, stress was applied to the excess threads, which then deformed the sample at the zero stress point. These problems were addressed by redesigning the cylindrical cyclic loading sample to include a shoulder at each end, as shown in Figure 3.10. In addition to modifying the sample design, an Instron alignment pro kit was also installed to the instrument to improve the alignment of the sample.

3.4 Sequential Weld Deposited Plate

An additional multi-pass weld plate was made by the NeT consortium for quantification of accumulated plastic strain by the author. From the raw work piece, a new parent plate test specimen was cut to dimensions 250 x 200 x 18 mm. Three weld grooves were milled into the plate to a depth of 6mm; one central, and one either side, at a lateral distance of 80 mm from the central groove, as shown in Figure 3.11. Prior to the welding process the raw work piece was heat treated for stress relief as described in section 3.2.1. The three weld grooves were deposited with a single pass, two passes and three weld passes respectively, using tungsten inert gas welding, according to the details shown in Table 3.1, and with the filler wire compositions listed in Table 3.2. The sequence of the welding process is annotated in Figure 3.12.

3.4.1 Samples for plastic strain analysis

Wire EDM was used to divide the multi-pass weld plate (Figure 3.11) transversely, into two halves, each one measuring 250 x 100 x 18 mm. This cut was made across the centre of all three welds. Figure 3.11(b) shows where each half was cut again, to extract two thin transverse slices, each one measuring 250 x 3 x 18 mm. One slice was left whole, and allocated for hardness measurement testing. The other slice was cut into three pieces,

each covering one weld groove as shown in the optical macrograph Figure 3.11(c). These individual pieces were allocated for texture, microstructure analysis (ref. section 3.5.3. and 3.5.2.) and plastic strain analysis using EBSD as described in Chapter 6.

3.5 Material Properties

The mechanical properties and material characterization of the parent austenitic stainless steel have been well defined by the NeT consortium. The chemical composition and monotonic tensile properties, at different temperatures, on the parent material, have all been documented [172,206]. Data relevant to this thesis are reproduced in Table 3.2 and Table 3.4. However, the NeT group lacked the following information;

- The grain size distribution in the three orthogonal planes (longitudinal, transverse and normal),
- The parent and weld material hardness
- The texture of the weld metal
- The extent of any Chemical compositional variations in the parent and weld materials

This information was needed to support the neutron diffraction and EBSD studies proposed for the present research and was obtained by the author as described in sections 3.5.1-3.5.6 below.

3.5.1 Specimen preparation

For optical, grain size, texture and chemical characterisations, a parent material sample (5 x 8 x 6 mm) was extracted from the end of the transverse slice as shown in Figure 3.13. To mount the specimens ready for surface preparation, first, seventy five percent of MetPrep conducting phenolic resin granules was added to the mounting mould, and then twenty five percent of Struers Condufast powder, containing iron particles, was added on

the top of the phenolic resin prior to hot mounting. When hardened, this resin mixture provides excellent conductivity for electrolytic polishing of the specimen surface.

The aim of the specimen preparation was to produce stress free surfaces with a mirror finish. The sample preparation steps and etching methods are summarised in Table 3.5. This preparation method was used consistently for samples undergoing optical microscopy, hardness measurement, Energy Dispersive X-ray spectroscope analysis (EDX) and EBSD.

3.5.2 Optical microscopy

A Leica DM-I5000M optical microscope was employed for the optical examination. The parent cuboid (5x8x6 mm) was examined in three orientations with respect to the weld (longitudinal, transverse and normal), as shown in Figure 3.14. Micrographs of the parent material in all three orientations are provided in Figure 3.15-3.17. Macrographs of the weld beads and micrographs showing the heat affected zone (HAZ) for the single pass, two pass and three pass welds, are presented in Figure 3.18-3.20 respectively. Optical macro and micrographs of the single pass, two pass and three pass weld metals were obtained from the sequential weld deposited plate samples (ID 1-2B refer Figure 3.5(a)) described in section 3.2.3. The optical images of the prepared surface of the parent material show an approximately equiaxed grain size, with the presence of twin boundaries and ridges along the planes D and B shown in Figure 3.3. Previous research [209,210] suggests that the development of ridges in the rolling direction (i.e. visible as lines on the transverse and normal sides), during solidification or casting, could be due to some of the non-uniform segregation of chromium and molybdenum. These ridges are not significantly reduced by a subsequent hot rolling process. The presence of a small percentage of ferrite (below 1% or 2%) in the wrought microstructure is not considered detrimental. However, the small amount of ferrite can form a preferential site for the

precipitation of $M_{23}C_6$ carbides and sigma phase [47]. Nevertheless, the presence of delta ferrite *is* beneficial in dissolving harmful impurities such as sulphur, phosphorus and boron [211]. An attempt was made, using EDX analysis, to investigate the chemical composition of these ridges and the outcomes are reported in section 3.5.5.

The fusion region of the single, two and three pass weld zones has undergone ferritic austenitic type solidification, where the austenite forms due to a peritectic-eutectic reaction. Ferrite (black) boundaries were formed around the austenite (white), in the material, at the end of the solidification process as seen in Figure 3.21. The columnar microstructure, solidification sub-grain boundaries (SSGB) and the solidification grain boundaries (SGB) are evident around and near the fusion boundaries. The SSGBs are normally identified as around cells or dendrites, and/or the boundaries that separate adjacent sub-grains as indicated in Figure 3.20. The SGBs are formed around groups of SSGB. At places where SSGBs and SGBs interact, boundaries with high angular mis-orientation result [47].

A skeletal ferrite morphology was observed in the single, two and three weld passes cases. The moderate cooling rate of solidification causes the austenite to consume the ferrite until the ferrite is enriched with elements promoting (chromium and molybdenum). At the same time, austenite promoting elements (nickel, carbon and nitrogen) are rejected. These rejected elements stabilize at lower temperatures, where diffusion is limited, and form skeletal ferrite. The microstructures in the fusion zone are not uniform. This is due to the difference in the cooling rate, resulting from the multi-pass welding. This leads to fine columnar crystal grains being generated during the first pass, whilst a coarse microstructure was observed near the weld cap of the second and third weld passes.

During multi-pass welding, the underlying preceding weld metal re-melted and recrystallized and columnar grains grew, adopting a similar orientation to the previous columnar zone. This process results in elongated coarse columnar grains. However, at the intersection of the first and second pass fusion boundaries, as shown in Figure 3.21, distinct columnar grains, oriented in different directions were observed across an overlap interface of each weld pass. This was due to the restriction of direct epitaxial growth of the grains [212].

3.5.3 Grain size measurement

The average grain size of metals has a significant effect on properties such as strength and ductility. Information on the grain size of the 'as received' material gives an initial reference, enabling a distinction from the deformed grains resulting from cyclic loading. The American Standard Test Method (ASTM) Mean Linear Intercept method was used to calculate the grain size, using both Leica software and by hand calculation [213]. The Mean Linear Intercept method is one of the most commonly used methods to determine the grain size. The procedure and any precautions to be considered are provided in ASTM Standards E112-12 [213].

For hand calculation of the average grain size five to eight straight lines are drawn randomly on micrographs for each of the surface orientations (longitudinal, transverse and normal). A minimum of 6 lines intersecting at least 100 grain are sampled. The average grain size in the longitudinal plane was 86μm (+/- 10 μm), in the transverse plane 68μm (+/- 15 μm) and in the normal plane 71μm (+/- 15 μm) respectively. The automatic linear intercept measurements calculated using the Leica software are 65 μm (+/- 5 μm) in the longitudinal, 69 μm (+/- 10 μm) in the transverse and 67 μm (+/- 15 μm) in the normal plane.

3.5.4 Chemical composition

The point scan methods of the EDX process were used on the polished and etched surface of the transverse face, to identify any chemical variation associated with the observed ridges (Figure 3.16 and 3.17). The point chemical compositions of the etched surface, on and away from the ridges (see Figure 3.22), are presented in Table 3.6. There appears to be a chemical difference of about 2.0 Wt. % of Chromium between the ridges, and the areas away from the ridges. However, this difference may be due to the path length difference caused by the surface topology of the etched specimen.

3.5.5 Texture analysis

The crystallographic texture is a measure of the degree to which the grains in crystalline samples are not randomly oriented. Manufacturing processes such as hot rolling and welding promote grains with a preferred orientation along certain macroscopic planes in the sample. For instance, in deposited weld metal, the grains are often orientated in the direction of the heat conduction path.

Texture analysis was carried out using EBSD on the sequential weld metal deposited plate samples as described in section 3.4, and on the parent cuboid. The texture analysis was carried out at the centre of the transverse plane (parallel to XY, refer to Figure 3.3) of the parent cuboid and through the centre of the first pass, second pass and third pass weld bead for the three-pass weld EBSD sample (refer to Figure 3.18(c)). An area covering between 4×10^7 to 8×10^7 data points, at a 1μm step size scan, was employed for the texture analysis. The grain orientation map and pole figures of the parent material and of three-pass weld material are presented in Figure 3.23-3.24. From the figures, it is clear that the weld metal exhibits a strong texture along {100} orientation. The underlying reason for this preferred orientation is that in face centered cubic materials the least close

packed atomic low index planes are {100}. This atomic plane offers the path of least resistance for the random atomic arrangement, in the molten liquid, to align with during solidification, for rapid grain growth along {100} direction. Simultaneously a few differently oriented grains, i.e. those not growing fast towards the former position of the heat source, grow very slowly and their development is terminated.

In order to evaluate the effects of texture, the NeT TG4 group carried out texture measurements on a cube of parent material, using neutron diffraction, at FRM-II Germany [214]. The γFe {111} and {200} peaks were examined for the evolution of texture. It can be seen that from Figure 3.25, the texture is weak, with a maximum multiple soft random distribution of 1.2.

3.6 Conclusions

The conventional sample, without shoulders, experienced buckling under cyclic loading due to the poor alignment. These problems were rectified by using a new sample design, and by using an Instron alignment pro kit. An elongated grain structure was observed (in plane D and B) in the optical microscopic analysis of parent cuboids. Insignificant texture was identified in the parent material and {100} texture in the three-pass weld metal, using the EBSD analysis. The EDX analysis of the base material appears to be a chemical difference about 2.0 Wt. %, however, the EDX analysis was not sensitive enough to pick up the chemical segregation in the ridges.

3.7 Tables

Table 3.1 Summary of the welding parameter [206]

Parameter	Pass 1, 2 and 3
Slot Dimensions	80×6 mm
Welding Process	GTAW/TIG
Filler Wire	AISI type 316L
Wire Diameter	0.9mm
Arc Polarity	DC Electrode (-)
Shielding Gas	Argon
Tungsten Electrode	2% Thoria
Electrode Diameter	3.2mm
Electrode Angle	30°, 0.5 mm flat
Gas Cup ID	12 mm
Arc On	Start +0s
Starting Current	50A
Start of Ramp Up	Start +0s
End of Ramp Up	Start +4s
Pulsing Frequency	1 Hz
Peak Welding Current	240 A
B/G Welding Current	200 A
Arc Voltage	9-11 V
Start of Wire Feed	Start +5s
Start of Travel	Start +6s
Travel Speed	76.2 mm/min
Weaving	None
End of Ramp Down; Final Current	5-10 A
Inter-pass Temp	20° C ± 10 °C

Table 3.2 Chemical composition of filler wire used for welding [206]

C	Cr	Cu	Mn	Mo	Ni	P	S	Si
0.020%	19.04%	0.05%	1.84%	2.1%	12.20%	0.018%	0.001%	0.49%

*ASTM A 751-96 standard was used for all chemical composition analysis

Table 3.3 List of stress free cuboids extracted from benchmark weld plate

Benchmark Plate ID	Extracted stress free cuboid	Number of cuboids extracted from each plate	Refer Figure	Heat Treated
1-1B	Parent	2	3.5(c)	No
1-2B	Top Weld	2	3.5(a)	No
1-2B	Bottom Weld	2	3.5 (a)	No
2-1B	Parent	1	3.5(b)	Yes
2-1B	Top Weld	2	3.5(b)	Yes
2-1B	Bottom Weld	2	3.5(b)	Yes

Table 3.4 Chemical composition of AISI 316L (N) austenitic stainless steel [172]

Element	C	Mn	Si	Cr	Ni	Mo	Cu	N
Wt%	≤0.03	1.6-2.0	≤0.5	17-18	12-12.5	2.30-2.70	≤0.3	0.06-0.08

Ti≤0.15 P ≤ 0.025 wt %, Ta+Nd+S≤0.01 wt%, Nb+Ta+Ti < 0.15 wt%, B ≤ 0.002, Co≤ 0.2 wt% and Fe balance

Table 3.5 Steps in the sample preparation for optical microscope, EBSD and macro hardness analysis

Method	Grit Paper No/	Force in lbs. / Voltage	Time in minutes
Grinding	240	3	2
Grinding	500	3	3
Grinding	800	3	4
Grinding	1200	3	5
Polishing	9μ	3	5
Polishing	6 μ	3	10
Polishing	1 μ	3	15
Electrolytic		22V	1-2
Electrolytic	60% nitric acid	2V	30 Sec

Table 3.6 EDX point scans chemical composition from etched surface

Element	Fe	Cr	Ni	Mo	Mn	Si
Wt.%	64.1	19.4	11.4	2.7	2.0	0.4
Wt.%	64.4	20.0	10.0	3.1	2.1	0.5
Wt.%	65.0	19.8	9.5	3.0	2.0	0.5

3.8 Figures

Figure 3.1 Manufacturing and specimen allocation flow chart

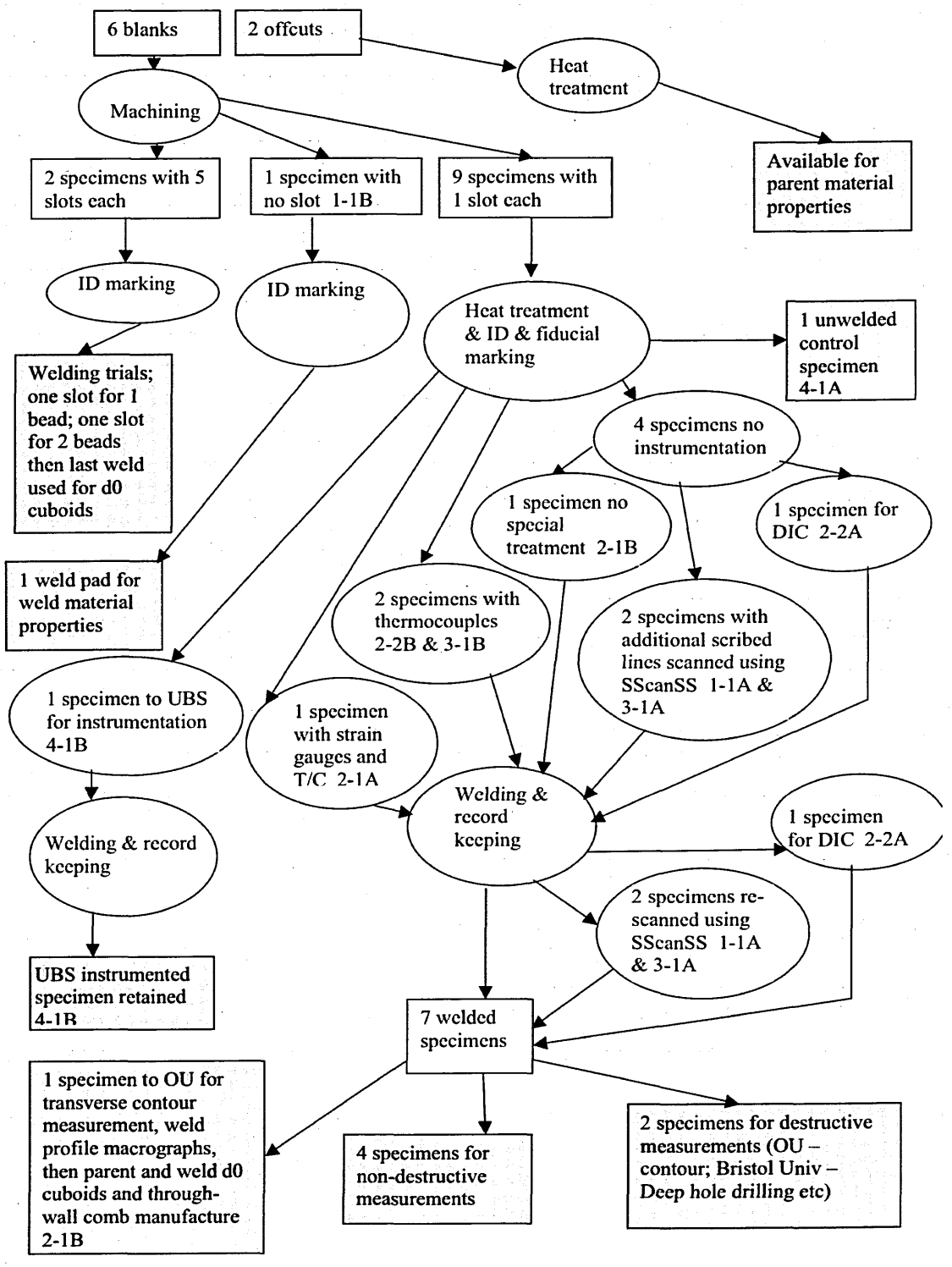

Figure 3.2 Benchmark extraction (a) original plate (b) extracted specimen from original plate [206]

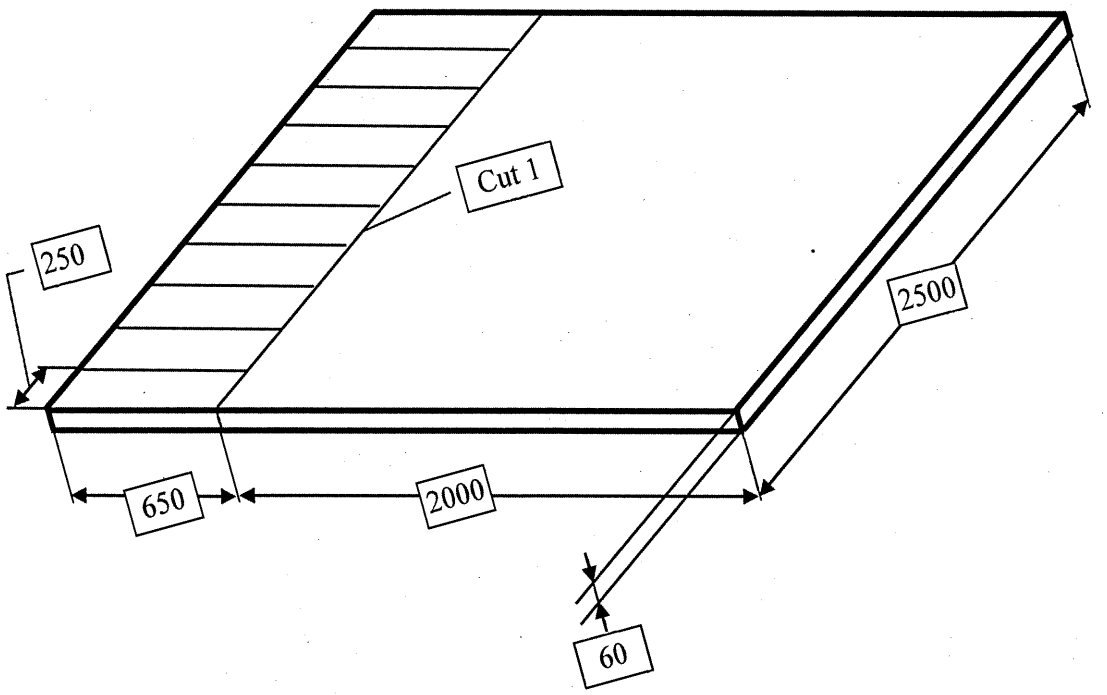

(a)

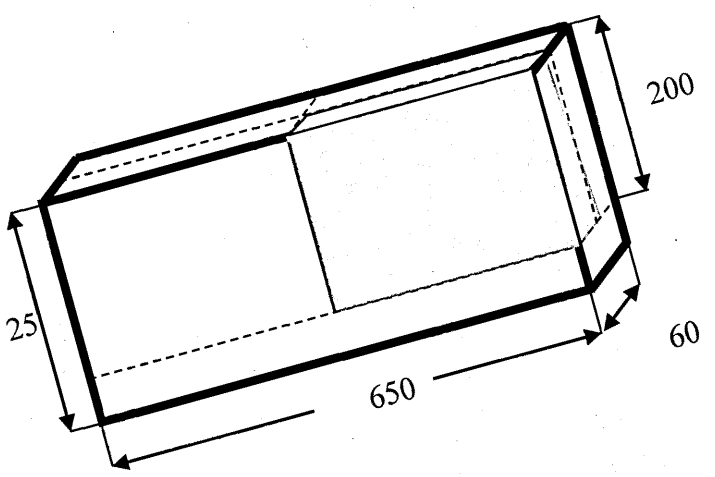

(b)

Figure 3.3 (a) Benchmark specimen dimensions (b) Benchmark specimen dimensions and slot configuration [206]

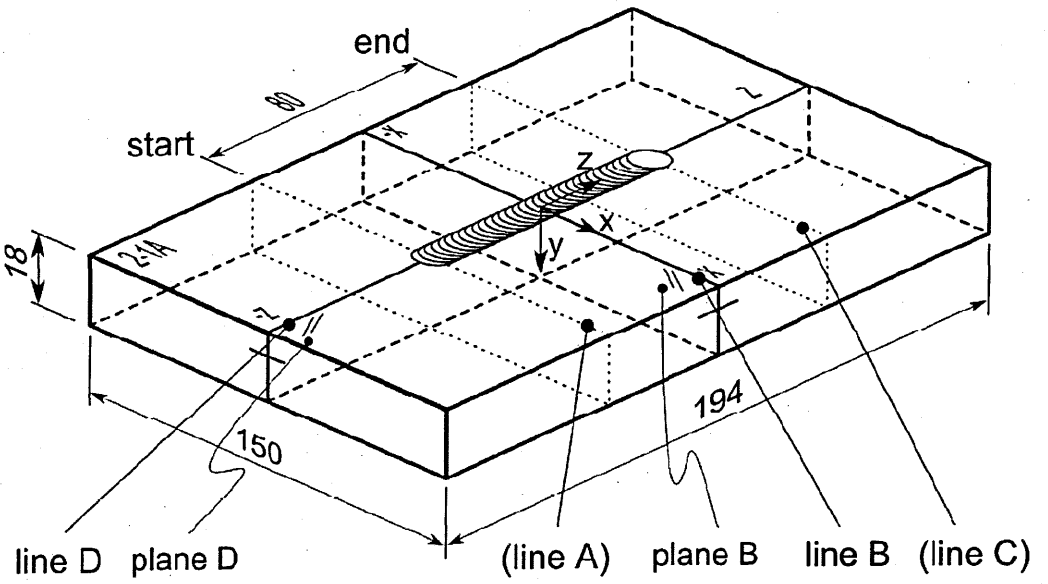

x = transverse, y = normal; z = longitudinal

(a)

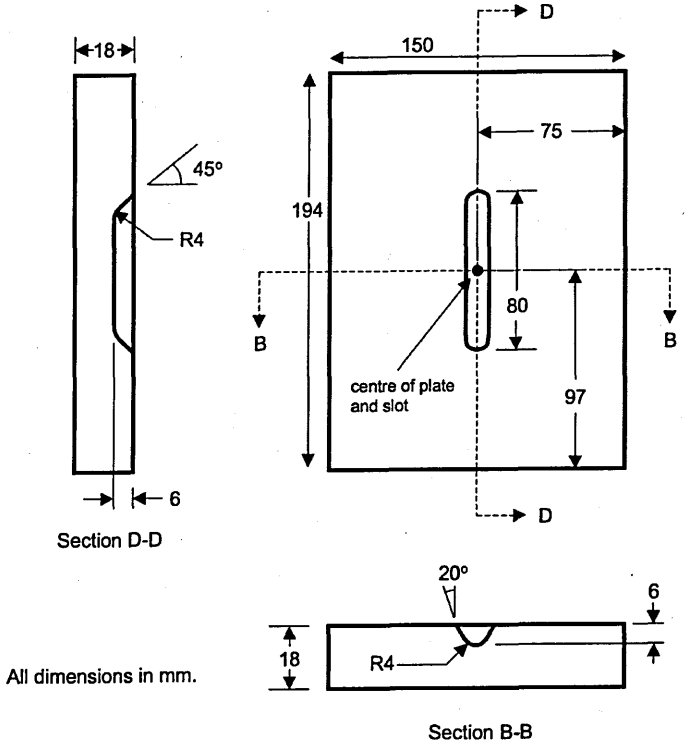

(b)

Figure 3.4 Tungsten Inert Gas (TIG) welding machine

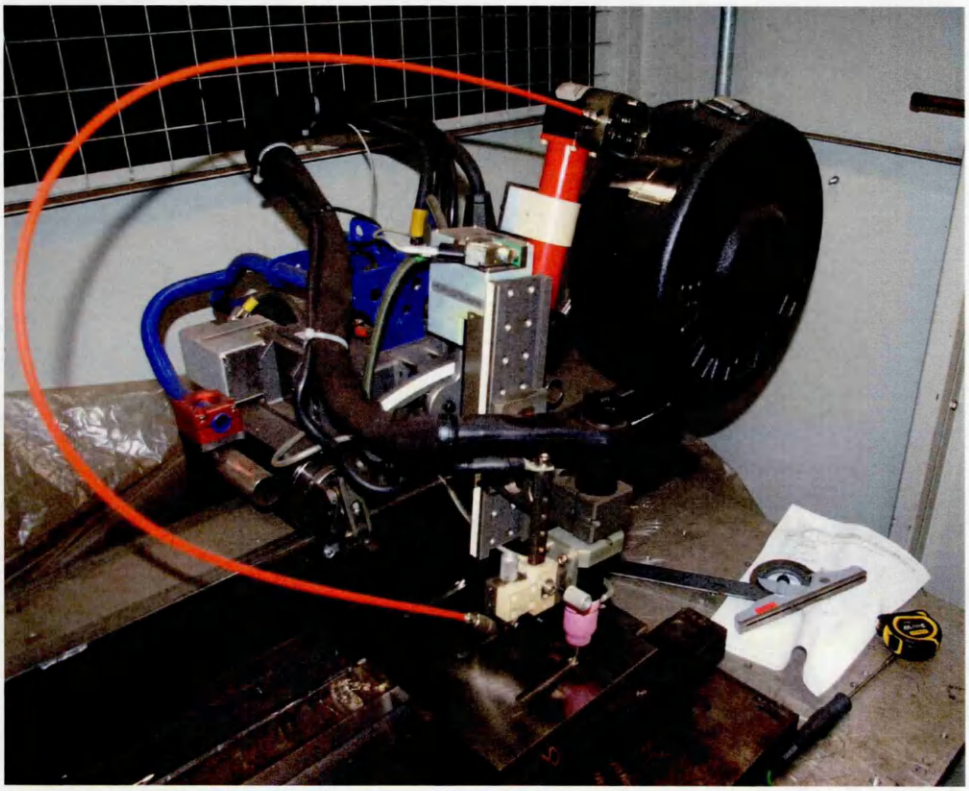

Figure 3.5 Weld benchmark plates allocated for extraction of stress free cuboids (a) Plate ID 1-2B and (c) Plate ID 1-1B

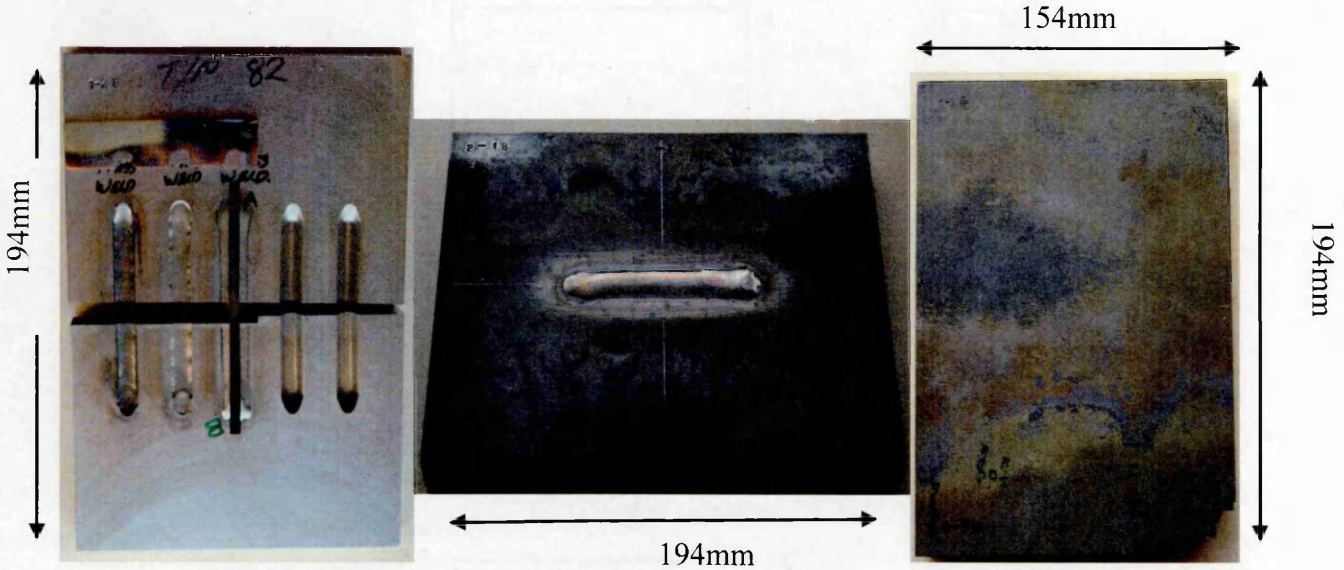

Note: Dimensions of the plate are provided in Figure 3.3.

Figure 3.6 Manufacture of stress free cuboids [206]

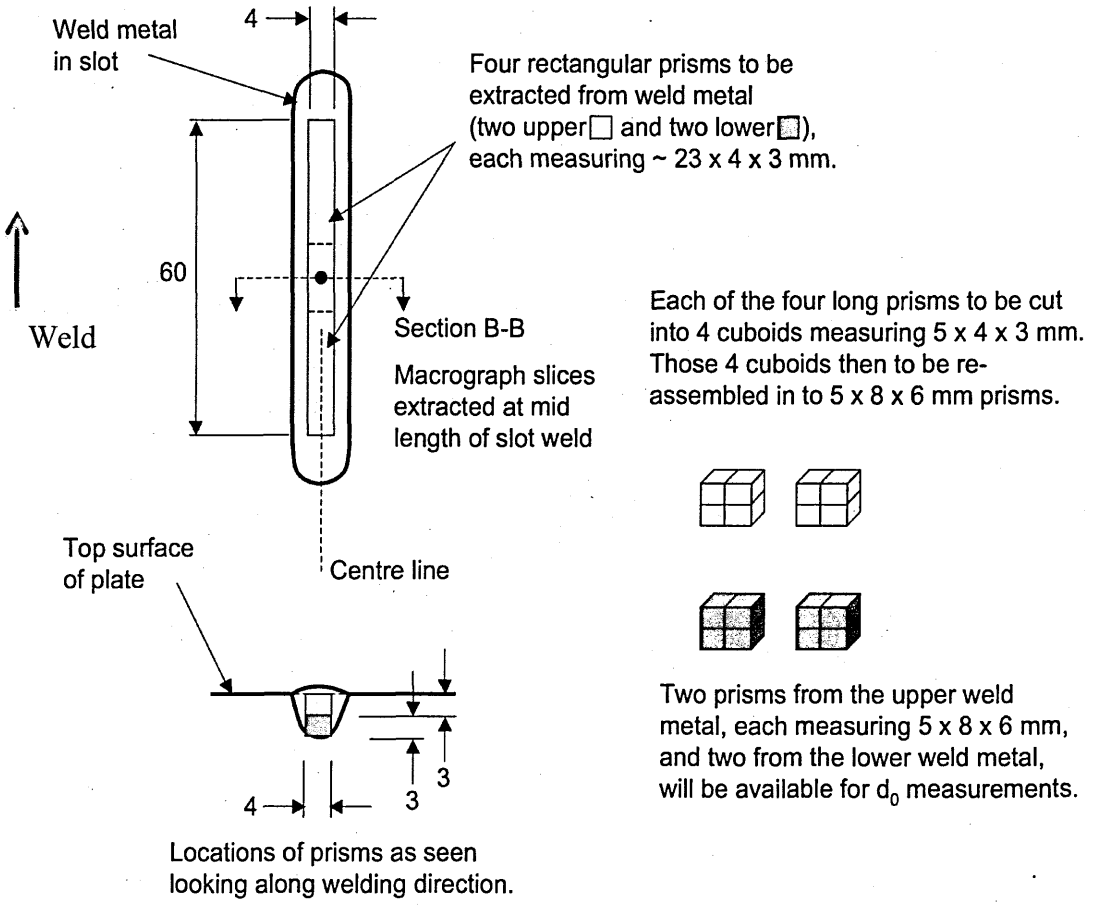

Figure 3.7 (a) Parent material block for cyclic loading analysis and (b) cyclic samples extraction

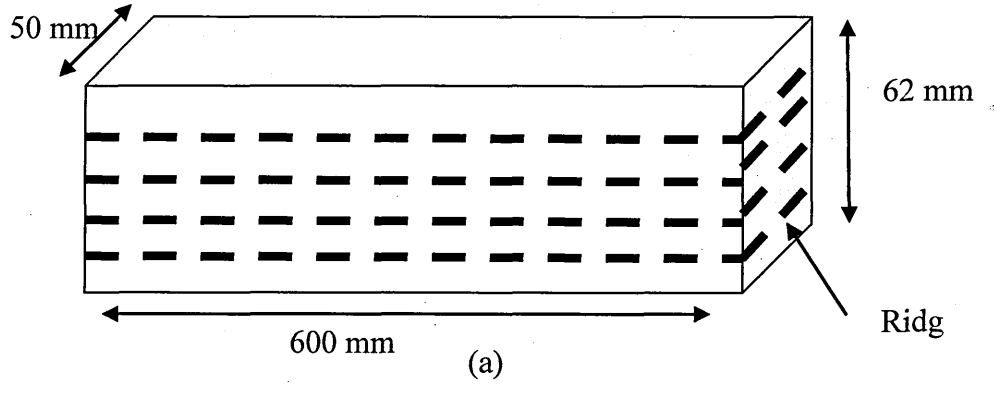

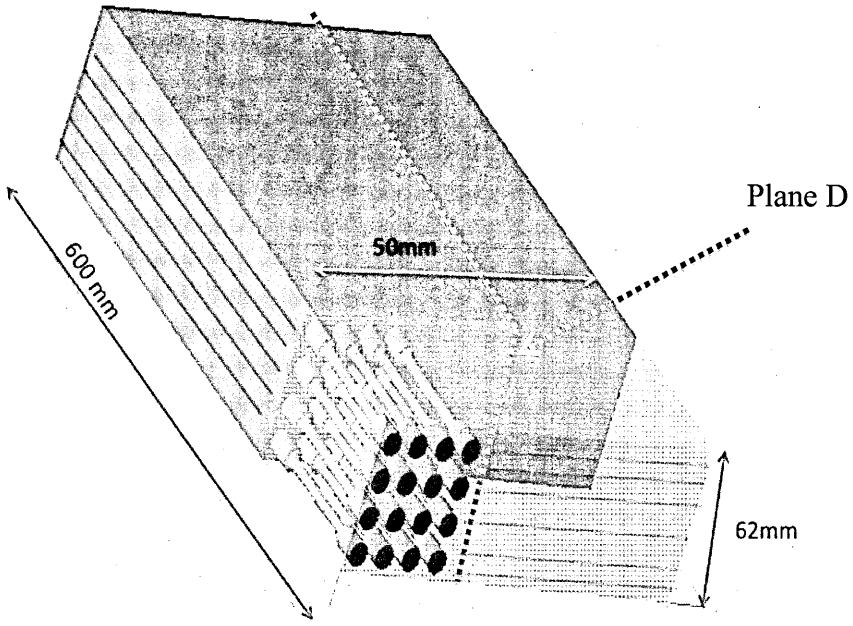

(b)

Figure 3.8 316L (N) cyclic loading samples design without shoulders

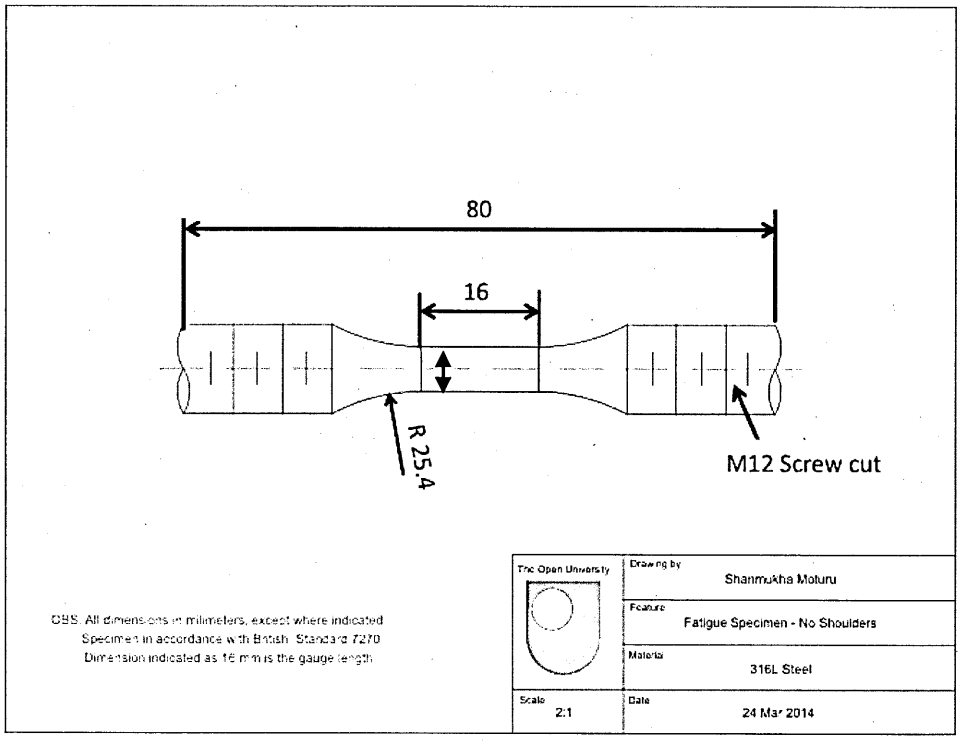

Figure 3.9 Stress vs. strain raw data plot for specimen without shoulders

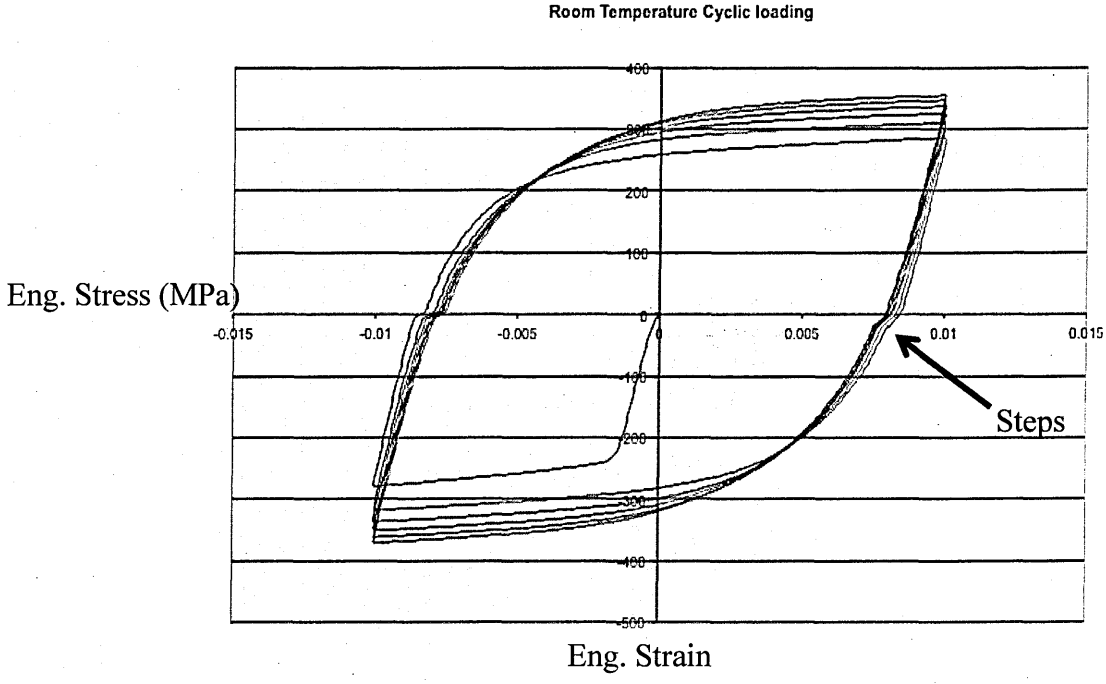

Figure 3.10 Cyclic loading sample design with shoulders all dimensions in mm

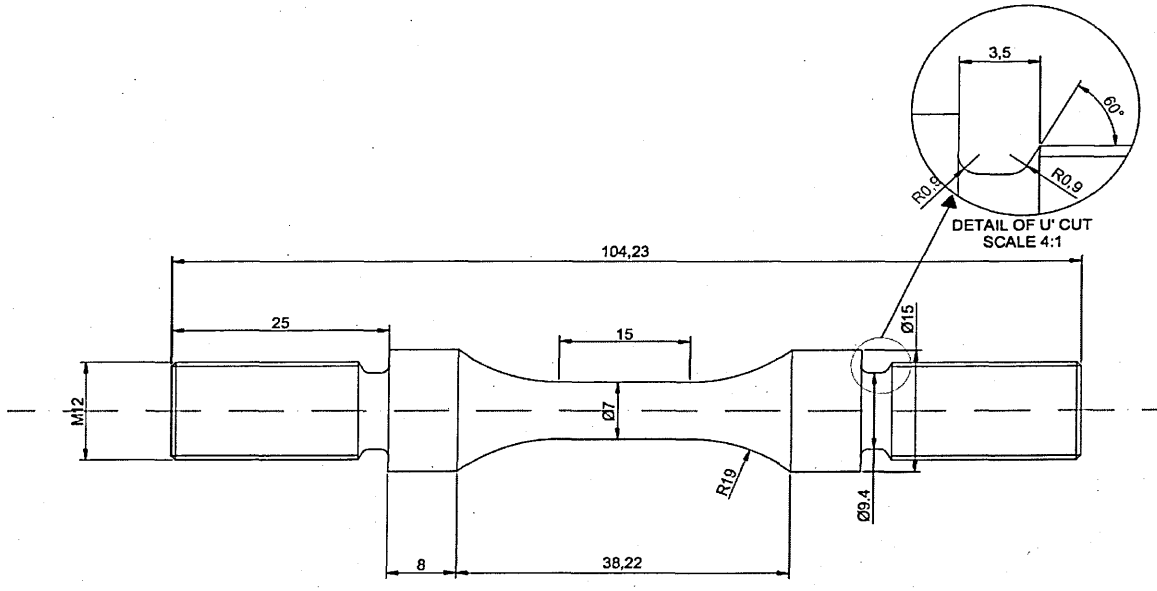

Figure 3.11 Multi pass weld plate (a) heat treated parent plate on welding table (b) weld transverse slice extraction (c) extracted weld samples for EBSD analysis (mounted)

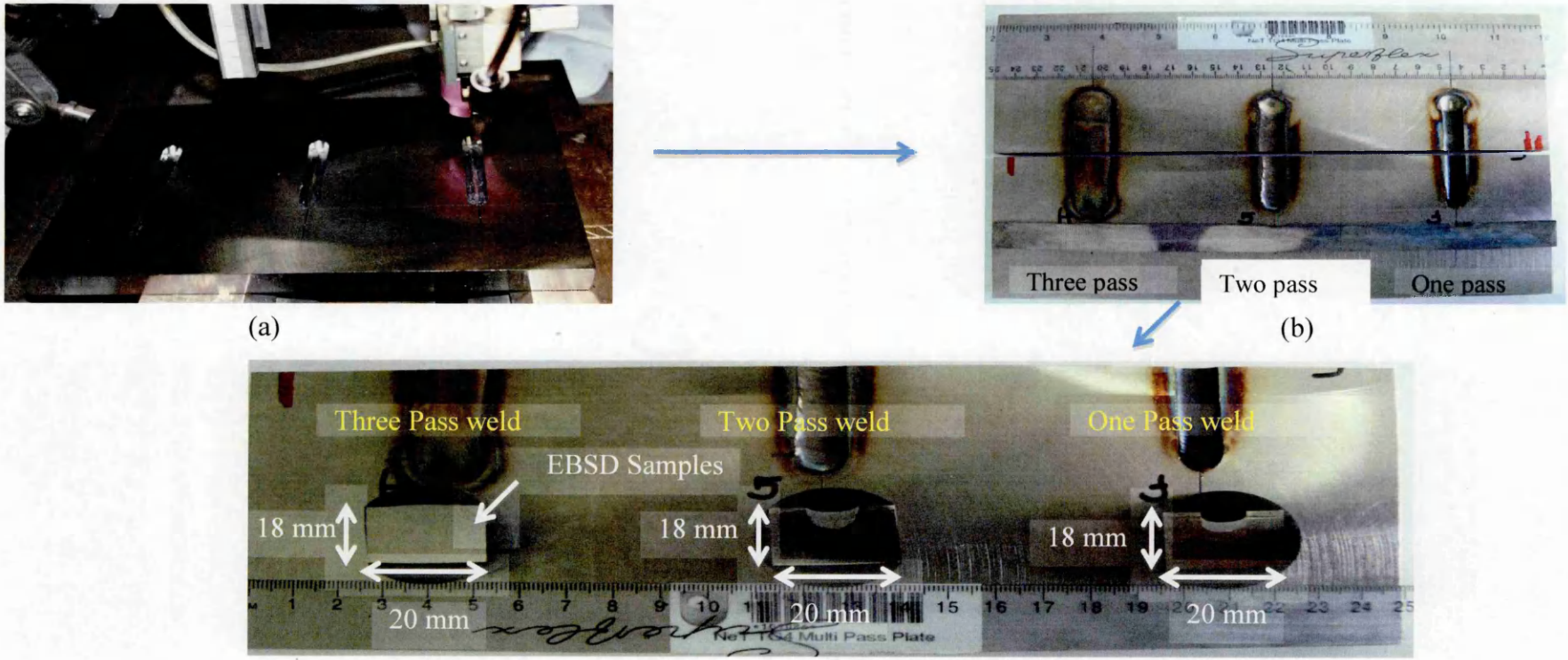

Figure 3.12 Multi pass weld sequences (dimensions of weld slots are similar to Figure 3.3(b))

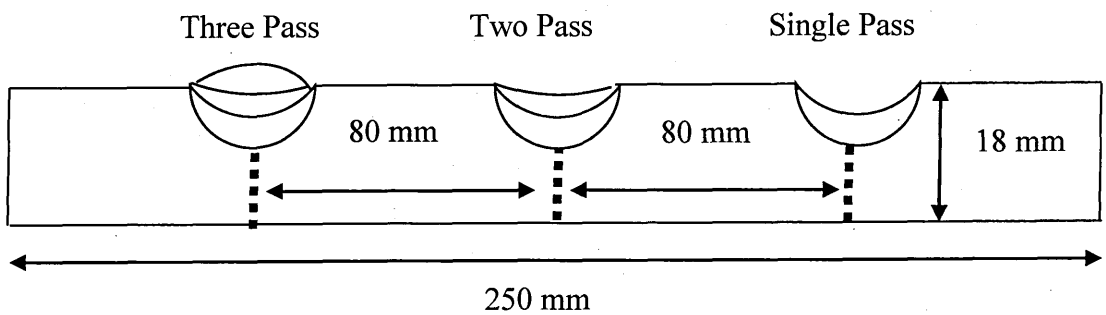

Figure 3.13 Weld transverse slice for material characterization

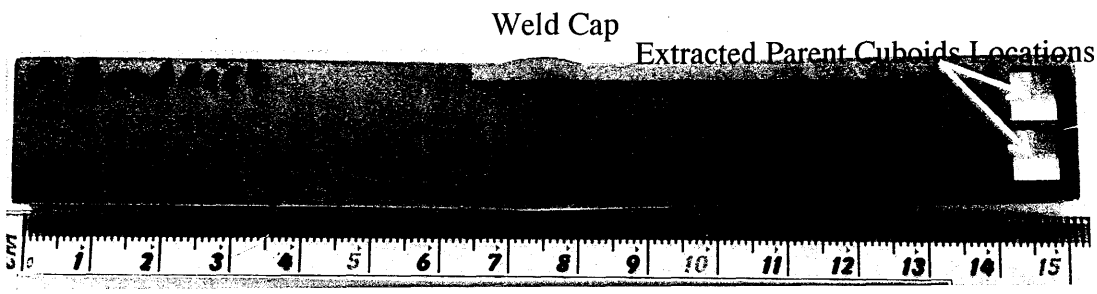

Figure 3.14 Orientation of extracted parent material cuboid used for optical metallography

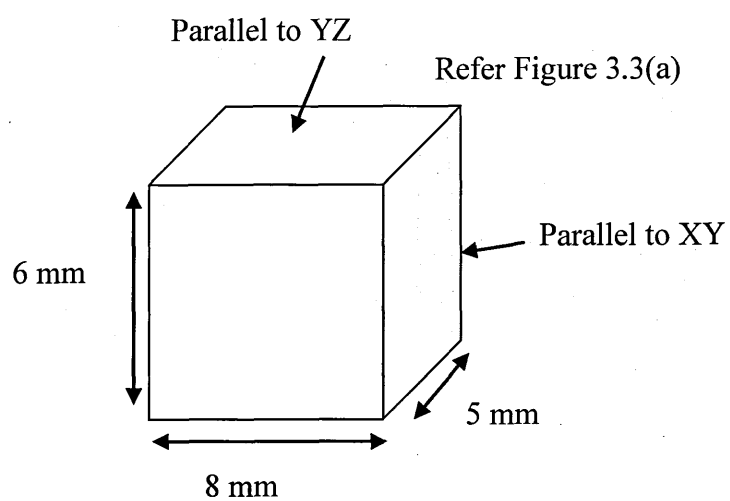

Figure 3.15 (a) Normal optical microscope image (parallel to XZ refer Figure 3.3 (a)) and (b) Grain size distribution plot

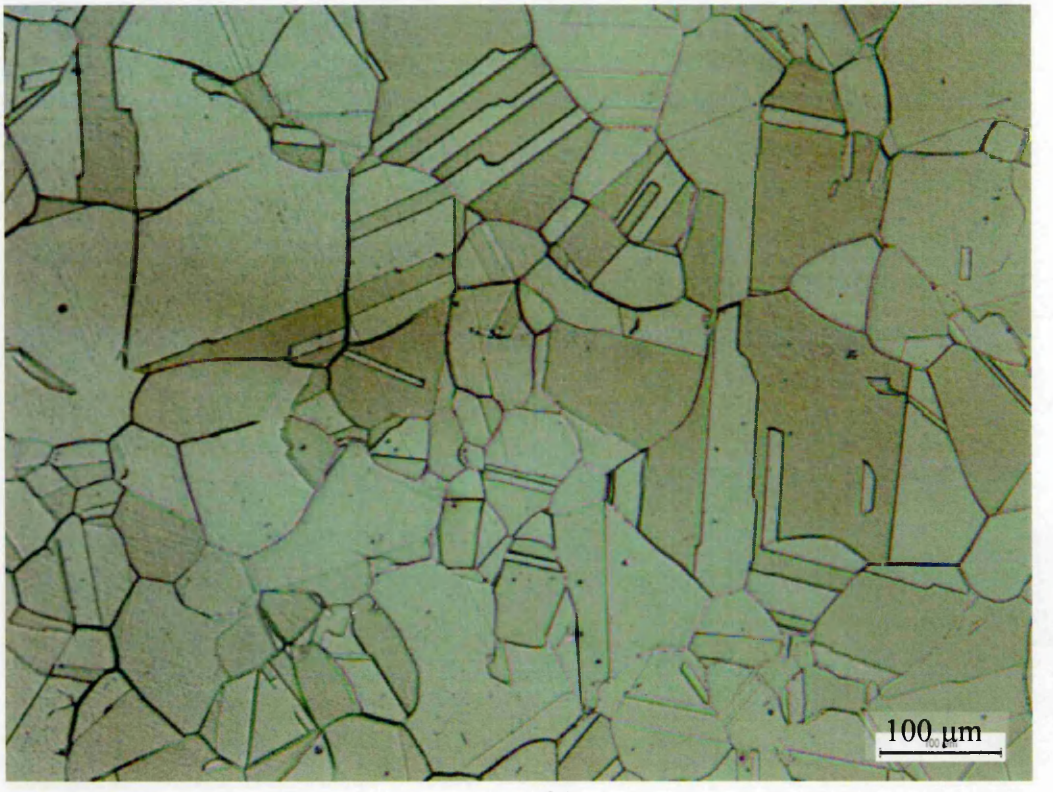

(a)

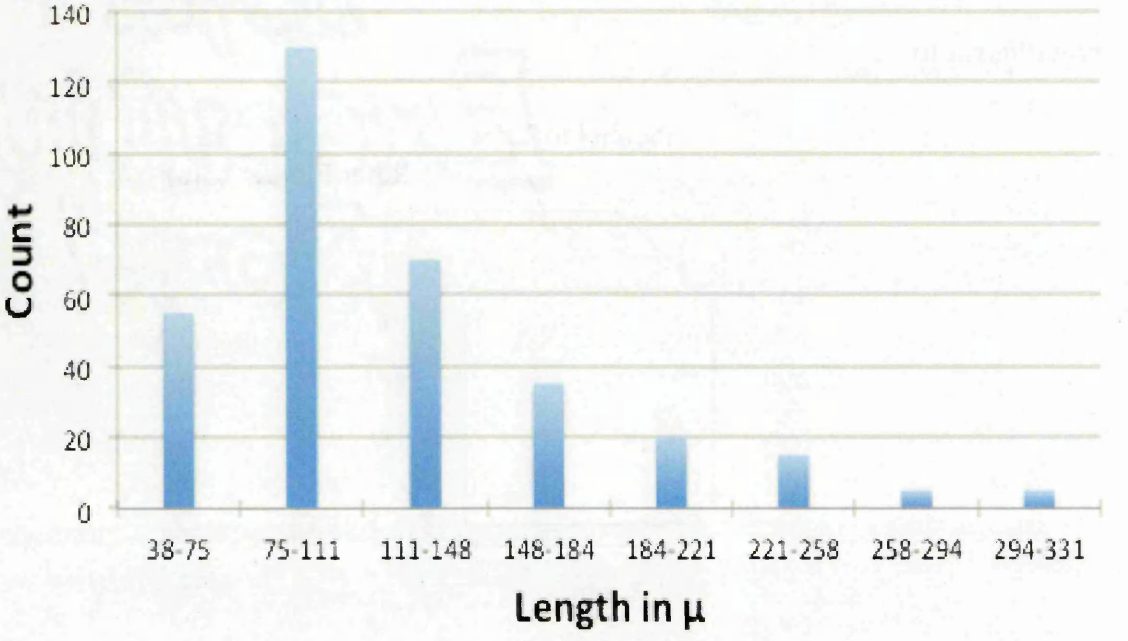

(b)

Figure 3.16 Longitudinal optical microscope image (parallel to YZ refer Figure 3.3(a)) and (b) Grain size distribution plot

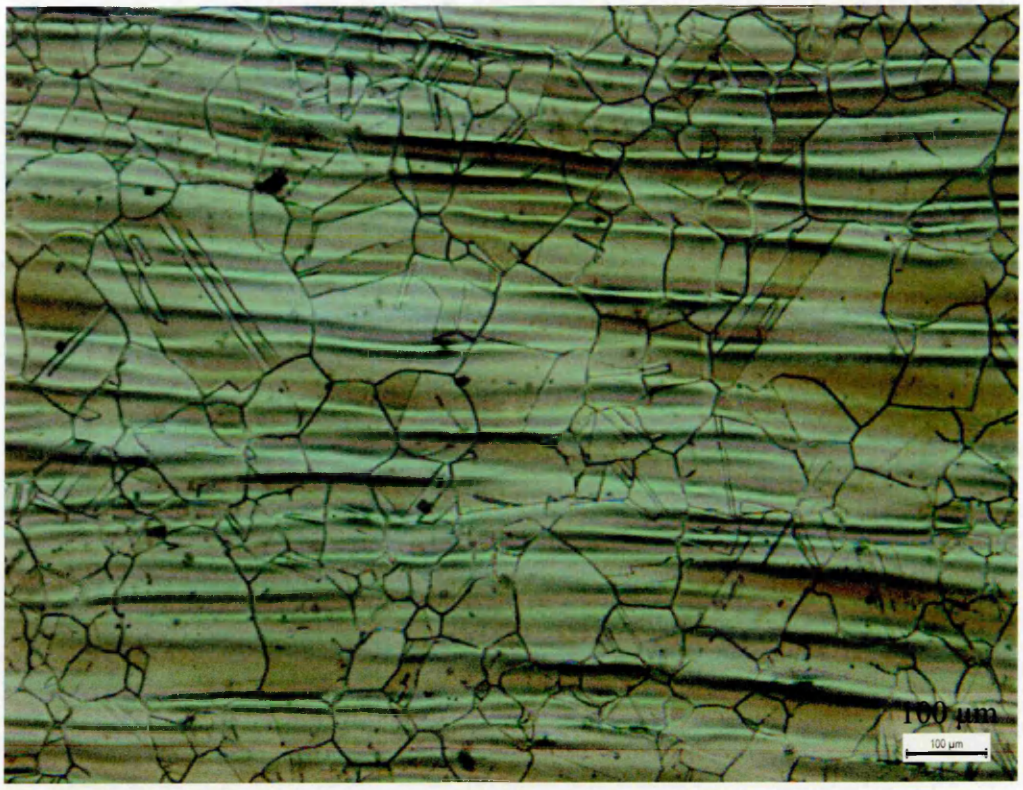

(a)

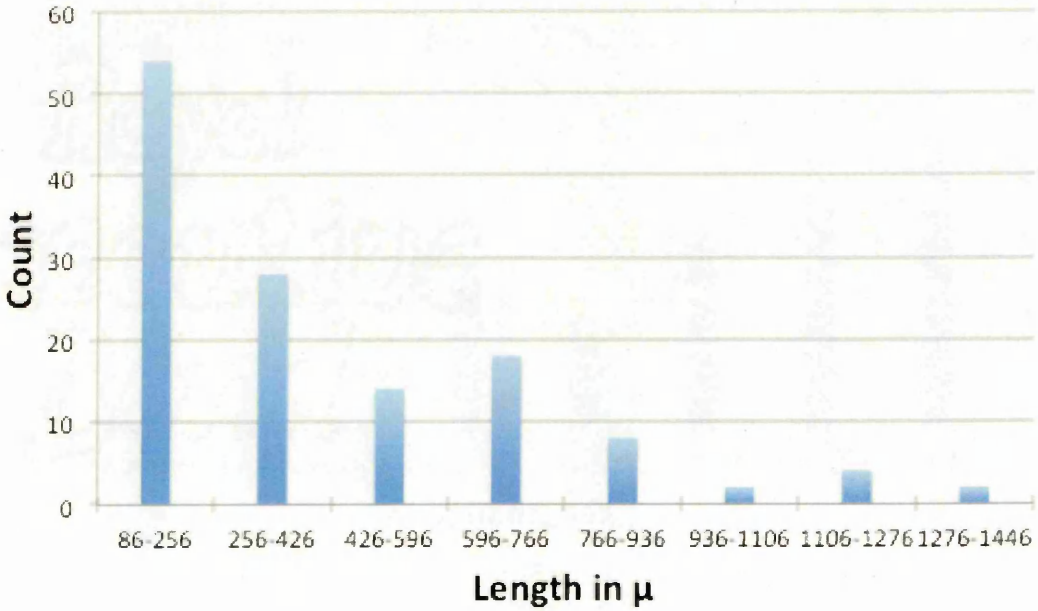

(b)

Figure 3.17 Transverse optical microscope image (parallel to XY refer Figure 3.3(a)) and (b) Grain size distribution plot

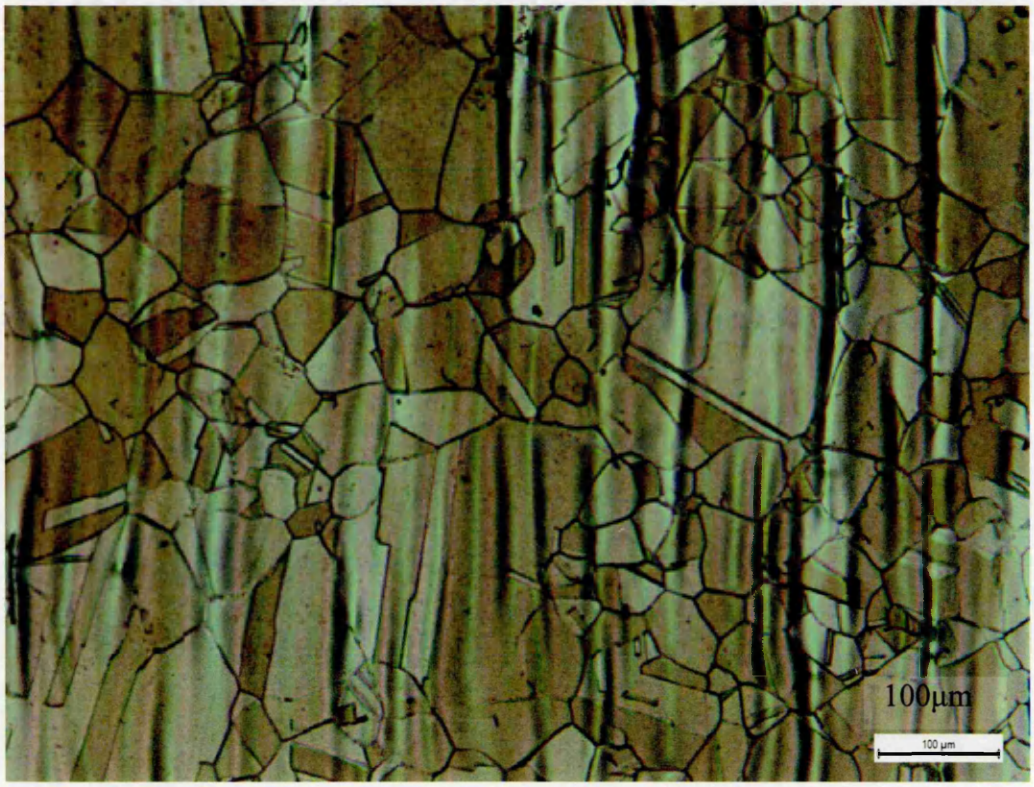

(a)

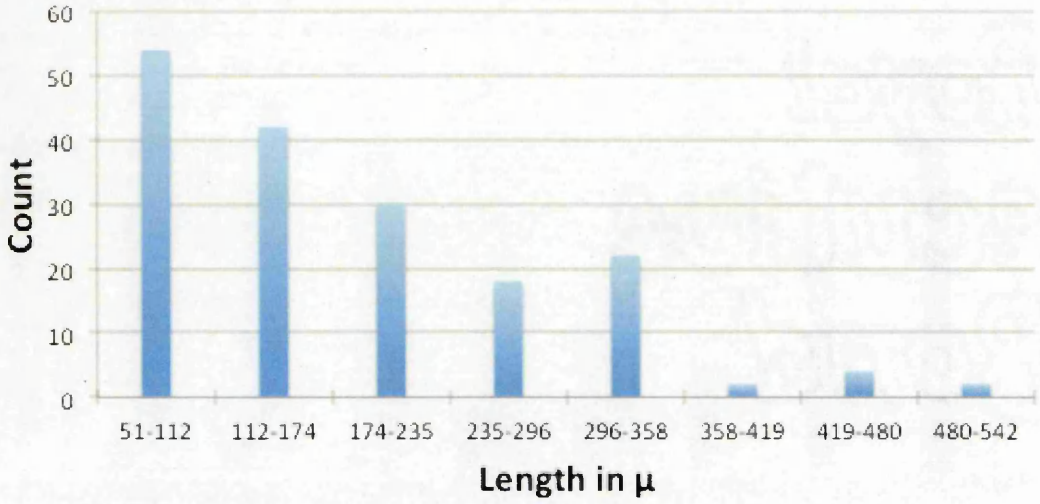

(b)

Figure 3.18 Optical macrograph of (a) single weld pass (b) two weld pass and (c) three weld pass

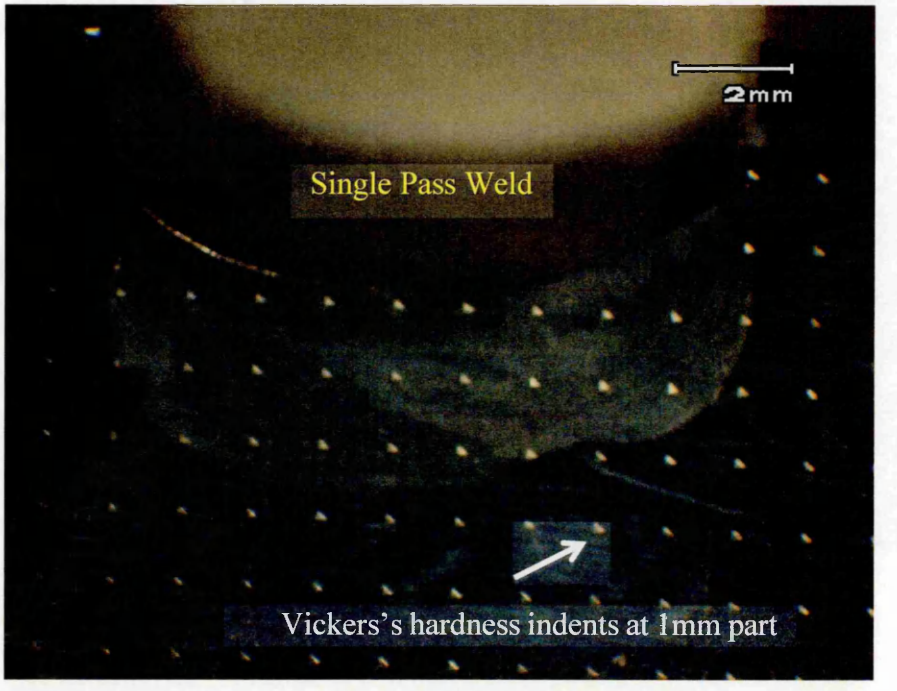

(a)

(b)

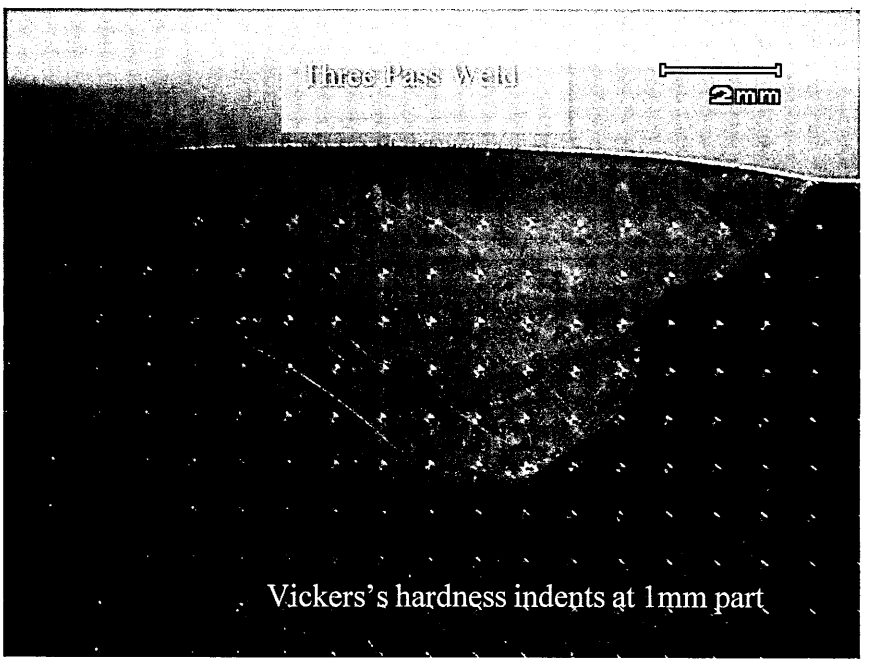

(c)

Figure 3.19 Optical micrograph of the HAZ of the single, two and three pass weld samples

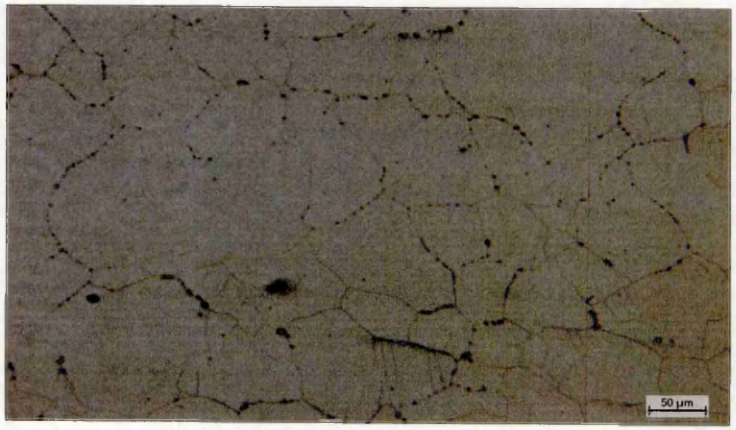

Single Pass Weld

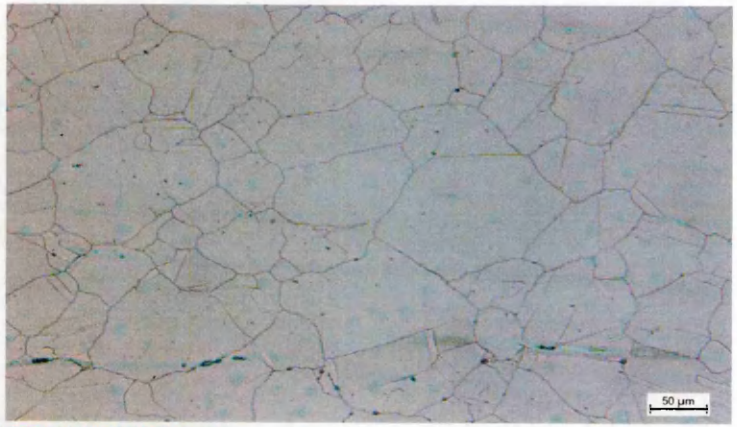

Two Pass Weld

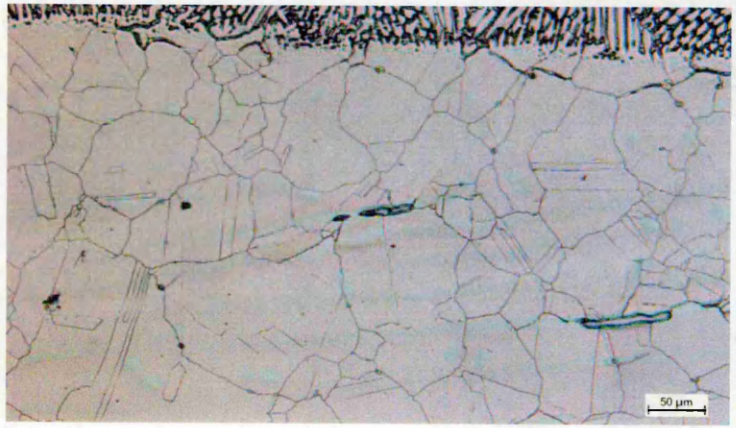

Three Pass Weld

Figure 3.20 Fusion boundary optical micrograph of single pass, two pass and three pass weld samples

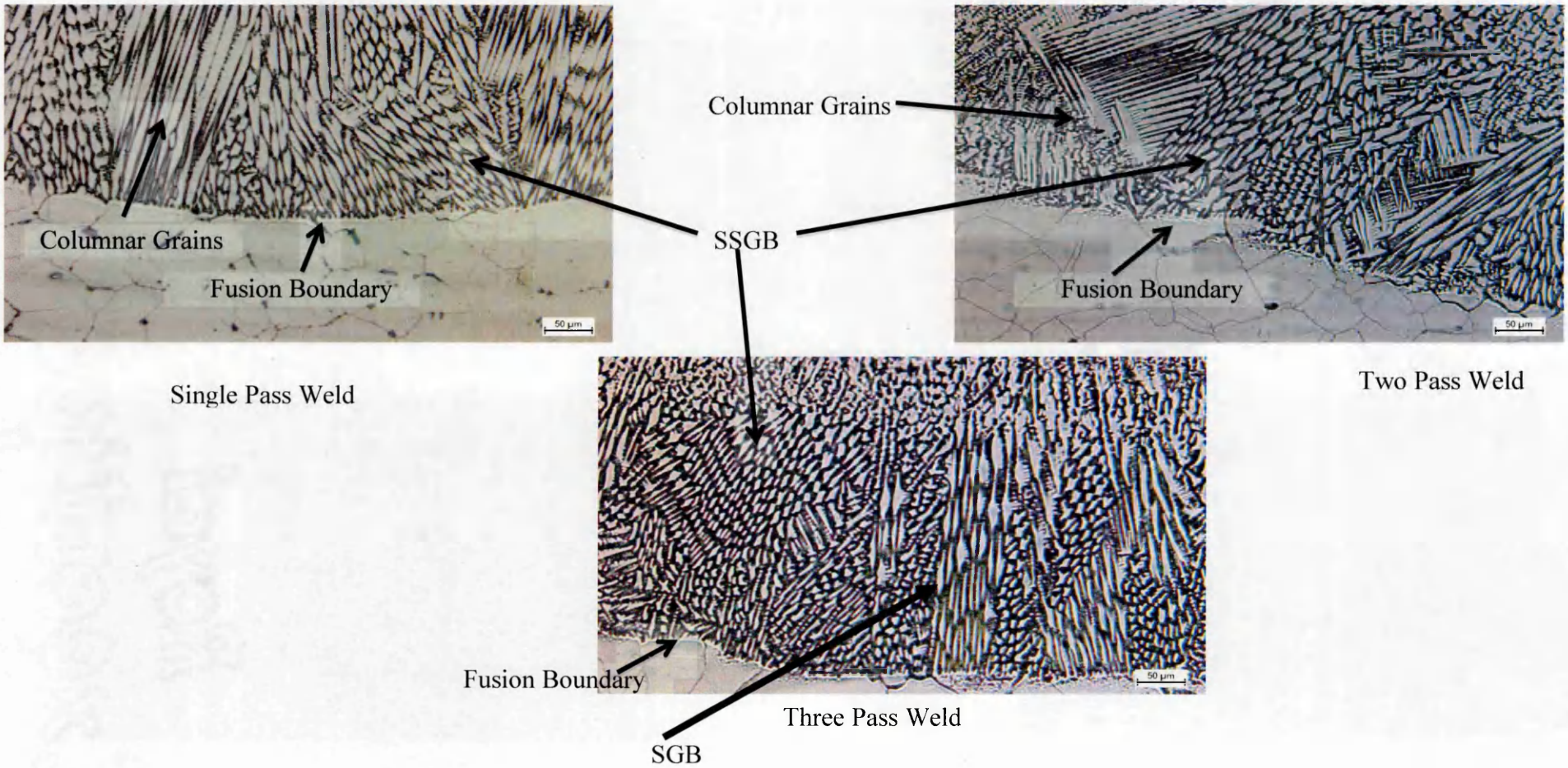

Figure 3.21 Recrystallized columnar grains at single and two pass weld boundaries

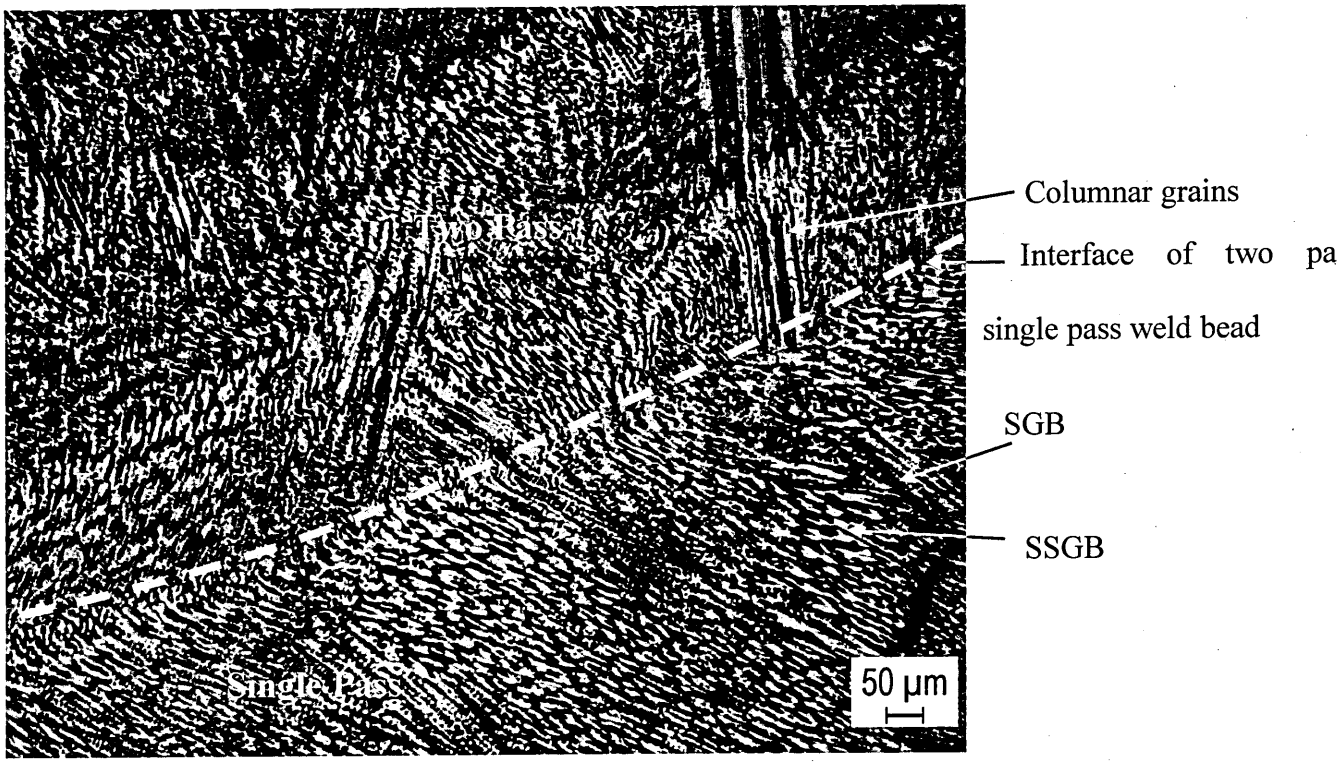

Figure 3.22 EDX point analysis location of SEM image

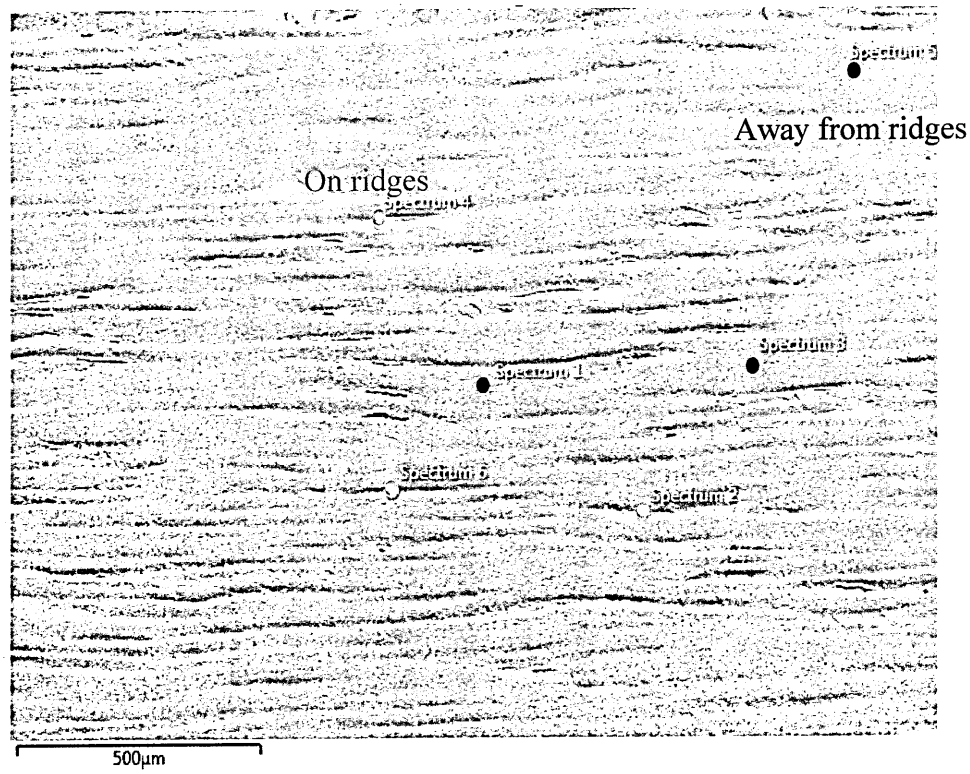

Figure 3.23 EBSD grain orientation map (a) parent material (b) three pass weld metal

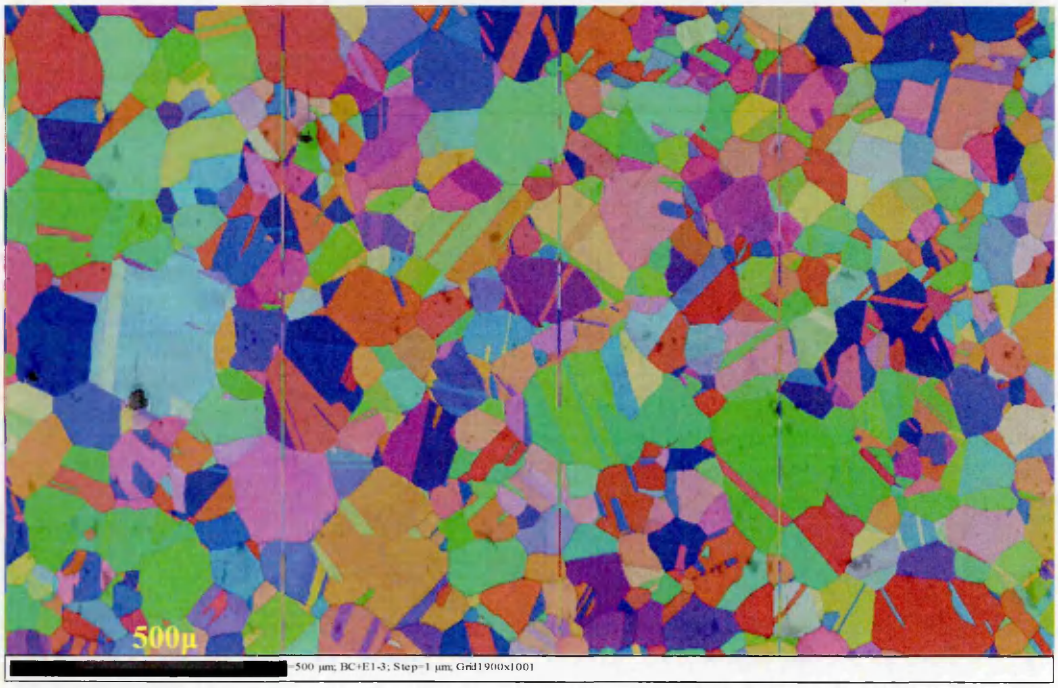

(a)

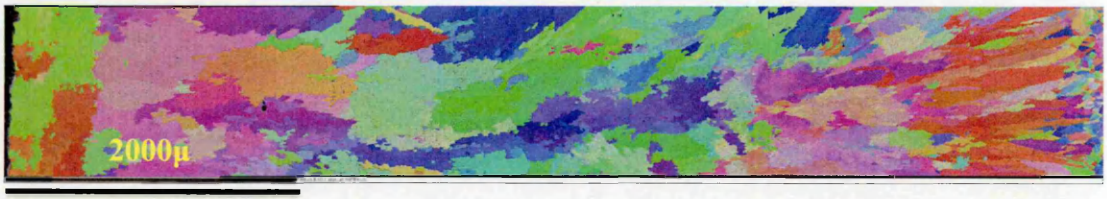

(b)

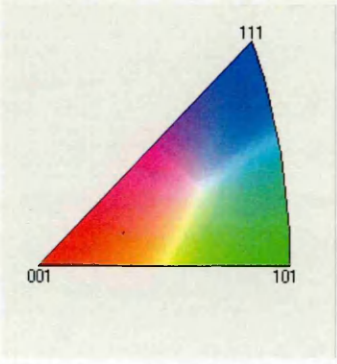

Figure 3.24 EBSD pole figure (a) parent material and (b) three pass weld material

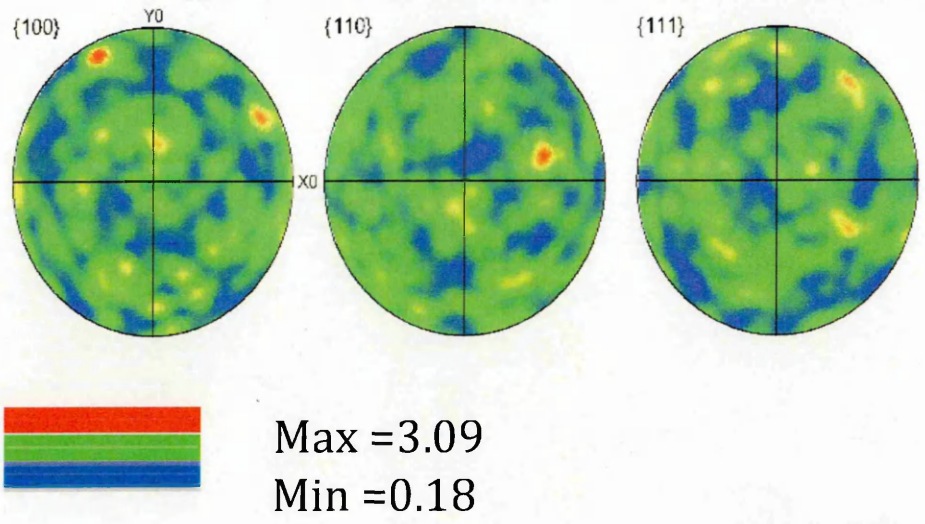

(a)

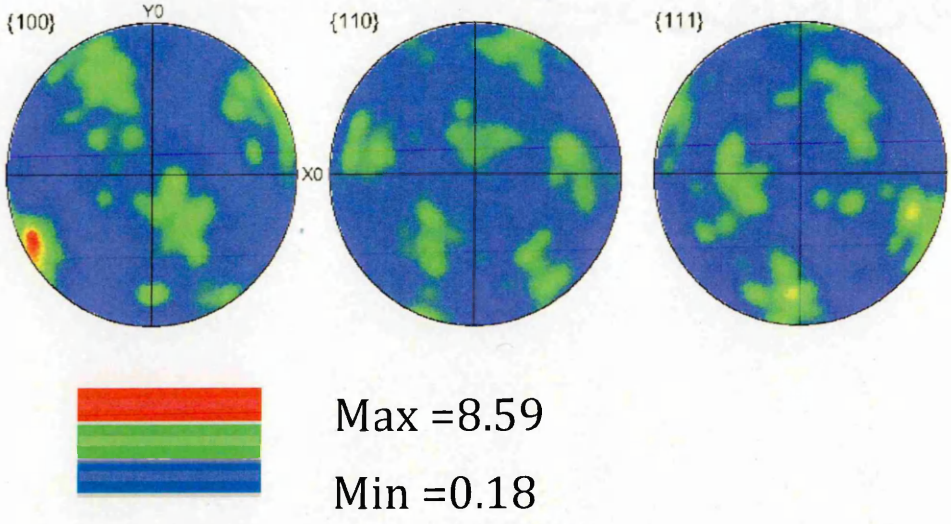

(b)

Figure 3.25 Neutron diffraction pole figures for heat treated base material specimens of (a) γ Fe {111} and (b) {200} rolling direction vertical [206]

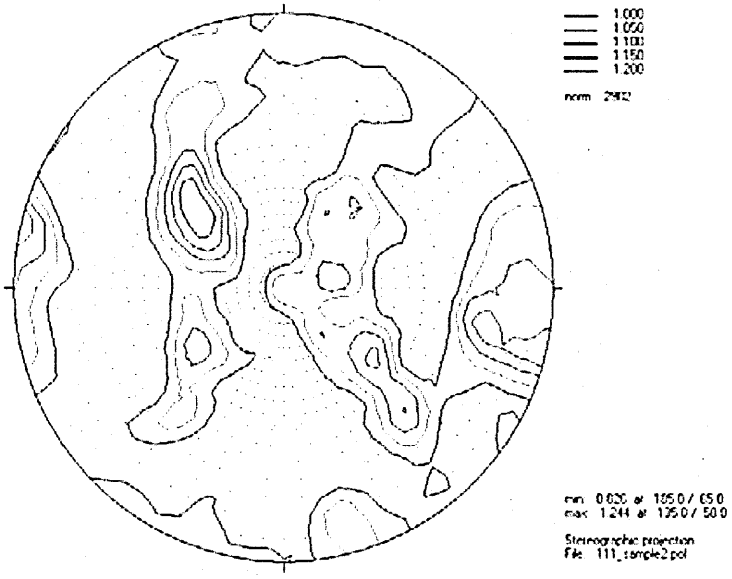

(a)

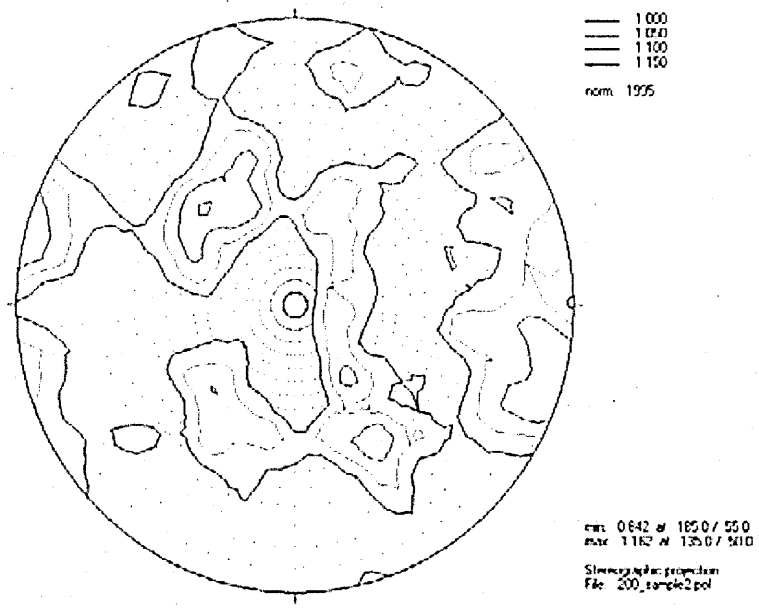

(b)

CHAPTER 4. BENCHMARK WELDMENT RESIDUAL STRESS CHARACTERISATION

4.1 Introduction

This chapter describes how neutron diffraction was used to evaluate the residual stresses present in a three-pass welded plate, a benchmark test component made from AISI type 316L austenitic stainless steel. Residual stresses, caused by welding, arise because of localized thermo-cyclic plastic deformation and differential contraction in the materials. The presence of residual stress can have a significant impact on the performance of the welded structure, as described in section 2.4 of Chapter 2. An accurate assessment and evaluation of stress and strain in a welded benchmark component is important in order to improve prediction methods and to understand the role of non-uniform thermal cyclic plastic deformation.

Neutron diffraction is a particularly suitable experimental technique for this research study, since it allows non-destructive measurement of residual elastic strain through the whole thickness of the welded plate. The material and geometric details of the test components have already been described in sections 3.1 and 3.2. Welded plate (ID 3-1A), and two sets of "stress free cuboid assemblies" from two different plates (IDs 1-2B and 2-1B), were supplied for the present study. The manufacturing details of the stress free cuboids have been described in section 3.3. Diffraction experiments carried out by other members of the NeT consortium, involving several measurements on the same plate (ID 3-1A), are listed in Table 4.1 List of residual stress measurements carried out on 3-1A weld plate.

The objective of the round robin experimental measurements, using different techniques, performed by separate teams, was to assess the accuracy and repeatability of residual stress measurements on a well-controlled benchmark weldment, and to thereby improve the reliability of measurements. Another objective was to compare the best experimental characterisation with a simultaneous weld residual stress prediction round robin exercise, aimed at improving weld computational mechanics and simulation methods. For this research thesis, residual stresses in the benchmark-welded plate (ID 3-1A) were measured using the VULCAN diffractometer at SNS facility, USA and ENGIN-X at the ISIS facility, UK. Details of these instruments have been described in section 2.4.1 of Chapter 2.

4.2 Sample and Instrument Preparations

To achieve the above objectives, and for the sake of a consistent comparison of experimental and simulation data, the NeT TG4 group developed protocols [172,215] for both measurements and simulations, defining the locations to be studied, in order of priority and reporting requirements.

4.2.1 NeT TG4 proposed measurement locations

The residual stress measurement points, for the NeT TG4 weldment benchmark defined in the measurement protocol [172] are grouped into nine sets listed in order of priority, as shown below and as indicated in Figure 4.1. A total of 137 measurement points, were written in MatLab vector style, where a colon specifies the distance increment between two consecutive measurements. For example, the first priority set (line BD) comprises 15 points, passing through the thickness of the plate (including the three

weld beads), where the first measurement point is located at 2 mm from the top surface of the plate and the following measurements are located at consecutive increments of 1 mm (i.e. 3, 4, 5, 6, 7… and 16 mm from the top surface).

Priorities of measurement points: cf. Figure 4.1

1) 15 positions on line BD: x = z = 0, y = [2:1:16].
2) 19 positions on line D5: x = 0, y =5, z = [-90, -70, -50: 5: -30, -20:10:20, 30:5:50, 70, 90].
3) 19 positions on line D9: x = 0, y =9, z = [-90, -70, -50: 5: -30, -20:10:20, 30:5:50, 70, 90].
4) 19 positions on line D2: x = 0, y =2, z = [-90, -70, -50: 5: -30, -20:10:20, 30:5:50, 70, 90].
5) 15 positions on Line D16: x = 0, y = 16, z = [-90, -70, -50:10:50, 70, 90].
6) 17 positions on Line B2: x = [-70, -50:10:-20, -15:5:15, 20:10:50, 70], y = 2, z =0.
7) 8 additional positions on line B2: x = [-17.5:5:17.5], y = 2, z = 0.
8) 17 positions on Line B2: x = [-70, -50:10:-20, -15:5:15, 20:10:50, 70], y = 16, z =0.
9) 8 additional positions on line B2: x = [-17.5:5:17.5], y = 16, z = 0.

Following welding, due to the rippled surface of the weld bead, it was not possible to identify exactly the origin of the welded plate at the top surface. Instead, a reference point on the bottom surface of the welded plate was identified precisely. Hence, the measurement positions, as defined by NeT TG4, are located relative to an origin at the bottom surface of the plate, identified with the help of a 3D laser scan and Strain Scanning Simulation Software (SScanSS)[126].

4.2.2 Sample alignment

During neutron diffraction experiments, the sample geometry and its alignment in the diffractometers determine the precise positioning of the sample and the reliability of the measurements. In order to achieve alignment, the following process was used:

1. Four steel balls, each of 12 mm diameter, were glued onto each corner of the welded plate and away from the measurement positions. These balls were used as reference points for the plate and are known as fiducial markers.
2. A 3D laser line scanner (see Figure 4.2) was used to generate a virtual, three-dimensional computer aided design (CAD) model of the welded plate with its fiducial markers as shown in Figure 4.3. The *x, y, z* co-ordinate points for each fiducial marker were measured relative to the laser scanner datum.
3. The CAD model was then imported into SScanSS software in order to generate and simulate a measurements plan.
4. With the welded plate specimen mounted on the instrument table, a laser tracker on the VULCAN instrument and a laser probe on the ENGIN-X instrument were used to measure the co-ordinate positions of the plate's fiducial markers to an accuracy within ±0.025 mm.
5. The SScanSS software merges the two different co-ordinate systems, of the sample and of the instrument table, into one coordinate system, so that the two components are aligned.
6. The table movement positions are verified with the facilities available to the user during the experimental process, as described in section 4.2.3.
7. Using this single co-ordinate system, SScanSS is then used to generate a series of co-ordinates for each proposed measurement point on the sample. Now the user

can specify which strain components are to be measured for each specific point or groups of points.

8. Finally, the series of sample measurement coordinates are imported into the main instrument control system to automatically drive the sample table movements.

4.2.3 Sample alignment facilities at neutron sources

Once the sample was aligned and the coordinates for each fiducial point generated by SScanSS, measurement locations were verified by moving the sample table to one or more fiducial points, before verifying any angular misalignment by rotating the table 90° either in a clockwise or anti-clockwise direction. These verifications were carried out with the help of an optical theodolite (available at ENGIN-X, ISIS UK) and a laser tracker (available at VULCAN, SNS, USA; see Figure 4.2). For both the instruments, a positioning accuracy of ±0.05 mm was achieved for the instrument table relative to the beam line.

4.2.4 Instrument alignment calibrations

The alignment of jaws and collimator may change from one instrument user to another and therefore it is good practice to check the jaws and collimator alignments prior to the start of the experiments. This was achieved using the standard method of observing the diffracted neutron intensity as a pin was scanned in directions parallel and perpendicular to the beam with a gauge volume of $20 \times 2 \times 3\ mm^3$ at the ENGIN-X instrument and $10 \times 2 \times 2\ mm^3$ at the VULCAN instrument respectively.

Calibration measurements were undertaken by measuring the diffraction spectra for materials of a known lattice parameter; for example iron and cerium oxide powders were used for the ENGIN-X experiment. Similarly, vanadium, diamond and silicon powders were used for the VULCAN experiment. The lattice parameters measured from the

experiment should match with reference values in the absence of any misalignment. However, in practice, there will be small discrepancies between the lattice parameters calculated from the calibration measurement in each detector bank, and the known lattice parameter. These discrepancies may arise for various reasons, including small remaining geometric misalignments. The discrepancy is accounted for by creating bank specific correction constants, from the ratios of the reference values compared to the measured values, and by multiplying all subsequent lattice parameter measurements by these constants. The calibrated powders' measurements during ISIS experiment are provided in Table 4.2 The ISIS instrument calibration measurements.

4.3 Stress Free Lattice Parameter (a_0)

The welding process, as described in section 2.2.1, deforms the material locally introducing residual elastic strains, which manifest as changes in lattice spacing of the material at the crystallographic length scale. In order to determine the strained lattice spacing, the reference unstrained lattice spacing (a_0) is necessary. The stress free lattice spacing can be measured from representative samples of material that are free from macroscopic stress. A representative stress free sample can be obtained simply by extracting it from an unstressed plate using a stress free cutting process. When a sufficiently small sample is extracted from a welded component, most of the macro stresses will be relaxed in the extracted sample. However, micro stresses within the grains and between the grains will remain in the extracted material. Likewise any changes in lattice parameter resulting from chemistry are unaffected by the cutting process [130,216]. Type I stresses are directionally independent, whilst type II and III are directionally dependent. For the present study, the strained lattice parameters were evaluated using weld and parent macro-stress free cuboids supplied by the NeT consortium. The

manufacturing of the macro-stress free cuboids has been described in section 3.3 and the calculation of the lattice strain (and hence the stress) in section 2.5.

The lattice parameters of stress-free cuboids set 1-2B were measured at both VULCAN (SNS) and ENGIN-X (ISIS) instruments, while, the lattice parameters for cuboids set 2-1B were measured only at ENGIN-X.

4.3.1 VULCAN stress-free lattice parameter measurements

Each a_0 cuboid was mounted onto a jig and measurements were performed under both static and constant slow rotation conditions. The purpose of static and constant slow rotation of stress free cuboids is to analyse the difference in measured stress free lattice parameter due to difference in the number of grains diffracted from static and constant slow rotation conditions of stress free cuboids. The jig comprised an electronic DC stepper motor with a table, as shown in Figure 4.4. Throughout the experiment, the lattice parameters in the longitudinal and transverse directions were measured from the north bank (bank 1), while keeping the normal direction in common with the south bank (bank 2), as shown schematically in Figure 4.6. In order to align the cuboid with the centre of the neutron beam, the sample table was moved manually until the centre of the cuboid aligned with the centre of the laser tracker. The NeT measurement protocol recommended a $3 \times 3 \times 3$ mm^3 gauge volume (described in section 2.5.1) for diffraction experiments. This gauge volume was selected based on the grain size and the size of the cuboid. The minimum number of grains required in a given gauge volume, for good counting statistics is approx. 10,000 [156,157]. However, due to the lack of availability of a 3 mm collimator at the VULCAN instrument, a 2 mm collimator was adopted for this experiment giving a gauge volume of $3\times3\times2$ mm^3. For these measurements, a counting time of approximately 10 minutes was allocated for each measuring point.

The 'counting time' is that required to achieve a high quality diffraction pattern from exposure of the measurement point to the neutron beam. Counting times are expressed in units of micro-amps, a unit which is proportional to the number of neutrons striking the heavy metal target, rather than an actual time.

4.3.1.1 a_0 Data analysis software

Data analysis software is used to read raw data collected from the neutron detectors, and then plot the diffraction lattice parameter (dhkl) as a function of time of flight (TOF). This plotted data is used for sequential Rietveld diffraction profile refinements, or single peak fitting, to provide an average cell lattice parameter or hkl spacing, measured from the neutrons diffracted within a given gauge volume. In this present measurement, a Rietveld profile refinement method 217 was used for the data analysis. An example of Rietveld profile fitting of raw data used in the evaluation of residual stress in a welded plate is shown in Figure 4.5. The Rietveld refinement uses a least squares approach to refine a theoretical line profile, until it matches the measured profile, thus providing an average (unit cell) lattice spacing. The equations required to determine elastic strain from lattice parameter measurements have been described in section 2.5. The General Structure Analysis System (GSAS) and SmartWare codes were used for Rietveld profile refinements analysis at VULCAN. At ENGIN-X, the ISIS in–house developed Open Genie analysis software, with GSAS software running at the backend, was used for the Rietveld profile refinements 218, using the space group and the lattice parameters provided in Table 4.3.

4.3.1.2 VULCAN a_0 results

As described above, during the VULCAN experiments, each cuboid was measured whilst stationary and during constant rotation about its longitudinal and transverse axes,

with the help of the jig, as shown in Figure 4.6. Depending on which continuous rotation axis is used, both bank 1 and 2 measured the average of longitudinal and normal direction, or the average of the transverse and normal directions. Whilst, in static mode, bank 1 measured the longitudinal and transverse directions and bank 2 measured two normal directions. A total of seven measurements were obtained for each a_0 cuboid from each detector bank. Table 4.4 (a), summarises the average lattice parameter measured for each cuboid for the respective detector banks.

As described in section 4.3, the extraction of small coupons should have relaxed the Type I stresses [219]. However, during an experiment, the path length from the sample to each bank will be different depending on the sample thickness [129]. As a result, bank specific average lattice parameters are used here for the evaluation of residual stress in the welded plate. The variation in lattice parameter, in terms of micro strain, is calculated using equation 4.1

$$\mu\varepsilon = \left(\frac{(a-a_0)}{a_0}\right) * 1000000 \qquad 4.1$$

Where 'a' is the measured lattice parameter and 'a_0' is evaluated by taking an average of the bank specific measurements in the stationary mode and whilst under constant rotation. Figure 4.7-4.8 and Table 4.4 (b), illustrate the variation in the measured a_0 expressed as the apparent micro-strain in the stationary mode and for constant rotation. The micro strains summarised in Table 4.4(b) are the averages of the longitudinal and transverse micro strains measured in Bank1 and the average of the normal micro strains measured in Bank 2. The micro strain variation for constant rotation is smaller than that for the static mode. In static mode, a maximum micro-strain of approximately -164 in the top weld a_0 cuboid was evident. Similarly, under constant rotation, a maximum micro strain of approximately -105 in the top weld a_0 was measured, see Figure 4.8.

4.3.2 ENGIN-X stress free lattice parameter measurements

Both sets of a0 cuboids (i.e. 1-2B and 2-1B) were mounted on a flat plate and carefully aligned using a theodolite. Figure 4.9 shows the cuboids glued onto the flat plate. This method of alignment was chosen, instead of the jig alignment used at VULCAN, as a result of the jig being damaged during transportation to ISIS. The same bank specific lattice parameter measurement approach was implemented in this experiment (i.e. longitudinal and transverse from bank 1, and normal from bank 2). A gauge volume of 3 $\times$ 3 $\times$ 3 mm^3 was used for this experiment. Each cuboid was rotated, at angular increments of 30°, anti-clockwise from 30° to −270° about its longitudinal and transverse axes. A counting time of 20 minutes (approximately) was used for this experiment. Open Genie software was used for Rietveld profile fitting, covering more than ten peaks, as shown in Figure 4.5, using the space group and initial lattice parameters, provided in Table 4.3.

4.3.2.1 ENGIN-X a_0 results

The measured micro-strain variation in the two sets of stress free cuboids at 30° increments of rotation about the longitudinal axis, and transverse axis, of each cuboid is presented in Figure 4.10-4.11, for the 1-2B a_0 set and Figure 4.12 for the 2-1B a_0 set. The average of the measured lattice parameter, at all angles for each rotational set, was used to evaluate the variation in terms of micro strain. Table 4.5 provides the average lattice parameters measured at 0°, 180°, 90° and 270°. Table 4.6 provides the average lattice parameters measured and standard deviation of micro strain at all angles. The micro strain was calculated using equation 4.1. The variations of measured micro strain in both weld and parent cuboids were up to ±200. During the stress free cuboid experimental setup, the possibility of the cuboid misaligning with the neutron beam is high, due to the irregular shapes of the imperfect cuboids as seen in Figure 4.9. Therefore, the possibility of the cuboids being incorrectly aligned was investigated, by undertaking repeat

measurements for the weld (top) cuboid set 1-2B. These results are presented in Figure 4.11 and show a similar trend to the original measurements. The repeated measurements show that the cuboids were aligned correctly and that the variation of measured micro strain in both weld and parent cuboids was not due to alignment problems. Further investigation was carried out to understand the variation in measured lattice parameters, by comparing the results with average lattice spacing measurements from different sources. Figure 4.13 shows the average lattice spacing measurement of the respective cuboids at different sources [220]. The average lattice spacing measurements performed at the reactor source are higher than at the spallation sources (VULCAN and ENGIN-X). One of the possible reasons is that at the reactor source, only single peak (i.e. 311 peak) lattice spacings are measured, while at the spallation source more than 10 peak (refer to Figure 4.5) lattice spacing measurements are averaged. Other possible reasons for this difference are described in section 4.6.1.

4.3.2.2 Uncertainty of data analysis

Material factors such as texture (affecting the intensity of peaks), grain size (affecting the number of neutrons diffracted) and partially immersed gauge volumes (affecting the peaks positions) can contribute to inconsistences (scatter) in the stressed and un-stressed lattice parameter measurements. These inconsistences in the experimental raw data were analysed using an error propagation method. This method calculates the uncertainty in lattice measurements, strain and stress, based on the statistical uncertainties associated with the peak fittings, as output from the GSAS software. The derived uncertainties are dependent on the measurement counting time.

4.4 Residual stress measurement in the welded plate

The residual stress measurements of the three-pass weld austenitic stainless steel plate are presented in two parts:

i) VULCAN and ENGIN-X results using 1-2B a_0 set

ii) ENGIN-X results using 1-2B and 2-1B a_0 sets

In both experiments, the lattice parameters, in the longitudinal and transverse directions of the welded plate, were measured from the north bank (bank 1), while keeping the normal direction as common in the south bank (bank 2). The residual stress measurements were performed at prescribed positions, as recommended by the NeT TG4 Protocol, along lines BD, D2, D5, D9 and D16 (along the welding direction) and lines B2 and B16 (perpendicular to the welding direction) see section 4.2.1. Each prescribed line of measurements was performed in order to investigate the effect of the weld thermal cyclic deformation at different depths of material (i.e. near and far away from the heat source). The average value of the top weld stress free lattice parameter was used for the evaluation of the residual stress in the area between 0 and 3 mm from the top surface. The bottom weld stress free lattice parameter was used for evaluation of the residual stress in the area between 4 and 8 mm from the top surface. Finally, the parent stress free lattice parameter was used for evaluation of the residual stress in the area between 9 and 16 mm from the top surface.

VULCAN weld plate residual stress results using 1-2B a_0 set

The residual stress measurements from the VULCAN and ENGIN-X instruments, along the defined lines in the three-pass weldment (ID 3-1A), are shown in Figure 4.14 to Figure 4.20. As the differences between the means of the rotated and non-rotated bank specific 1-2B a_0 stress free values are very small (refer to Table 4.4), all stress values were calculated using average non-rotated, bank-specific data. The average stress free

values of the top weld, the bottom weld and the parent materials were used, depending on the measurement location, see section 4.2.2. The directions of the stress components are defined, with reference to the weld bead, as indicated in Figure 3.8.

ENGIN-X weld plate residual stress results using 1-2B and 2-1B a_0 sets

Table 4.5 and Table 4.6, summarise the average lattice parameters and standard deviations of the micro strains for each cuboid. The residual stress measurements from the weld plate using 1-2B and 2-1B a_0 sets are shown in Figure 4.21. The difference between the measured strains and stresses, using stress free reference measurements from sets 1-2B and 2-1B a_0, is small. This is because the stress-free lattice parameters for sets 2-1B and 1-2B were similar as evidenced in Table 4.6. Therefore, in the remainder of this thesis, only VULCAN and ENGIN-X results using cuboid set 1-2B are discussed. The average of eight a_0 measurements, i.e. two longitudinal direction measurements at 0° and 180° and two transverse direction measurements at 0° and 180° from bank-1, were used for evaluating the longitudinal and transverse residual stresses in the welded plate. Similarly four measurements of normal stress free lattice parameters from Bank 2 were used for evaluating the normal residual stress.

4.5 Validation of the Residual Stress Measurements

It is advantageous to compare the present measured residual stresses with independent measurements made on the same weldment (ID 3-1A) by other members of the NeT group [15,46,139,157,221,222]. The residual stress measurements of weld plate ID 3-1A were analysed at two different neutron reactor sources Helmholtz Zentrum Berlin (HZB) and Forschungs Neutronenquelle Heinz Maier Leibnitz (FRM-II). Stress free cuboids (set 1-2B), were measured at both reactor sources. At FRM-II, averages of the stress free lattice parameter values were obtained by rotating the a_0 cuboids constantly around one axis as

described in section 4.3.2.1. At HZB, averages of the stress free lattice parameter values were obtained by rotating the a_0 cuboids at different Omega angles (from 0° to 180° at 1° increments) during an April 2009 experiment. A repeated experiment was conducted in October 2009, where averages of the stress free lattice parameter values were obtained by continuous rotation of the a_0 cuboids. The measured results obtained from FRM-II and HZB are compared with the present ENGIN-X and VULCAN stresses in Figure 4.22-28. At the HZB and FRM-II reactor neutron sources, 311 peaks were used to analyse the residual stress in the welded plate. Figure 4.13 presents the average lattice parameters measured at reactor and spallation sources for 1-2B set. The possible reasons for differences in the measured lattice parameter are explained in section 4.6.1.

4.6 Discussion

The present study has tried to identify and understand the issues affecting residual stress measurements in austenitic weldments and helped to improve the reliability of residual stress measurements using neutron diffraction.

4.6.1 a_0 analysis

Figure 4.10 to Figure 4.12 shows the variation in lattice parameters measurement expressed as micro-strain, with rotational angles, for stress-free reference cuboid sets 1-2B and 2-1B sets. The variations with angle are surprisingly high in the parent material (±200 micro strain). The following factors could have caused these variations:

1. The presence of crevices was evident in the reconstructed cuboids which can offset the centre of the sample gauge volume, as shown schematically in Figure 4.29 in the same way that partial gauge volume immersion can generate pseudo strains as described in section 2.5.1 [142].

2. The presence of super glue (containing hydrogen), used to bond the cuboid assemblies, can introduce pseudo strains. Hydrogen has a very large attenuation coefficient due to its large incoherent scattering cross section. The neutron weighted centre of gravity shifts (towards the neutron beam) away from the geometric centre of the measurement volume.
3. An inhomogeneous population of diffracting grains (i.e. average of plane D and B elongated grains) at angles 30°, -30°, -60°, -120°, -150°, -210° and -240°, when compared to the uniform grain sizes exposed at angles of 0°, 90°, 180° and 270°. This is shown schematically in Figure 4.30. This will have particular marked effect when there are anisotropy texture and grain size in the material.
4. At 30°, -30°, -60°, -120°, -150°, -210° and -240°, different elongated grain size (i.e. plane D, B and through thickness of the plate) will reduce minimum number of diffracting grains in a given gauge volume and generate pseudo strain in measured residual stresses [223,224].
5. The edges of the cuboids are not parallel to each other as seen in Figure 4.9. When a_0 cuboids are rotated from 0° to 180°, the possibility of a shift in the geometric centre of the gauge volume is high. As a result of this, the population of the grains changes, and the total number of grains diffracting alters with respect to the previous position. This effect is shown on the diagram shown in Figure 4.31.
6. The segregation of solute atoms can cause a steep variation in the strain free lattice spacing of the parent material [132].
7. At the spallation source the detectors are fixed, however at the reactor source the detectors are not fixed. The possibility of misalignment of detectors and imperfect alignment of a_0 cuboids [143] is high, due to imperfect edges of cuboids.

In comparison to the parent a_0 cuboids, in welded a_0 cuboids the micro-stresses will be moderately high, due to the presence of bigger grains and chemical variations in the weld metal. In addition the presence of texture in the weld metal can lead to higher error in profile or single peak data analysis. Also, generation of significant pseudo strains can occurs, due to bigger grain size [117,131,225]. The 1-2B weld a_0 cuboid showed higher micro-strain uncertainties in comparison to the 2-1B weld a_0 cuboid. The reasons for such uncertainties in a_0 weld values could be associated with following effects.

i) As described in section 3.2.3, the 1-2B stress free cuboids were extracted from the 1-2B trial plate, while 2-1B cuboids were extracted from the 2-1B three pass welded plate. In the 1-2B trial plate weld slots were manufactured very close to each other and due to this, the sequence of weld deposits in each slot interacted with each other. As a result of this, the material's plastic deformation was significantly higher in comparison to that of the three-pass weld plate. Figure 4.32 shows evidence of the interaction of the weld thermal cyclic loading for each slot, revealed by Vickers hardness measurements.

During the a_0 extraction process, the macroscopic unloading of stress may transfer unequal loads to the surrounding grains, due to the anisotropic stress-strain properties of the grains. The unloading process may induce elastic strain of those grains located adjacent to plastically strained grains. This in turn hinders elastic relaxation and leads to a change in the intergranular stress, between the welded plate and the welded a_0 samples. These intergranular stress states will have a significant effect on evaluation of residual stress of the welded plate at a reactor source [140].

ii) The 2-1B a_0 cuboids were extracted from one of the seven welded plates. These plates were solution annealed before welding; hence, any strain developed, due to the machining process, was relaxed, unlike the 1-2B a_0 cuboids.

iii) The 2-1B parent a_0 cuboids have much higher measured macro strain than 1-2B a_0 cuboids see Figure 4.10(c) and Figure 4.12(c). This is due to the 2-1B parent cuboid being heavily coated with paint and super glue (containing hydrogen) see Figure 4.9. Due to this, the 2-1B parent cuboid assemblies introduce higher pseudo strains than the 1-2B parent cuboid assemblies.

4.6.2 Weld residual stress

Line BD: The aim of performing the line BD measurements was to measure the distribution of stress through the 18mm thickness of plate, and to also understand the effect of the non-uniform thermal cyclic deformation through the thickness of the specimen. Figure 4.14, shows the measured residual stress profiles in the longitudinal, transverse and normal directions along line BD. The longitudinal and transverse stresses measured at VULCAN and ENGIN-X increased gradually from the bottom of the plate to the fusion boundary (i.e. 6 mm) and reduce slightly from the fusion boundary to the weld cap (2mm). However, the normal stresses measured at VULCAN and ENGIN-X remain constantly below ±60MPa from the bottom of the plate to the weld cap. The variation between ENGIN-X and VULCAN stress measurements is typically, approximately ±50 MPa. However, at two specific measurement points; at 6 and 7 mm from the top surface, there is a greater variation of stress, up to 100 MPa (c.f. Figure 4.14). ENGIN-X longitudinal stress appears to be systematically higher than VULCAN longitudinal stress.

Figure 4.22, compares measured stresses along line BD, obtained from different neutron diffraction experiments at HZB, FRMII, SNS and ISIS. The residual stress measurement profiles, even though from different instruments, follow a similar trend. However, in the area below the weld between 6 and 18 mm from the top surface, the variation in measured magnitude in the longitudinal direction is high (up to 150MPa). An important contributor to these variations is the uncertainty in the stress free measurements as discussed earlier. In addition, the reactor source is only sampling a single 311 peak, whereas the spallation source samples several reflections covering more than 10 peaks.

Line D2: The aim of taking line D2 measurements was to evaluate the residual stress distribution, along the welding direction in the plate, associated with the final weld pass. The line is located only 2 mm below the surface of the plate. In Figure 4.15, it is clear from the results that significant tensile residual stresses have developed in all three directions, in the vicinity of the three-pass weld deposit. The longitudinal residual stress profile exhibits a high magnitude of tensile stress along the welded region balanced by compressive stress in the bulk material. At the weld start and stop positions, more pronounced peaks in the residual stress profiles are noticed. At the weld start, the deposition of the weld filler material will be continuous only when the required arc voltage has been established. Similarly, at the weld stop, the deposition of filler material terminates only when the arc voltage drops below threshold voltage. During this period of time, the transient nature of the temperature field will lead to localised differences in microstructure and strain history [226,227].

In the longitudinal direction, the VULCAN results are showing a clear stress peak at the weld start and stop (i.e. -40 and +40 mm). The longitudinal stress variation between the spallation (VULCAN) and the reactor source (FRM-II and HZB) was about ±50MPa as shown in Figure 4.23. In the transverse direction, both the spallation and reactor source

measurements in the parent zone are in good agreement but in vicinity of weld material i.e. from -40 to 40 mm the variation between the spallation and reactor source was about ±50MPa. Similarly in the normal direction the stress measured at spallation and HZB reactor source shows variation of ±50MPa, while FRM-II shows variation of ±100MPa.

Line D5: The line D5 measurements were performed in order to quantify the extent to which the first weld pass metal has cyclically hardened as a result of localized heating associated with the second and third weld passes. The line was located 5 mm below the surface of the plate. Figure 4.16 shows a similar trend in residual stress results as occurred in line D2 measurement results. The ENGIN-X and VULCAN results along line D5 are in reasonably good agreement with each other, except in the normal direction (just prior to the weld stop) at 20 and 30 mm see Figure 4.16. The residual stress measurements, made at the different sources, along line D5, are compared in Figure 4.24. The stress profiles in the longitudinal, transverse and normal directions show small variations, except at 30mm and -30 mm as seen in Figure 4.24.

Line D9: The aim of taking the line D9 measurement was to quantify the extent to which the parent metal has cyclically hardened as a result of localized heating associated with three weld deposits. As described in section 2.2.1, this zone is expected to have cyclically yielded. Figure 4.17 shows the residual stress results of the long line D9. The ENGIN-X measurements along line D9, at a depth of 9 mm, as shown in Figure 4.17, indicate residual stress levels up to 50 MPa greater than the VULCAN results. The material in the area between -30 mm and 30 mm from the weld mid-length, parallel (longitudinal) and perpendicular (transverse) to the welding direction, has undergone cyclic yielding and developed a maximum residual stress of 350 (±50) MPa.

In the longitudinal direction, the ISIS, FRMII and HZB results are in good agreement as seen in Figure 4.25. While in the transverse and normal direction the residual stresses measured at different neutron sources correlated very well with each other.

Line D16: The aim of taking the line D16 measurement was to analyse the elastic strain developed due to the distortion of plate and the effect of multi-pass welding 113,114. Line D16 is located 16 mm below the surface of the plate. The ENGIN-X measured stresses along line D16 are up to 100 MPa higher than the VULCAN data, and this is shown in Figure 4.18. The most marked discrepancy is in the longitudinal direction distance between Z = -70 mm to +20 mm. The longitudinal stress profile rises smoothly from approximately zero, at both ends of the line, to a central maximum of 250 MPa (±50). The transverse component lies within the range ±100 MPa throughout the length of the line, with an abrupt increase from -100 MPa to 100 MPa at between -40 and 40 mm. The residual stress measurements taken along line D16, at the different neutron sources are presented in

Figure **4.26**. The ENGIN-X residual stress measurement profile, in all three directions, showed higher variations when compared to the other measurements already taken.

Line B2: The aim of taking the line B2 measurements was to understand the effect of radial weld thermal heating. Rosenthal has described that the weld heat distribution, in a plane perpendicular to the heat source, is defined radially from the centre of the heat source [42]. Hence, the weld heat will be at a maximum nearest to the heat source and gradually decreases as we move away from heat source. As a result, the material nearest the heat source deforms cyclically, thereby developing tensile stress, while at the far end of the plate, balancing compressive stresses have developed. The residual stress results along line B2 are presented in Figure 4.19. Line B2 is located 2 mm below the surface of the plate (c.f. Figure 4.3 Three dimensional point cloud mesh of test specimen with

fiducial points). The ENGIN-X residual stress measurements along line B2 are generally in good agreement with the VULCAN results. The residual stress measurements along line B2 as taken at the different neutron diffraction sources are presented in Figure 4.27. The stresses along line B2 follow a similar trend of profile to earlier results.

Line B16: The reasons for taking line B16 measurements are the same as those for line D16. Line B16 is located 16 mm below the surface of the plate (c.f. Figure 4.3). The longitudinal and transverse stress profiles along this line again reveal compressive stresses towards the ends of the line, with more tensile stresses in the broader central region see Figure 4.20. The longitudinal stress has a value of approximately -200 MPa at either end of the line, rising to 200 MPa in the broader central region covering the distance -20 mm to 20 mm. The transverse component is approximately zero outside of this central region, and ~50 MPa within it. The normal component is between -50 Mpa and 0 MPa throughout the length of the line, but with an apparent, slight increase in the central region. The residual stress measurements along line B16 as taken at the different neutron diffraction sources are presented in Figure 4.28. In all three directions, the stress profiles along line B16 are in good agreement with the FRM-II results.

To summarize, at both experiments (VULCAN and ENGIN-X) three orthogonal components of stress were measured at different depths in the welded plate covering a minimum of 76 common locations on the 3-1A welded plate. The residual stress measurement carried out at the spallation sources showed a variation of approximately ±50MPa in all three orthogonal components. However, the measurements performed at neutron spallation sources and reactor sources showed difference of approximately ±100MPa. Further investigations need to be carried out to understand the possible contributions to these.

4.7 Difference in lattice parameter measured at VULCAN and ENGIN-X experiments

In this section the potential origins of the difference between the measured residual stress from ENGIN-X to VULCAN are discussed. At both instruments a LiF /ZnS scintillator detector type was used to monitor the diffracted neutrons [121,123] Further details of the instruments design and layout are described in section 2.4.2. Table 4.7 summarises the average differences in bank-specific measured lattice parameters and micro strain for the same stress free cuboids. The measured lattice parameter difference for the top weld a_0 cuboid is approximately 0.0004 Å from bank 1, and the measured lattice parameter difference for the bottom weld and parent a_0's cuboid is approximately 0.0004 Å, which approximately equates to ±350 micro strain. The average lattice parameter difference for the bottom and parent a_0 cuboid from bank 1 is 0.00002 Å and 0.000005 Å respectively, while from bank 2 the top weld a_0 cuboid is 0.000075 Å.

Similarly the residual stress measurements along line BD and line D9 from ENGIN-X and VULCAN show large apparent discrepancies in the measured stress. The underlying reason for these discrepancies was investigated further by comparing the lattice parameter measurements as shown in Figure 4.33. The averages of the differences in lattice parameters, for the longitudinal and transverse directions (measured from bank 1) are 0.0000102 Å and 0.0000012 Å respectively. While for the normal direction (measured from bank 2), the average of the differences in lattice parameters is 0.0007483 Å which is much greater and approximately equal to ±640 micro-strain.

The lattice parameter difference in bank 2 is much higher than bank 1 for both stress free cuboids and welded plate. The difference in lattice parameter measurements between the instruments is one of the main contributors to the variation in residual stress from one

experimental measurement to other. The difference in lattice parameter for bank 2 may be related to technical issues such as malfunction of electronic circuit of the bank 2 detector or software issues in analysing the raw data from the bank 2 detector. These technical issues will affect in recording TOF of neutron during experiments or detector software interpretation the recording raw data wrongly. Further investigation is required to understand the problem and to identify which instrument detector may have technical issues. However, the micro strain variation, resulting from the different lattice parameters measured in Bank 2, as seen in Figure 4.33(c), is not visible in Figure 4.33(d), because differences in absolute magnitude of the lattice parameters measured in Bank 2, are compensated for by using bank specific stress free reference measurements.

4.8 Conclusions

Residual stress measurements on the NeT TG4 benchmark specimen ID 3-1A were carried out at the neutron spallation sources at the ISIS facilities (UK) and SNS facilities (USA). At both experiments, three orthogonal components of stress were measured at 76 common locations on the same plate. Significant variations in stress free lattice parameters were measured in both weld and parent materials; up to ±200 micro strain relative to the average value. However, by averaging the multiple measurements (i.e. bank specific) at different angles, a representative stress free lattice parameter was provided.

The ENGIN-X and VULCAN stress measurement results, shown here, are comparable with those measurements carried out by the other NeT members, at different source experiments, on the same test specimen. Many of the residual stress measurements from the spallation and reactor source experiments vary within ±100 MPa. The following are judged to be the main causes for the variations in measured residual stress.

1. Differences in the measured lattice parameter of stress free cuboids for both parent material and weld metal.
2. The observed variation in stress free lattice parameters may be associated with crevices and the use of super glue to create assembled stress free cuboids of irregular shape that are difficult to align. The use of such composite cuboids should be avoided in future.
3. Another possible contribution to the variation of residual stress measured at reactor neutron sources versus spallation neutron sources comes from the manufacturing history of the welded plates from which the stress free cuboids were extracted.
4. The Bank 2 lattice parameters measurements appear to show a large systematic difference between the ENGIN-X and VULCAN facilities that should be investigated further.

4.9 Tables

Table 4.1 List of residual stress measurements carried out on 3-1A weld plate

Source	Instrument	Sample	a_0 ID
FRM II	STRESS SPEC	±3-4°	1-2B
HZB	E3	±3-4°	1-2B
ISIS	ENGIN-X	No	1-2B and 2-
SNS	VULCAN	No	1-2B
JRC		No	1-2B

Table 4.2 The ISIS instrument calibration measurements

Fitting Range msec	Material	Angle degree (°)	Bank-1 North			Bank-2 South			Difference (micro-strain)
			Lattice Parameter (Å)	Error	Uncertainty (Micro-strain)	Lattice Parameter (Å)	Error	Uncertainty (micro-strain)	
13000-40K	CeO_2	-45	5.41114	2.50E-05	4.620	5.41113	2.90E-05	5.3593	1.848
	Fe	-45	2.86653	3.40E-05	11.861	2.86639	3.50E-05	12.210	48.841

Table 4.3 Space group and the lattice parameters used in GSAS

Space Group	Lattice parameter (a=b=c)	$\alpha = \beta = \gamma$
FCC	3.596376 Å	90°

Table 4.4 (a) Stress free cuboids measured lattice parameters (b) Micro strain evaluated for 1-2B set from VULCAN experiment

Stress Free Cuboid	Non-Rotating-Bank 1		Non-Rotating-Bank 2		Rotating-Bank 1		Rotating-Bank 2	
	a_0	a_0 error	a_0	a_0 error	a_0	a_0 error	a_0	a_0 error
Top Weld	3.596043	0.000131	3.59578	0.000135	3.596119	0.0001075	3.596366	0.0001155
Bottom Weld	3.596560	0.000088	3.59615	0.000096	3.5962325	0.000102	3.596331	0.0001115
Parent	3.597209	0.000084	3.597000	0.000096	3.5969155	0.000075	3.5970935	0.000080

(a)

Stress Free Cuboid	Non Rotation Bank 1		Non Rotation Bank 2		Rotation Bank 1		Rotation - Bank 2	
	με	με error	με	με error	με	με error	με	με error
Top Weld	-10.5	50.36	-80.6	50.2	-34.3	44.0	57.5	47.1
Bottom Weld	45.6	36.73	36.7	37.5	-13.7	41.1	19.1	46.7
Parent	18.0	31.5	31.5	35.0	-24.7	30.0	20.1	33.2

(b)

Note: a_0: Is the average of the measured stress free lattice parameters for each cuboid, and a_0 error: is the average fitting error

Table 4.5 Stress free cuboids measured lattice parameters at ENGIN-X ISIS

Stress Free Cuboid	1-2B Stress Free Cuboids				2-1B Stress Free Cuboids			
	Bank 1 at 0° and 180°		Bank 2 at 90° and 270°		Bank 1 at 0° and 180°		Bank 2 at 90° and 270°	
	a_0 (Å)	a_0 error	a_0 (Å)	a_0 error	a_0 (Å)	a_0 error	a_0 (Å)	a_0 error
Top Weld	3.59566	0.0000465	3.5957875	0.0000515	3.59582	0.0000463	3.59555	0.000056
Bottom Weld	3.5960825	0.0000428	3.5957875	0.000045	3.59632	0.0000488	3.5957825	0.00005
Parent	3.5967725	0.0000383	3.5965475	0.0000418	3.596922	0.0000398	3.596385	0.00004

Note: a_0: Is the average of the measured stress free lattice parameters for each cuboid, and a_0 error: is the average fitting error

Table 4.6 Mean and standard deviation of ISIS stress free lattice parameters measurements

Cuboids	Stress Free Cuboid	Average of Measured Stress- Free Lattice				Standard Deviation of Micro			
		Bank 1 Specific		Bank 2 Specific		Bank1 Specific		Bank 2 Specific	
		a_0 (Å)	a_0	a_0 (Å)	a_0 error	μ	με	με	με
1-2B	Top	3.5956	0.000	3.595	0.0000	8	2.71	44.	4.06
	Repeated	3.5956	0.000	3.595	0.0000	9	1.72	65.	2.43
	Bottom	3.5959	0.000	3.595	0.0000	1	2.44	82.	3.52
	Parent	3.5966	0.000	3.596	0.0000	8	1.47	45.	2.23
	Top	3.5958	0.000	3.595	0.0000	8	2.5	57.	4.40
	Bottom	3.5962	0.000	3.596	0.0000	1	2.86	61.	2.64
2-1B	Parent	3.5967	0.000	3.596	0.0000	8	2.51	64.	2.84

Table 4.7 Difference in lattice parameter measurements for stress free cuboid made using the VULCAN and ENGIN-X instruments

Stress Free Cuboids	Measured Lattice Parameter (Å)								Difference in measured lattice parameter between VULCAN and ENGIN-X		
	VULCAN				ENGIN-X				Longitudinal and Transverse	Normal	Average
	Bank-1		Bank 2		Bank-1		Bank 2		Bank 1	Bank 2	Bank 1 and 2
	a_0	a_0_ error	a_0	a_0_ error	a_0	a_0_ error	a_0	a_0_ error	a_0	a_0	a_0
Top Weld	3.596043	0.000131	3.59578	0.000135	3.59566	0.0000465	3.5957875	0.000051	0.0003830	-0.0000075	0.0001877
Bottom	3.59608	0.000088	3.59615	0.000096	3.5960825	0.0000428	3.5957875	0.000045	-0.0000025	0.0003625	0.0001800
Parent	3.596772	0.000084	3.597	0.000096	3.5967725	0.0000383	3.5965475	0.000041	-0.0000005	0.0004525	0.0002260

4.10 Figures

Figure 4.1 Measurement position marked on a virtual model of TG4 test specimen 3-1A according to priorities list

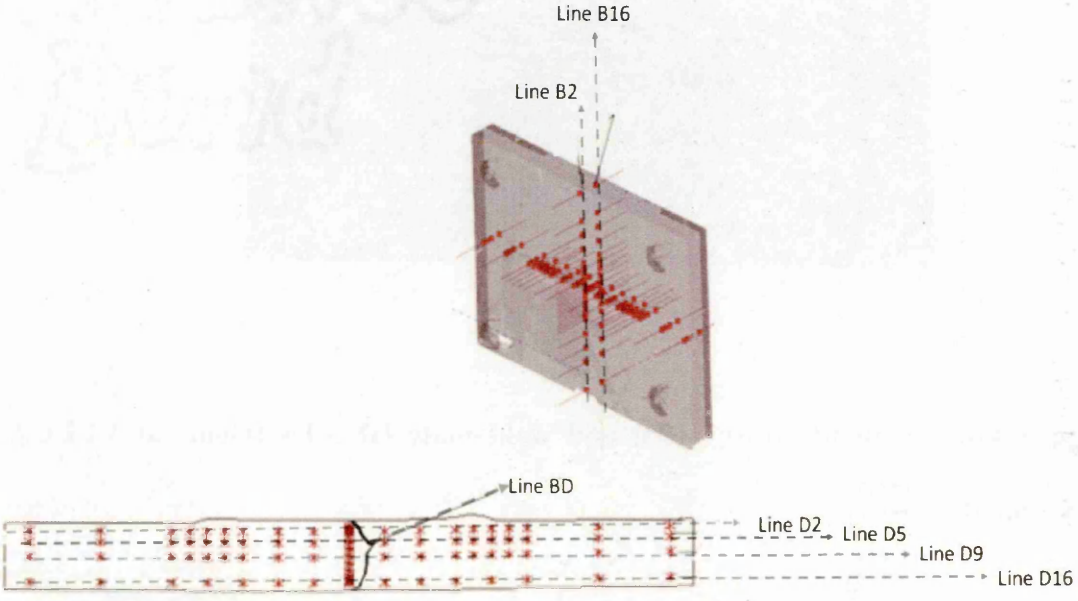

Figure 4.2 Laser scanner (left), laser tracker (right)

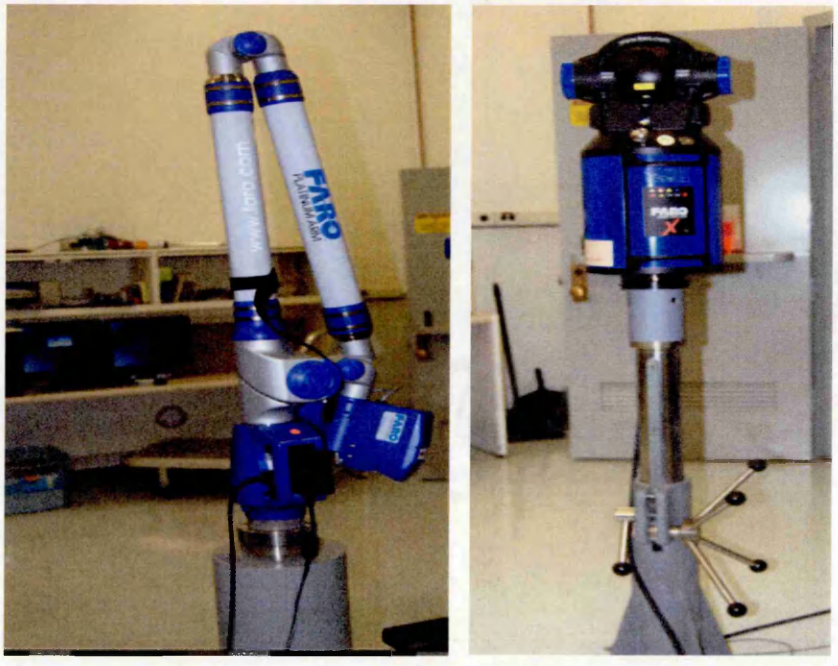

Figure 4.3 Three dimensional point cloud mesh of test specimen with fiducial points

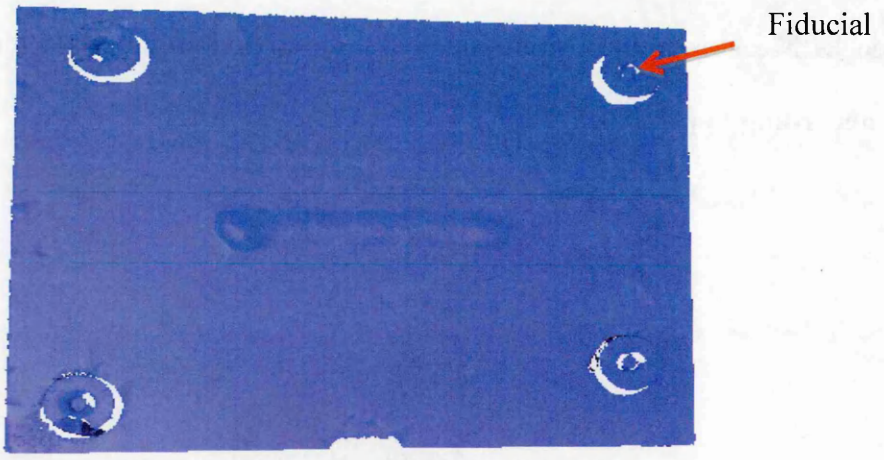

Figure 4.4 a_0 Cuboid on Jig (left) and weld plate ID 3-1A (right) at VULCAN instrument

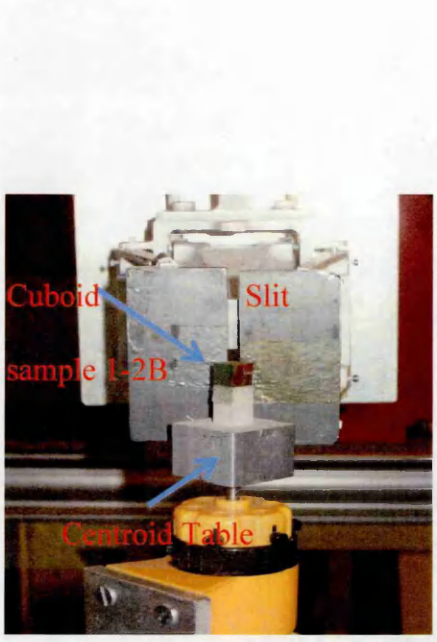

Jig

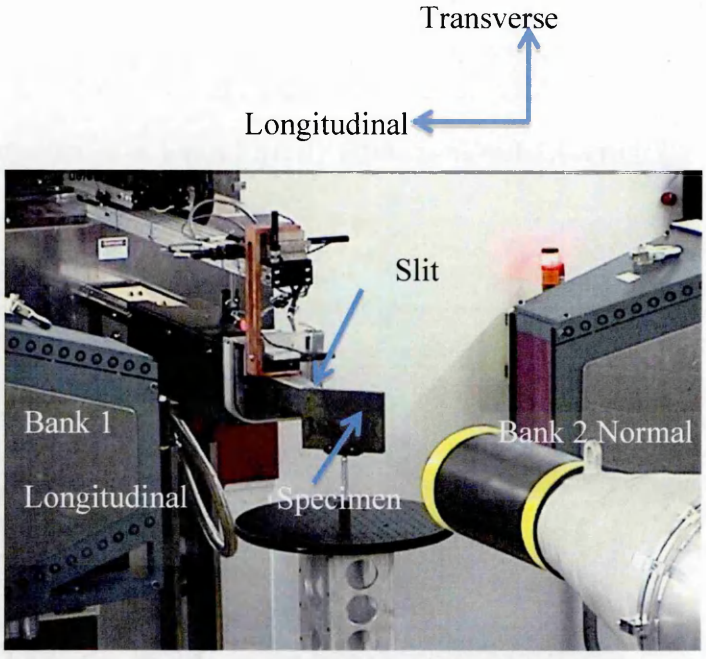

VULCAN instrument: Welded plate setup

Figure 4.5 The GSAS profile fitting by covering more than 10 peaks

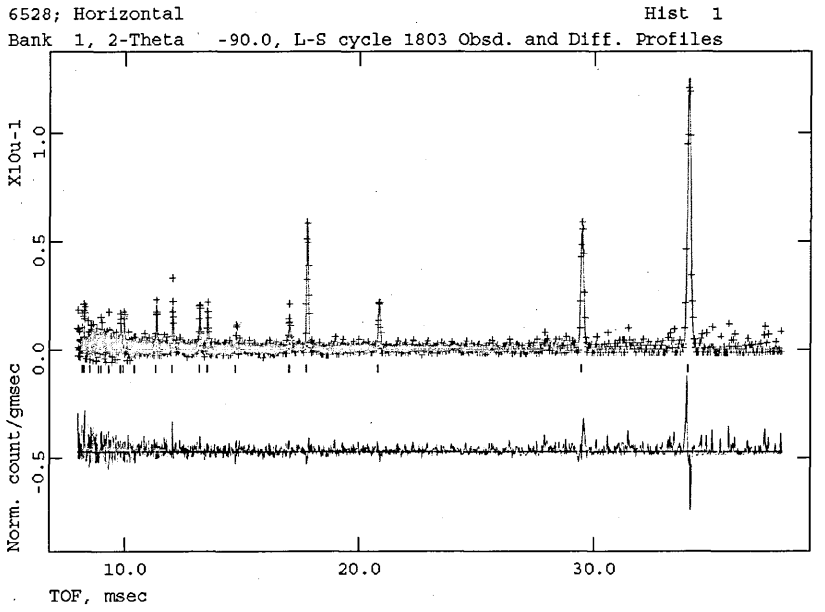

Figure 4.6 Schematic diagrams showing the directions within the stress free reference specimens in which the cell lattice parameter was measured in each detector Bank 1 (North) and Bank 2 (South) (a) Rotation about transverse axis (b) Rotation about longitudinal axis

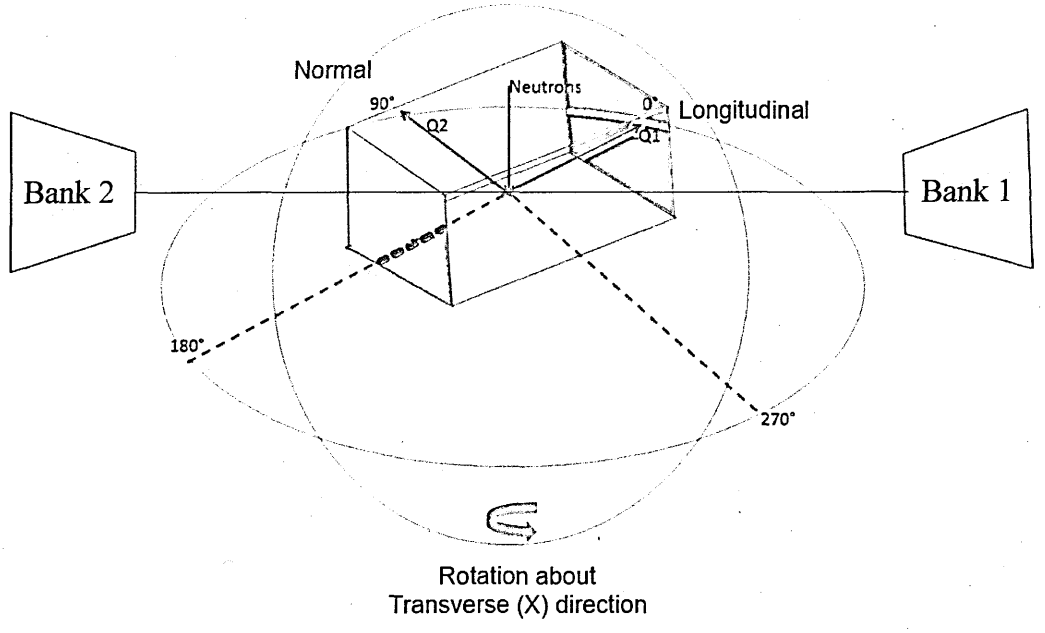

(a)

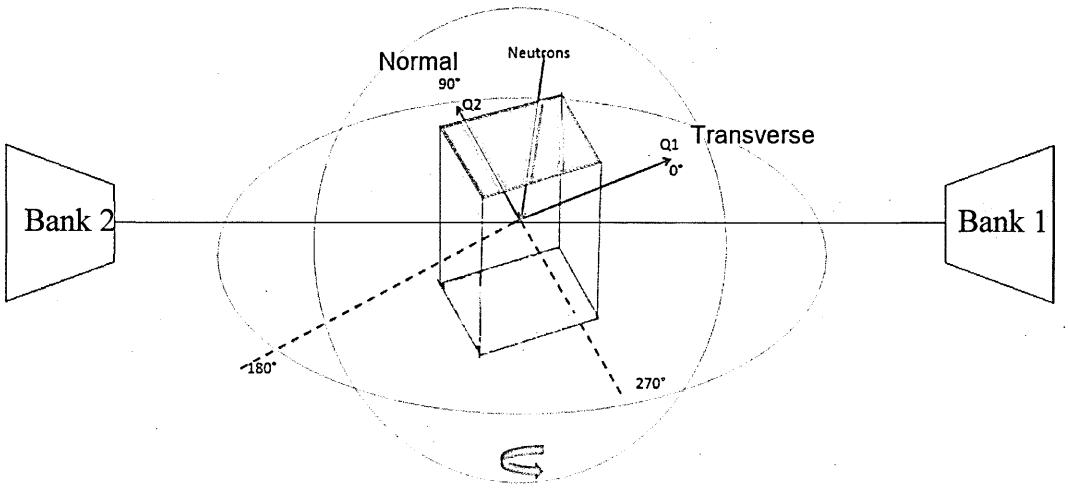

Rotation about
Longitudinal (Z) direction

(b)

Figure 4.7 Measured micro strain of 1-2B cuboids when stationary (VULCAN)

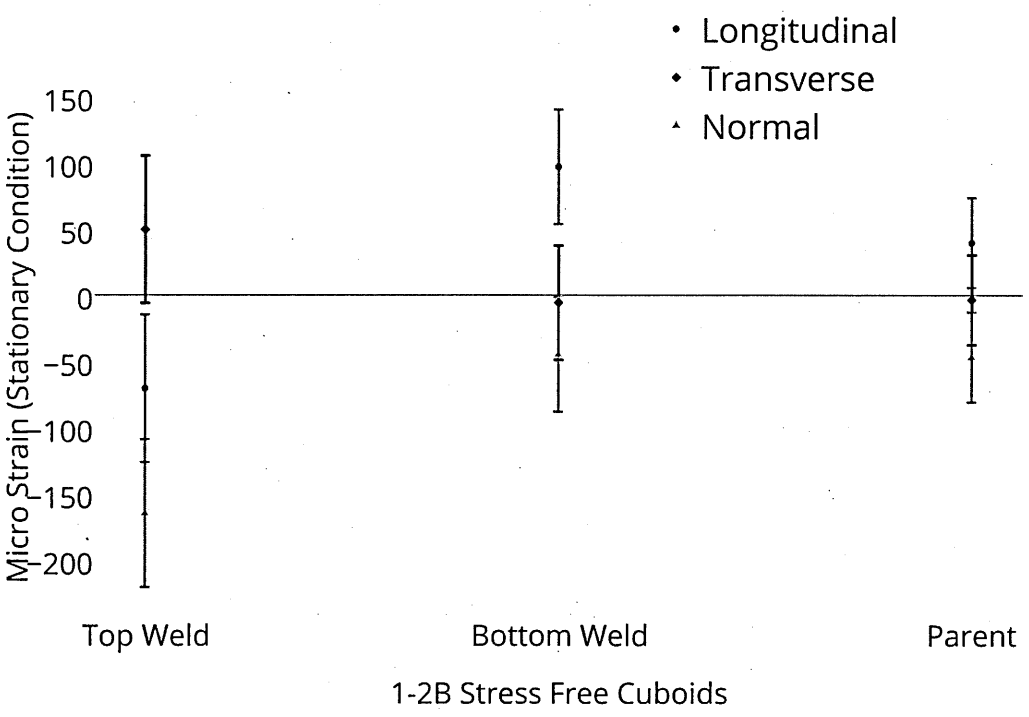

Note Bank 1 measured Longitudinal and Transverse and Bank 2 measured Normal

Figure 4.8 Measured micro strain of 1-2B cuboids under constant rotation (VULCAN)

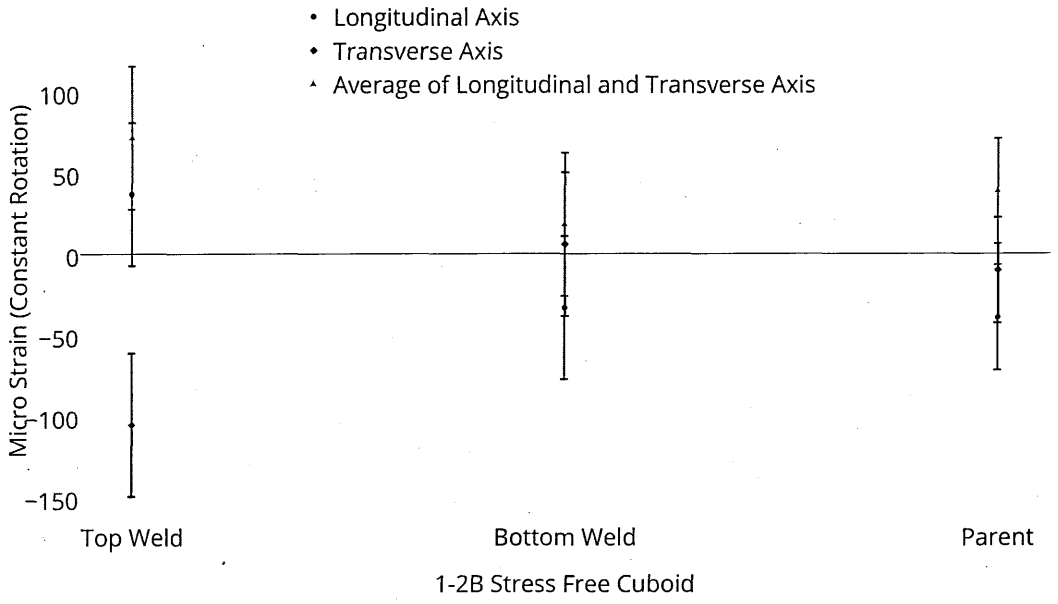

Note Bank 1 and 2 measured Longitudinal, Transverse and Normal depending on the rotation axis

Figure 4.9 Stress free reference specimens mounted for measurements at ENGIN-X instrument in order (left to right): weld (top), weld (bottom) and parent for set 1-2B and set 2-1B

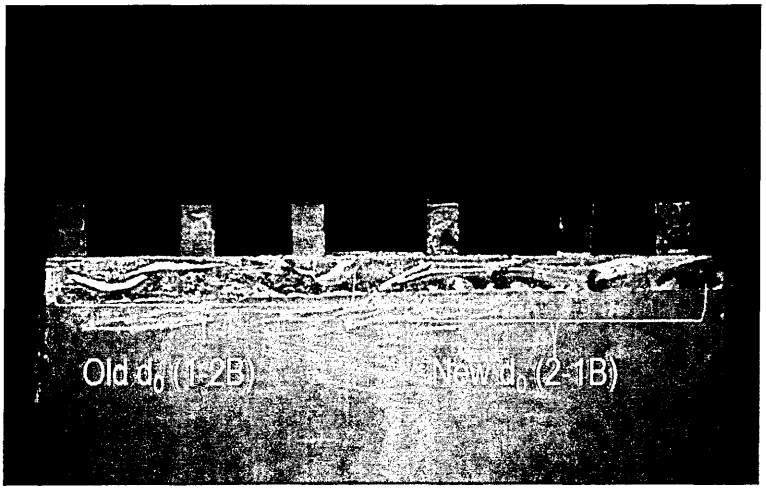

Figure 4.10 Variation in measured micro strain with angle of rotation of the stress free reference specimens 1-2B for (a) weld (top); (b) weld (bottom) and (c) parent

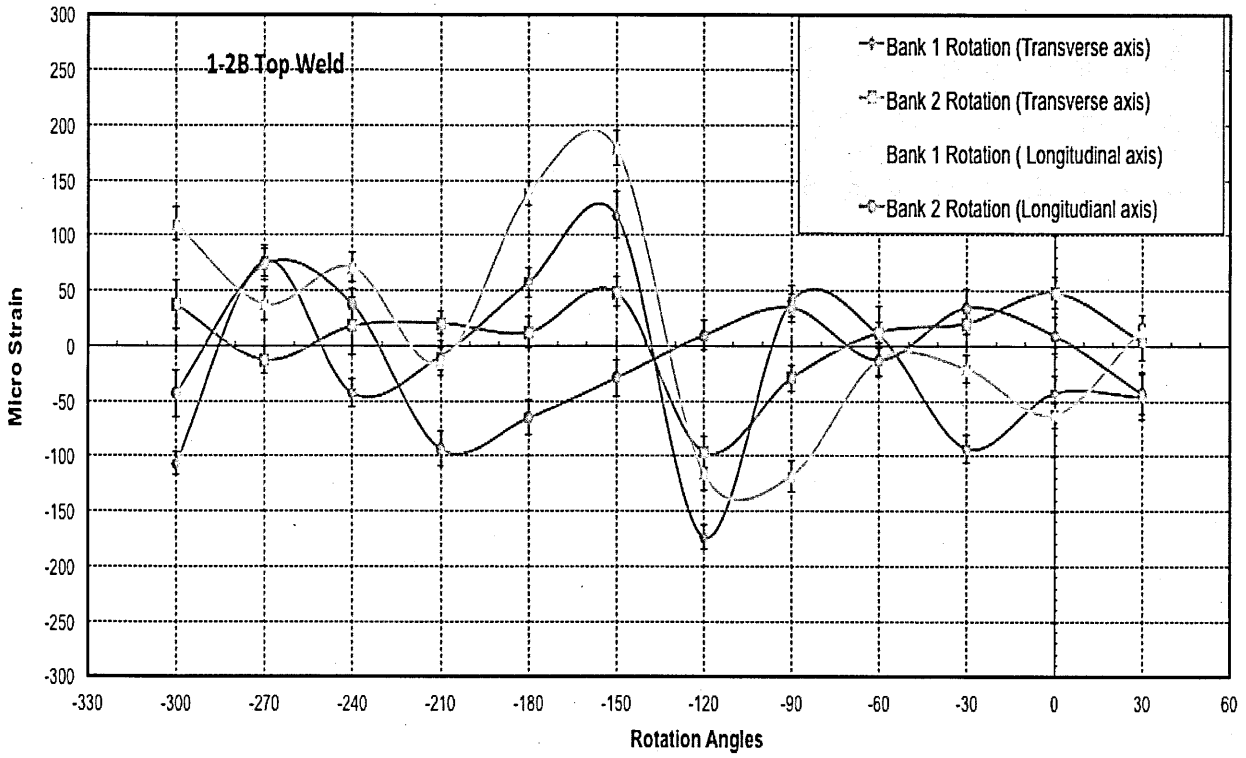

(a)

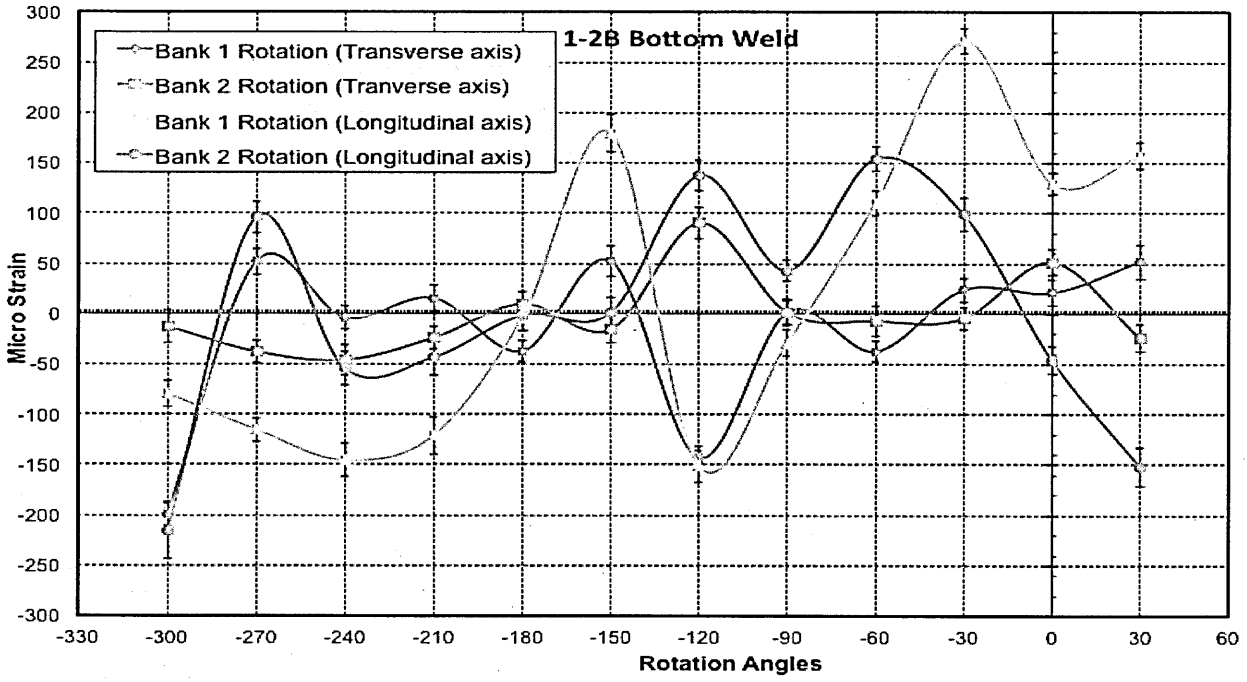

(b)

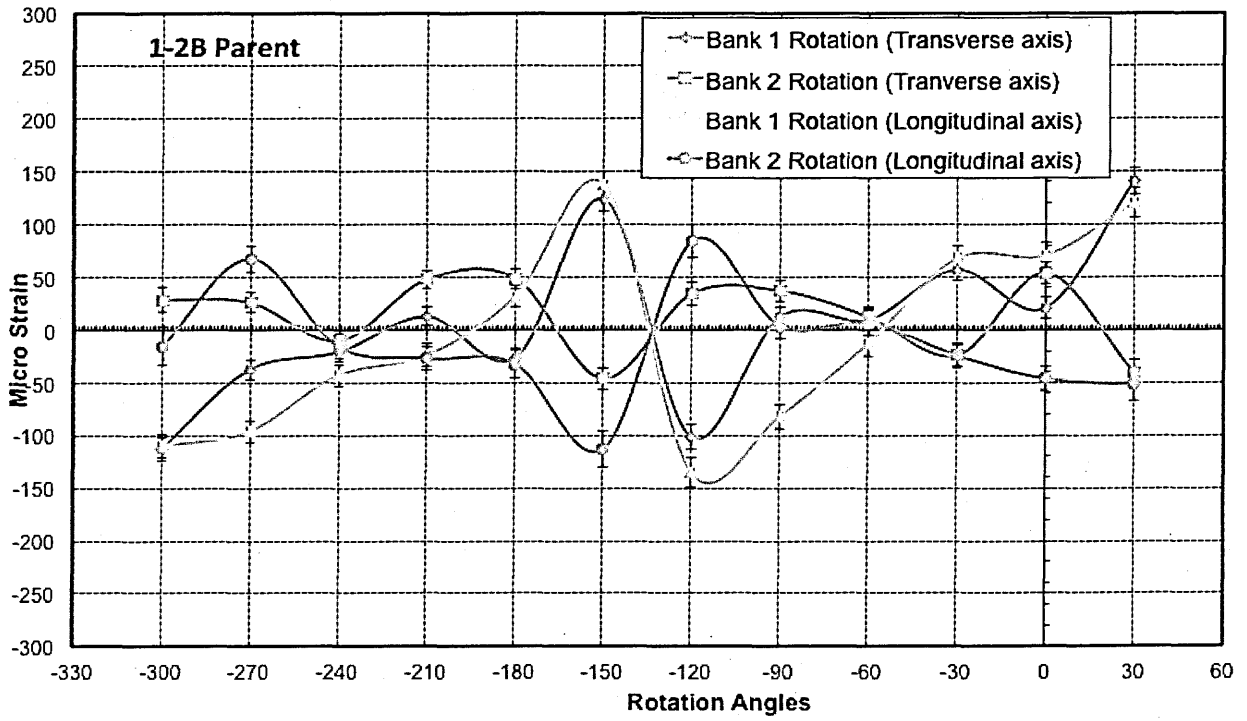

(c)

Figure 4.11 Re-measured variation in measured micro-strain of the weld (top) stress free reference specimen 1-2B

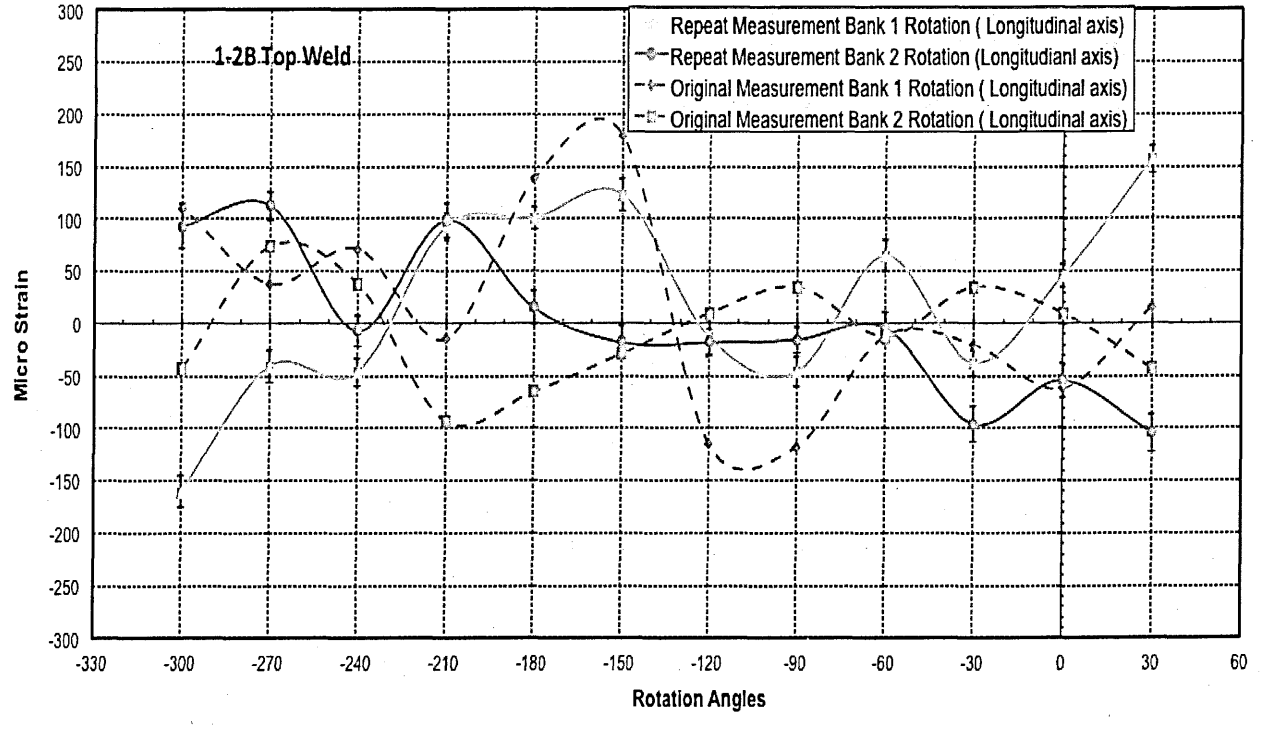

Figure 4.12 Variation in measured micro strain with angle of rotation of the stress free reference specimens 2-1B for (a) weld (top) (b) weld (bottom) and (c) parent

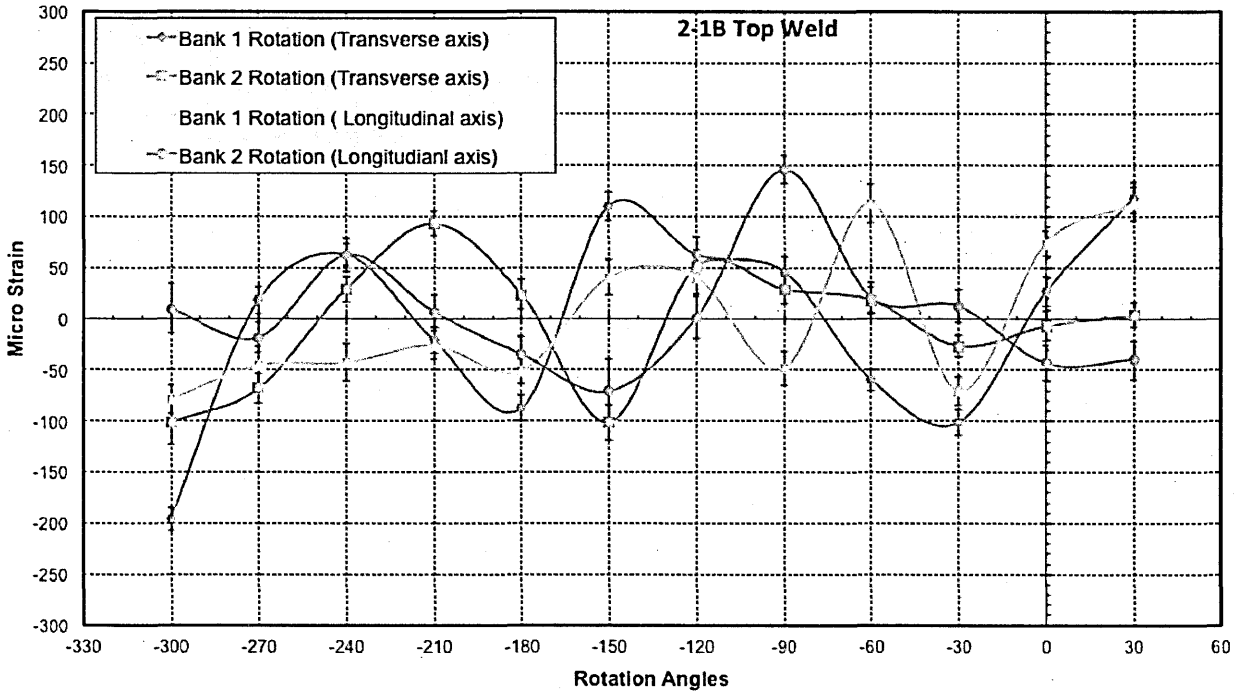

(a)

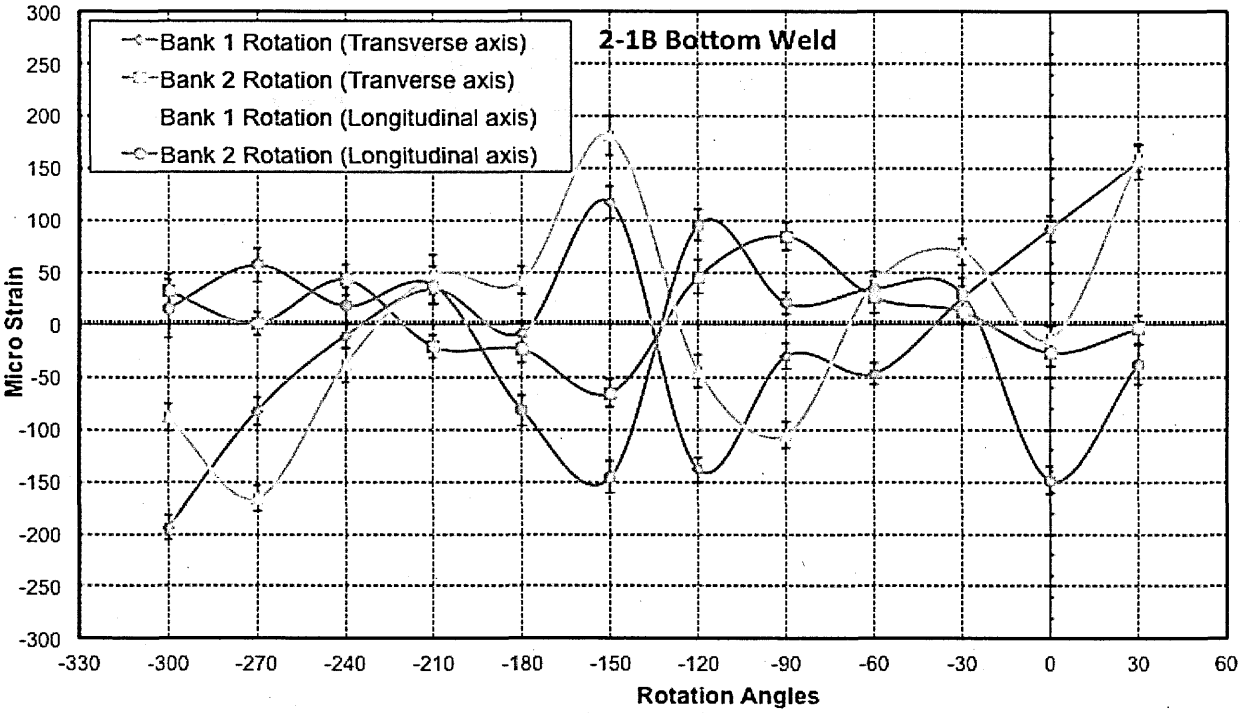

(b)

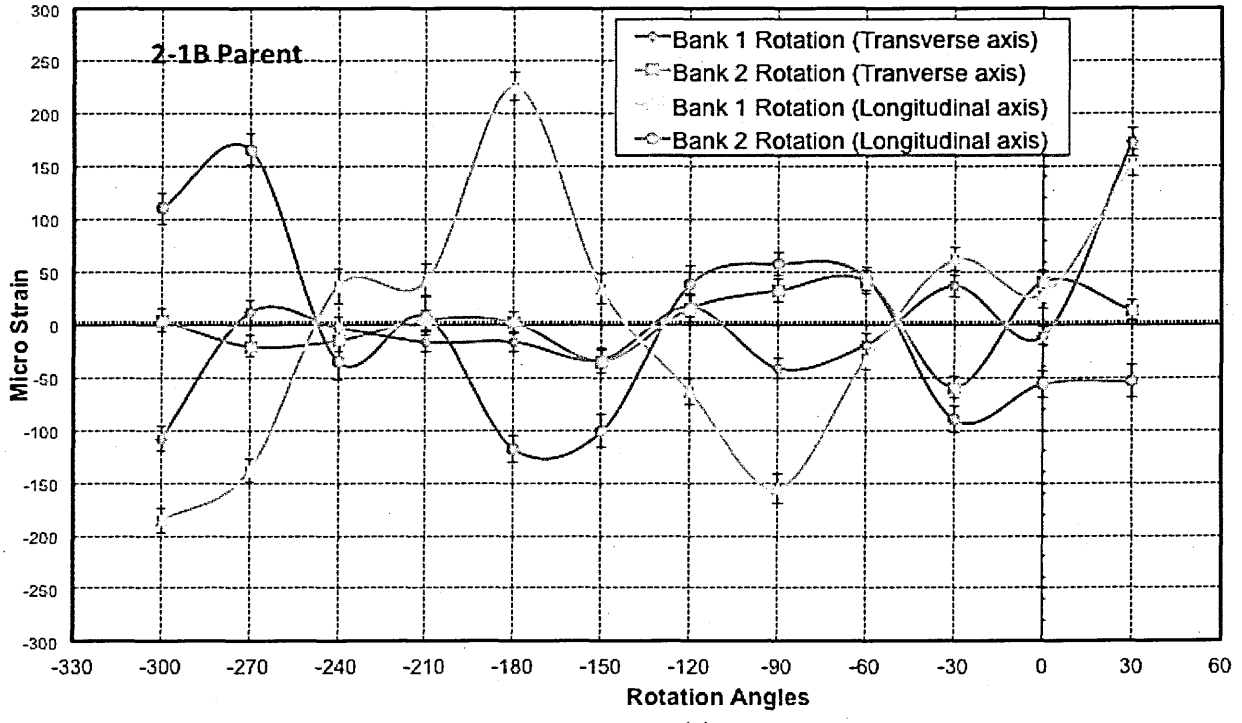

(c)

Figure 4.13 Variation in measured 'a' spacing of stress free cuboids at different sources

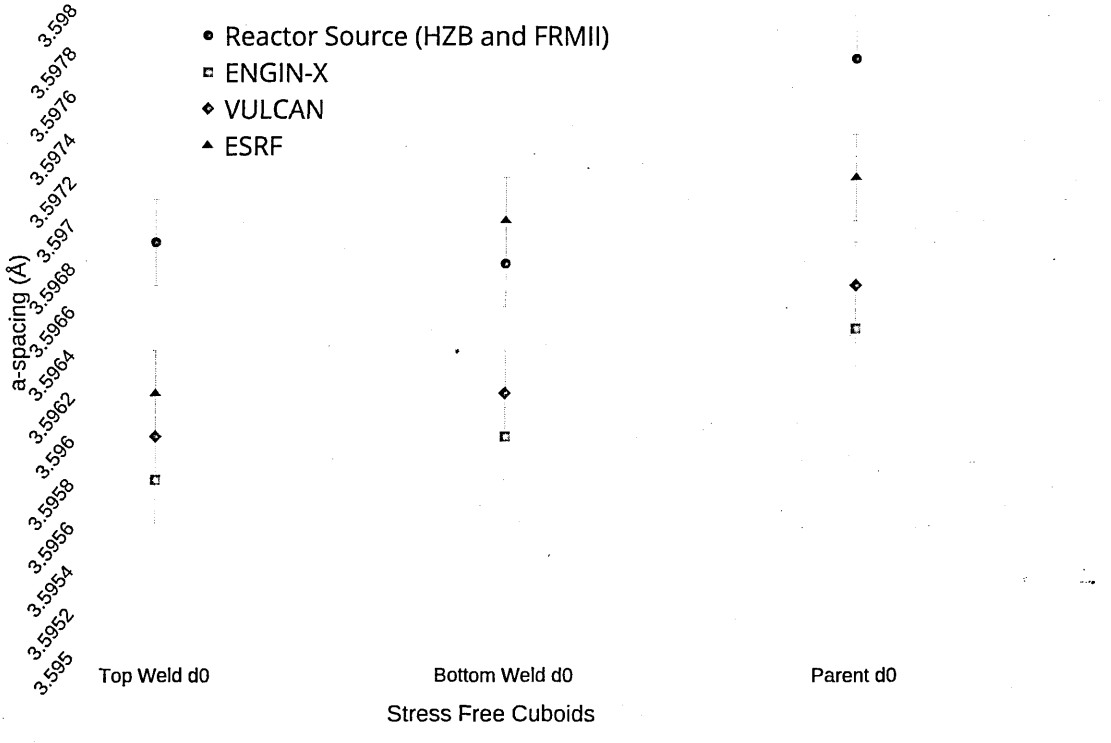

Figure 4.14 Residual stresses through the thickness of the plate along line BD, measured at ENGIN-X (ISIS) and VULCAN (SNS), using 1-2B a_0 cuboids

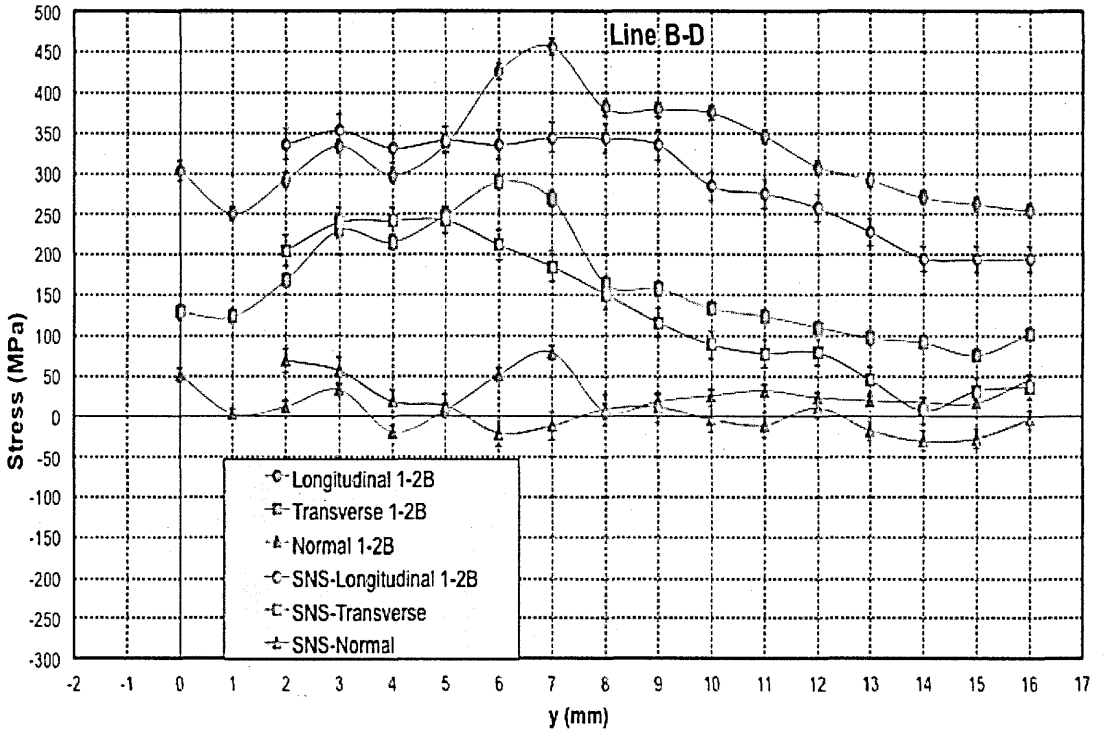

Figure 4.15 Residual stresses 2 mm below the top surface along line D2, measured at VULCAN (SNS) , using unstressed lattice parameter of 1-2B a0 cuboids

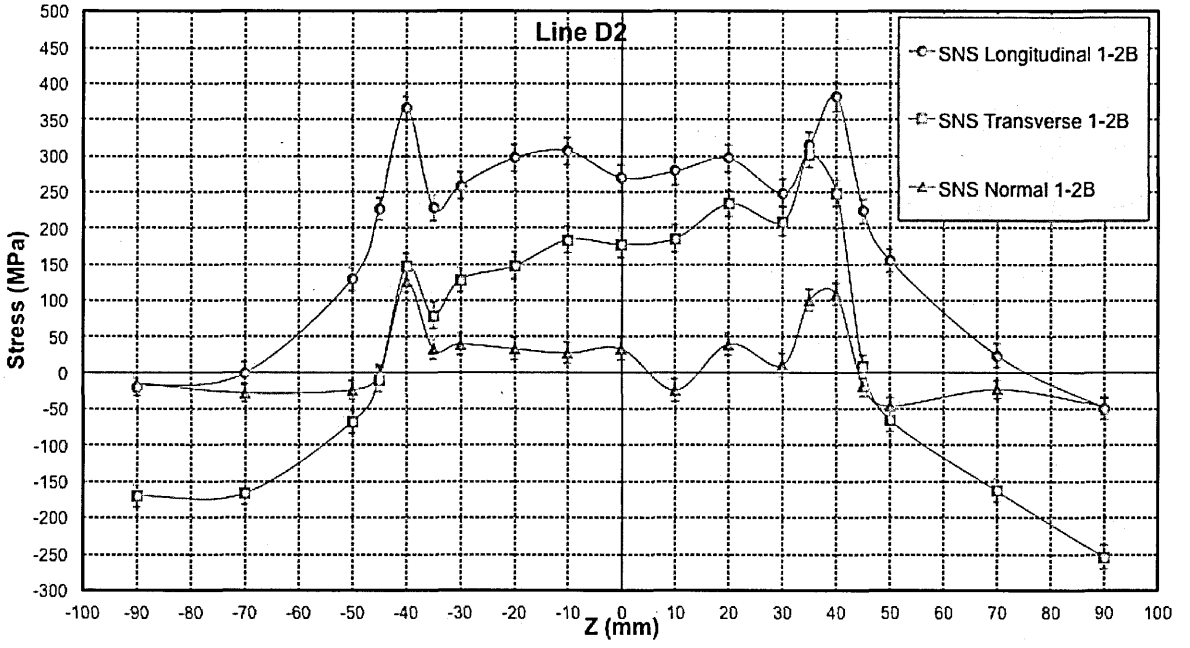

Figure 4.16 Comparison of residual stresses 5 mm below the top surface along line D5, measured at ENGIN-X (ISIS) and VULCAN (SNS), using 1-2B a_0 cuboids

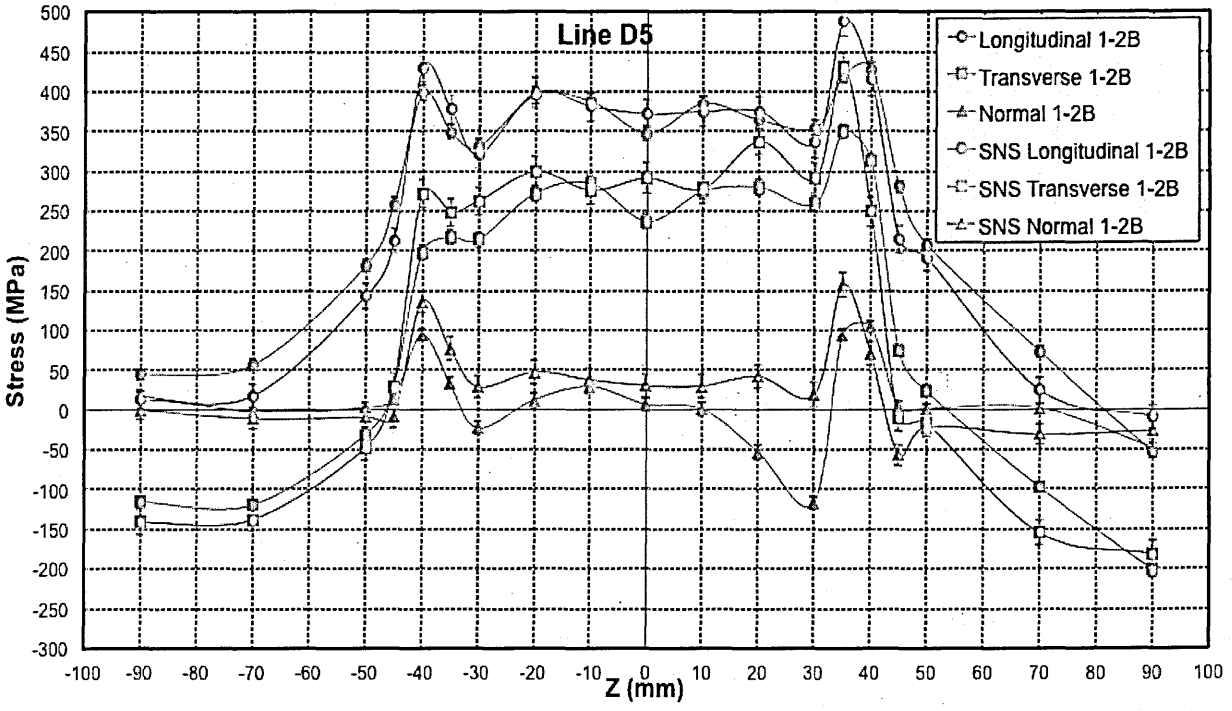

Figure 4.17 Comparison of residual stresses 9 mm below the top surface along line D9 measured at ENGIN-X(ISIS) and VULCAN (SNS) using 1-2B a0 cuboids

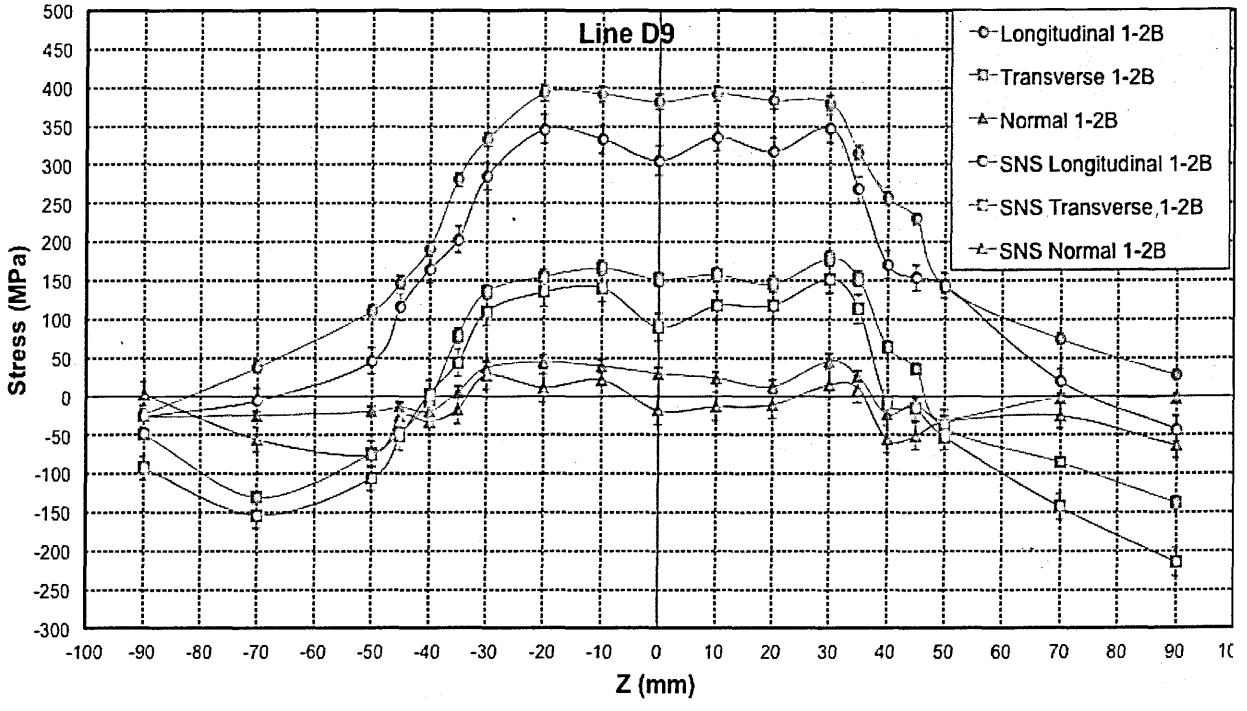

Figure 4.18 Comparison of residual stresses 16mm below the top surface along line D16, measured at ENGIN-X (ISIS) and VULCAN (SNS), 1-2B a_0 cuboids

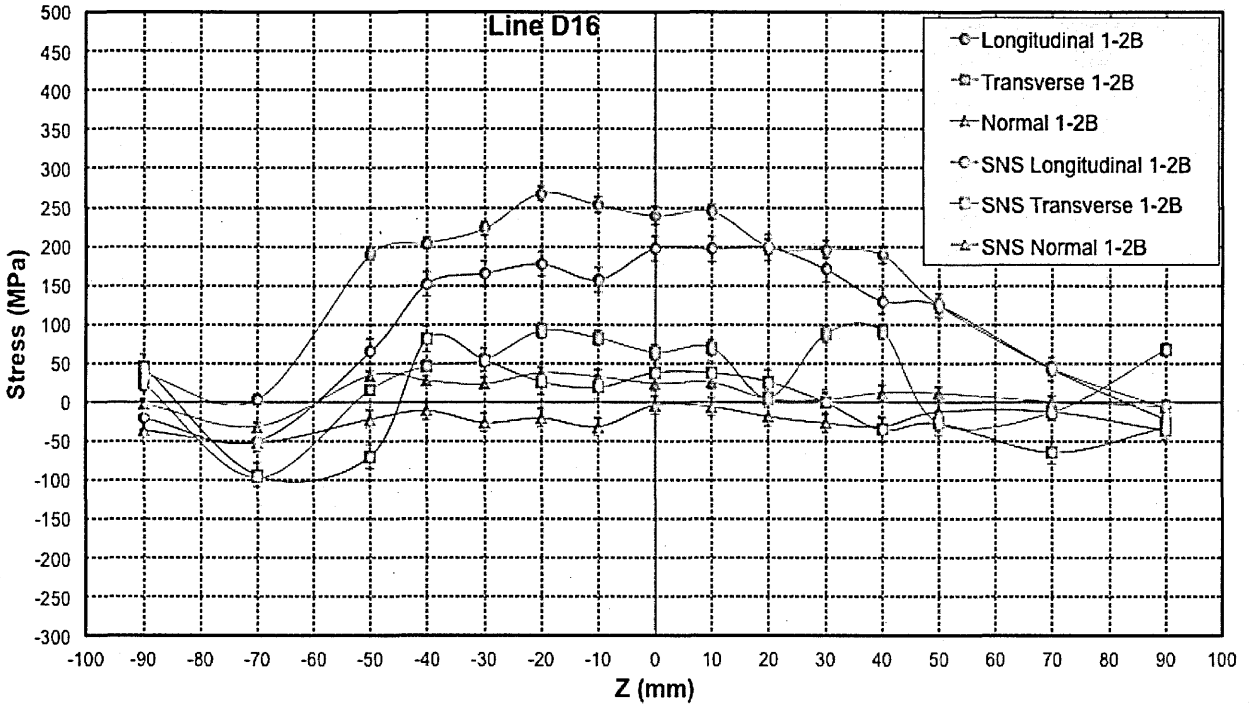

Figure 4.19 Comparison of residual stresses 2 mm below the top surface along line B2, measured at ENGIN-X (ISIS) and VULCAN (SNS), using 1-2B a_0 cuboids

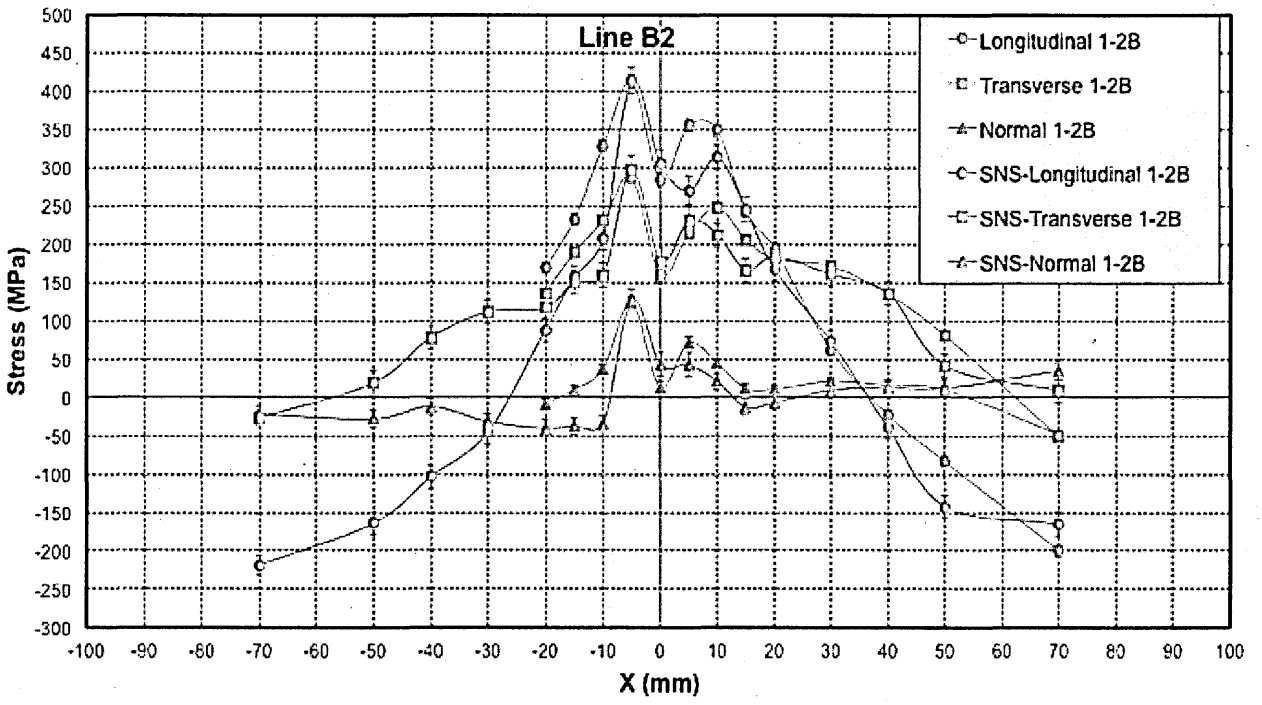

Figure 4.20 Residual stresses 16mm below the top surface along line B16 measured at VULCAN (SNS), using unstressed lattice parameter of 1-2B a_0 cuboids

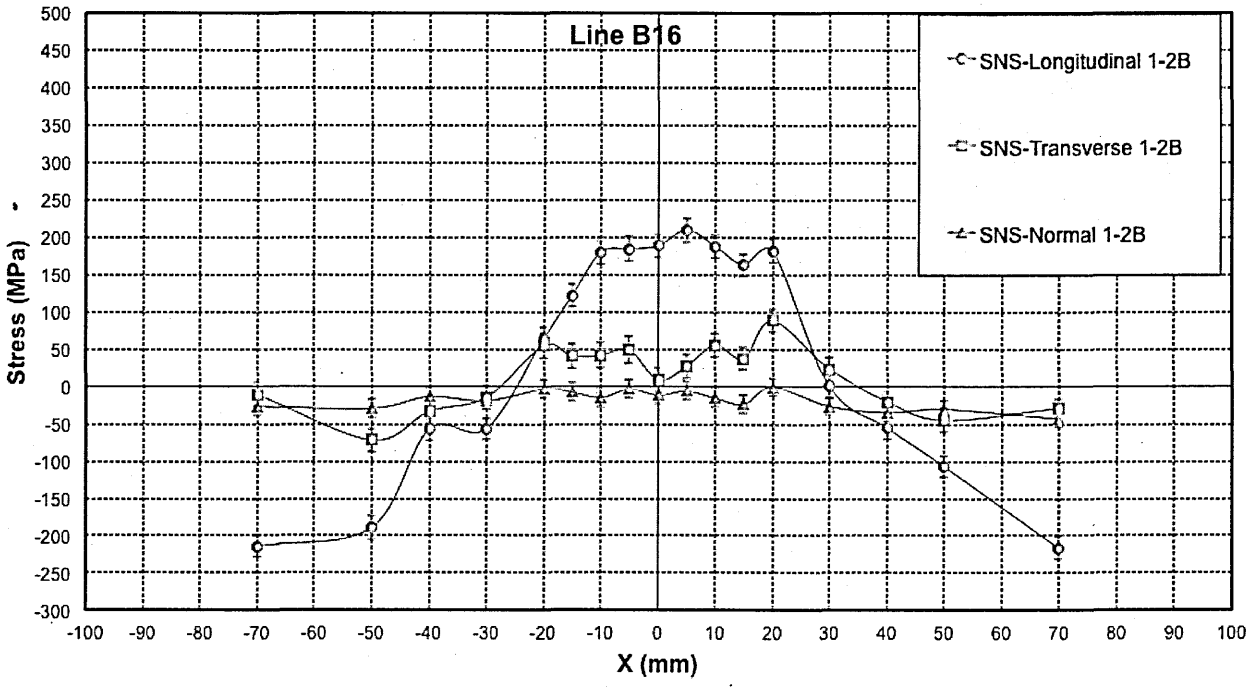

Figure 4.21 ENGIN-X: (a) measured micro strain and (b) residual stress measurement along line BD, using 1-2B and 2-1B a_0 cuboids

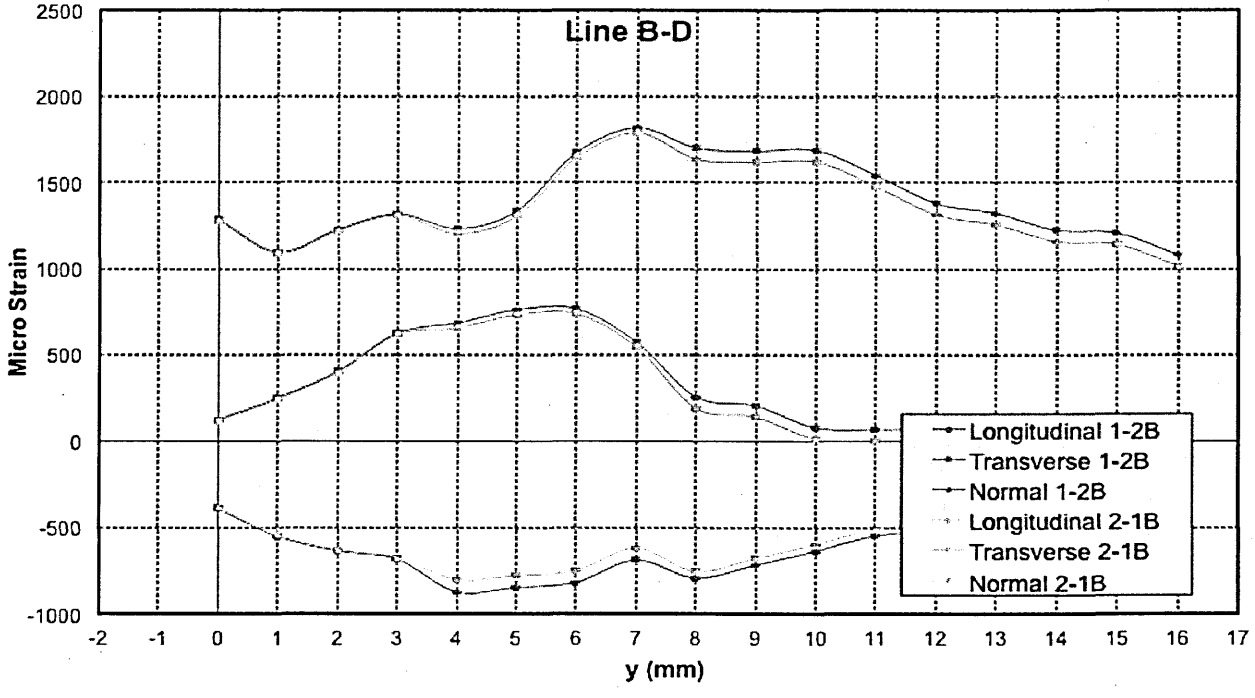

(a)

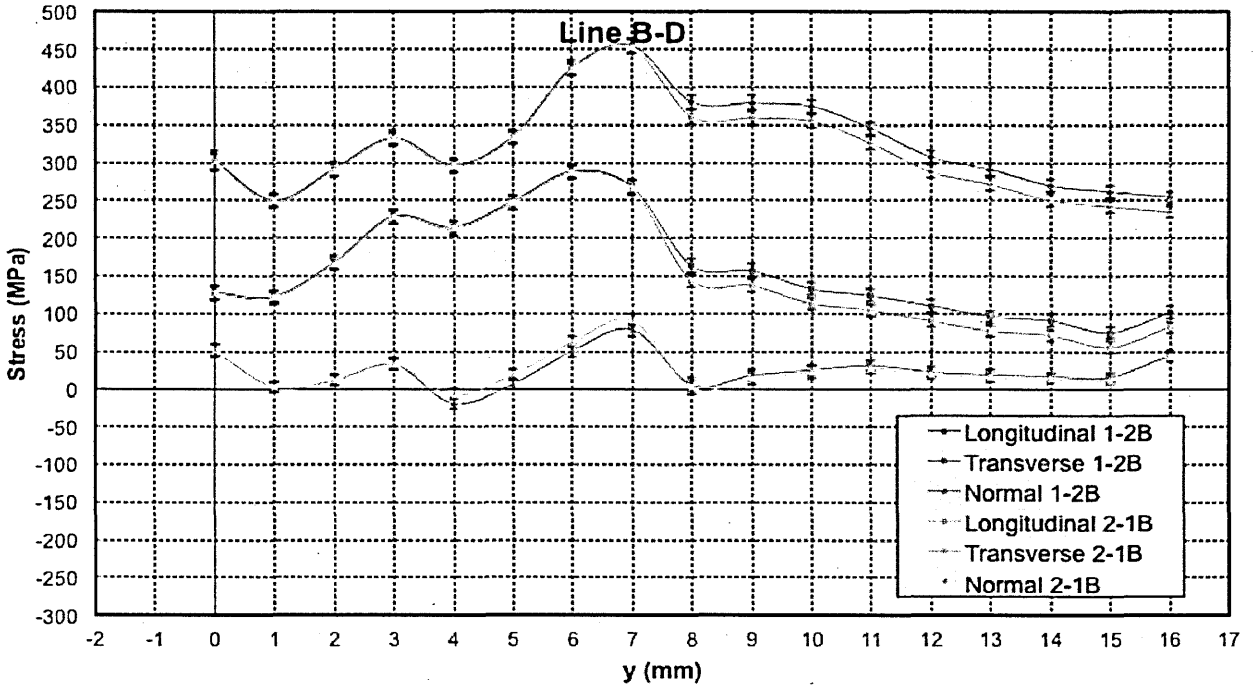

(b)

Figure 4.22 Line BD: Comparison of residual stress measured at different neutron source (a) Longitudinal (b) Transverse and (c) Normal

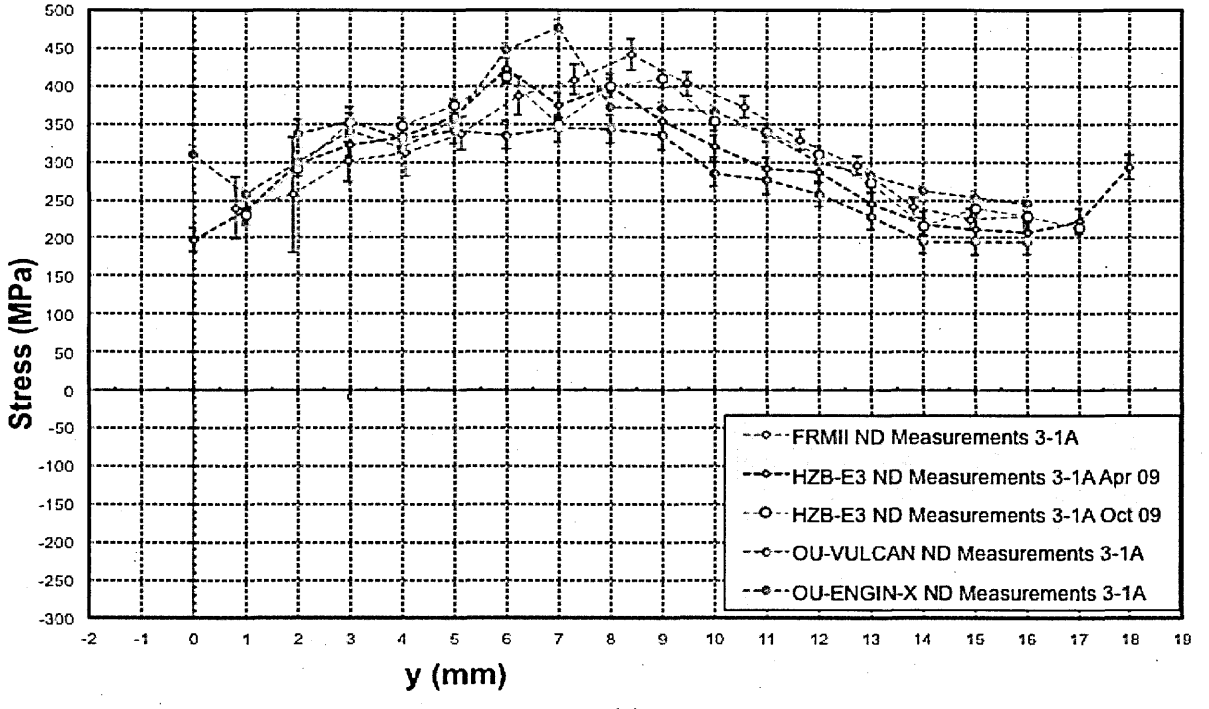

(a)

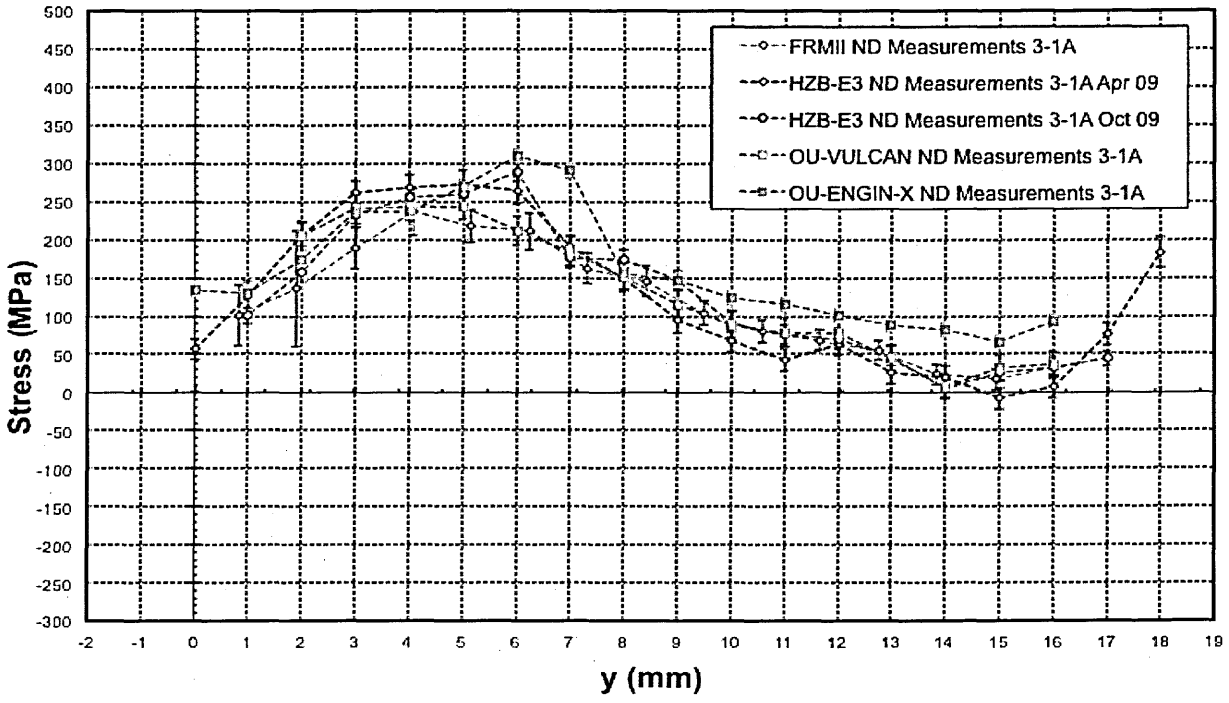
FRMII ND Measurements 3-1A
HZB-E3 ND Measurements 3-1A Apr 09
HZB-E3 ND Measurements 3-1A Oct 09
OU-VULCAN ND Measurements 3-1A
OU-ENGIN-X ND Measurements 3-1A
Stress (MPa)
y (mm)

(b)

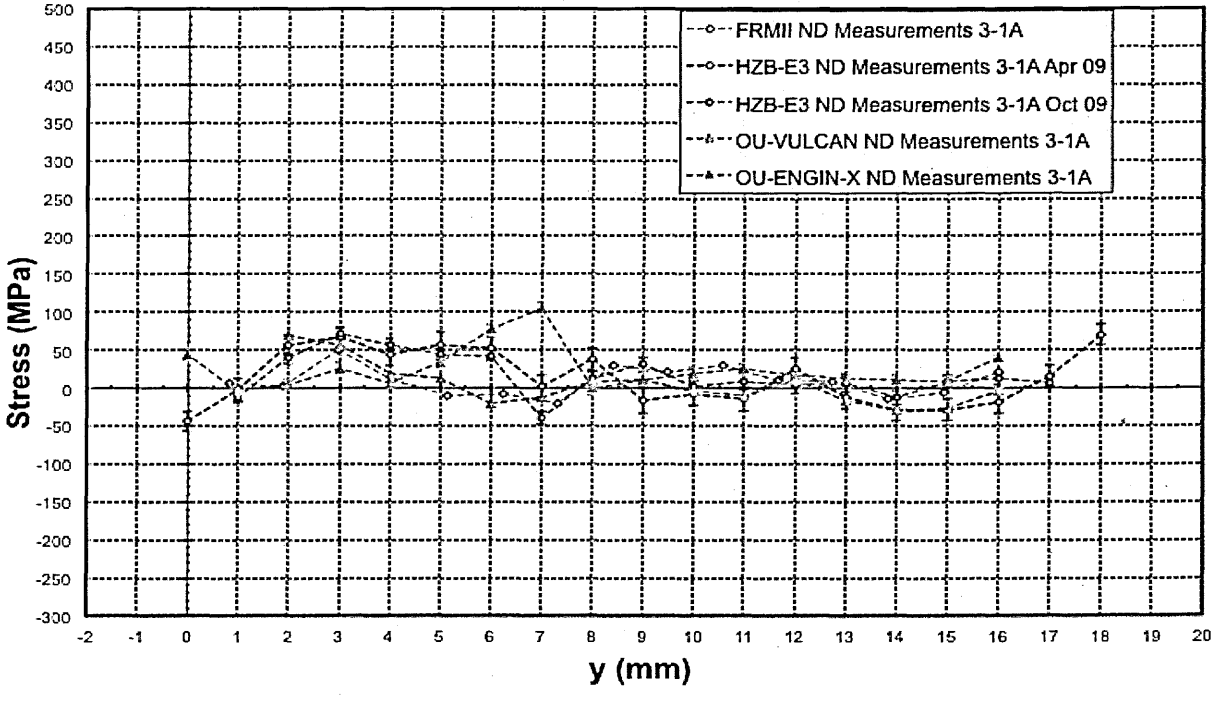
FRMII ND Measurements 3-1A
HZB-E3 ND Measurements 3-1A Apr 09
HZB-E3 ND Measurements 3-1A Oct 09
OU-VULCAN ND Measurements 3-1A
OU-ENGIN-X ND Measurements 3-1A
Stress (MPa)
y (mm)

(c)

Figure 4.23 Line D2: Comparison of residual stress measured at different neutron sources (a) Longitudinal (b) Transverse and (c) Normal

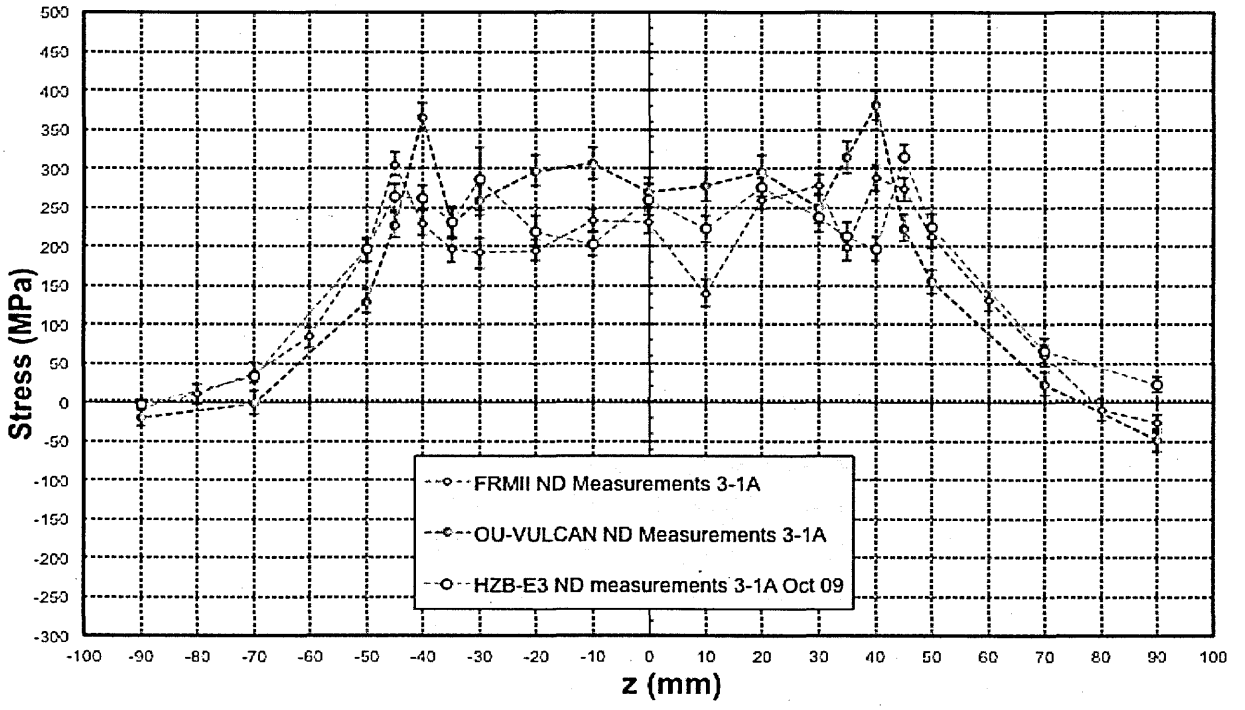

(a)

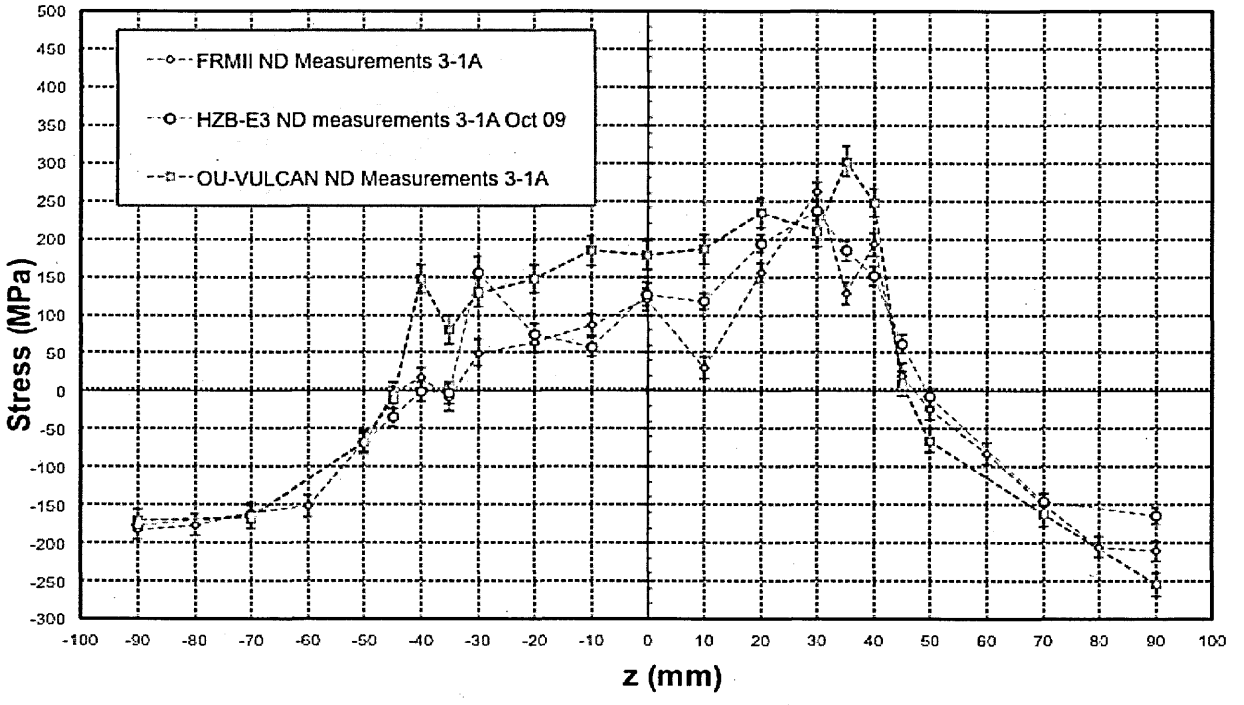

(b)

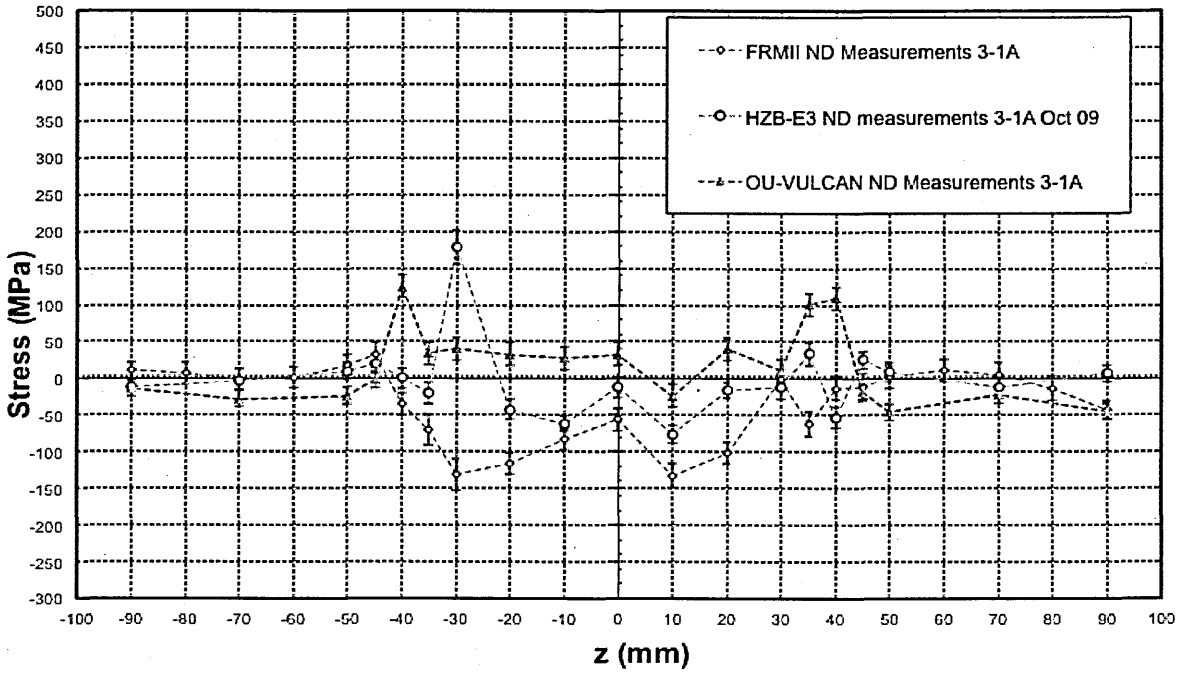

(c)

Figure 4.24 Line D5: Comparison of residual stress measured at different neutron source (a) Longitudinal (b) Transverse and (c) Normal

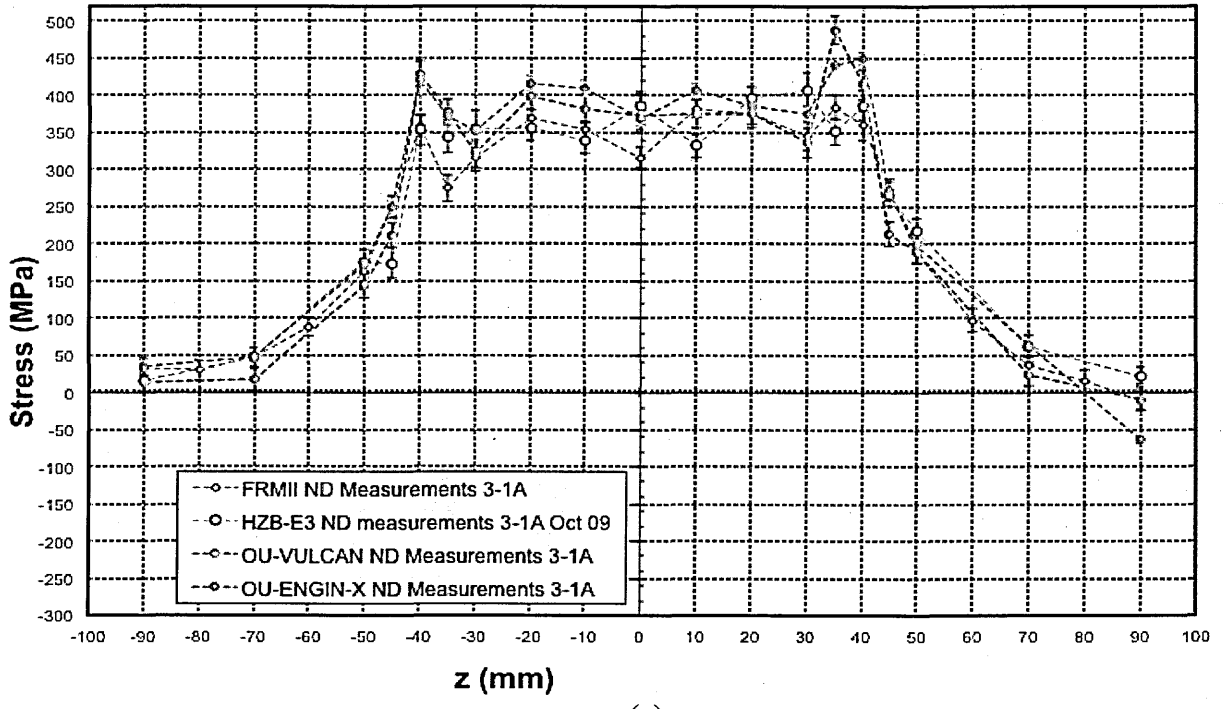

(a)

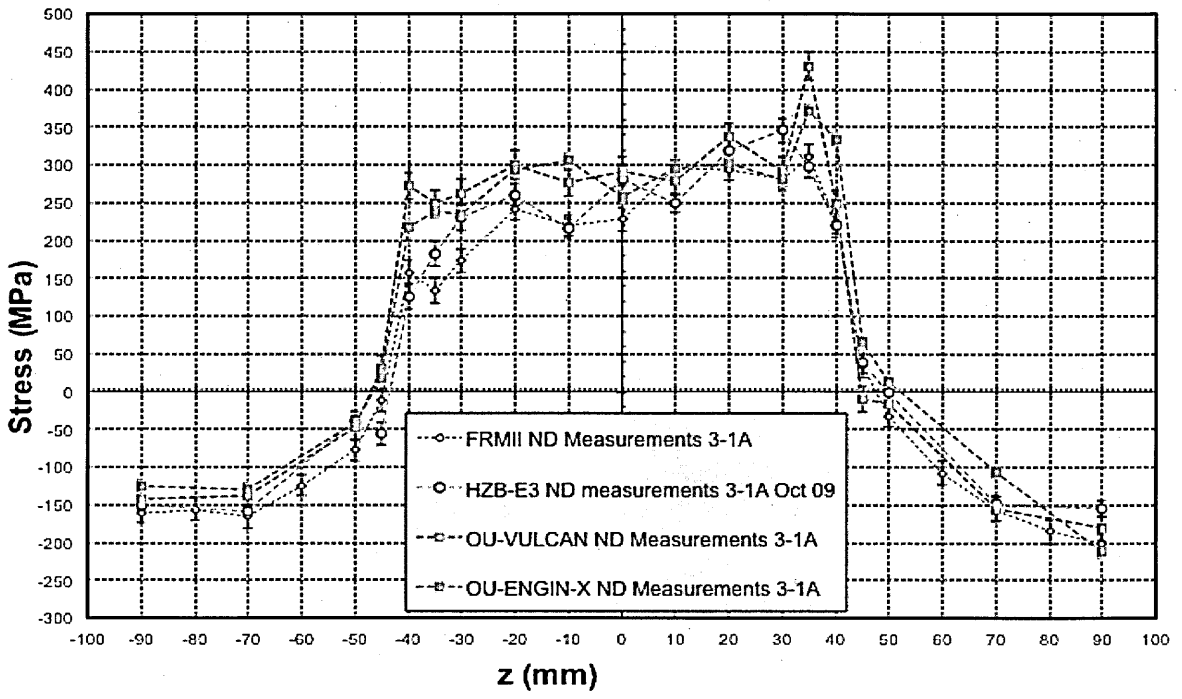
Stress (MPa)
z (mm)
FRMII ND Measurements 3-1A
HZB-E3 ND measurements 3-1A Oct 09
OU-VULCAN ND Measurements 3-1A
OU-ENGIN-X ND Measurements 3-1A

(b)

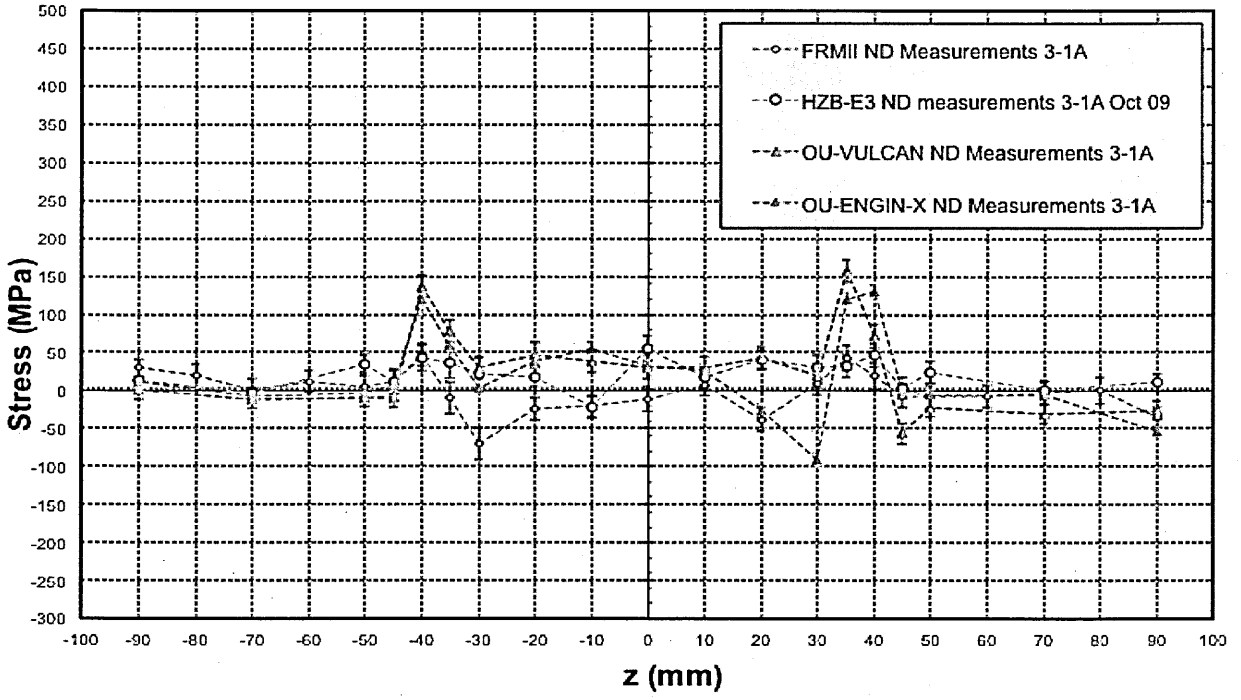
Stress (MPa)
z (mm)
FRMII ND Measurements 3-1A
HZB-E3 ND measurements 3-1A Oct 09
OU-VULCAN ND Measurements 3-1A
OU-ENGIN-X ND Measurements 3-1A

(c)

Figure 4.25 Line D9: Comparison of residual stress measured at different neutron sources (a) Longitudinal (b) Transverse and (c) Normal

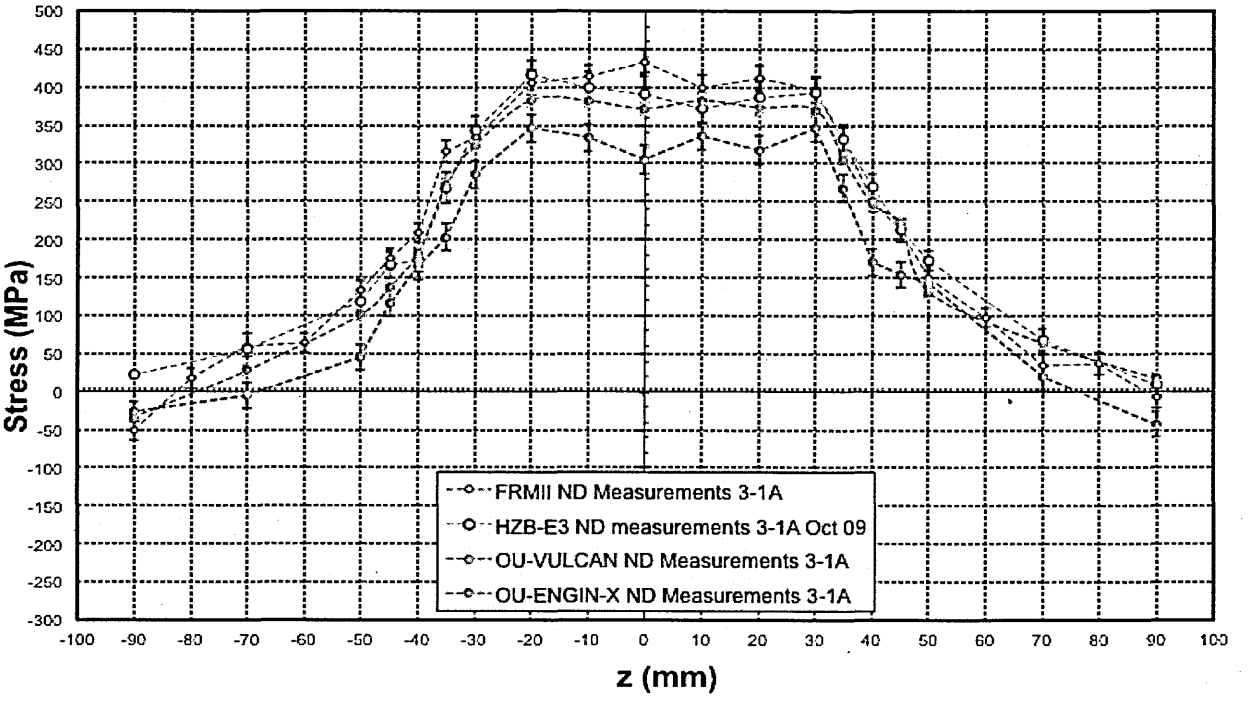

(a)

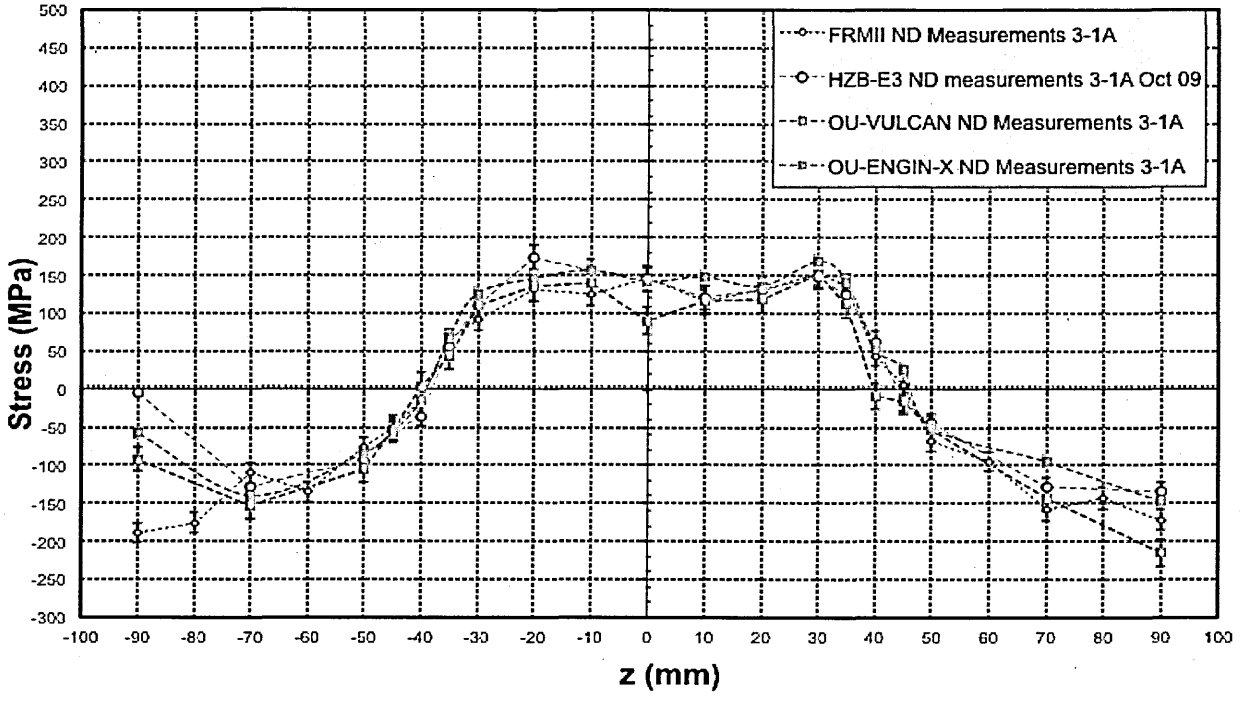

(b)

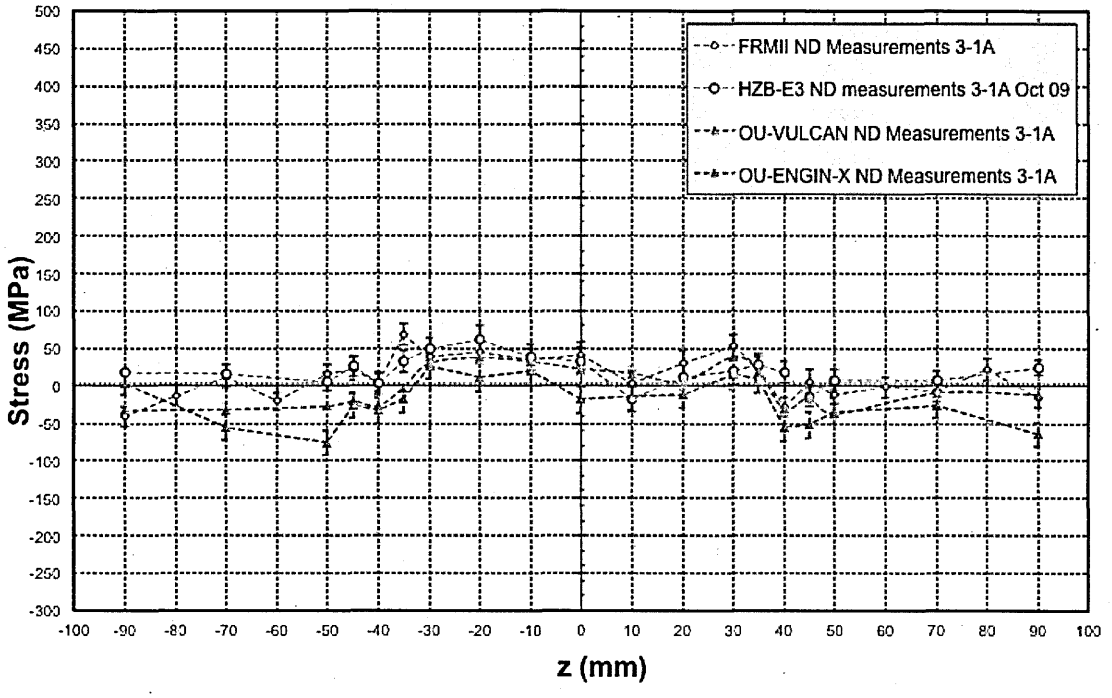

(c)

Figure 4.26 Line D16: Comparison of residual stress measured at different neutron sources (a) Longitudinal (b) Transverse and (c) Normal

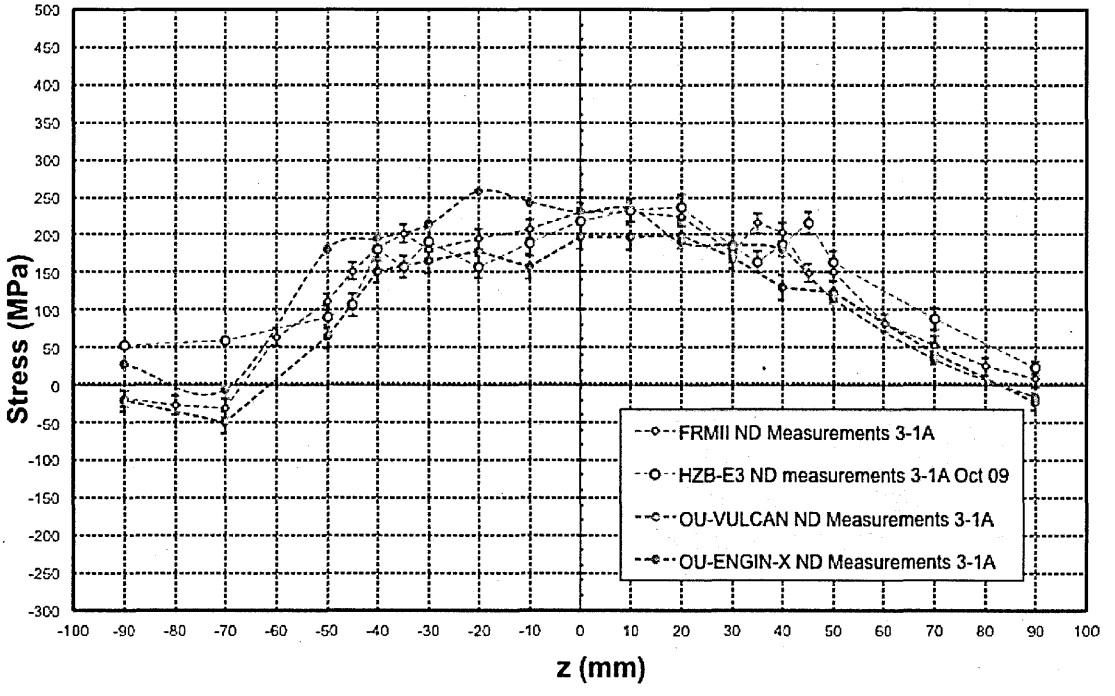

(a)

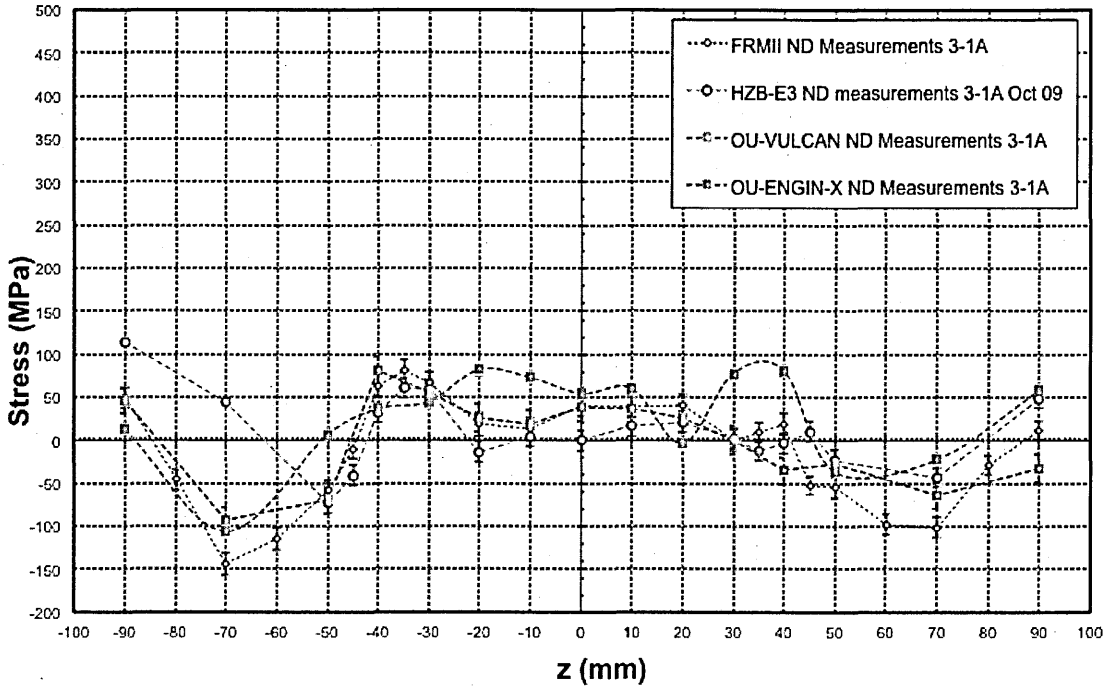
FRMII ND Measurements 3-1A
HZB-E3 ND measurements 3-1A Oct 09
OU-VULCAN ND Measurements 3-1A
OU-ENGIN-X ND Measurements 3-1A
Stress (MPa)
z (mm)

(b)

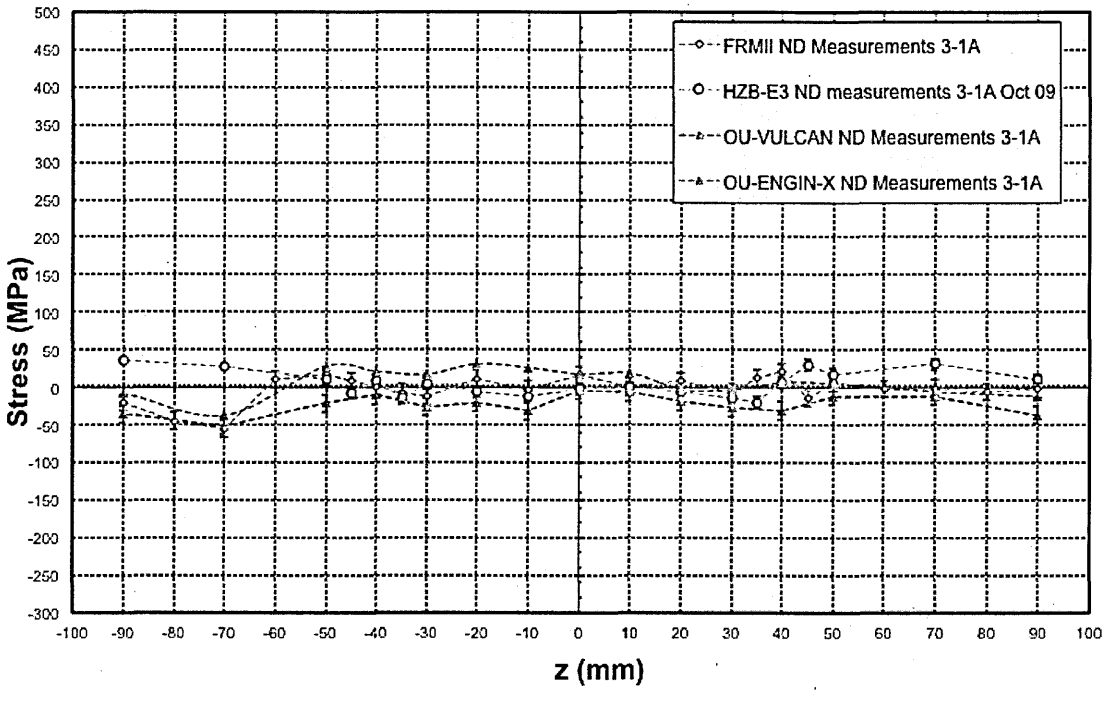
FRMII ND Measurements 3-1A
HZB-E3 ND measurements 3-1A Oct 09
OU-VULCAN ND Measurements 3-1A
OU-ENGIN-X ND Measurements 3-1A
Stress (MPa)
z (mm)

(c)

Figure 4.27 Line B2: Comparison of residual stress measured at different neutron sources (a) Longitudinal (b) Transverse and (c) Normal

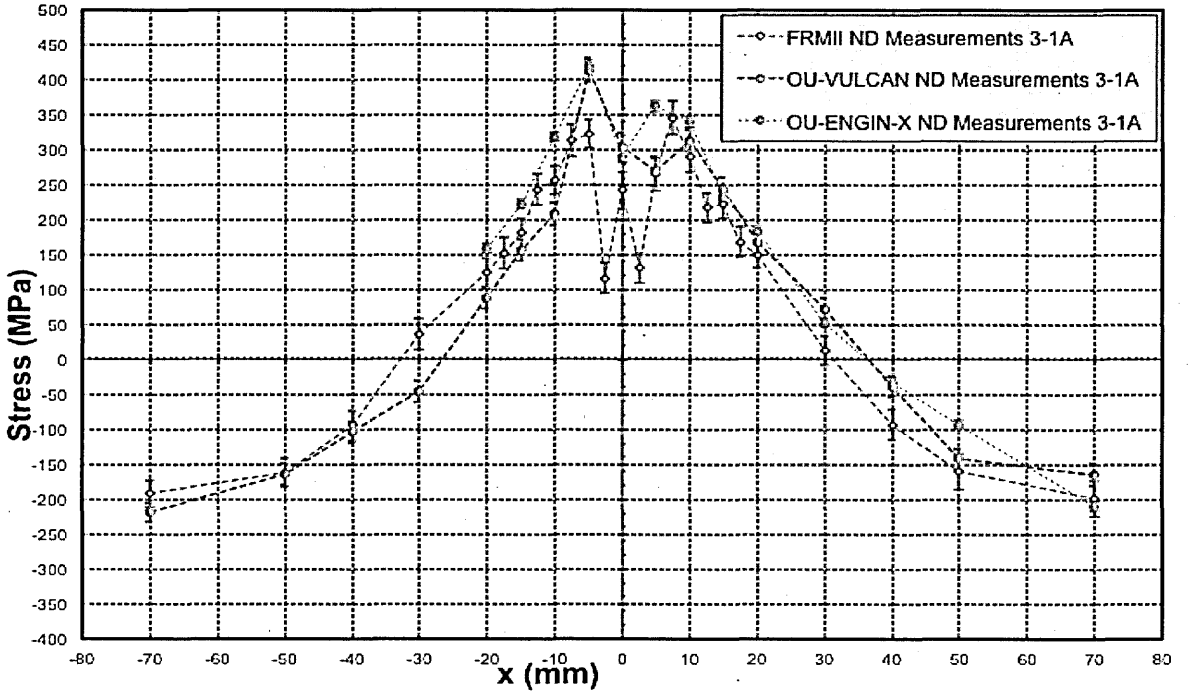

(a)

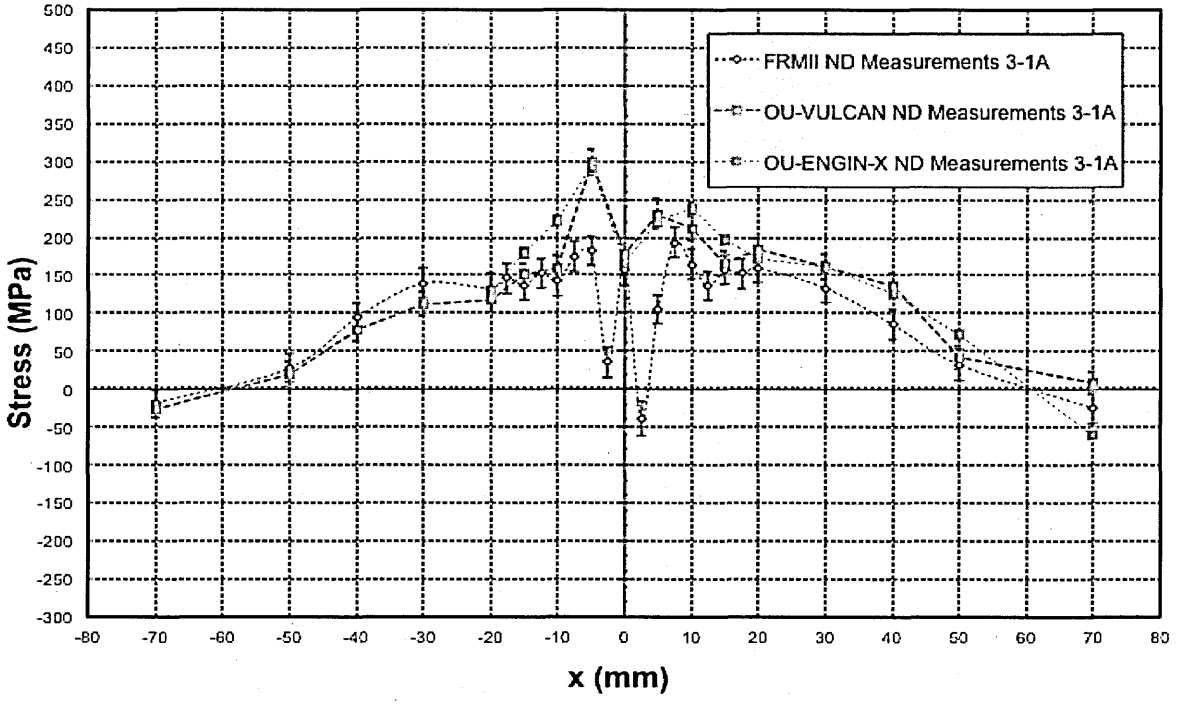

(b)

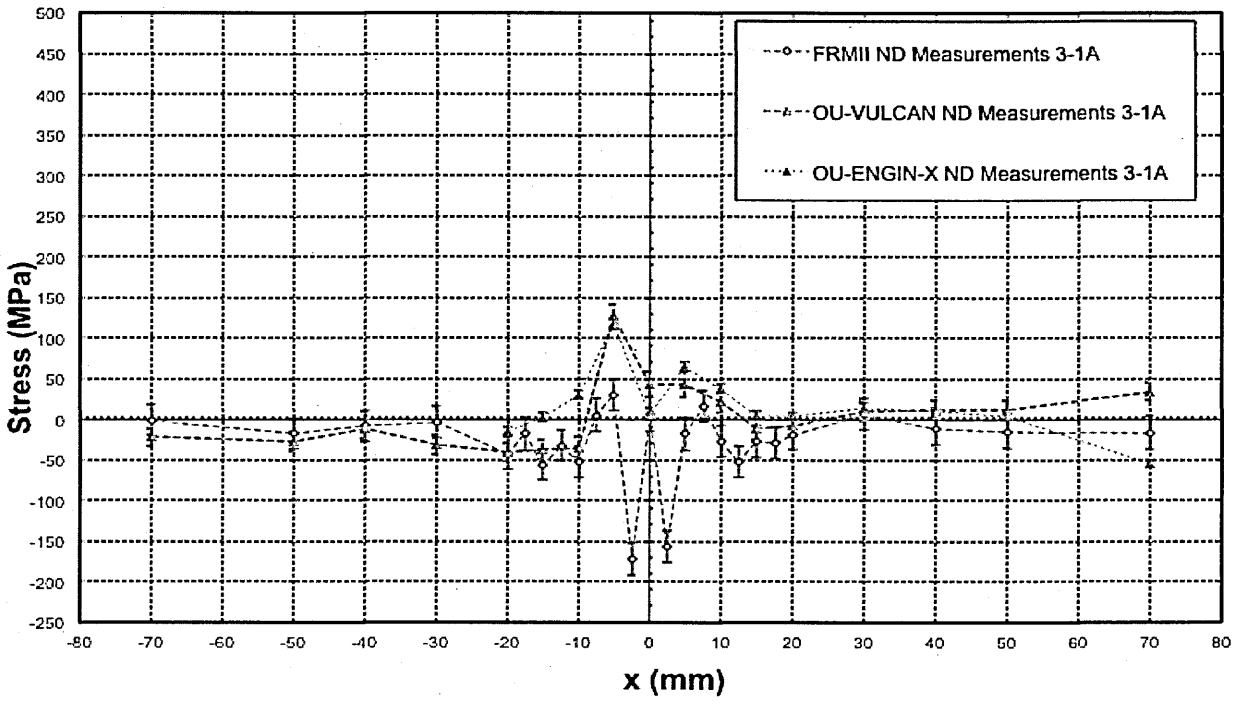

(c)

Figure 4.28 Line B16: Comparison of residual stress measured at different neutron sources (a) Longitudinal (b) Transverse and (c) Normal

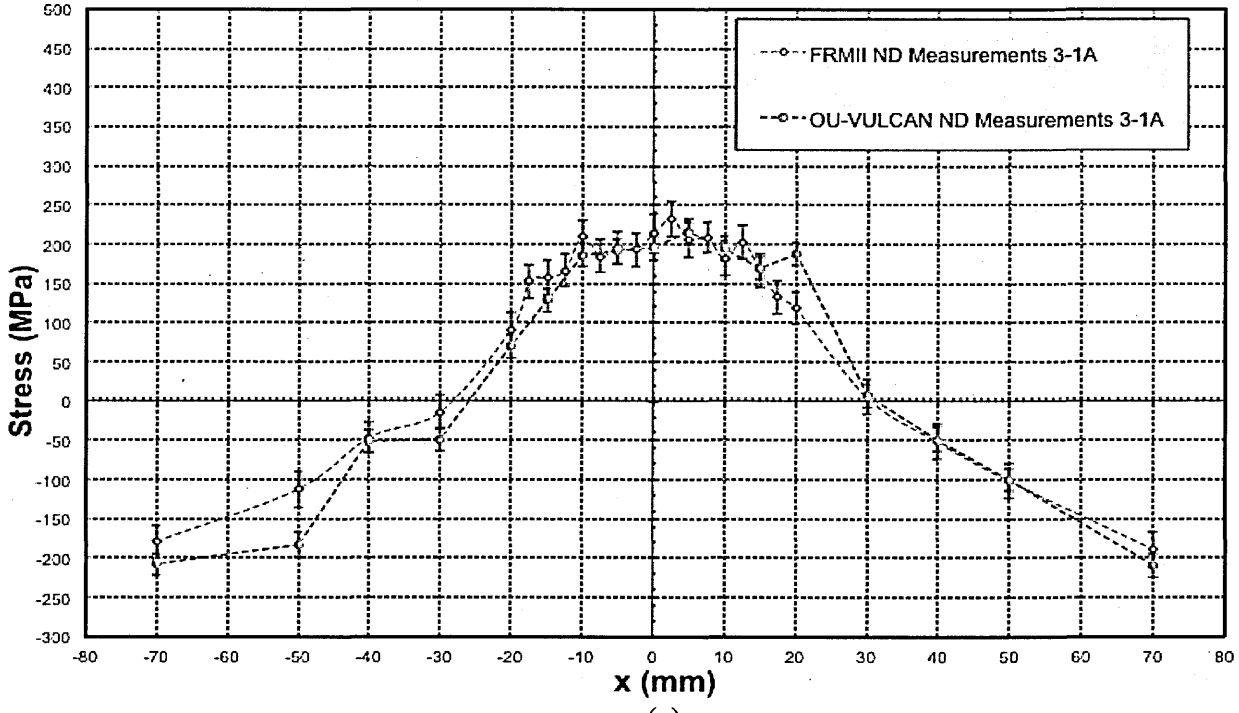

(a)

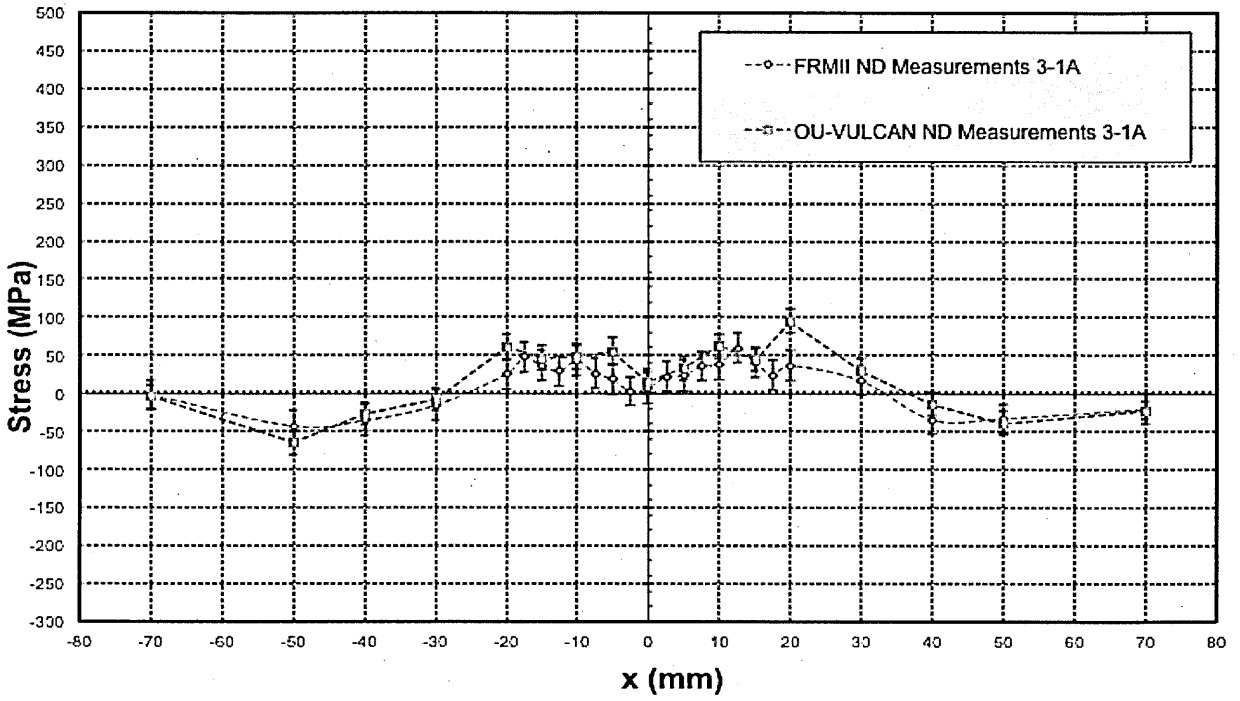
FRMII ND Measurements 3-1A
OU-VULCAN ND Measurements 3-1A
Stress (MPa)
x (mm)

(b)

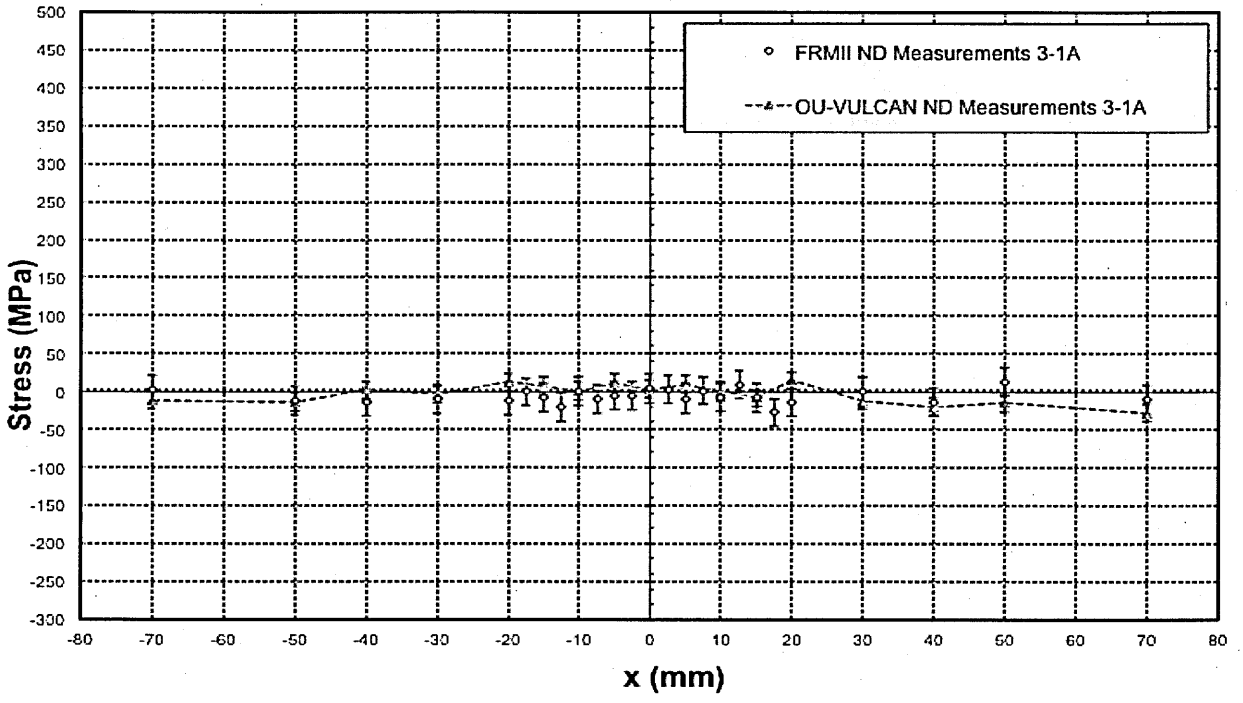
FRMII ND Measurements 3-1A
OU-VULCAN ND Measurements 3-1A
Stress (MPa)
x (mm)

(c)

Figure 4.29 Crevice effect on gauge volume

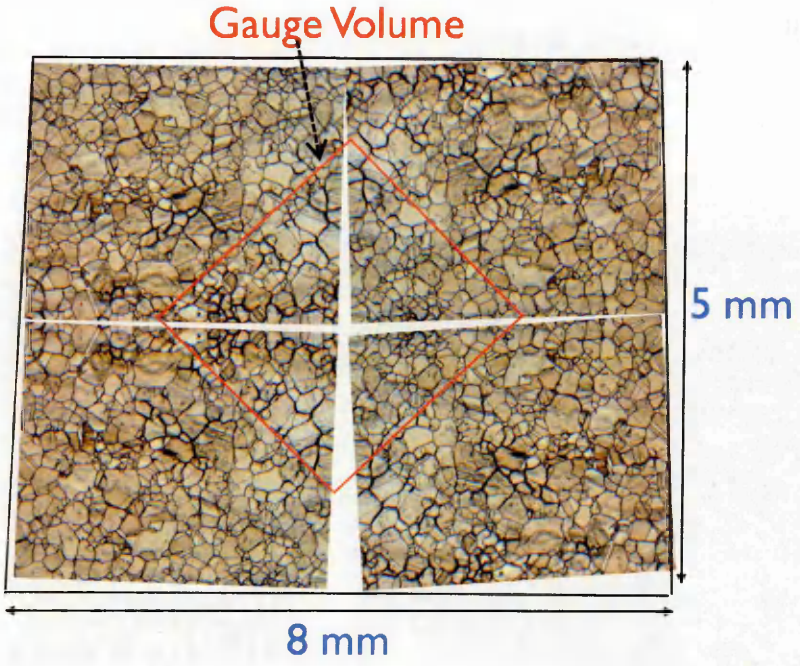

Figure 4.30 (a) Gauge volume measuring grains in only one plane (i.e. Plane D or Plane B refer Figure 3.3 (a)) at 0°, 180°, 90° and 270° and (b) gauge volume measuring average of two plane (i.e. plane D and B) at 30°, 60°, 120°, 150°, 210°, 240° and 300°

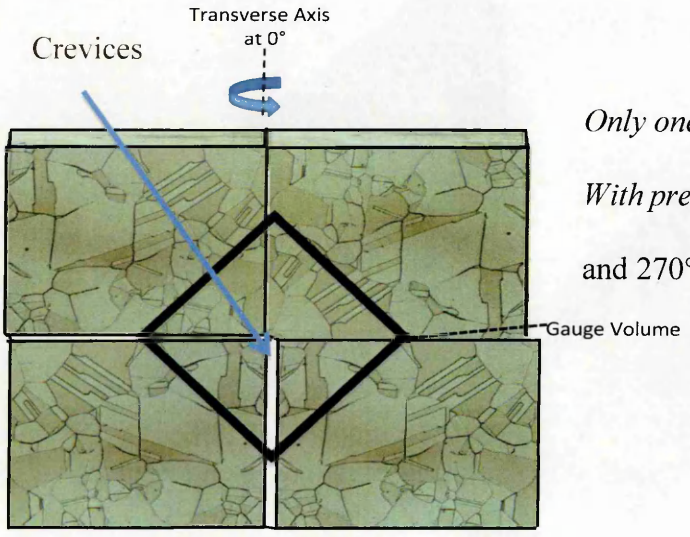

Only one-plane grain populations

With presents of crevices at angles 0°, 180°, 90° and 270°

(a)

Misfit of approximately 50μ and presents of hydrogen glue

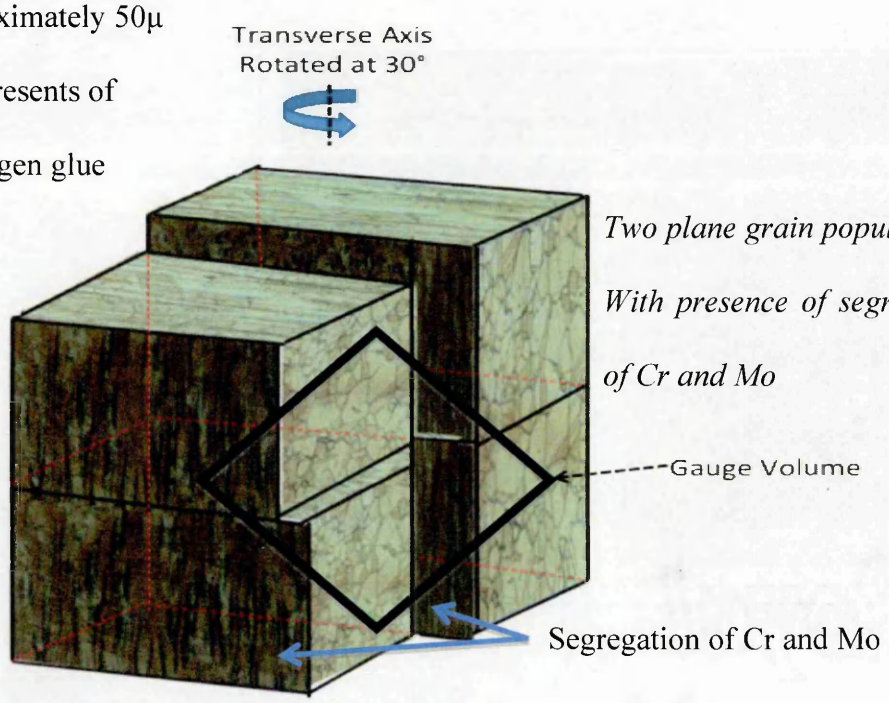

(b)

Figure 4.31 Grain positions and population variation from 0° to 180° due to a shift in the sample geometry centre relative to the sample gauge volume

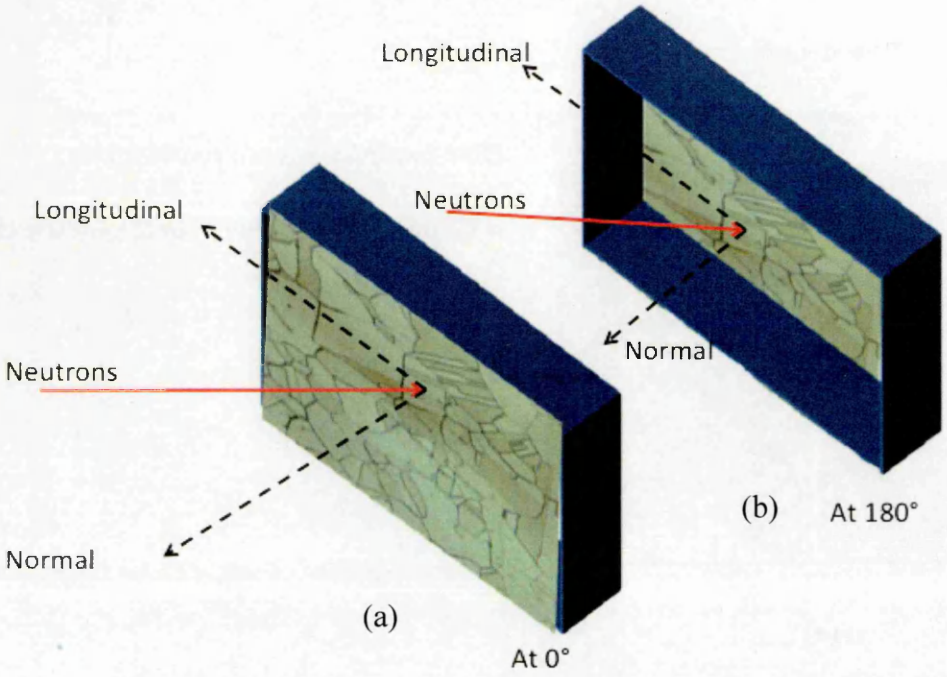

Figure 4.32 Vickers hardness test on weld trail plate 1-2B

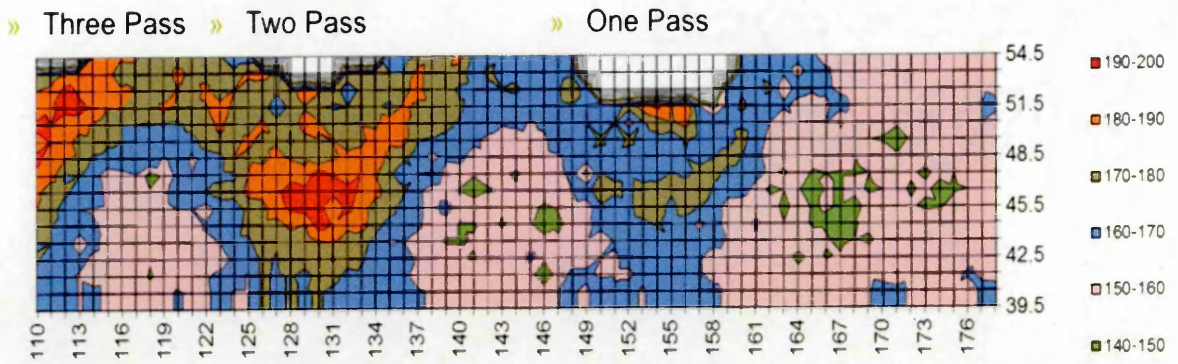

Figure 4.33 Line BD comparison of measured lattice parameters from SNS (VULCAN) and ISIS (ENGIN-X) in: (a) Longitudinal direction; (b) Transverse direction; (c) Normal direction and (d) Micro strain

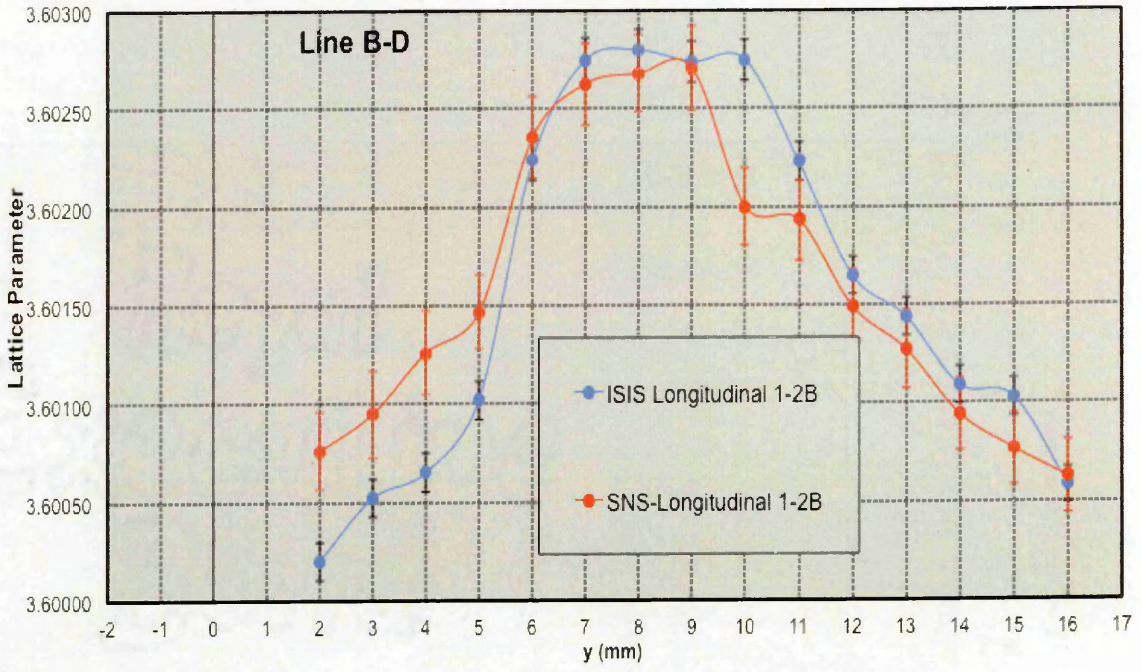

(a)

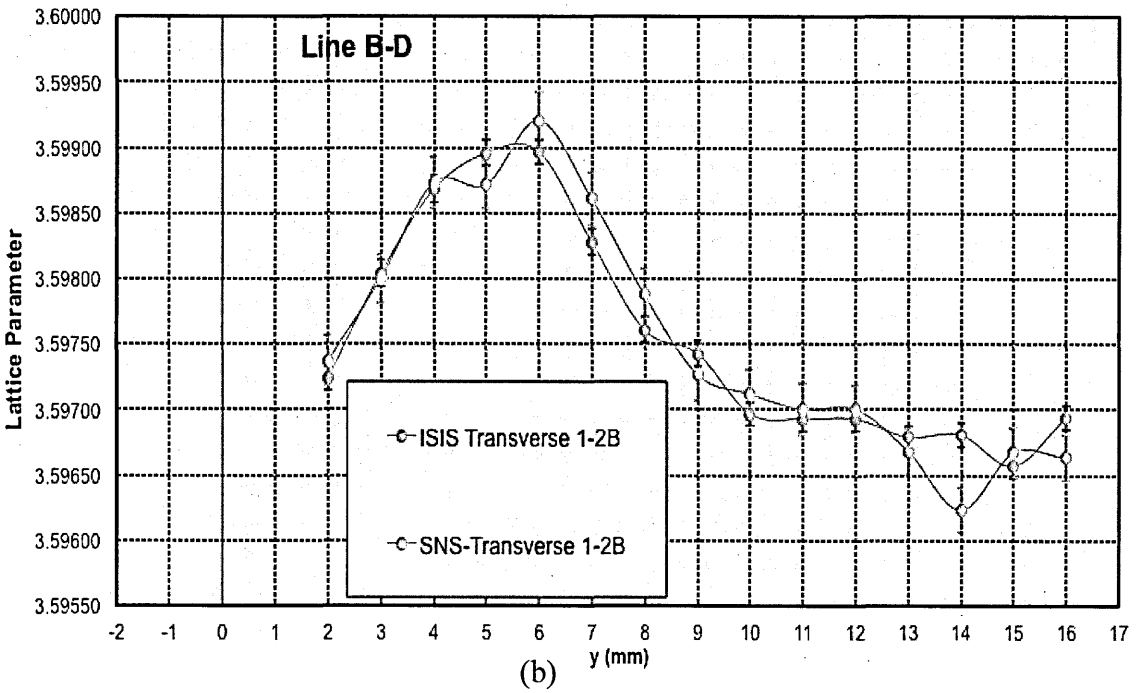
Line B-D
Lattice Parameter
3.60000
3.59950
3.59900
3.59850
3.59800
3.59750
3.59700
3.59650
3.59600
3.59550
-2 -1 0 1 2 3 4 5 6 7 8 9 10 11 12 13 14 15 16 17
y (mm)
ISIS Transverse 1-2B
SNS-Transverse 1-2B

(b)

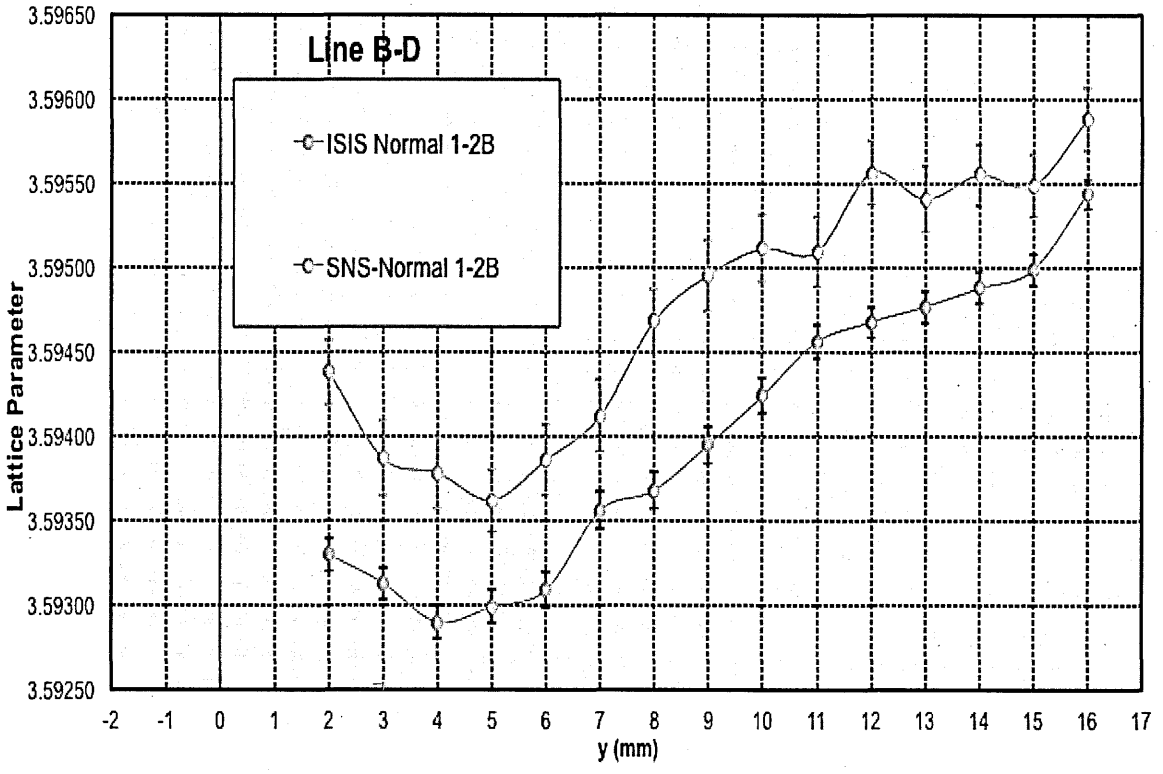
Line B-D
Lattice Parameter
3.59650
3.59600
3.59550
3.59500
3.59450
3.59400
3.59350
3.59300
3.59250
-2 -1 0 1 2 3 4 5 6 7 8 9 10 11 12 13 14 15 16 17
y (mm)
ISIS Normal 1-2B
SNS-Normal 1-2B

(c)

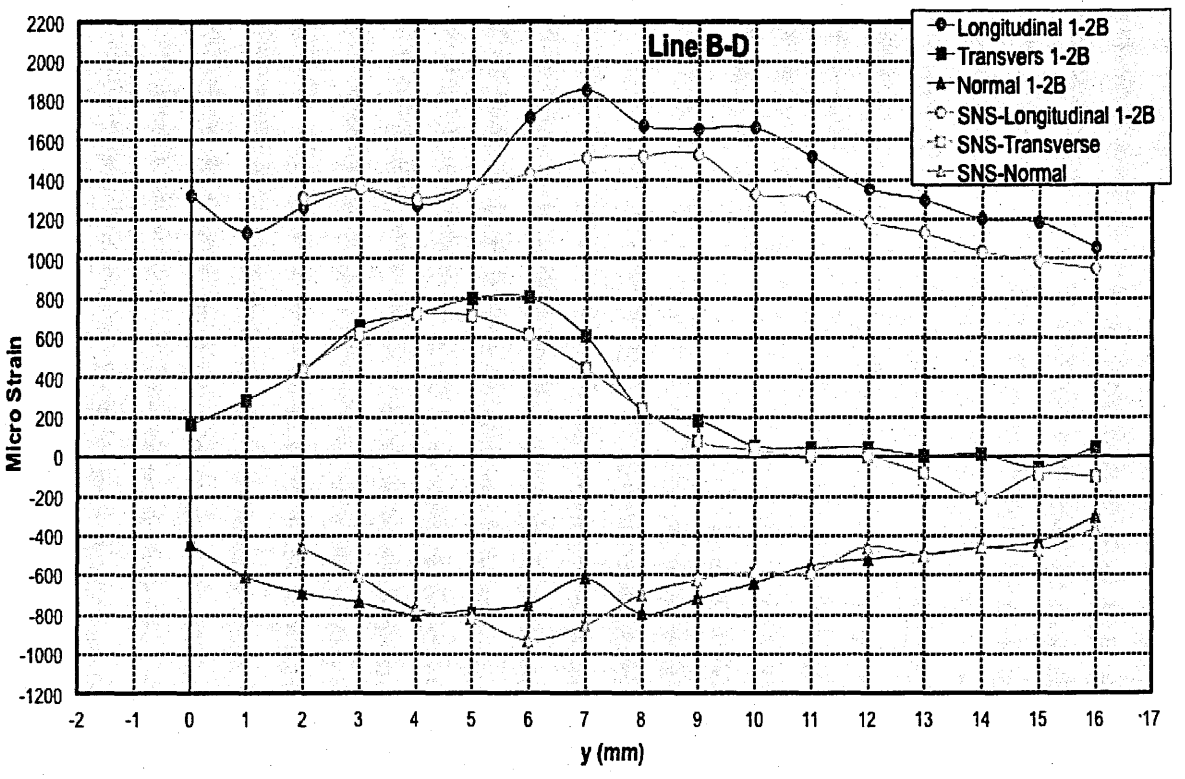
Line B-D
Longitudinal 1-2B
Transvers 1-2B
Normal 1-2B
SNS-Longitudinal 1-2B
SNS-Transverse
SNS-Normal
Micro Strain
y (mm)
2200
2000
1800
1600
1400
1200
1000
800
600
400
200
0
-200
-400
-600
-800
-1000
-1200
-2
-1
0
1
2
3
4
5
6
7
8
9
10
11
12
13
14
15
16
17

(d)

CHAPTER 5. CYCLIC DEFORMATION BEHAVIOUR

5.1 Introduction

Finite element (FE) analysis is widely used for predicting heat transfer, fluid flow, stress distributions and dynamic behaviour in the design of power station pressure vessel and piping systems. Increasingly, the technique is being applied to characterise residual stresses in welded structures where they may impact the life or integrity of plant [222,228–230]. However, the accuracy of weld simulation predictions is normally reliant on the input material properties, the definition of the constitutive elastic-plastic material model, and the considered assumptions of the simulation [171]. Some elastic-plastic hardening models commonly used have been introduced in section 2.3.5 of Chapter 2.

FE predictions of cyclic stress-strain behaviour have been validated with experimental cyclic stress-strain data [11–17], and the fitted model parameters implemented in simulations of material and structural behaviour to predict weld residual stresses. This chapter investigates the influence of strain rate, and the type of loading cycle, on the stress versus strain properties of 316L austenitic stainless steel that need to be modelled in weld residual stress simulations. This chapter first introduces the parameters to be studied, then describes the experimental work, followed by modelling and discussion of the results.

5.2 Choice of Test Conditions

Weld thermal loading effectively cyclically deforms material surrounding the heat source under displacement control. Depending on the proximity to the heat source, material will experience different strain ranges and strain rates due to the non-uniform time dependent weld thermal gradients. The strain hardening of the material varies depending on the applied strain range, strain rate and temperature. Therefore, in testing to determine the cyclic

deformation properties of a material it is very important to select an appropriate strain range, strain rate and temperature. Material surrounding the weld heat source will first expand and experience compressive strain due to constraint from material away from the heat source. In contrast, during weld cooling, the material will contract with decreasing temperature, but is constrained by the surrounding material. As a result of this, tensile strains are developed in the material. In this research study, in order to replicate weld deformation behaviour, the parent material is cyclically deformed in compression-tension cycles. Table 5.1 lists the strain controlled cyclic deformation tests of solution annealed parent material carried out at both room and high temperatures.

5.2.1 Strain range

Strain ranges of ±1.25% for symmetric cyclic deformation, and -1.25% to 0.02% for asymmetric cyclic deformation of parent material at both room and high temperature were adopted. In multi-pass welding, the strain range of the weld deformation cycle generally reduces from one weld deposit to next with increasing distance from heat source, as described in section 2.2.1 of Chapter 2. Depending on the weld heat input parameters, the highest plastic strain range is observed close to the fusion boundary; during the welding of austenitic stainless steel this is of the order of ±2.5% [63]. Due to the limited material available and the high probability of losing data due to specimen buckling at high temperature, a strain range of ±1.25% was adopted for this research study. This is expected to be close to the mean strain range of multiple weld passes. For asymmetric cyclic loading approximately one half of the symmetric strain range was chosen.

5.2.2 Temperature

The accumulated plastic strain due to each weld pass contributes to cyclic work hardening of the material. However, at high temperature, the material can experience dynamic

recovery, annealing and softening. This can reduce the strain introduced at lower temperatures. The cooling rate of the weld metal decreases very slowly from 600°C to room temperature. In the temperature range 650°C-300°C austenitic stainless steel 316L (N) experiences Dynamic Strain Ageing (DSA). As described in section 2.3.3 of Chapter 2, with decreasing strain rate (i.e. cooling rate) the material gets more strain hardened than at a fast strain rate. In this research study cyclic deformation tests of parent material were performed at 550°C. The reasons for selecting this temperature are; (a) above 600°C the recovery of the plastic deformation of material is high and (b) there is a higher risk of sample buckling during compression loading at higher temperatures.

5.2.3 Strain rate

As described in section 2.2.1 of Chapter 2, the heating rate and cooling rate of weld metal varies with distance from the heat source. Likewise, the plastic strain rate associated with the welding process varies during weld heating and cooling cycles. The strain rate during heating is in excess of 1×10^{-2}/sec, and during cooling reaches 1×10^{-3}/sec between 750°C and 350°C and falls steadily as the temperature drops [63]. In this research study, due to limitations of the test machine, strain rates of 4×10^{-4}/sec and 4×10^{-5}/sec were selected for the cyclic deformation tests. Details of the design, extraction and heat treatment of the test samples has been given in section 3.3. Using an Instron 8862, the test samples were cyclically deformed at both room and elevated temperatures (550°C). Details of the cyclic loading experimental setup are given in section 5.3.

5.3 Cyclic Stress-Strain Tests

The British standard BS7270 [208] was followed for the program of cyclic deformation tests performed at room and high temperatures. An Instron 8862 slow strain servo electric test instrument with a 100kN capacity and equipped with a heating furnace was used for all the

tests. The alignment of the slow strain cyclic loading instrument is very important in avoiding buckling of the samples, and to ensure a uniform distribution of load is applied to the gauge volume of each sample. The instrument was aligned according to ASTM E1012-14[231]. Alignment was achieved by using a sample fitted with eight strain gauges (as shown in Figure 5.1), and using Instron AlignPro (IAP) fixture equipment and software [232]. Linear strain gauges EA-09-062AQ-350/E were spaced at 90° intervals around the circumference, glued with M-Bond 600 adhesive and protected with M-Coat C (both made by Vishay Precision Group Ltd). The strain gauges were aligned parallel to the long axis of the test specimen, with a tolerance of ±2 degrees. The IAP software allows the user to correct for both concentric and angular misalignment, whilst the sample is preloaded at between 50-100 N.

A Eurotherm-3216 electronic controller was used to control the furnace to maintain a uniform temperature. Two calibrated n-type thermocouples were used to monitor the specimen temperature for the high temperature tests. These thermocouples were connected at both ends of the gauge volume of the sample with the help of clamps, as shown in Figure 5.2. The cyclic loading tests were programmed using Instron Bluehill software. Symmetric cyclic deformation is routinely used in examining the mechanical properties of materials where the sample is deformed, as shown in Figure 5.3. However, this is not representative of the asymmetric cycle deformation experienced close to real welds. In this research study, a new approach of asymmetric cyclic deformation, as shown in Figure 5.4 Asymmetric cyclic loading with the first cycle loading in compression (a) stress vs strain loops (b) strain vs time was adopted.

5.3.1 Asymmetric cyclic deformation

As seen in Figure 5.4, an asymmetric cyclic test begins with compression, following the path from '*A*' to '*B*' in the figure. Between '*A*' and '*B*', the sample is deformed in

compression up to -1.25% and then unloaded from '*B*' to '*C*'. However, from point '*C*' onwards, at each increment of tensile strain, the Bluehill software measures the strain difference between point '*C*' and current strain, to evaluate whether the desired relative strain range to '*D*' is achieved or not. Once the desired relative strain range 'D' is achieved, unloading commences from point '*D*' to '*E*'. From point '*E*', the deformation of the sample continues under relative strain control. This type of asymmetric cyclic deformation is more representative of predicted real weld asymmetric cyclic loading as shown in Figure 5.5 [66]. Symmetric cyclic loading test results, at both room and high temperature (550°C), are given in Figure 5.6-5.8. Similarly, the asymmetric cyclic loading test results, at both room and high temperature, are presented in Figure 5.9-5.13. The results were described in section 5.5.1. All experimental cyclic tests were performed on 'solution annealed' parent material. These experimental test results are used to assess the performance of finite element simulation of welding cycles based on a Lemaitre Chaboche hardening model [109] fitted to symmetric cycle stress-strain data.

5.4 Finite Element Modelling Of Cyclic Loading

This section describes FE analysis performed to predict the hysteresis loops (i.e. stress vs strain curves) resulting from the symmetric and asymmetric cyclic loading tests at room and high temperatures. The simulations were carried out using Abaqus FE software. Figure 5.14 shows a schematic of the geometry simulated. To simplify the simulations, an axisymmetric model was used with a symmetry plane at the sample mid-length as shown in Figure 5.14. Second order quadrilateral elements with reduced integration were used. A total of 2625 elements were generated to create a uniform mesh of element size 0.1 mm. Using the Abaqus tabular amplitude function, the sample loading was defined by applying a cycling displacement on the top edge of the model, as shown in Figure 5.14.

The displacement for the asymmetric cyclic loading simulation was based on the experimental strain range (i.e. -1.25% to 0.02%). The temperature was set at 25°C and 550°C for the room and high temperatures models, respectively. An accurate elastic-plastic constitutive material model is required to achieve reliable stress vs strain FE prediction for symmetric and asymmetric cyclic hardening tests. A 5-parameter mixed hardening (refer to section 2.3.5 of Chapter 2) Lemaitre-Chaboche [109] model is provided in Abaqus [24,46] and was used in FE analysis. The mixed hardening model is designed to predict the stress-strain curve at high accuracy in comparison to other models[24,178]. Chaboche parameters for the NeT TG4 316L(N) stainless steel from Muransky [22] were used in the present analysis, see Table 5.2. Here it should be noted that Muransky [22] fitted his model to symmetric cyclic stress-strain data (strain range ±1.5% and strain rate 4×10^{-4}/sec) relevant to the NeT TG4 components.

It is worth mentioning that the mixed hardening model takes into account both the Bauschinger effect and cyclic hardening. Before simulating the behaviour of the test, the cyclic stress-strain results of Muransky [22] were reproduced, see Figure 5.15. Predicted stress-strain behaviour for symmetric vs asymmetric cyclic tests based on the Muransky model is presented in Figure 5.16. Table 5.3 summarises the materials cyclic test data used for deriving the five parameters of the mixed hardening model. The kinematic hardening parameters C_i and γ_i were fitted to the monotonic tensile tests results up to 5% true plastic strain for the parent material, and 2% for the weld metal as recommended in the R6 procedures[171]. Whilst, from the cyclic test data, the locus of the peak stress values, of each half cycle, versus the cumulative plastic strain, was used for fitting the isotropic hardening of the material. For isotropic hardening, the parameters Q_∞ and b are defined from the second cycle of symmetric cyclic loading. Optimized parameters for the mixed hardening model for 316L stainless steel have been fitted by Smith et al. [21,233] so, these parameters are validated and should be capable of predicting the stress-strain curve accurately.

5.5 Discussion

The material hardening constitutive model used in weld FE simulation has a crucial influence on the accuracy of predicted residual stress and plastic strains in welded joints. The input parameters for a hardening model are usually evaluated from the symmetric strain controlled cyclic and monotonic tensile test data [22,171]. However, in real welding processes the material undergoes asymmetric cyclic hardening, see Figure 5.5. The tests show that asymmetric cyclic deformation exhibits a different hardening rate in comparison to symmetric cyclic loading; refer Figure 5.18 and Figure 5.20. The symmetric cyclic tests of 316L (N) material at both room and high temperature show a higher strain hardening rate than the corresponding asymmetric tests. This suggests that in welding simulations, more accurate results might be obtained from using a mixed hardening model where the input parameters are derived from asymmetric cyclic hardening test data.

According to the Rosenthal equation (see section 2.2.1 of Chapter 2), near the weld heat source, the peak temperature achieved during a weld thermal cycle is very high. The initial cooling rate during the weld thermal cycle is also very fast, due to the heat sink of surrounding parent material. However, as the distance from the weld increases, both the peak temperature and the cooling rate decrease [46]. Therefore, in a real welding process the heating and cooling rates (and hence the strain rate) are non-uniform throughout the sample. Most of the material hardening leading to tensile stress occurs during the cooling process. At temperatures between 650°C to 300°C, the austenitic stainless steel exhibits Dynamic Strain Ageing (DSA), see the serrated stress strain curve in Figure 5.8. While in this range of temperature, the material experiencing a faster strain rate will exhibit less strain hardening than that subjected to a slower strain rate, due to DSA. Thus, it is very important to test at representative strain rates in this temperature range when generating data for calibrating material hardening models.

5.5.1 Discussion on experimental results

Figure 5.6 presents stress-strain results for symmetric cyclic loading at room temperature for a strain range of ±1.25% (strain rate 4×10^{-4}/sec) and ±1.0% (strain rate 4×10^{-5}/sec). It is clear from the figure, that the material strain hardens more with a strain range of ±1.25% than with ±1.0%. In addition, the faster strain rate, 4×10^{-5}/sec, increases the strain hardening. The effect of strain rate is clearly evident in the first compression cycle, with the higher strain rate giving greater monotonic strain hardening. At room temperature, material deforming at a faster strain rate accelerates dislocations, piling up at grain boundaries and increasing dislocation interactions with defects more than in the material deformed at the slower strain rate.

During welding, both the peak temperature and the cooling rate in the parent material decrease gradually with an increasing number of passes, due to the increasing distance from the heat source. As a result of this, as each weld is deposited, the material cyclically strain hardens over a different strain range and at different strain rates, for example see Figure 5.5. However, most weld simulations material mixed hardening models are based on constant strain rate, constant symmetric strain range cyclic data [21,22,46,233]. However, the present results show that strain rate at room temperature has a significant effect on hardening behaviour see Figure 5.6.

After six cycles of symmetric deformation of 316L(N) material, (i.e. 30% to 40% cumulative plastic strain), the rate of strain hardening of the material is much lower than in the first three cycles (Figure 5.6). This is because, during the initial cycles, the rate of increasing dislocations density, interactions between them and pile up of dislocation at grain boundary is high in comparison to later cycles (>3 cycles), due to planar slip mode (refer section 2.3.4). In planar slip mode, the activation of secondary slip (including cross slip) is

very difficult. As a consequence of this, higher dislocation density is noticed at the grain boundary.

Pham et al. [27,177], dislocation structure studies in cyclically deformed 316L material, have clearly indicated the formation of a higher density of planar dislocation structures piled up at the grain boundary, with the help of TEM analysis. However, with an increasing number of cycles, the applied energy is consumed by changing the dislocation structures, activating more slip planes and annihilation of dislocations etc.

Figure 5.7 shows a comparison between the symmetric cyclic deformation results, tested at 25°C versus 550°C, at a strain range of ± 1.25% and a strain rate of 4×10^{-4}/sec. At high temperatures, the material has lower monotonic yield strength in compression than at room temperature, and cyclically hardens more, due to DSA (ref section 2.3.3). However, it is evident that the rate of cyclic hardening decreases significantly from the eighth cycle onwards. Figure 5.8 shows the effect of strain rate on cyclic hardening of the material tested at 550°C, due to DSA (see Section 2.3.3). At high temperatures, the cyclic deformation of the material at a faster strain rate exhibits a low yield point and lower strain hardening than the material deformed at slower strain rates.

At slower strain rates, the mobility of dislocations reduced due to the pinning effect of the formation of solute atmosphere around dislocations (refer section 2.3.3). In such circumstances, in order to maintain the stress flow, additional dislocations are generated, which results in higher strain hardening of the material. As a consequence, the material undergoes more strain hardening at a slower strain rate than at a fast strain rate, due to dynamic strain ageing (refer section 2.3.3). The effect of dynamic strain ageing at a slow strain rate becomes more significant from the third cycle onwards. This is because, with increasing numbers of cycles, the dislocation density and the interaction of solute atom with dislocations increases, as a result material gets more strain hardened. Figure 5.9 and Figure

5.10 shows the results from asymmetric cyclic loading performed at room and high temperature. These results are compared with symmetric cyclic loading, both at a strain rate of 4×10^{-4}/sec. It can be observed from the obtained results, asymmetric cyclic deformed materials are less strain hardened than those undergone through symmetric cyclic deformation (see Figure 5.18 and Figure 5.20).

The first monotonic compression (i.e. elastic deformation) of asymmetric cyclic loading (see Figure 5.9) does not match with symmetric cyclic loading. This is due to the formation of steps as described in section 3.3.1 of Chapter 3. However, in comparison to symmetric cyclic hardening at room temperature, the strain hardening of material in asymmetric cyclic deformations is significantly lower (see Figure 5.9 (a)). A similar difference is seen at high temperature (see Figure 5.10). At high temperature, the material is relatively soft in comparison to material at room temperature. As a result of this, material gets more strain hardened than at room temperature. Figure 5.11(a,b) shows the effect of strain range on asymmetric cyclic strain hardening at 25°C and 550°C. At a fixed strain rate of 4×10^{-4}/sec, the material gets more strain hardened at the high strain range than material deformed at the low strain range. Unsurprisingly the proof stress in the first monotonic compression does not change with strain range. However by changing the strain rate the first monotonic compression does change as seen in Figure 5.6 and Figure 5.12.

Figure 5.12 (a,b), shows the effect of strain rate on asymmetric cyclic strain hardening at 25°C and 550°C. Reducing the strain rate from 4×10^{-4}/sec to 4×10^{-5}/sec, reduces the proof stress as seen in Figure 5.12 (a) in room temperature and increases the proof stress as seen in Figure 5.12(b) at high temperature. Similar strain hardening of the material was noticed in symmetric cyclic loading test results seen previously in Figure 5.6 and Figure 5.8. It is clear from Figure 5.11 and Figure 5.12 that at both room and high temperature, changing the strain rate, changes the degree of strain hardening of material. However, under asymmetric

cyclic loading, the strain hardening of the material tends to saturate at around 20% accumulated plastic strain see Figure 5.20. Further details about the Figure 5.20 are explained in next section. In symmetric cycling, the strain hardening of the material tends to saturate at around 50% accumulative plastic strain (see Figure 5.18). Paul et al. [86], Man et al.[234], Polak et al. [235] have studied the strain hardening of austenitic stainless steel material at room temperature for different strain ranges. All of them noticed a significant variation in strain hardening during symmetric cyclic loading with increasing strain range from 0.2% to 2.0%, whilst showing a tendency towards saturated strain hardening after 6 cycles. Similarly, in this research study, we have noticed significant strain hardening of material with increasing strain range at both room and high temperature and a tendency towards saturated strain hardening after 6 cycles, as seen in Figure 5.6 and Figure 5.11.

Figure 5.13, shows a comparison between the results of asymmetric cyclic stress-strain at both room temperature (25°C) and high temperature (550°C). At high temperature, the material hardening is much higher than in the material tested at room temperature. In Figure 5.13(a), at high temperature the shift observed in the hysteresis loops are due to the way the cyclic loading was programmed within the software (Bluehill software), but also due to the serrations in the stress-strain loops.

5.5.2 Validation of predicted cyclic loading results

Symmetric and asymmetric cyclic stress-strain behaviour, at both room and high temperatures, for a strain range of ±1.25% shown Figure 5.16 has been predicted using the 5-parameters mixed hardening model fitted to symmetric stress-strain data by Muransky [22]. The simulated symmetric cyclic loading results show a similar cyclic hardening trend to that observed in the experimental results (Figure 5.17). Likewise, the simulated asymmetric cyclic stress-strain results show similar strain hardening to the experimental results as shown in Figure 5.19.

Figure 5.17 compares predicted and experimental symmetric cyclic test results at both room and high temperature. In the case of room temperature, a good correlation is obtained between the two sets of results apart from the first quarter of the first cycle. But, at high temperature large discrepancies are observed between the Muransky model and the present experimental results. Similar discrepancies between experimental results and a mixed hardening prediction at high temperature have also been observed by Joosten et al [178]. Figure 5.19 compares the experimental asymmetrical cyclic data with FE predictions. As seen in Figure 5.19, the predicted stress-strain loops are in good correlation with the experimental results in comparison to the symmetric cyclic stress-strain predictions.

An alternative way of assessing the accuracy of the model's prediction of plastic strain and stress in a cyclic test is to compare the values of peak stress and accumulated plastic strain at the tip of each loop with measurements, as shown in Figure 5.18(a). At room temperature, the tensile peak stress predictions agree reasonably well with the experimental results (showing a difference of up to 20MPa) and the experimental compression peak stress is under predicted by up to 30MPa see Figure 5.18(a). At high temperature the predicted stresses agree reasonable well with the experimental results for the first three cycles performed at a strain rate of 10^{-4}, see Figure 5.18 (b), but with increasing cycles the peak stresses results are significantly under predicted. The measured peak stresses are considerably affected by decreasing in strain rate from 10^{-4} to 10^{-5} which is not accounted for in the model. At slow strain rates (i.e. 10^{-5}), the dynamic strain ageing affect is significantly enhanced with increasing cyclic deformation, as described earlier. Similarly the peak stress vs. accumulated plastic strain trajectories for asymmetric stress-strain cycles at both room and high temperature are presented in Figure 5.20. Interestingly the Muransky [22,57] model gives a reasonably good estimate of the peak stress vs. accumulated plastic strain trajectories for asymmetric stress-strain cycles at both room and high temperature. But it

should be noted that, the peak stress prediction was affected by decreasing the strain rate from 10^{-4} to 10^{-5} at high temperature due to dynamic strain ageing, as seen in Figure 5.20(b).

Muransky [22,57] mixed hardening model was designed to predict symmetric cyclic stress-strain behaviour accurately. But the model used data from different materials using a variety of strain rates (see Table 5.3). This might explain why the model shows poor correlation with the present symmetric cyclic tests done at 550°C. The results presented in Figure 5.17(b) and Figure 5.18(b) call into question the robustness of the validation for residual stress simulations [21,22,233].

In conclusion, the Chaboche model parameters of Muransky [22,57] for 316L(N) stainless steel poorly represent the high temperature symmetric cyclic hardening behaviour. However, the published parameters represent well the asymmetric cyclic loading, which is the type of deformation that occurs in parent or heat affected zone material during the welding process. This may be due to, the parameter used in the simulation are derived from higher strain amplitude than asymmetric cyclic loading. As result of this, the Chaboche model is capable of predicting the low strain hardening of the material.

5.6 Conclusions

The cyclic hardening of NeT TG4 parent material type 316L(N) stainless steel has been examined using constant strain range symmetric and asymmetric cyclic tests, at room temperatures and 550°C, and at different strain rates. The cyclic hardening of the austenitic stainless steel material varied significantly depending on strain range and strain rate. The material that cyclically deformed during asymmetric cyclic loading, sustained very less plasticity than the material deformed symmetrically because of the smaller strain range. 316L(N) material at room temperature underwent more strain hardening at a faster strain rate. However, at high temperatures, due to dynamic strain ageing, the material underwent

higher strain hardening at a slower strain rate. At 550°C, a published Chaboche hardening model for 316L(N) stainless steel predicted less strain hardening during symmetric deformation, than occurred in the experimental results. However, at both room and high temperatures, the Chaboche model predicted reasonably well the maximum strain hardening during asymmetric deformation, which is the type of deformation that occurs in the base metal surrounding a weld deposit.

5.7 Tables

Table 5.1 List of cyclic loading tests on type 316L (N) stainless steel

S.No	Cycle Type	Strain Range	Strain Rate	Temperature	Number of Cycles
1	Symmetric	±1.25%	4×10^{-4}/sec	25°C	6
2	Symmetric	±1.0%	4×10^{-5}/sec	25°C	6
3	Asymmetric	-1.0% - 0.02%	4×10^{-4}/sec	25°C	12
4	Asymmetric	-1.0% - 0.02%	4×10^{-5}/sec	25°C	7
4	Asymmetric	-1.0% - 0.02%	4×10^{-4}/sec	25°C	12
5	Symmetric	±1.25%	4×10^{-4}/sec	550°C	12
6	Symmetric	±1.25%	4×10^{-5}/sec	550°C	12
7	Asymmetric	-1.25% - 0.02%	4×10^{-4}/sec	550°C	12
8	Asymmetric	-1.0% - 0.02%	4×10^{-5}/sec	550°C	12
9	Asymmetric	-1.25% - 0.02%	4×10^{-5}/sec	550°C	12

Table 5.2 Chaboche mixed hardening model parameters for type 316L (N) stainless steel to Muransky [22]

Temperature	Yield Stress at zero strain	C_1 (MPa)	γ_1	C_2 (MPa)	γ_2	$Q\infty$	b
20°C	125.60	156435	1410.85	6134	47.19	153.6	6.9
550°C	90.90	64341	1410.8	5227	47.19	150.6	6.9

Table 5.3 List of cyclic test performed by NeT TG4 consortium [21,57,233,236]

S.No	Group	Test	Material	Test Control	Test Rate	Parameters derived
1	Warsaw University of Technology (WUT)	2-Tensile	316H base metal 316L weld metal	Extension control	1mm/min	Non-linear kinematic
2	AMEC Foster Wheeler Ltd	2-Tensile	316L base metal	Strain Control	4×10^{-4}/sec	Non-linear isotropic
3	VTT Manufacturing Technology	Cyclic	316L,316H	Strain Control	4×10^{-5}/sec	Mixed hardening
4	Serco-UK	Cyclic	316L,316H	Strain Control	4×10^{-4}/sec	Mixed hardening
5	Australian Nuclear Science and Technology Organisation (ANSTO)	Cyclic	316L,316H	Strain Control	4×10^{-5}/sec	Mixed hardening
6	National Research Institute for Materials	Cyclic	316L,316H	Strain Control	4×10^{-5}/sec	Mixed hardening

5.8 Figures

Figure 5.1 Eight strain gauges fitted to a samples

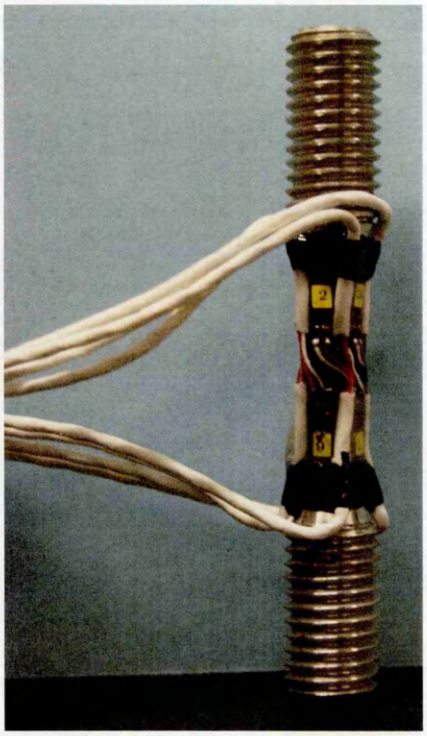

Figure 5.2 N-Type thermocouples fixed on both ends of gauge volume with the help of clamps

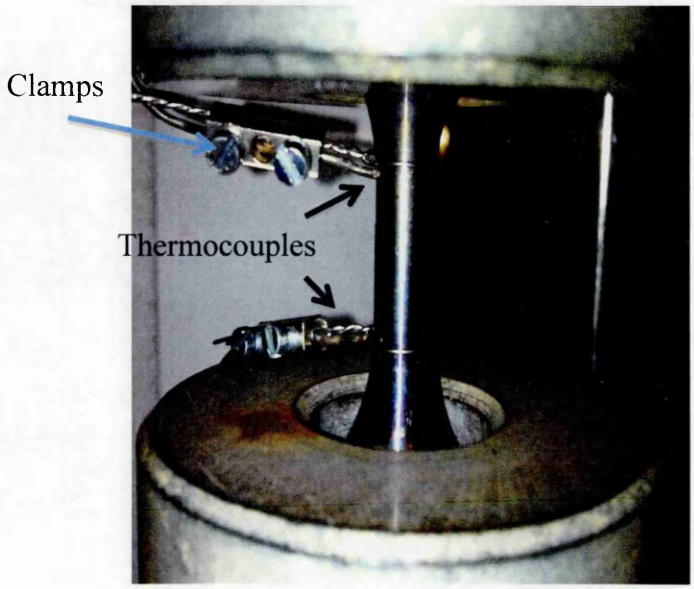

Figure 5.3 Symmetric cyclic loading (a) stress vs strain loops (b) strain vs time

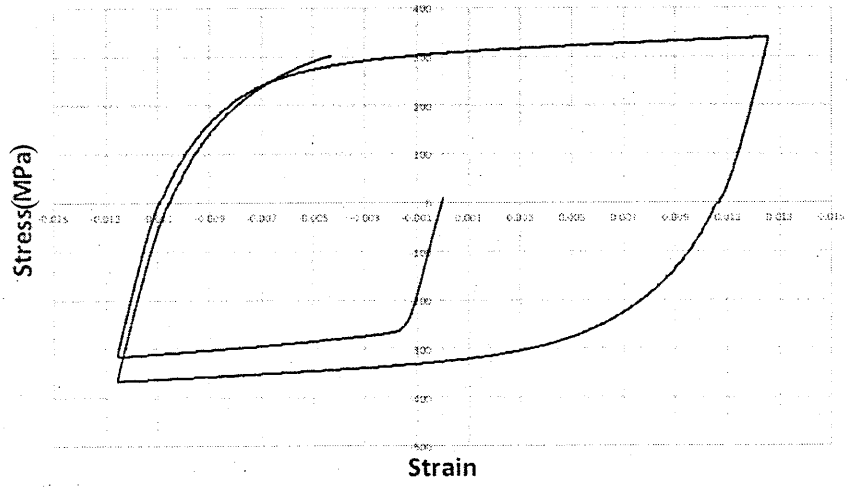

(a)

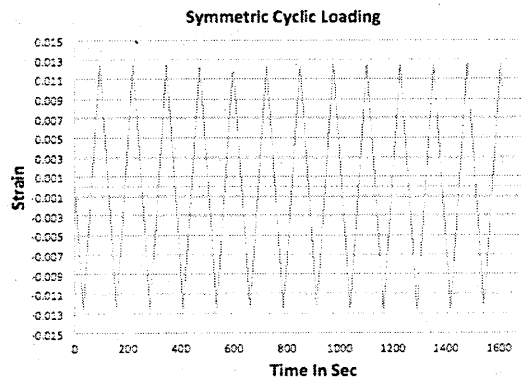

(b)

Figure 5.4 Asymmetric cyclic loading with the first cycle loading in compression (a) stress vs strain loops (b) strain vs time

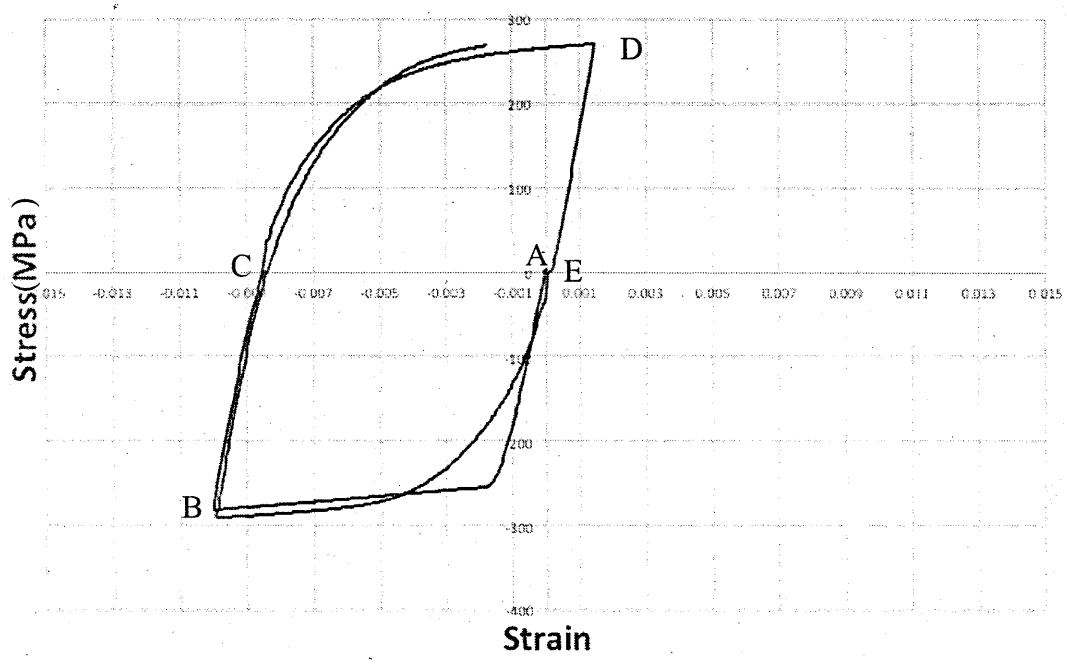

(a)

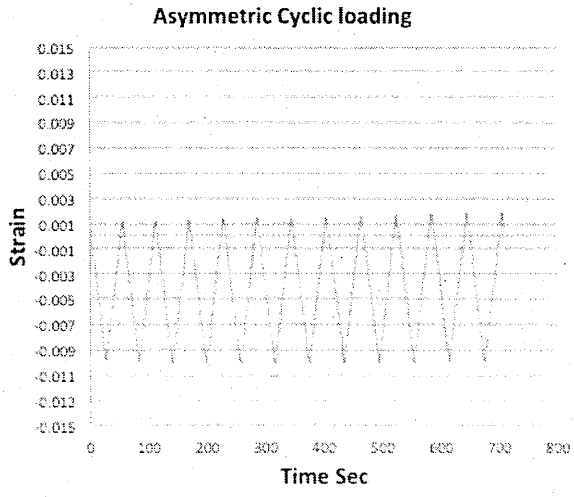

(b)

Figure 5.5 FE weld stress vs strain predictions near HAZ [63]

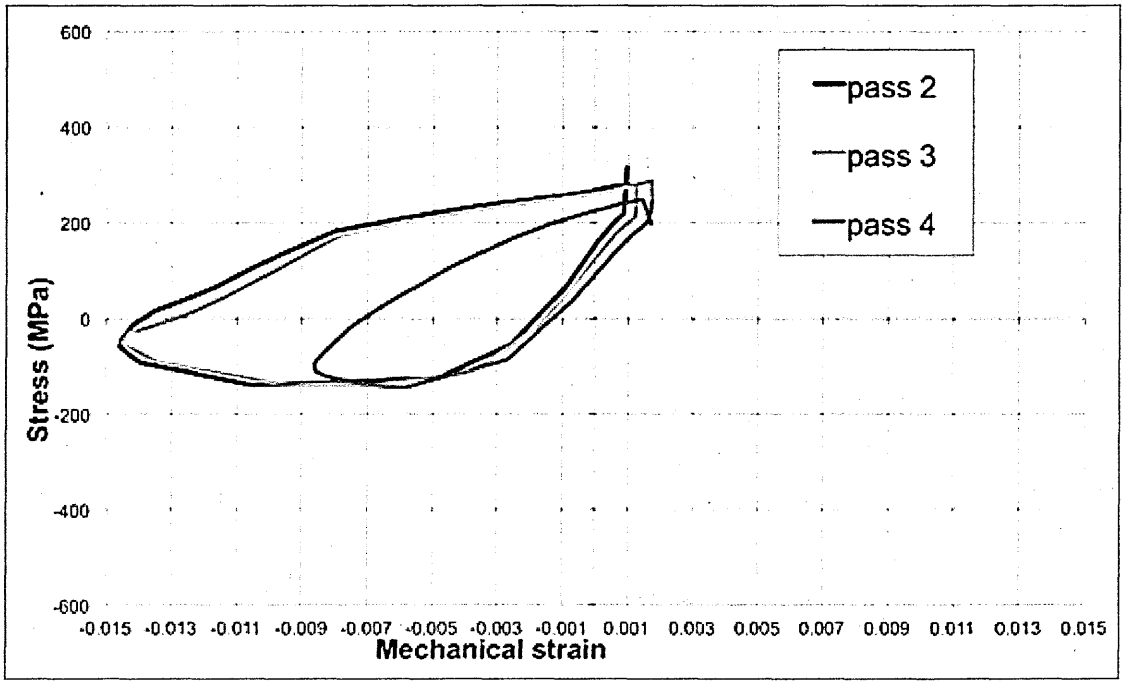

Figure 5.6 Room temperature symmetric cyclic loading test results for a strain range of ±1.25% and strain rate 4×10^{-4}/sec compared with a strain range of ±1.0% at strain rate 4×10^{-5}/sec

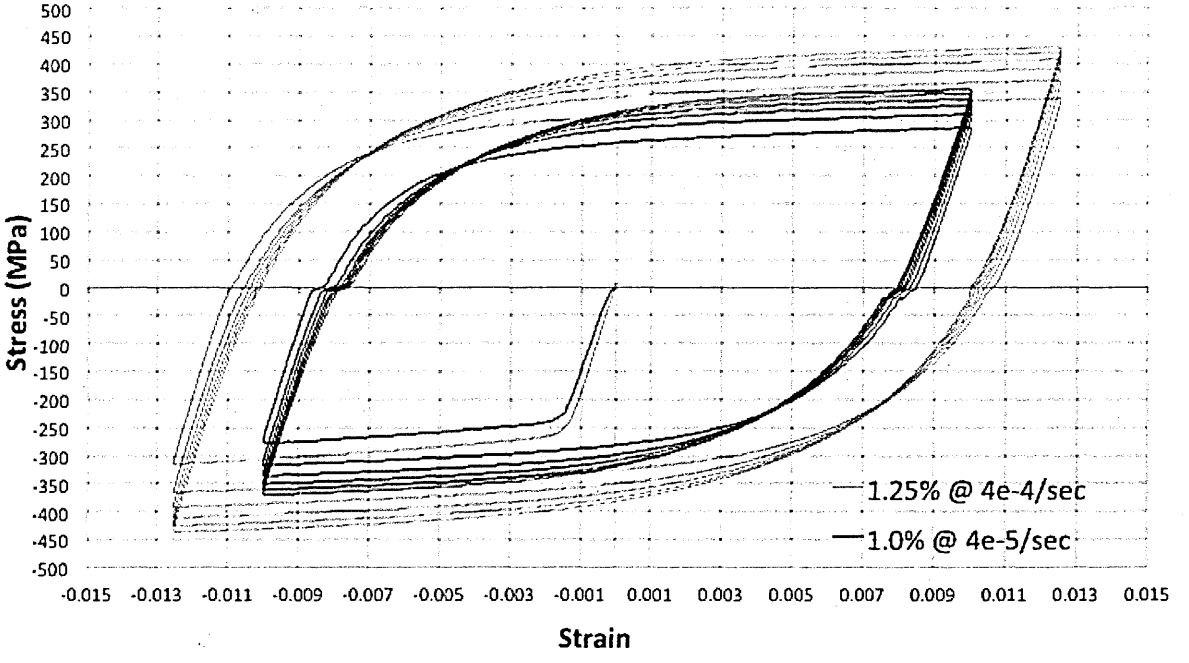

Figure 5.7 Room and high temperature (550°C) symmetric cyclic loading result for a strain range ±1.25% at strain rate 4×10^{-4}/sec

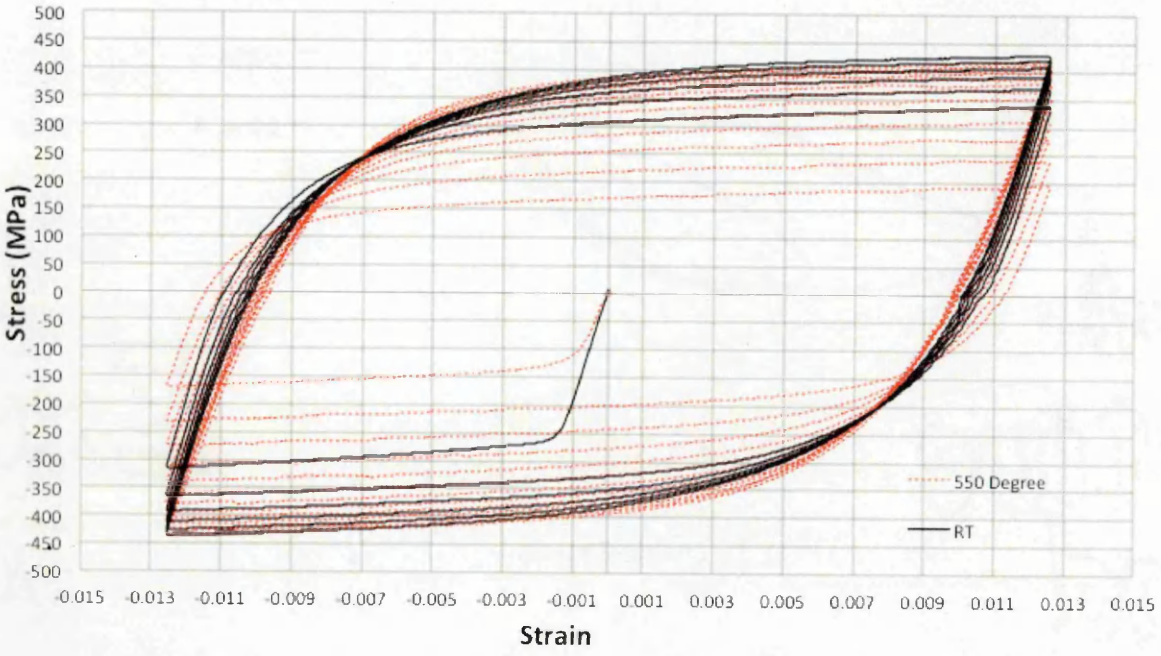

Figure 5.8 High temperature (550°C) symmetric cyclic loading results for a strain range ±1.25% at strain rate of 4×10^{-5}/sec

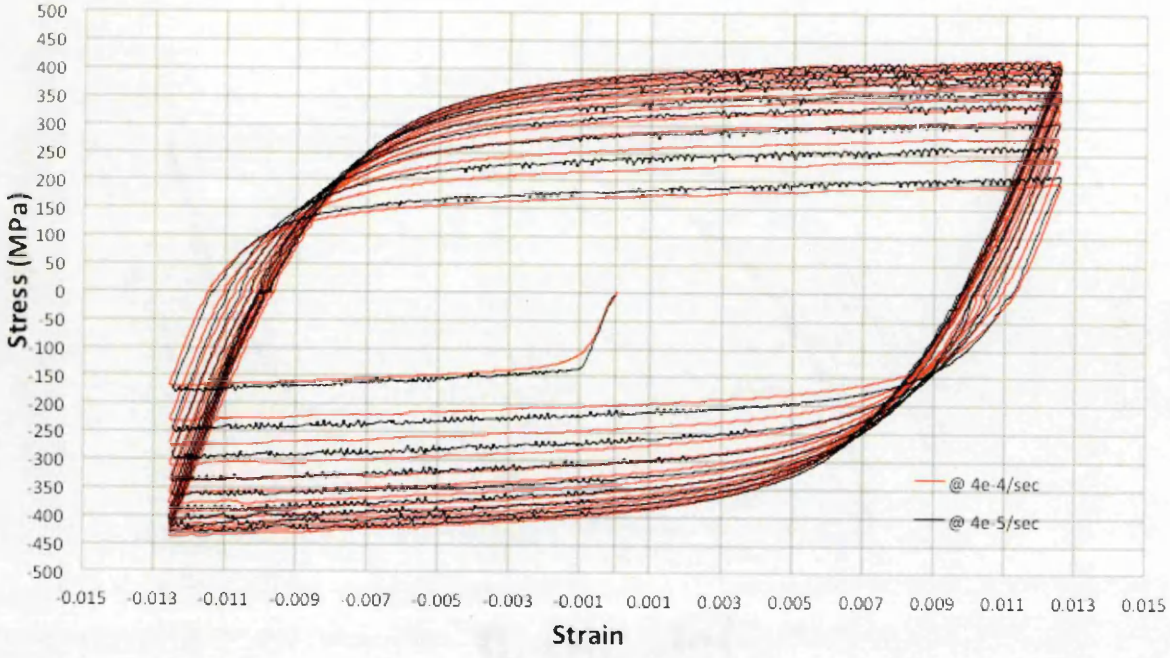

Figure 5.9 Comparison of asymmetric and symmetric cyclic loading test results at room temperature for (a) strain ranges -1.25% to 0.2% and ±1.25% at a strain rate 4×10^{-4}/sec (b) strain range of -1.0% to 0.25 and 1.0% at a strain rate 4×10^{-5}/sec

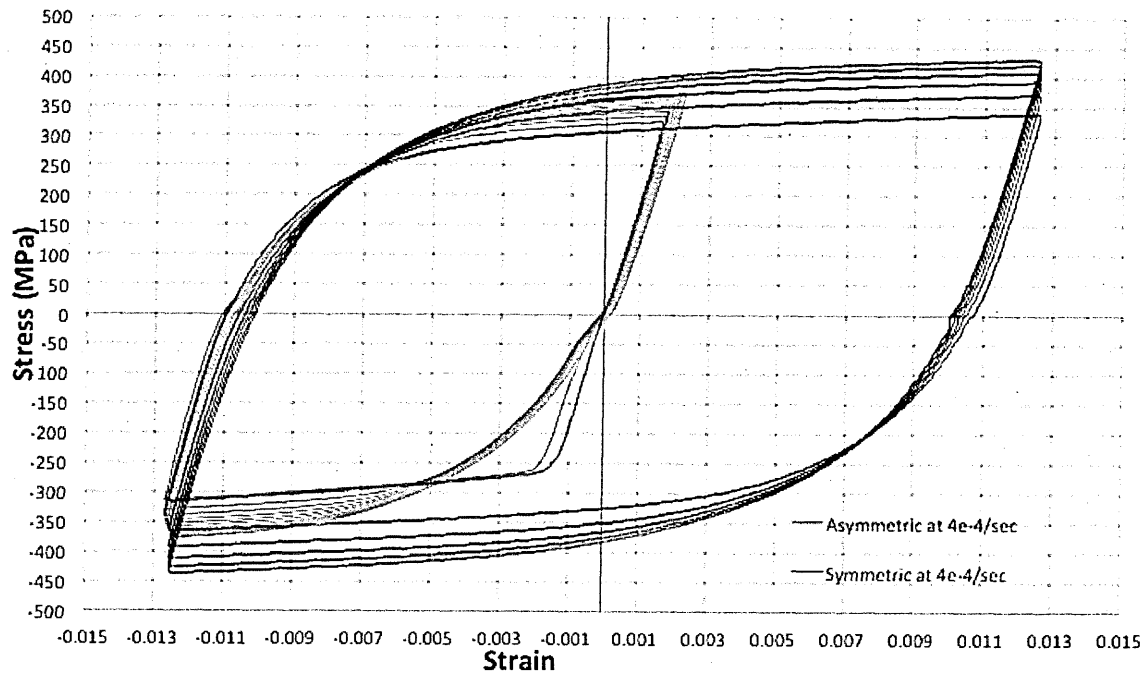

(a)

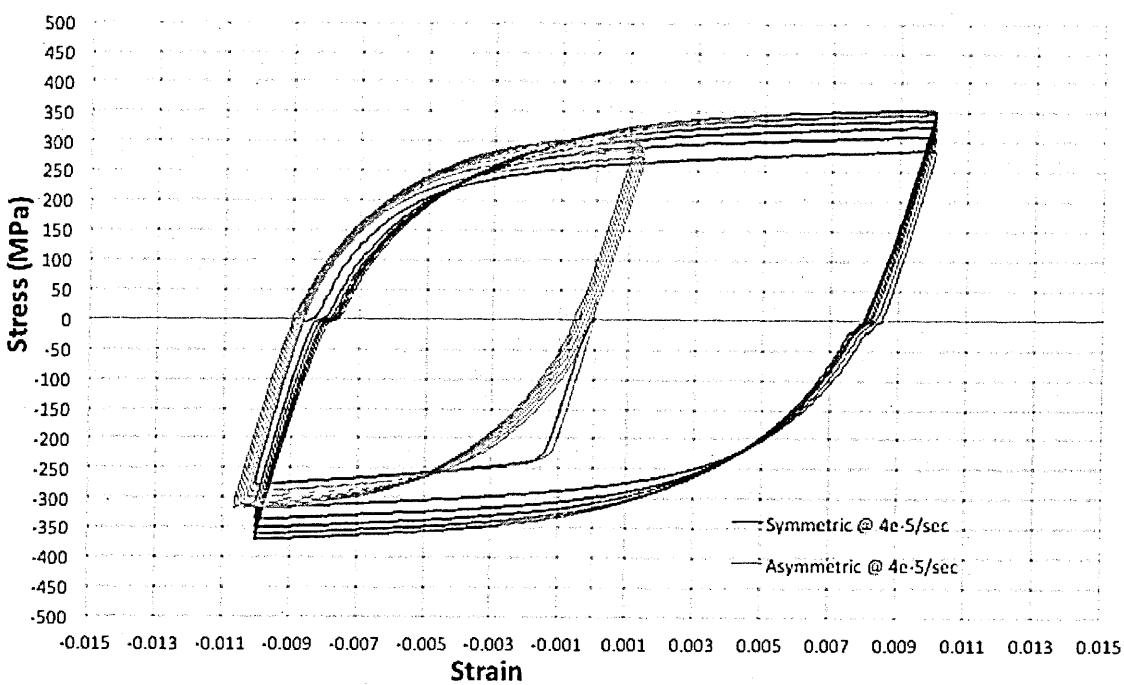

(b)

Figure 5.10 Comparison of asymmetric and symmetric cyclic loading test results at 550°C for a strain range of -1.25% to 0.2% ; 1.25% at a strain rate of 4×10^{-4}/sec.

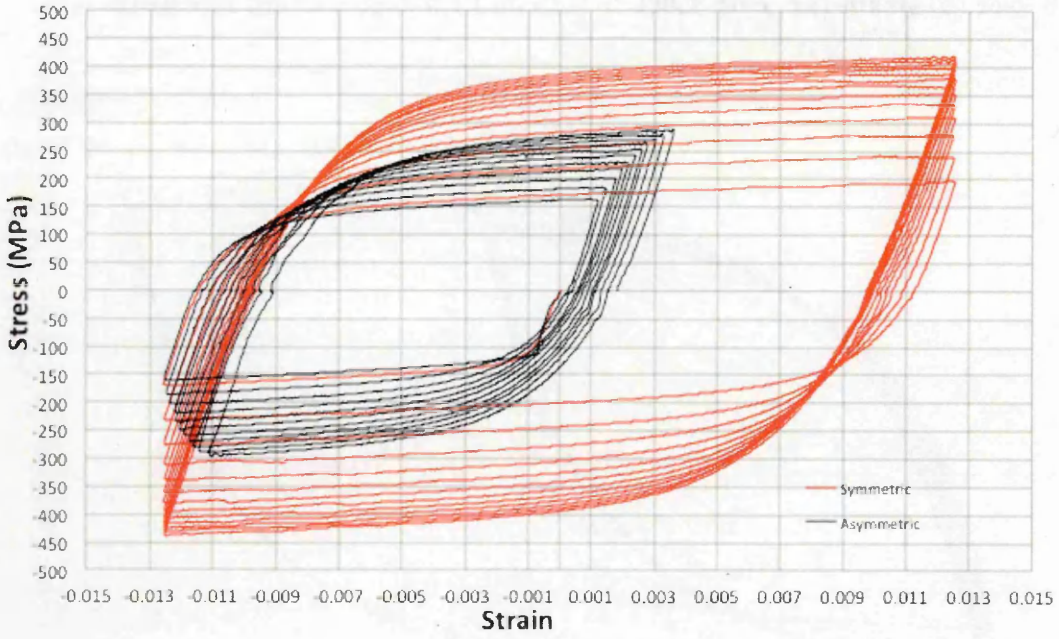

Figure 5.11 Asymmetric cyclic loading strain range effect in room and high temperature test: (a) 25C strain range -1.25% to 0.02% vs -1.0% to 0.02% at4×10^{-4}/sec (b) 550°C strain range -1.25% to 0.02% vs -1.0% to 0.02% at 4×10^{-4}/sec

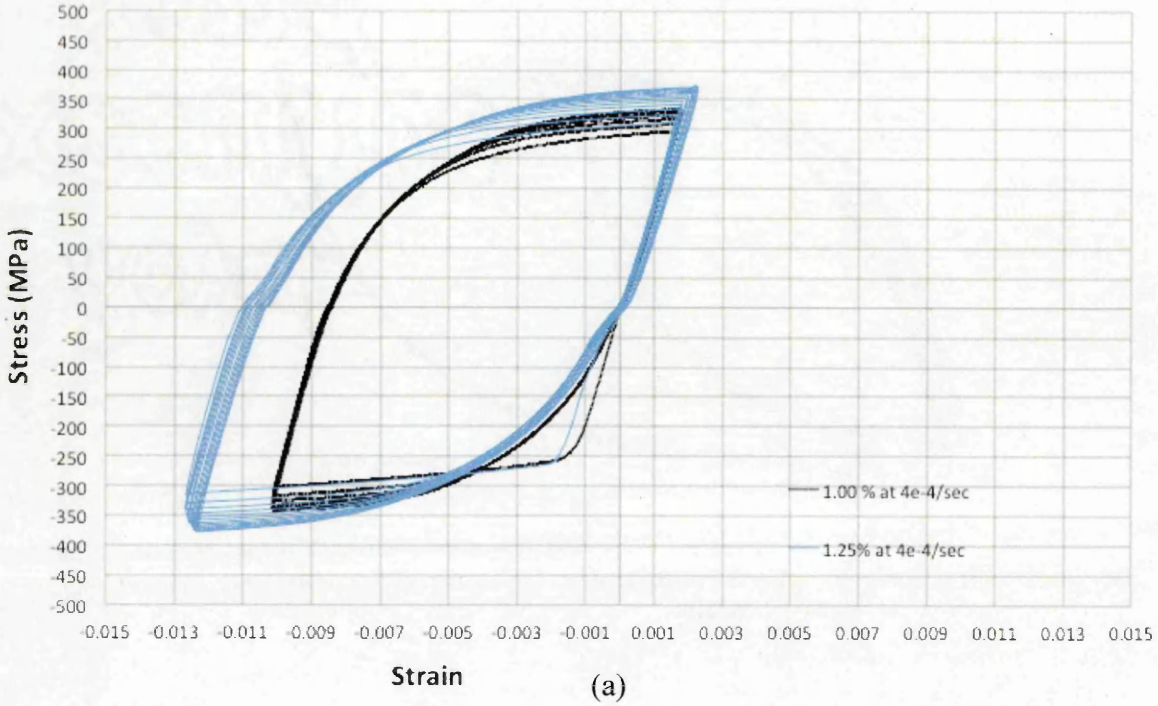

(a)

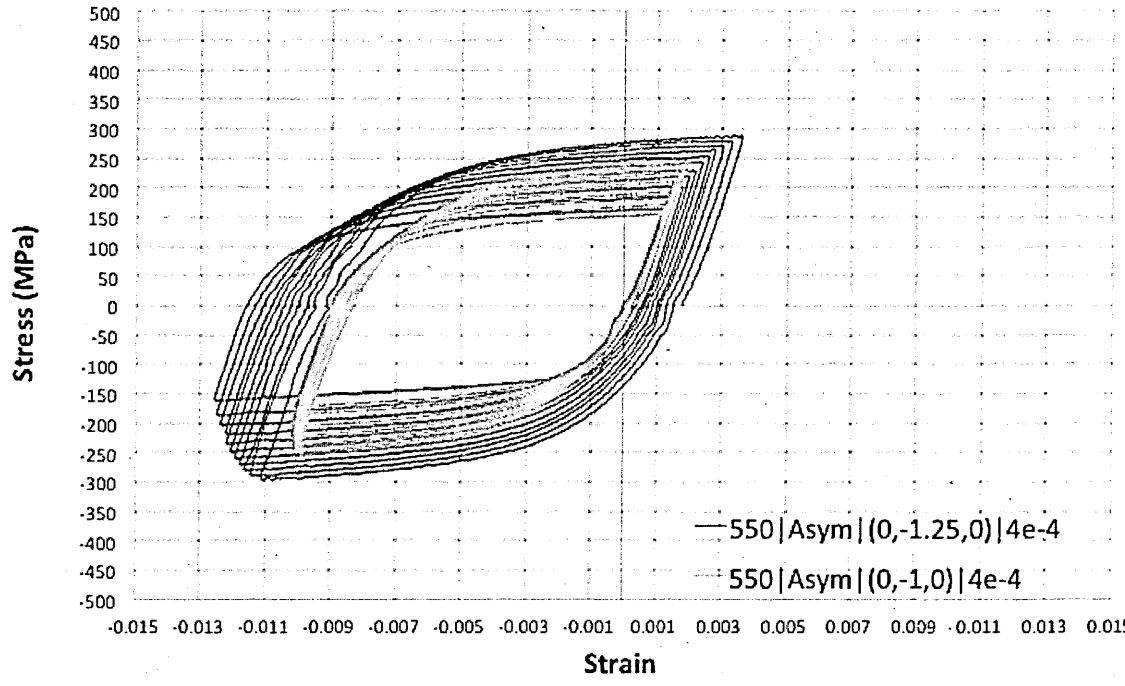

(b)

Figure 5.12 Asymmetric cyclic loading strain rate effect in room and high temperature test: (a) 25C strain rate -1.0% to 0.02% at 4×10-4/sec vs 4×10-5/sec (b) 550°C strain range -1.25% to 0.02% at 4×10-4/sec vs 4×10-5/sec

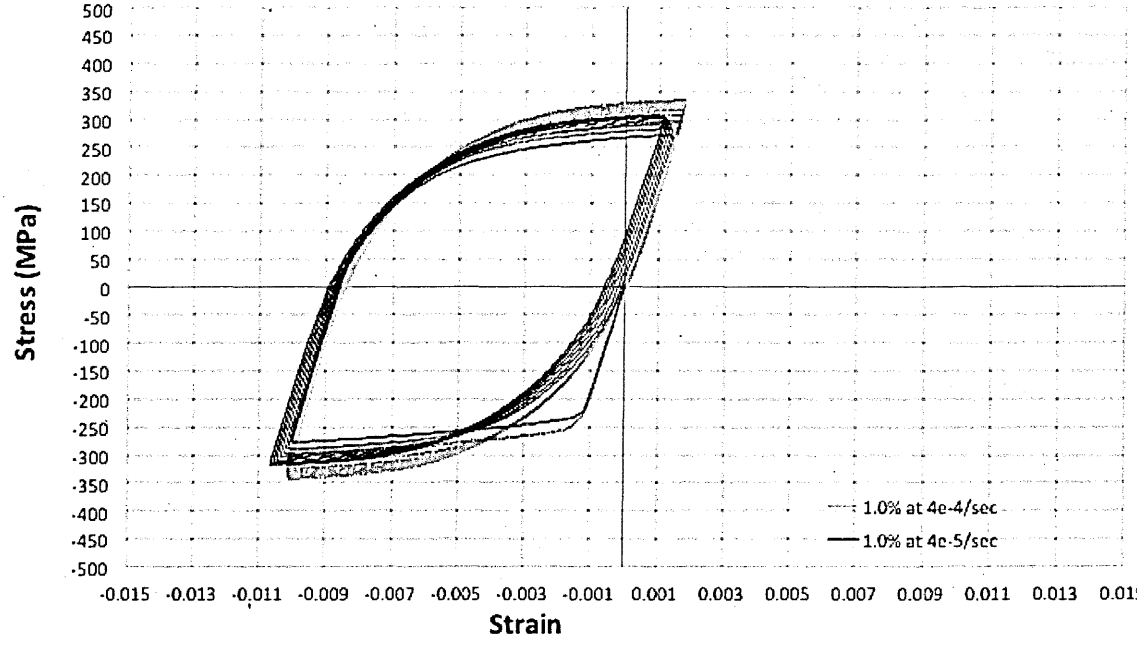

(a)

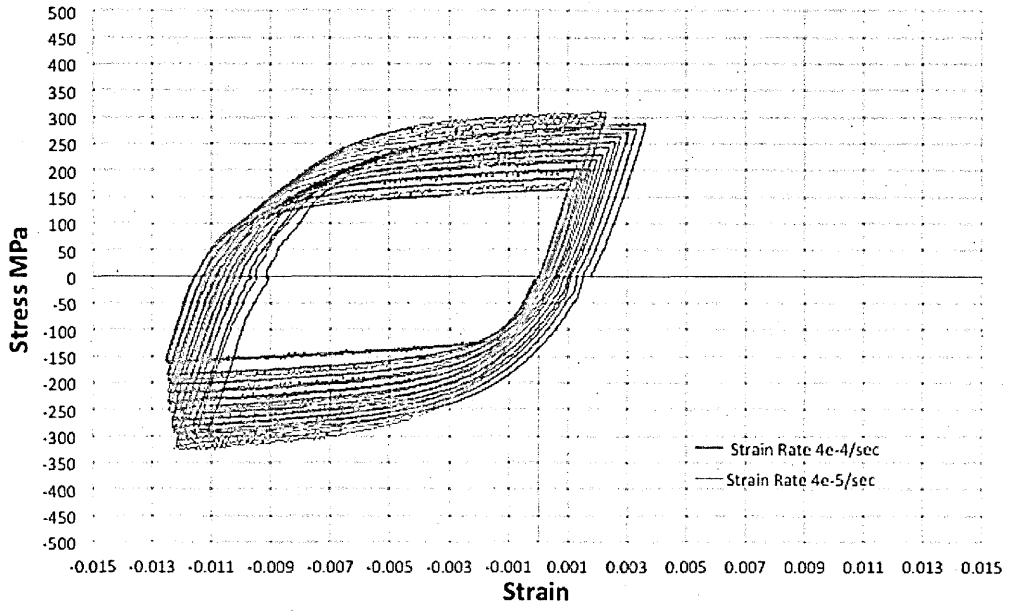

(b)

Figure 5.13 Room and high temperature asymmetric cyclic loading (a) strain range -1.25% to 0.02% at strain rate 4×10^{-4}/sec and (b) -1.0% to 0.025% at strain rate 4×10^{-4}/sec

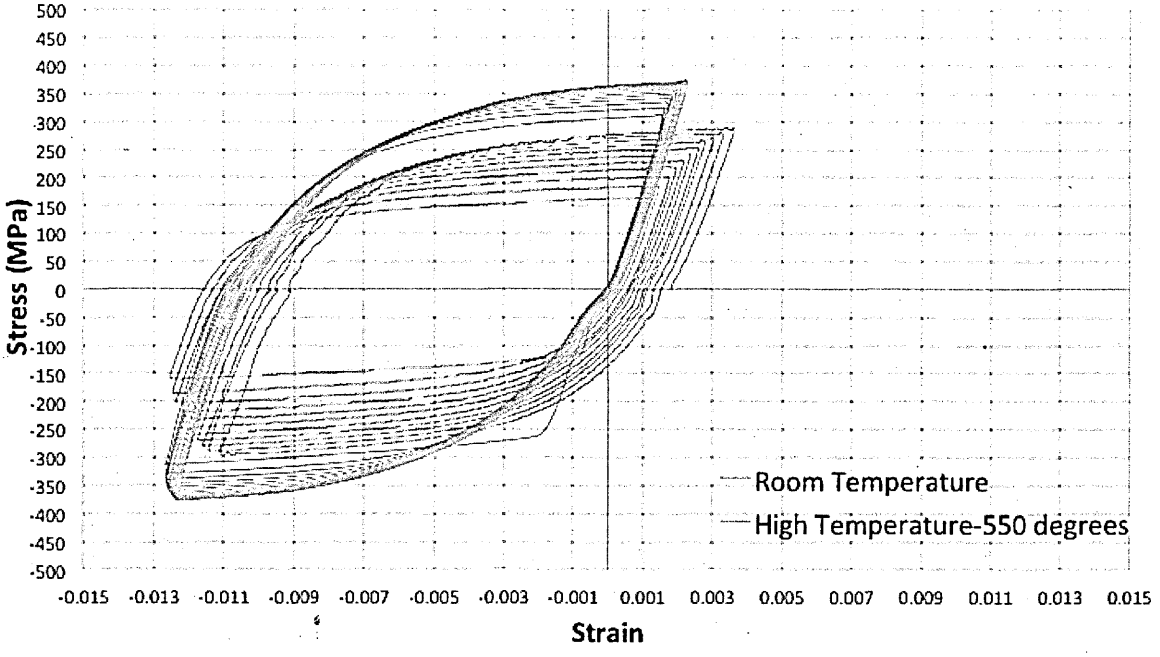

(a)

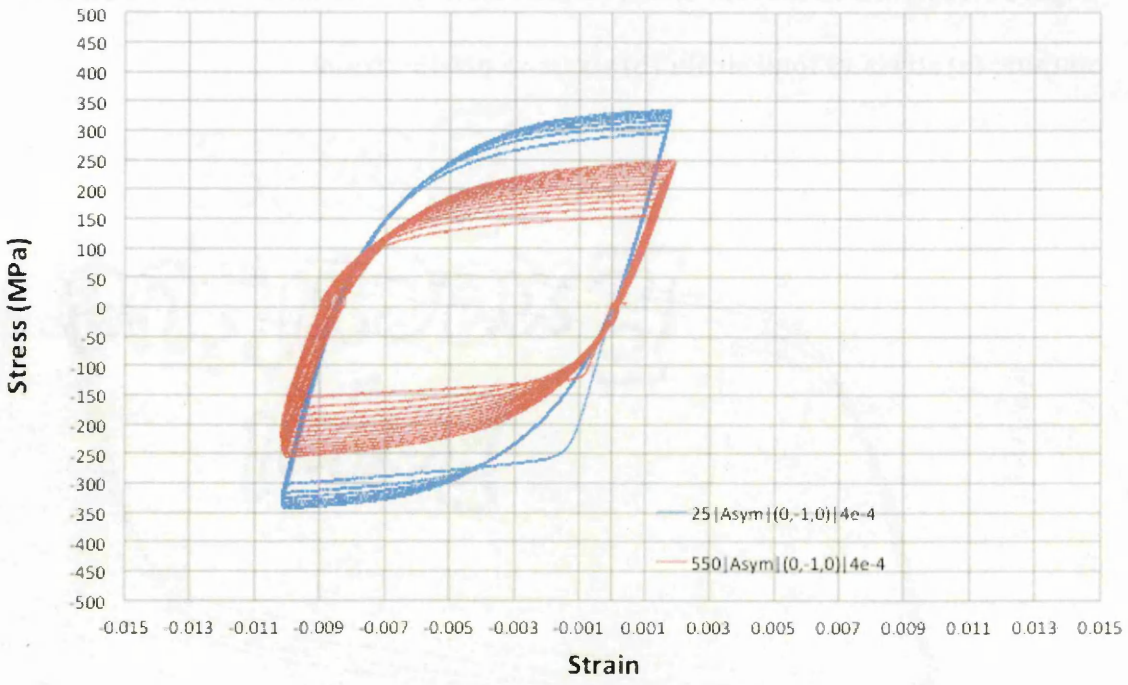

(b)

Figure 5.14 Axisymmetric finite element model used for symmetric and asymmetric cyclic stress-strain simulations

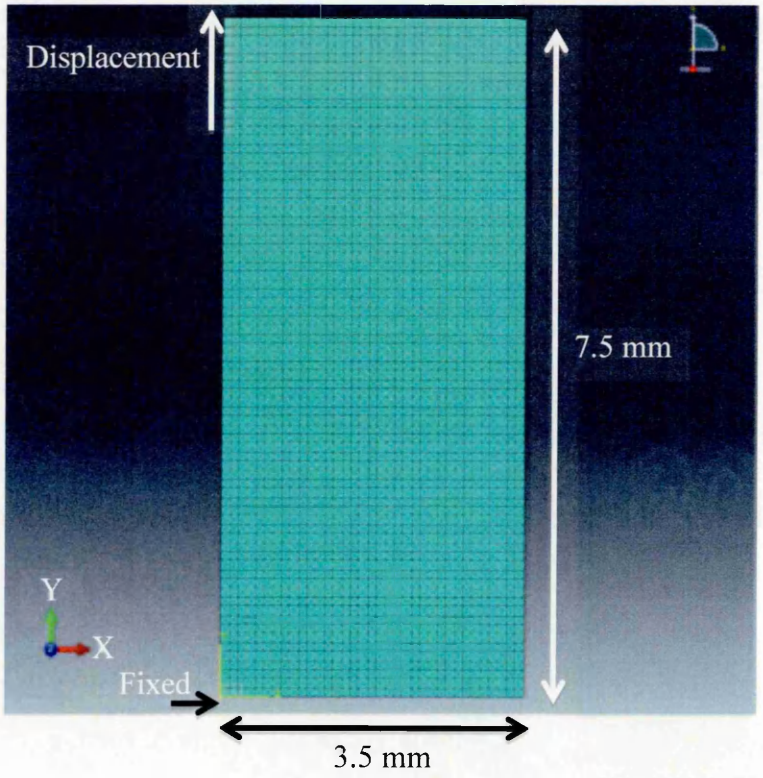

Figure 5.15 Symmetric cyclic stress-strain results of Muransky [22] reproduced by the author: (a) stress vs total strain (b) stress vs plastic strain

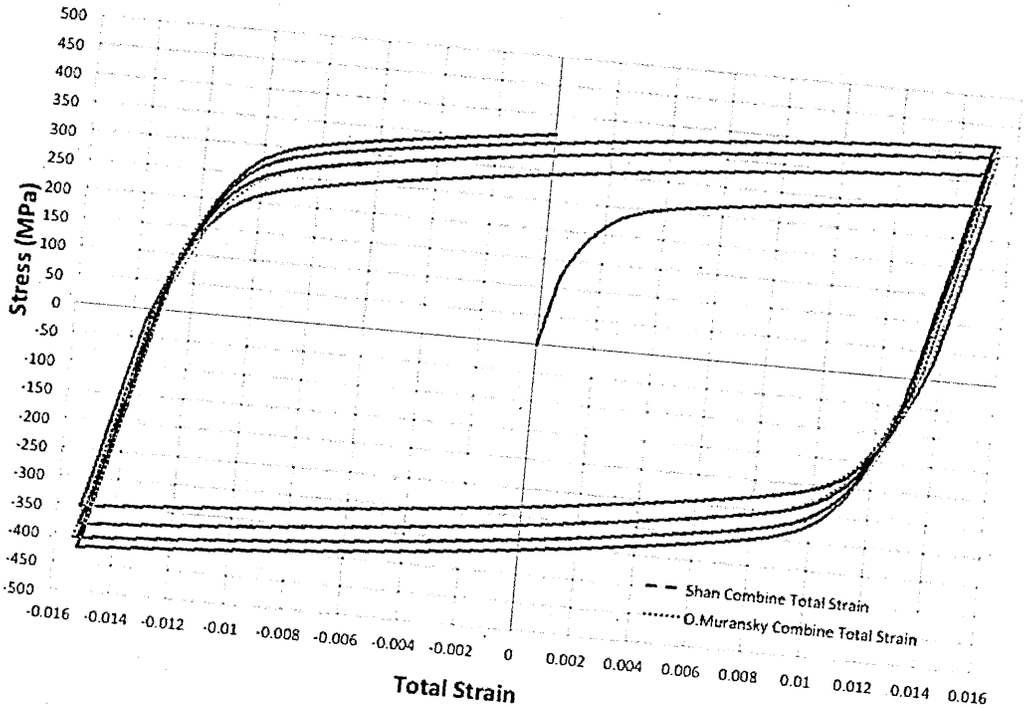

(a)

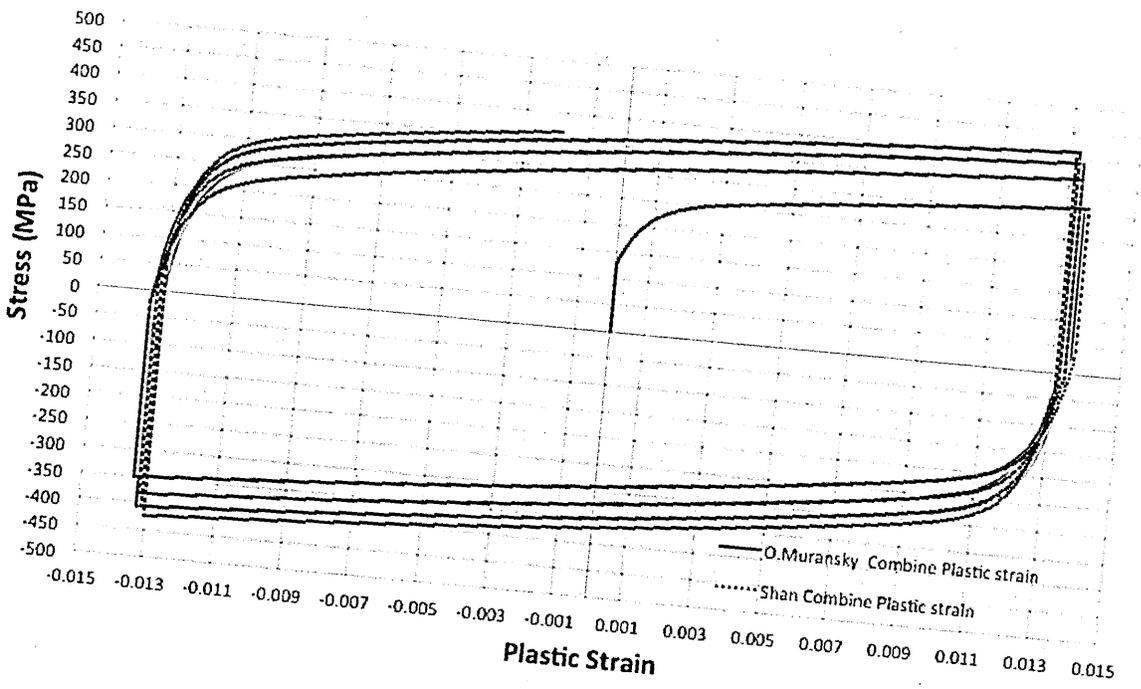

(b)

Figure 5.16 Comparison of mixed hardening predictions based upon Muransky [22] for symmetric and asymmetric cycles at (a) room temperature and (b) high temperature (550°C)

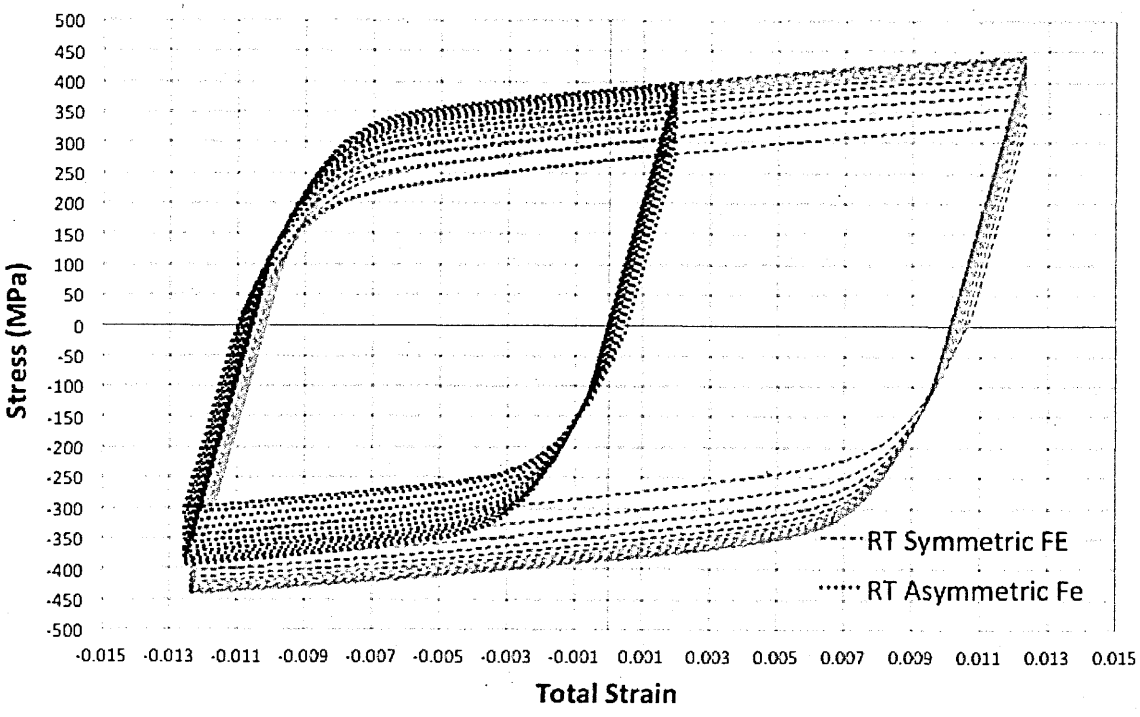

(a)

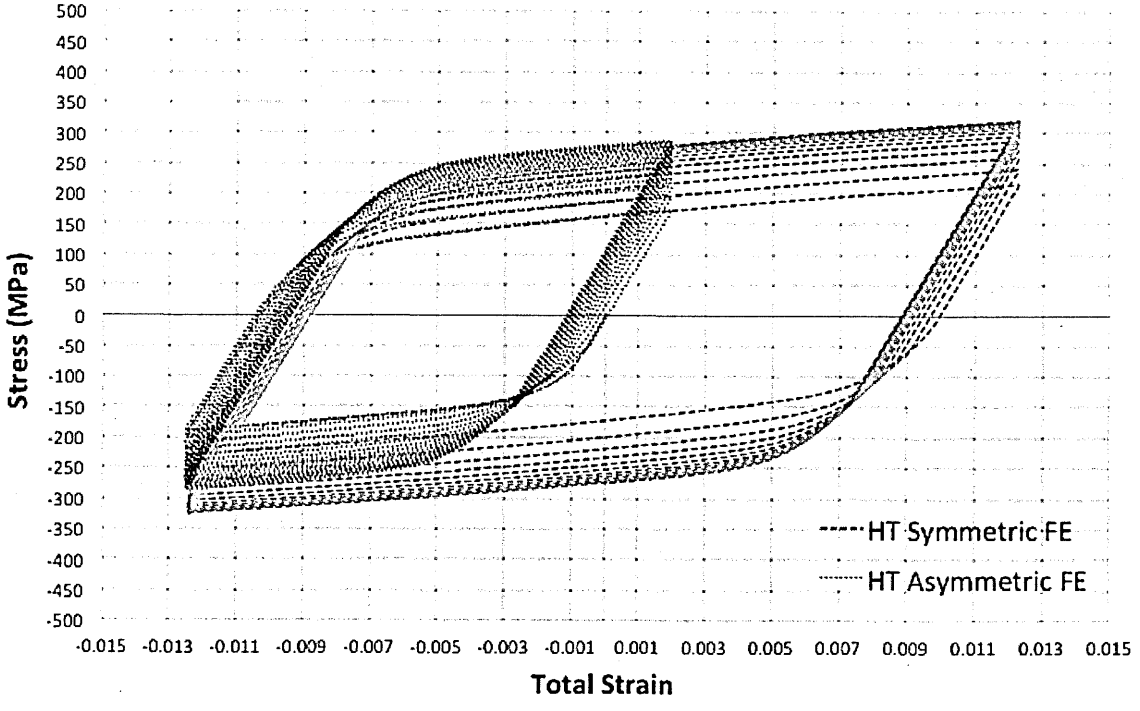

(b)

Figure 5.17 Comparison symmetric cyclic loading prediction vs experimental results, strain range 1.25% (a) room temperature (RT) and (b) high temperature (HT)

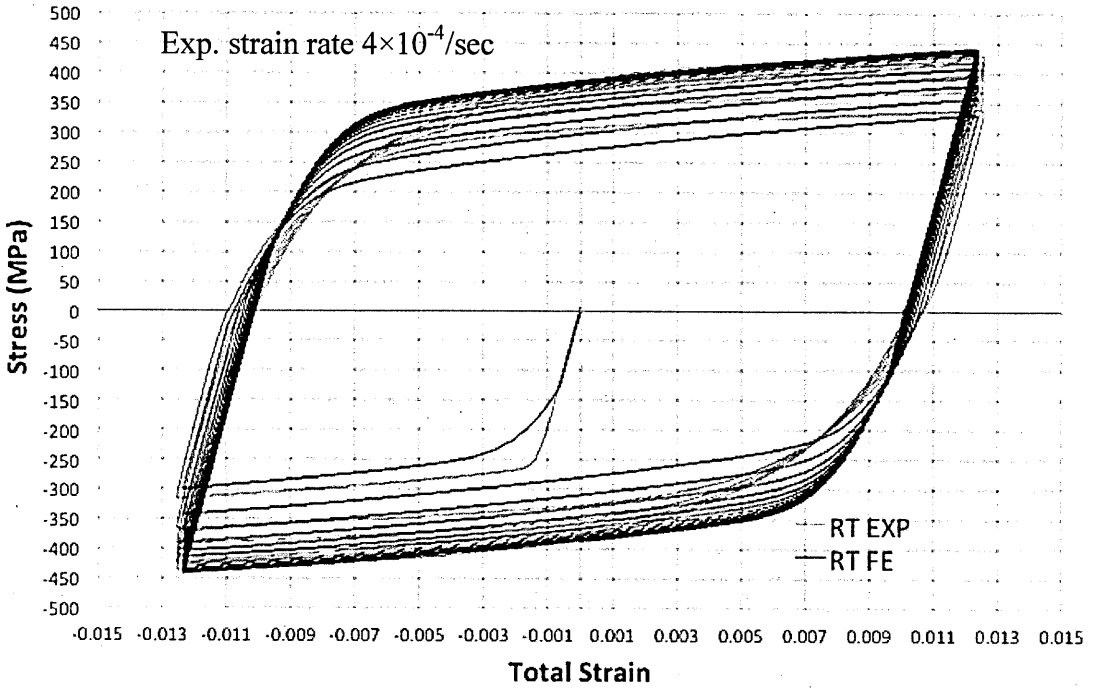

(a)

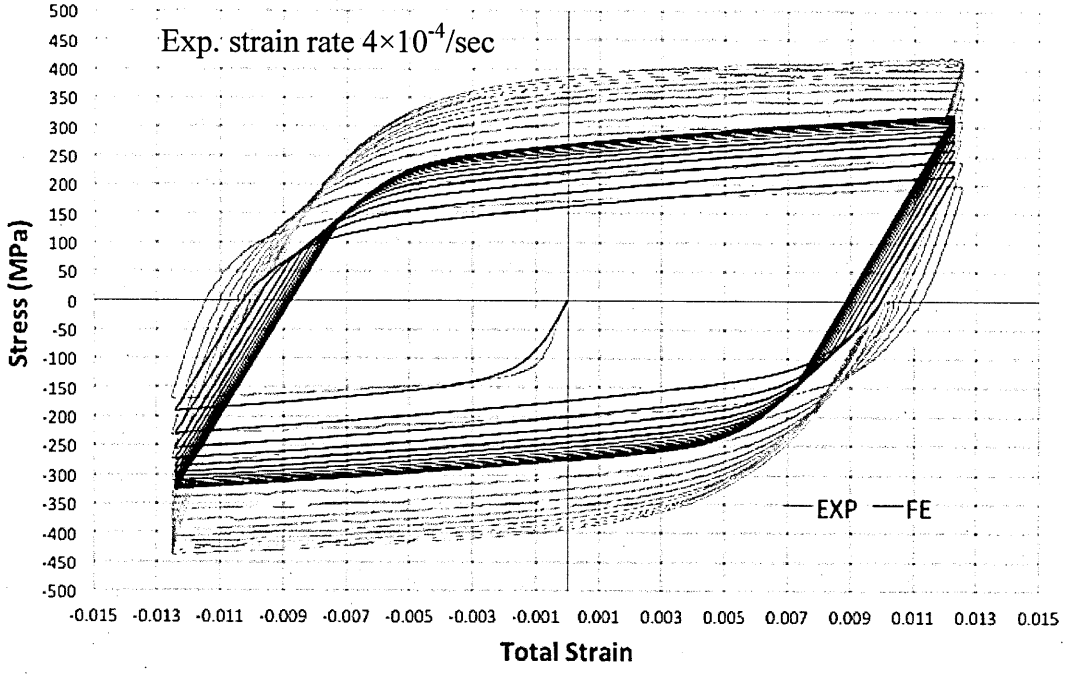

(b)

Figure 5.18 Comparison of predicted versus measured strain hardening for (a) room temperature symmetric peak cyclic stress vs cumulative plastic strain (b) high temperature symmetric peak cyclic stress vs cumulative plastic strain

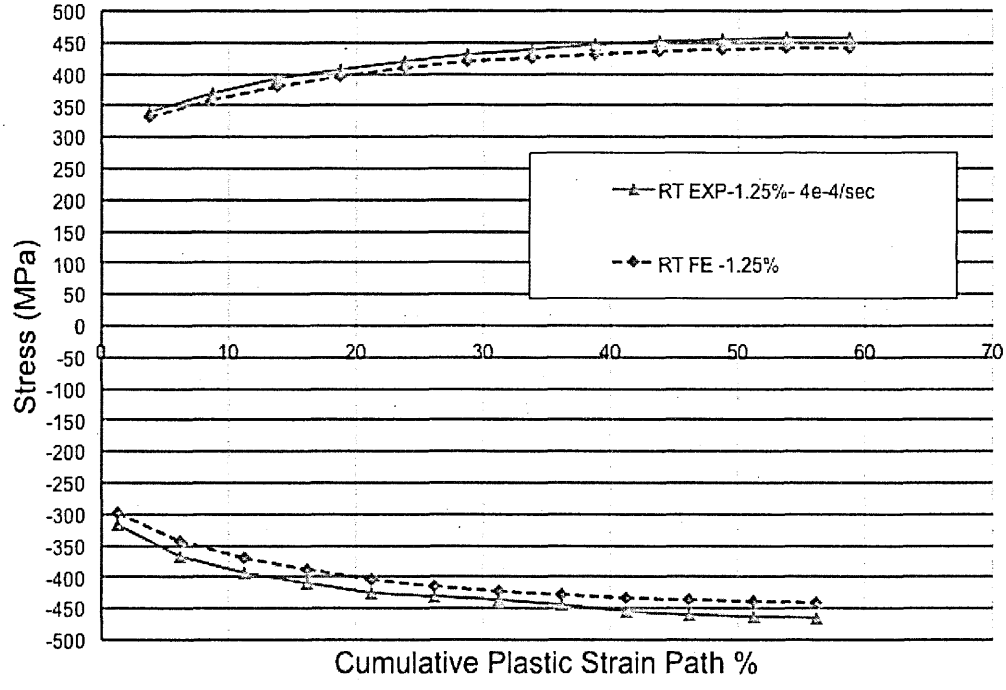

(a)

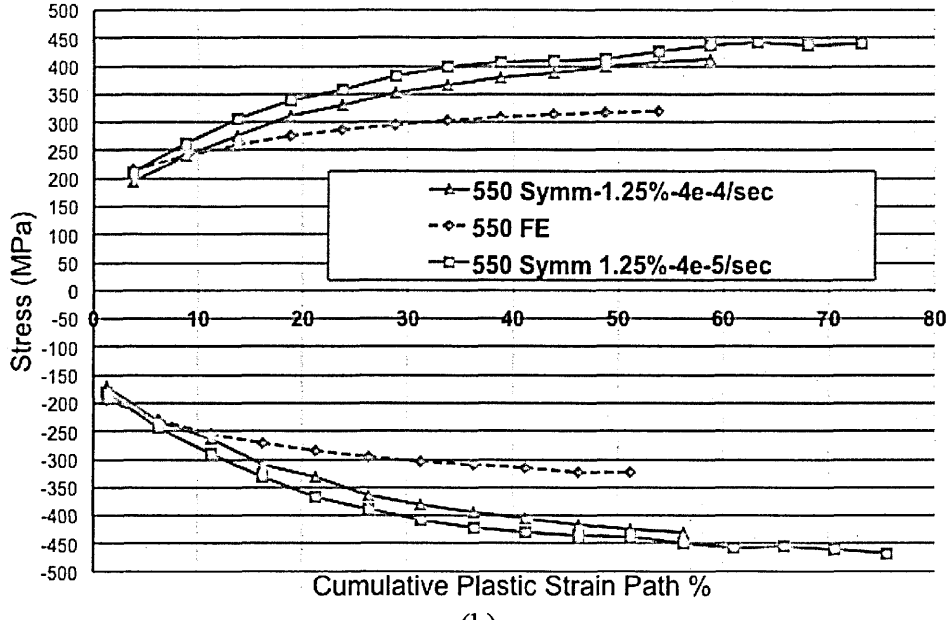

(b)

Figure 5.19 Comparison asymmetric FE results vs experimental cyclic loading results strain range 1.25% (a) room temperature (RT) and (b) high temperature (HT)

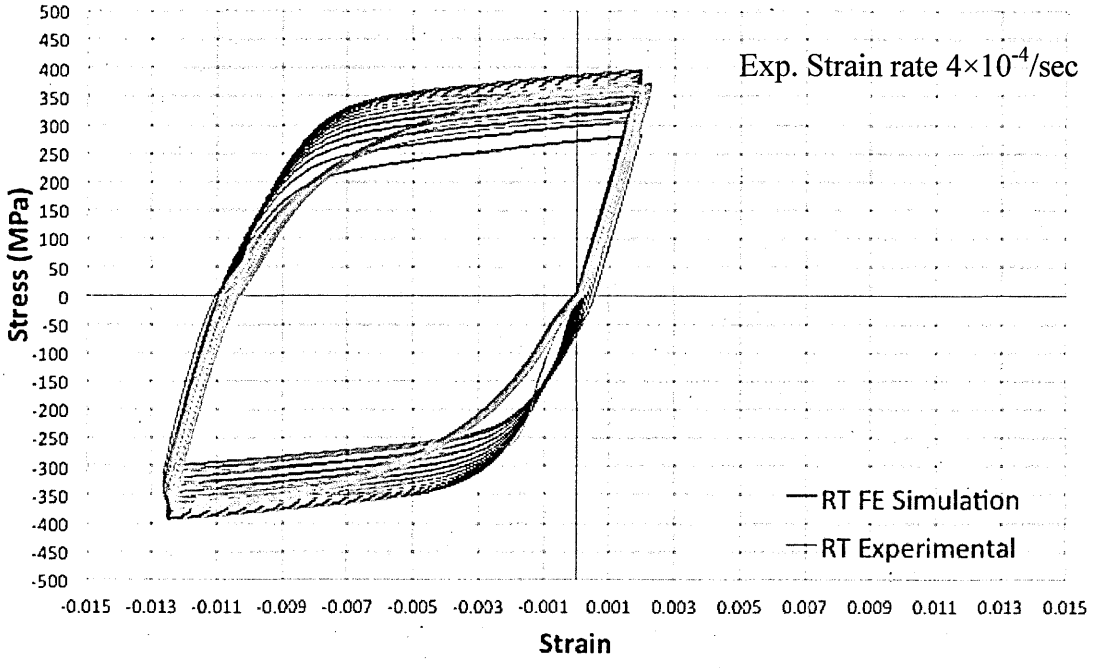

(a)

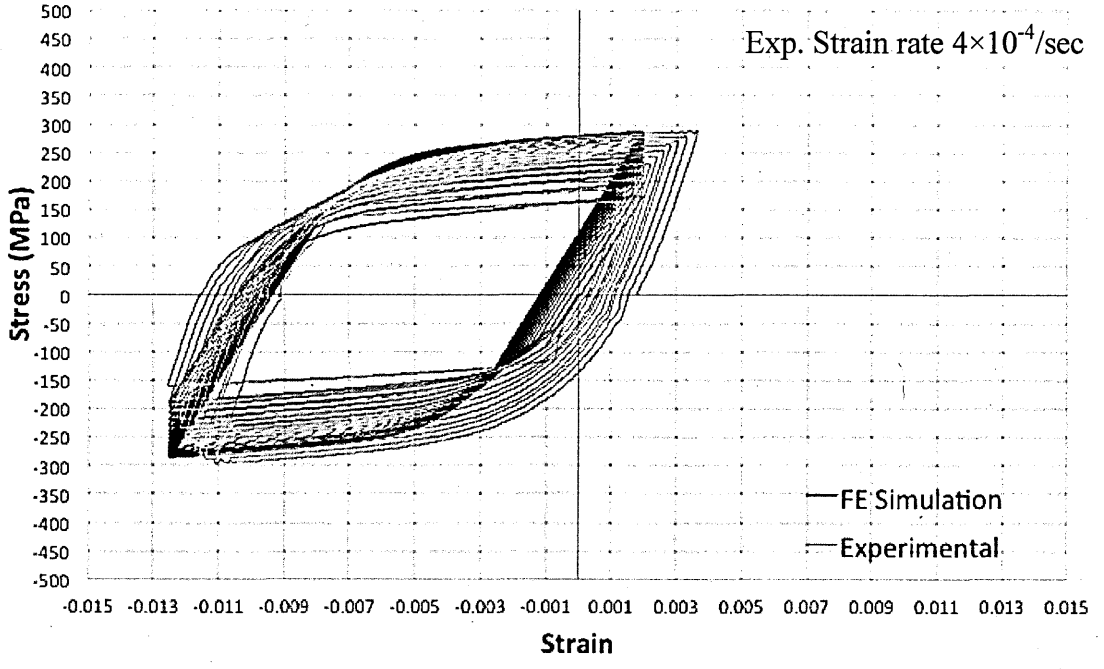

(b)

Figure 5.20 Comparison of predicted versus measured strain hardening for (a) room temperature asymmetric peak cyclic stress vs cumulative plastic strain (b) high temperature asymmetric peak cyclic stress vs cumulative plastic strain

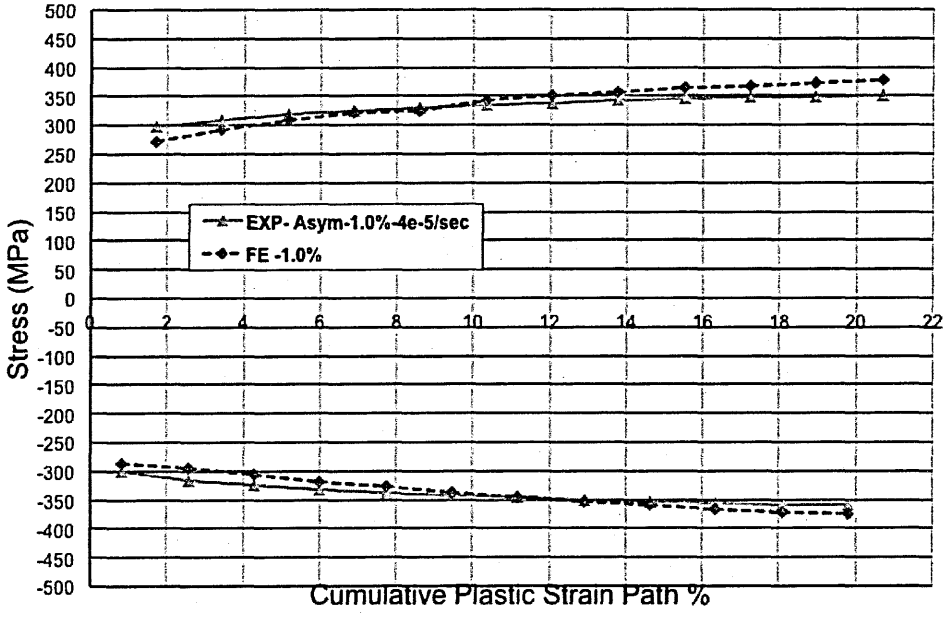

(a)

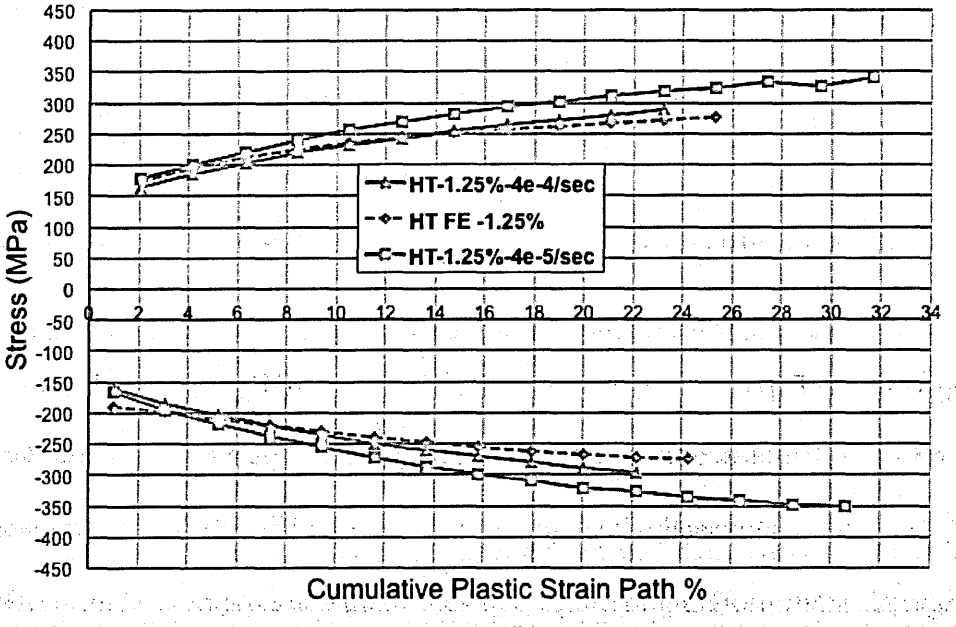

(b)

CHAPTER 6. WELDMENT PLASTIC STRAIN CHARACTERISATION

6.1 Introduction

Welding introduces plastic strain into the base materials being joined owing to material yielding associated with differential thermal expansion/contraction. It is important to quantify the plastic strain accumulated, since it can increase the susceptibility of austenitic stainless steel to stress corrosion cracking [10,30,193,198]. Electron backscatter diffraction (EBSD) has previously been used to map the distribution of plastic strain on a microscopic scale [237–239]. The influence of the welding parameters, welding techniques and stress-controlled cyclic loading, on microstructure and stress corrosion cracking, has been well analysed by others using EBSD [49,170,240–244]. However, to date, the accumulated plastic strain due to each weld pass deposited has not been quantified. Moreover, little experimental research has been done where EBSD measures of plastic strain have been compared with hardness testing and finite element analysis.

The influence of strain-controlled, or stress-controlled, symmetric cyclic deformation on the microstructure, mechanical properties and lattice misorientations in austenitic stainless steel, is well studied in the literature, where samples have been deformed up to failure [177,191,201,203,245,246]. However, there is no published research work available to explain the influence of strain-controlled asymmetric cyclic loading on lattice misorientations, after only a small number of cyclic loading cycles.

The objective of this chapter is to quantify, using EBSD, the cumulative plastic strain resulting from multi-pass welding and from uniaxial strain-controlled cyclic loading of

316L(N) materials. Two independent sets of samples; welded (multi-pass welded plate) and both symmetrically and asymmetrically cyclically deformed, were deformed at room and high temperature, to quantify the cumulative plastic strain. Cumulative plastic strain is summation of the plastic strain, at the end of each cycle.

Following the EBSD experiments, Vickers macro hardness tests were performed on all the samples to validate the EBSD results. This validation was further supported by comparison with published finite element predictions, available from the NeT consortium [22].

6.2 Uniaxial Tensile Test

Using an electro discharge machine (EDM), several flat tensile samples were extracted from the block of as received 316L(N) material (described in section 3.6). Figure 6.1 provides the design and dimensions of the flat tensile sample. The set of flat tensile samples were deformed up to set levels of plastic strain (Table 6.1) under constant strain rate, at both room temperature and at high temperature (550°C).

6.2.1 Uniaxial room temperature tensile test (RTT)

An Instron screw-driven testing machine, with a 50 kN load cell, was used to deform the 316L (N) material, under uniaxial tension, at room temperature. The specimens were held in place using mechanical wedge grips, which were attached to the instrument using universal joints. Prior to the tensile test, the specimens were preloaded (to 70 MPa) and then unloaded (to 0 MPa) to help the specimens settle in the grips. Table 6.1, lists the tensile tests conducted at a constant extension rate of 1 mm per minute, until the required strain was obtained. The machine was controlled by Instron Bluehill software. For room temperature testing, a calibrated extensometer was mounted onto the specimen gauge

length using a static axial clip (refer Figure 6.2). The results from the room temperature flat tensile tests are discussed in section 6.2.3.

6.2.2 Uniaxial high temperature tensile test (HTT)

An Instron 8862 machine with a load capacity of 100 kN was used for all high temperature (550 °C) tensile tests. The machine was equipped with a split furnace, with a side window. Eurotherm 3215 controllers were used to control the furnace temperature. The tensile specimens were held securely using in-house manufactured holders refer Figure 6.3. Calibrated type-N thermocouples, and a high temperature extensometer, were mounted onto the specimen gauge length, with the help of clamping device and ceramic cords respectively refer Figure 6.4. Table 6.1 lists all the high temperature tensile tests, conducted under strain control, and at a strain rate of 4×10^{-4} per second, until the required strain was obtained. Prior to deforming, each specimen was held at 550 °C for 30 minutes, to enable a steady temperature of within ±1°C to be sustained for the duration of the test.

6.2.3 Tensile test results from room temperature and high temperature experiments

From the recorded data, the true stress vs true strain graphs are provided in Figure 6.5. The flow curve of the specimen tested at room temperature to 5% plastic strain shows serrations with a variation of approximately 10 MPa early on in the readings. This variation was due to a slip of the strain gauge during the experiment. However, this small experimental setup error will not affect the plastic strain calibration when using EBSD.

At high temperature, the yield stress of the material is lower than it is at room temperature. Therefore, the material exhibits a lower flow stress at a given strain than in the room temperature test. During the high temperature tensile tests, serrations were evident

on the stress vs. strain curves of Figure 6.5. This is due to dynamic strain ageing (ref. Section 2.3.3).

6.3 EBSD Experimental Setup

For EBSD measurements, a Zeiss Supra 55VP, scanning electron microscope equipped with a field emission gun (FE-SEM) and with a NordlysF EBSD detector, was used. The SEM accelerating voltage was set to 20 keV. The working distance (WD) was 15±0.1 mm, and the objective aperture size was set at 120μm (max) in the high current mode. Table 6.2 summarizes other parameters used in this EBSD experimental setup. The sample was positioned at 70° (from the horizontal) and inserted into the vacuum chamber of the scanning electron microscope (SEM). HKL fast acquisition software was utilized for data acquisition, then Channel 5 software was used to analyse the data.

All EBSD measurements were performed on a rectangular grid of points with a step size of 1 μm, using the beam-scanning mode under dynamic focus conditions and with a SEM magnification of 200×. EBSD indexing was based on the HKL database of materials; Iron *FCC crystal structure,* with space group 225, F m3m. The orientation maps were collected from an area of 500 × 1400 μm, covering more than 100 grains.

6.4 Hardness Test Setup (validation of EBSD results)

Hardness is a measure of a material's resistance to plastic deformation or damage, for example indentation or scratches. In this study, the Vickers *macro* hardness test method was adopted to measure the hardness of the uniaxial tensile deformed samples, welded samples and cyclically deformed samples. Hardness tests were performed according to the British Standard ISO 6507-1:2005 [247]. The instrument used was a Struers Duramin A300 machine, equipped with a diamond pyramidal indenter. To make the indentations, a load

of 5 kgf was applied for 10 seconds. More details on the indents and spacing are given later in section 6.7.3. The hardness test results for the multi weld pass sample are presented in Figure 6.6.

6.5 Weld Plastic Strain Analysis

Section 3.5 has described the multi-pass welded plate, the welding parameters and the extraction of the weld samples. The extracted samples underwent a similar surface preparation to that described in section 3.4.2. The aim of the work presented in this section, was to quantify the plastic strain that developed due to multi-pass welding.

6.5.1 Experimental setup

Using the screen crosshairs the edges of the samples were aligned and positioned parallel to the electron beam scans. Each area was positioned along the central axis of the sample with reference to the weld bead width, as seen in Figure 6.7. All EBSD maps were acquired from the bottom of the plate to the weld cap along the Y-axis in plane B (refer to Figure 3.3).

Four measurements were performed on each scanned image or stage position. Once the set of four measurements was completed, the SEM stage was moved manually to a new location (with an approximate overlap of 10% with the previous area). The stage movements were limited to the X-axis only, so the working distance could be maintained constant throughout the experiments. At each new area, the SEM was refocused and the working distance checked. The accumulated lattice misorientations, induced by each weld deposit, were measured using three different EBSD metrics: Kernnel Average Misorientation (KAM), Low Angle Grain Boundary fraction (LABf) and Average Intragrain Misorientation (AMISa) see section 2.6.4. Figure 6.8-6.10, shows the EBSD

misorientation results of the welded samples. Once the EBSD analysis was completed on each welded sample, the samples were allocated for macro hardness testing.

6.6 Cyclic Plastic Strain Analysis

The design of the uniaxial cyclic loading samples and their extraction from the bulk material has been described in section 3.3. In section 5.3 of Chapter 5, the setup of the cyclic loading experiments is reported. In this section, only the EBSD experimental setup for analysing cyclic plastic strain is explained. The same EBSD settings as described in section 6.3 were adopted for this analysis. Figure 6.11 shows the gauge length of the cyclically deformed sample, bisected along the mid plane, parallel to the loading direction. The extracted sample was surface treated as described in section 3.5.1. Four EBSD measurements were taken at the centre of the mid plane, parallel to the loading direction. Table 6.3 lists the experimental parameters used in the mechanical tests performed on the cyclically deformed samples, at room and high temperature. Figure 6.12-13 show the EBSD measured lattice misorientation induced by cyclic plastic strain. The remaining parts of the bisected samples were used for Vickers hardness testing.

6.7 Discussion

When a material is deformed in tension or compression beyond its yield point, even though the spatial distribution of the strain at the macroscopic level is uniform, at the microscopic scale there is a non-uniform distribution of strain. This results from the anisotropic mechanical properties of each grain. Due to these anisotropic properties, the accumulated dislocations generate localized misorientations within, and between, the grains. The density of dislocations increases with increasing strain and hence the degree of lattice misorientation also increases [177,192,195,197,198,248,249]. Despite this extensive literature,

there are no publications explaining the effects of plastic strain accumulation following deposit of each bead during welding. In addition, no record has been found regarding the influence of isotropic hardening on the lattice misorientations resulting from just a small number of symmetric and asymmetric deformations (i.e. below 12 loading cycles). The experimental findings presented here help to fill this knowledge gap.

6.7.1 EBSD plastic strain correlations for 316L(N) stainless steel

The degree of correlation between intragranular misorientations and induced plastic strain was investigated. The surfaces of deformed 316L(N) stainless steel samples were prepared as described in section 3.5.1 and the prepared samples inserted into the vacuum chamber of the SEM mounted on a pre-tilted (70° from horizontal) sample holder. For flat deformed samples, two to four orientation maps were collected from measurement areas approximately at the centre of the gauge volume, along a plane parallel to the loading direction (see Figure 6.14).

The accumulation of misorientations, as a function of plastic strain introduced by uniaxial tensile load, was quantified using the AMISa metrics (refer section 2.6.4). The AMISa vs. tensile plastic strain correlations are shown in Figure 6.15 (a). The KAM and LABf tensile plastic strain correlations are provided in appendix Figure A.6.1 and A.6.2. The error bars for each EBSD metric were calculated from the +/- standard error of the mean metric values from all orientation maps collected at different locations on both the deformed and non-deformed samples.

The KAM, LABf and AMISa increased approximately linearly with strain level. The difference between the room temperature EBSD plastic strain calibrations and high temperature EBSD plastic strain calibrations is significant. In evaluating the misorientations of the deformed material, the KAM and LABf metrics consider only

intragranular misorientations between 0.15°-2° and 2°-15° respectively. However, as the strain increases, the density of high angle misorientation >15° tends to increase, which affects the misorientation evaluation when using KAM and LABf metrics. While at zero strain the orientation noise and the presence of low angle boundaries in the material will affect the EBSD metric results, offsetting the intercept on the Y axis, as seen in Figure 6.15(a) [192,194]. The AMISa metric evaluates the misorientation across the whole grains and it is more sensitive, even at higher strains than KAM, or LABf .

In Figure 6.16, EBSD plastic strain correlation for the 316L(N) material evaluated in this research study are compared with published plastic strain correlation for 316H and 304L materials [194,250]. The room temperature EBSD correlation for 316L(N) agreed very well with Angeliu et al. [250]. At high temperature, Githinji's [28] EBSD correlation for 316H material shows higher values of misorientation than in 316L (N) material. This is due to Githinji's use of aged 316H material and a strain rate of 1×10^{-5}/sec in his high temperature (550°C) tests. The presence of carbides will increase the strain hardening of the material as well using a slower strain rate due to dynamic strain ageing. However, in all material at both room and high temperature the misorientation increases linearly with plastic strain up to 10% [195,197,251]. Similarly, in this research study, the misorientation increased linearly with plastic strain.

6.7.2 EBSD equivalent yield stress correlation for 316L(N) stainless steel

As describer earlier in section 6.2, the parent materials were monotonically deformed to a defined series of plastic strains (refer to Figure 6.5). For each defined plastic strain, the corresponding final peak tensile stress achieved during the test (refer to Figure 6.5) was also used to establish an EBSD misorientation correlation with an equivalent yield stress at that strain level. The AMISa vs. equivalent tensile yield stress correlations are shown in Figure 6.15(b). This correlation is helpful to quantify the equivalent yield stress from EBSD

data and enables comparison with the results on the residual stress along line BD (refer section 4.2.1 and Figure 4.1).

During each weld bead deposit, the base material is plastically deformed through strain ranges (refer section 7.1 and Figure 7.5 of Chapter 7) that are different at each position through the thickness. As a result, the base material develops anisotropy strains through the thickness. This was evident in the residual stress measurements, evaluated along line BD (refer Figure 4.22(a) of Chapter 4) using neutron diffraction. The longitudinal stress through thickness of the plate are higher than the yield stress of the material. This enables the author to compare the EBSD quantified equivalent yield stress (i.e. bulk 'plastic stress') with the measured residual stress (i.e. 'bulk elastic stress'). The results are discussed in section 7.3 of Chapter 7.

6.7.3 Plastic strain and equivalent yield stress correlation for 316L(N) stainless steel from macro hardness test

Once the EBSD analysis was completed on the flat tensile samples deformed to 2.5%, 5%, 10%, 15% or 20% strain at either room or high temperature, and on the gauge volumes of the cyclically deformed samples, they were subjected to macro hardness testing. A total of 90 to 100 indents were placed, in rows along the loading direction, on each deformed sample. The horizontal and vertical spacing between each indent was 1 mm. The average of the hardness measurements for the room and high temperature tensile specimens, strained to 0%, 2.5%, 5%, 10%, 15% and 20% was calculated and is shown as a function of induced strain in Figure 6.17(a). Similarly, the average of the hardness measurement as a function of monotonic yield stress is shown in Figure 6.17(b), for both room and high temperature tensile specimens. At both room and high temperatures, the hardness of the material showed linear correlation with the induced strain and monotonic yield stress. The

hardness, plastic strain and equivalent yield stress correlations are consistent with EBSD correlation results.

6.7.4 Characterizing accumulated misorientation due to the deposit of each weld bead

The welded sample can be broadly divided into two; a predominantly monotonically deformed zone and a predominantly cyclically deformed zone, depending on the thermal and deformation histories of each volume. The weld metal (i.e. final weld deposit) comes under the category of tensile deformed zone, due to the high peak temperature (above 1000°C). Any compressive strain during heating will be nullified once the material has reached melting temperature. Therefore, only tensile deformation that has developed during cooling will contribute to weld metal deformation. The grain size, texture and degree of deformation in the weld metal is completely different from the base metal and therefore any misorientation correlation with monotonically introduced plastic strain will differ from those observed for the parent stainless steel material.

During welding, the temperatures in the HAZ and the parent material can reach up to 1000°C. As explained in section 2.3.3, stainless steel deformed at temperatures between 300-650°C exhibits dynamic strain ageing (DSA). Results of investigations on the influence of strain rates, in ranges similar to those resulting from the non-uniform heating and cooling rates of welding, were presented in Chapter 5. At the high temperature, the relationship between misorientation and strain hardening is affected by DSA. From Figure 6.5, it is clear that the monotonic yield stress is not consistent at the higher temperature in comparison to that at room temperature, due to this effect.

The varying temperature- time profiles at different distances away from the heat source, through the thickness of the plate, during single pass and two pass welding, are shown in Figure 6.18. From this graph, it is clear that welding causes temperature transients in the

plate around the heat source, which can cause the material to deform asymmetrically (refer to sections 5.3.1 of Chapter 5). Transverse slices extracted from the stainless steel plate with a single-pass, a two-pass and a three-pass weld (as described in section 3.4.1) were used to quantify the plastic strain resulting from each weld pass. The transverse slice (with respect to the weld direction) is the best choice to characterize the accumulated plastic strain. The transverse slice will show the total effect of the heat source on microstructure changes and thermo-mechanical deformation around the weld. EBSD maps of the parent, heat affected, fusion and weld zones (identified on the based of the microstructure of the welded sample) are shown in Figure 6.19.

In Figure 6.19, the EBSD maps of the fusion zones show delineated patterns of colour within the large columnar grains, these are solidification sub-grain boundaries (SSGB). The grain boundaries of the dendrites in the fusion zone and the weld region were clearly defined in the EBSD microstructure map although they were hard to identify in the optical microscope images Figure 3.20. Figure 6.19 shows the colour variation between the grains of the parent zone and the weld region, following each weld pass deposit. There is a difference of degree of colour gradation within the grains. This is due to increasing plastic strain in the region from the parent zone to the weld region. The sharply delineated regions with small variation of colour with in the grains are due to low angle boundaries and the diffuse colour gradations result from stored geometrically necessary dislocations.

The misorientation distributions within and between grains, following each weld deposit, are shown in Figure 6.20-21. It is clear, as we move from the single pass to the three-pass weld (refer A to B direction in Figure 6.20 for deformation in the parent zone, HAZ and fusion zone), that the deformation of the material increases following each weld pass. The observed deformation in the region from the bottom of the plate to the fusion zone (refer to A to C direction in Figure 6.20) and the misorientation variation within a

grain, increase up to the fusion boundary. Figure 6.8-6.10 show the angular misorientations introduced by single pass, two pass and three pass welding respectively, using different EBSD metrics. Figure 6.22-25, compare the spatial variation of the KAM, LABf and AMISa metrics with the measured harnesses for the parent, single pass, two pass and three pass samples respectively. As noted in Figure 6.22-25, the pattern of variation of each EBSD metric exhibited significant variation from one metric to another. The possible reasons for this variation between each EBSD metric are described in sections 6.7.4.1 and 6.7.4.2.

6.7.4.1 Degree of misorientation variation from the bottom of the plate to fusion boundary due to each weld bead deposit.

1. During a single pass deposit, the peak temperature from the bottom of the plate to the fusion boundary increases from 500°C-1100°C as shown in Figure 6.18(a). At this temperature range the yield point of the material is lower than at room temperature, so the material deforms more easily. At any point (say at the bottom of the plate), with increasing temperature from room temperature to 500°C, the magnitude of deformation increases, consequently the density of dislocation and the interactions of those dislocations increase gradually. As a result of this, the low angle misorientations included in the KAM (i.e. < 2°) will gradually increases and eventually exceed the defined threshold limit and develop misorientation above 2°. Hence, KAM value increases form bottom of the plate to fusion boundary gradually as the material is deformed to higher strains. In contrast to KAM, the LABf consider the misorientation between 2° to 15° as low angle grain boundary and the misorientation above 15° as high angle grain boundary. With increasing distance from bottom of the plate to stain affected zone (SAZ) (i.e 13 to 7mm), LABf shows very less misorientation variation between each weld bead deposit.

At this region (i.e 13 to 7mm), the degree of deformation is less than in the SAZ and HAZ. This is because the peak temperature in the HAZ and SAZ is higher than the base metal. Due to this, the HAZ and SAZ material deforms more than in the parent zone. However, from the SAZ to fusion boundary (i.e. 7 to 0 mm), LABf clearly shows the additional accumulated misorientation due to each weld bead deposit (refer Figure 6.9). The $AMIS_a$ results too clearly indicate the accumulation of misorientation due to each weld bead deposit (refer Figure 6.10).

2. In all EBSD metric results the degree of misorientation increases significantly in the SAZ compared to the parent martial. This is because, by the end of first weld bead deposit, the fusion boundary, HAZ and the SAZ region have experienced one cycle of deformation (starting from compression during heating, and tensile during cooling). While the deposited weld metal experiences only tensile stress, because the strain developed during heating will be nullified by melting. During the second weld pass deposit, the fusion boundary in the HAZ and SAZ region undergoes a second cyclic deformation but at a lower temperature due to increases in distance form heat source. Figure 6.18(b), shows the weld temperature distribution during the single and two pass weld deposits from bottom of the plate to fusion boundary. Therefore with increasing numbers of weld bead deposits, the fusion boundary in the HAZ region and SAZ undergoes more cyclic deformation, as result the degree of misorientation increases, as seen in Figure 6.8-6.10.
3. At 12 mm from the fusion boundary, the parent material of the single pass, shown in Figure 6.23, LABf shows 0.25°, whilst AMISa shows 0.9° and KAM measured 0.32°. This is due to the presence of an elongated grain as shown in Figure 6.26. The presence of an exceptional grain in the parent material raised further question on the accuracy of the EBSD results. Because the LABf and AMISa are sensitive

to the grain size of the material. The grain size calculation was performed using optical microscopy on single, two pass and three pass weld samples (i.e. from parent zone to heat affected zone refer Figure 6.7) at 200x magnification. The American Standard Test Method (ASTM) Mean Linear Intercept method was used to calculate the grain size, using Leica optical microscopy software. The difference of grain size at HAZ (i.e.1-3 mm) and parent zone (i.e. 7-11mm) for all sample are differing approximately between 5-10μm, see Figure 6.27. While in SAZ (i.e. 3-7mm), the grain size of single pass and two pass samples are agreeing well. However, the grain size of three pass sample in SAZ are differing approximately 5-10μm with single pass and two pass samples. The difference of grain size from parent to HAZ in all three samples are not significant in comparison to the grain noticed at 12mm in parent zone. Therefore the difference of grain size in each sample will not have significant effect in EBSD analysis.

6.7.4.2 Misorientation variation in the weld metal

After the solidification of the weld metal, the microstructure of columnar grains, solidification sub-grain boundaries (SSGB), and the solidification grain boundaries (SGB) are seen the fusion zone, as seen in Figure 3.20. The SSGBs and columnar grains have grown along <100> direction or along thermal gradients at higher temperatures. As a result of this, the dislocation density between the SSGB and within the columnar grains, is low. The SSGBs are characteristically low angle grain boundaries with a lower angle misorientation approaching zero [47]. While, SGBs are high angle grain misorientations characteristically greater than 30° and dislocation pile up along them [47]. The presence of SSGB and large grains will increase the values of LABf and AMISa within the weld metal in comparison to the HAZ, SAZ and the parent metal.

6.7.5 Quantifying plastic strain and equivalent yield stress from macro hardness

A transverse slice from the single pass, two pass and three pass-welded plate was extracted using EDM. Hardness tests were performed on the welded samples to measure the additional hardening of the material developed by each weld pass, and to identify any interaction between each weld pass. The Vickers hardness map of the multi-pass welded plate is also presented in Figure 6.6. Details of the sequential weld deposits for this weld plate were given in section 3.4 of Chapter 3. The plate was distorted to some extent during the three pass weld bead deposits. The distorted plate was positioned carefully in order to avoid any slope during the two pass weld bead deposits. However, the distorted plate was not positioned correctly during the single pass weld bead deposits. As a result, the single pass weld bead was deposited at an angle. This effect was clearly noticed in the hardness map shown in Figure 6.6.

Comparing the high temperature calibrated hardness curve, shown in Figure 6.17 (a and b), with the measured hardness of the weld pass samples shown in Figure 6.6, through thickness (along Line BD), gives the corresponding plastic strain and the equivalent yield stress distribution in the respective weld pass samples, as presented in Figure 6.28. The accumulation of yield stress and strain resulting from each weld deposit can be clearly observed in Figure 6.28.

6.7.6 Quantitative weld plastic strain and equivalent yield stress from EBSD analysis

Quantification of weld metal plastic strain using the misorientation calibration curve obtained for the parent material is not appropriate because its microstructure and texture are different from the base material. However, the cumulative plastic strain in the region

from the fusion boundary to the base material following each weld deposit can be quantified using the high temperature plastic strain correlation curve, refer section 6.7.1. The plastic strain and yield stress distributions resulting from each additional weld pass, were evaluated by comparing the EBSD metrics from each weld with the high temperature plastic strain and equivalent yield stress correlation curves, (refer to Figure 6.15 and in appendix Figure A.6.1 and Figure A.6.2). The strain and equivalent yield stress distributions, along line BD from the bottom of the plate to the HAZ (i.e. along the y-axis of Figure 3.3), resulting from each weld pass, are shown in Figure 6.29-6.32.

In the parent zone (i.e. 10-13mm in Figure 6.30), approximately 4% plastic strain (from KAM) and 160 MPa of equivalent monotonic yield stress was recorded for each samples (i.e. KAM derived plastic strains for all the parent, single pass, two pass and three pass samples). However, from 10 to 0 mm the KAM derived plastic strains increase gradually as we move from the parent material towards the fusion boundary (4.3% strain and 170 MPa yield stress for the single pass was recorded, see Figure 6.30). The second weld pass developed a higher strain of 5.2% in the surrounding material than in the single pass deposit (see Figure 6.31). Finally, the third weld pass deposit induced a strain of 6.3% plastic strain and 245 MPa yield stress (see Figure 6.32). In all the welded samples the largest plastic strains were in the HAZ.

The weld plastic strains and yield stress quantified from the LABf metric are presented in Figure 6.29-32 and broadly correspond with those quantified from KAM. The LABf quantification indicates strains of 3.75%, 2.5% and 4.5 % in the HAZ of the single pass, two pass and three pass samples respectively. Similarly, the yield stresses observed in the HAZs of the single pass, two-pass and three-pass welds are 130 MPa, 90 MPa and 158 MPa respectively. In the parent material, 0.5% strain and 20 MPa yield stress were recorded for all of the samples.

The plastic strain quantified from the AMISa metric is presented in Figure 6.29-6.32. In comparison to the strains calculated using KAM and LABf metric, the AMISa metric consistently showed more strain. This is due to AMISa consider the misorientation from 1° to higher degree of misorientation with in a grain. However, significant cumulative plastic strain was evident when moving from the parent zone to the HAZ. The maximum plastic strain in the HAZ adjacent to the fusion boundary was approximately 5.3% strain for the single pass and two-pass, while 9% strain was seen in the three pass weld. Similarly, at the fusion boundary, a yield stress of 192 MPa was obtained for the single pass and two pass weld samples and 320 MPa for the three pass weld. The parent zone, i.e. 11-13 mm approximately showed 3.0% plastic strain and 100 MPa yield stress.

The plastic strain and the equivalent yield stress through the thickness of the parent material located at 80 mm, between the three pass and the two pass welds (as seen in Figure 6.6 of hardness map) was quantified using the KAM, LABf and AMISa metrics. Throughout the thickness of the sample see Figure 6.29, approximately 3.6% (KAM), 0.5% (LABf) and 2.5% (AMISa) of plastic strain was noticed for the parent material. Similarly, yield stresses of 150 MPa (KAM), 20 MPa (LABf) and 80 MPa (AMISa) were obtained.

6.7.6.1 Comparing the quantified plastic strain with previous published work

Figure 6.33-35, compares the plastic strain results (using AMISa) obtained from the present research work with those in the published literature. Figure 6.33(a) presents the quantified plastic strain for a 304L weld sample (Angeliu et al. [250]) and the 316L(N) sample used in this research study using the AMISa metric. Figure 6.33(b) shows the series of selected areas used for plastic strain analysis in the welded 304L sample. While, Figure 6.7 shows a series of selected areas used for plastic strain analysis in the welded 316L sample. At the fusion boundary, the 304L sample showed a higher plastic strain of 10%, and 9% showed in the three-pass 316L(N) sample. With increasing distance from the fusion

boundary to the parent, the plastic strain in the 304L sample decreased significantly faster than the 316L three-pass sample. The average plastic strain difference between both samples was 2.5%. However, in the parent zone (i.e. 11-13 mm), both samples showed a plastic strain of 0.3% approximately. The distance from the heat source 'r' (refer to equation 2.1, section 2.2.1 of Chapter 2) to the areas used for the EBSD plastic strain analysis, is higher than in the 316L(N) as illustrated in Figure 6.33(b). As a result of this, the peak temperature at the areas selected in the 304L sample, used for EBSD measurement, is lower than in the 316L(N) material. As a result, with increasing distance from the heat source (i.e. perpendicular), the material deforms less in comparison to material through the thickness.

Figure 6.34 compares the plastic strain for alloy 600 [197] and 316L(N) using the AMISa metric. At the fusion boundary 8% plastic strain was recorded in the alloy 600 weld sample, while 9% plastic strain was recorded in the 316L(N) weld sample. Saez-Maderuelo [197] suggests that a large grain size has affected the plastic strain analysis at the fusion boundary in 600 alloy. Whilst in the 316L(N) sample, the grain size is uniform throughout the thickness of the sample, as shown in Figure 6.34. A plastic strain of 12% was measured at 1 mm from the fusion boundary of alloy 600 dropping to 2.3% in the base material [197]. Similarly 316L(N) showed 9% plastic strain at the fusion boundary decreasing to 2.3% in the base material.

Figure 6.35 compares the quantified plastic strain for alloy 690 [198] and 316L(N) using the AMISa metric. At the fusion boundary for alloy 690, 17% plastic strain for the bottom-weld coupon (i.e. root weld) and 14% plastic strain for the middle and top weld coupons, was recorded. While for 316L(N), 9% for three-pass, 5% for two-pass and 1-pass welds were recorded at the fusion boundary. As described in Chapter 2 (section 2.2.1) and Chapter 7 (section 7.1 and Figure 7.5), the material near the fusion boundary undergoes cyclic

deformation during each weld bead deposition. The fusion boundary of alloy 690 has undergone many more than 3 cyclic deformations due to multi pass deposition. As a result of this, the weld root of alloy 690 deformed more than in the 316L(N) material. In addition, the weld parameters (i.e. current, voltage, speed of weld, heat input and interpass temperature) used for alloy 690 were higher than the weld parameter used for the 316L(N) material. As described in section 2.2.1 of Chapter 2, the weld parameters define the solidification structure, area of fusion boundary, grain size, and magnitude and distribution of plastic strain from the heat source. Due to all these factors, the strain noticed in alloy 690 is higher than in the 316L(N) material.

The EBSD instrument parameters (such as acceleration voltage, step size scan, binning rate, number of frames etc.), weld parameters and the material used by others for plastic strain analysis were completely different from the parameters used in this research study. However, both published literature studies and the present research study showed consistently higher plastic strain around the fusion boundary that decreased when moving from the fusion boundary to the parent zone.

6.7.7 ABAQUS plastic strain prediction

ABAQUS weld simulations were performed by the NeT TG4 consortium to predict the plastic strains and residual stresses in and around three pass welds similar to those of the present study [15,24,55,57,167,215]. Details of the thermal and mechanical modelling of the welds are available [22]. The values of predicted equivalent plastic strain (PEEQ) at positions through the thickness of the plate using a mixed hardening model (as described in section 2.3.5), were obtained from the authors (Muránsky, Hamelin, Smith, *et al.* 2012 [22]). The results are presented in Figure 6.36.

6.7.8 Validating EBSD weld plastic strain results

Figure 6.37 (a, b, c) show comparisons between the plastic strain distributions through the thickness of the plate immediately below the centre of the weld as calculated from EBSD and macro hardness measurements and as predicted from ABAQUS (PEEQ) calculations. The plastic strains calculated from the EBSD metrics are in relatively good agreement with the ABAQUS prediction in the region from the parent zone to the HAZ.

The strains calculated from the AMISa and macro hardness test results are in good agreement with predicted PEEQ. The strain and yield stress increases gradually from the parent zone, and reduces at the fusion boundary. In general EBSD, macro hardness and the simulation predictions (PEEQ and PE) all show the same pattern but at different magnitudes. However, in the HAZ the PEEQ predicted much less strain than the hardness and EBSD quantified plastic strains. Muransky et al. [22,57], considered an annealing model in weld simulation. They predicted that the strain will be completely annihilated at the fusion boundary near the HAZ area, since the temperature reaches or exceeds 1000 °C.

6.7.9 Characterizing cyclic loading plastic strain

The HAZ, SAZ and the parent material around the weld deposit undergo cyclic deformation [222] at different strain rates (resulting from different cooling rates Figure 6.18). As seen in Figure 6.12 and Figure 6.13, after six cycles of loading at 25°C, there was no significant variation in the EBSD misorientation metrics: KAM, LABf or AMISa. This was the case for both symmetric (i.e. from 0% to 43% total cumulative plastic strain) and asymmetric (i.e. from 0% to 25% total cumulative plastic strain) cyclic loading. However, after twelve symmetric cyclic loadings at 25°C (i.e. 58% cumulative plastic strain), a significant increase in AMISa was noted in all the cyclically loaded samples but the KAM and LABf results still showed very little increase. The possible reason for the difference

between the symmetric and asymmetric cyclic loading misorientation is described later in this section.

At 550°C, symmetrically loaded samples deformed up to 58% strain, showed an increase in AMISa compared to those similarly loaded at 25°C. Conversely, asymmetrically loaded samples deformed to 25% at 550°C, show lower values of AMISa, LABf and KAM than similarly deformed samples at 25°C. A possible reason for the reduced misorientation is that during cyclic loading; the cyclic hardening and cyclic softening compete with each other as described in section 2.3.4 of Chapter 2. When a material deformed at lower strain range, less dislocation are generated than the material deformed at high strain range. As a result, the contribution of back stress [67] towards the strain hardening of the material is less in low strain range than the material deformed at high strain range. Due to this, the cyclic softening of material will occur faster in a material deformed at low strain range than the material deformed at high strain range [93]. During the cyclic softening, the density of statistically stored dislocations increases due to the formation of a low density cell type microstructure. They are randomly distributed and have no geometrical consequence, whereas EBSD analyses the strain from the geometrically necessary dislocations, and not from statistically stored dislocations.

The factors influencing the significantly different behaviours of KAM, LABf and AMISa for both symmetric and asymmetric cyclic loading at room and high temperatures are:

1. In strain controlled cyclic loading, the dislocation density increases as a consequence of the imposed strain amplitude. The dislocation density, the dislocations structure, and the cyclic hardening or softening, is dependent of the imposed strain amplitude [100,104,106,234,235,252,253]. Therefore, in symmetric deformation, the strain hardening of the material is higher than in asymmetrically

deformed material, which affects the EBSD metrics in asymmetric cycles (refer Figure 6.12 and Figure 6.13).

2. During the reverse phase of the cyclic loading, some of the dislocations developed in the first or previous cycles will annihilate themselves by interacting with opposite sign dislocations. With increasing deformation, more planar tangled structures are formed. This obstructs dislocation movement and cross slip is activated. This in turn enhances dislocation annihilation mechanisms [254,255].

3. The low stacking fault energy of austenitic stainless steels impedes the cross-slip of dislocations during the early cycles of deformation. As a result high dislocation densities are formed at the grain boundary, whilst in middle of the grain, much less dense dislocations are formed [27,177,255]. Hence KAM and LABf results show minute change because they measure local misorientations within a grain.

6.8 Conclusion

This is the first comprehensive study using three EBSD metrics, KAM, LABf and AMISa, to investigate the accumulation of plastic strain and hardening during multi pass welding of austenitic stainless steel 316L, and to compare it with the hardening due to strain-controlled symmetric and asymmetric cyclic loading. In the HAZ and SAZ, the EBSD (KAM, LABf and AMISa), macro-hardness test results and the plastic strain predictions, are in broad agreement with each other. In the HAZ and SAZ, each weld bead deposit has introduced higher plastic strain. The EBSD metrics showed a gradual increase of plastic strain and equivalent yield stress from the parent zone to the fusion boundary. Quantified plastic strain from the EBSD and hardness analysis for the parent material indicates that the material deforms plastically.

From parent zone to fusion boundary, the predicted PEEQ plastic strains show a similar trend to the experimental results, but at different magnitudes. The EBSD results and macro hardness results depend on variations in microstructure and dislocation density (which develops lattice misorientation), whilst the ABAQUS PEEQ predictions ignore any microstructure and dislocation density. Both EBSD and hardness measurement on the HAZ near the fusion boundary of the single pass weld, showed significant decreases of plastic strain due to annealing. However, the EBSD analysis and the hardness test results clearly contradict the annealing conditions used in the weld simulation for the fusion boundary near the HAZ. The annealing model implemented in the single pass weld simulation clearly needs to be improved for accurate strain and stress prediction.

The EBSD analysis of samples, under strain controlled symmetric and asymmetric cyclic loading, confirms that the EBSD metrics KAM and LABf are insensitive to cyclic deformation whilst the AMISa metric is sensitive to cyclic deformation. The annihilation of dislocations and fluctuations of dislocation density within a grain, caused by cyclic loading, has significantly affected the KAM and LABf analysis. From the symmetric and asymmetric accumulated misorientation analysis, it is reasonable to conclude that in strain controlled cyclic loading, none of the EBSD metrics are reliable to assess the plastic strain, below 58% cumulative plastic strain.

Similarly, the strain and yield stress evaluated in the weld pass sample using KAM and LABf were lower than the strain and yield stress evaluated from AMISa and hardness testing. It is concluded that the yield stress and plastic strain evaluated using AMISa metric and hardness tests are best for comparing and validation of ABAQUS PEEQ predictions.

6.9 Tables

Table 6.1 List of flat tensile test at 25°C and 550°C

Sample No.	Temperature °C	Maximum Strain %	Strain Rate (s^{-1})
1	25	0	4×10^{-4}
2	25	2.5	4×10^{-4}
3	25	5.0	4×10^{-4}
4	25	10	4×10^{-4}
5	25	15.0	4×10^{-4}
6	550	0.3	4×10^{-4}
7	550	1.25	4×10^{-4}
8	550	2.5	4×10^{-4}
9	550	5.0	4×10^{-4}
10	550	10.0	4×10^{-4}
11	550	15.0	4×10^{-4}

Table 6.2 Summarized EBSD settings

Bands Detected	Hough Resolution	Number of Frames averaged	Camera Binning	Acquisition Time in ms	Average Indexing Rate
5-7	120	4	4×4	16.2	98%

Table 6.3 List of cyclic loading test at 25°C and 550°C

Sample No.	Temperature °C	Number of Cycles	Cycle Loading Type	Strain Range %	Strain Rate (s^{-1})
1	25	12	Symmetric	±1.25	4×10^{-4}
2	25	6	Symmetric	±1.00	4×10^{-5}
3	25	12	Asymmetric	-1.25 to 0.02	4×10^{-4}
4	25	7	Asymmetric	-1.00 to 0.02	4×10^{-5}
5	550	12	Symmetric	±1.25	4×10^{-4}
6	550	12	Symmetric	±1.25	4×10^{-5}
7	550	12	Asymmetric	-1.25 to 0.02	4×10^{-4}
8	550	12	Asymmetric	-1.25 to 0.02	4×10^{-5}
9	550	12	Asymmetric	-1.00 to 0.02	4×10^{-4}

6.10 Figures

Figure 6.1 Flat tensile sample design with all dimensions in mm

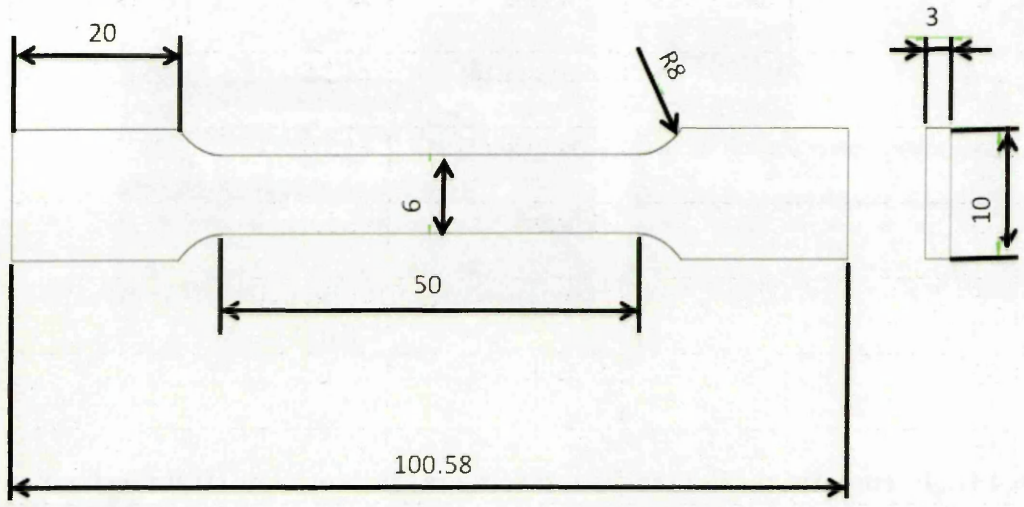

Figure 6.2 Room temperature flat tensile test (a) Instron flat tensile instrument (b) Sample holders and extensometer

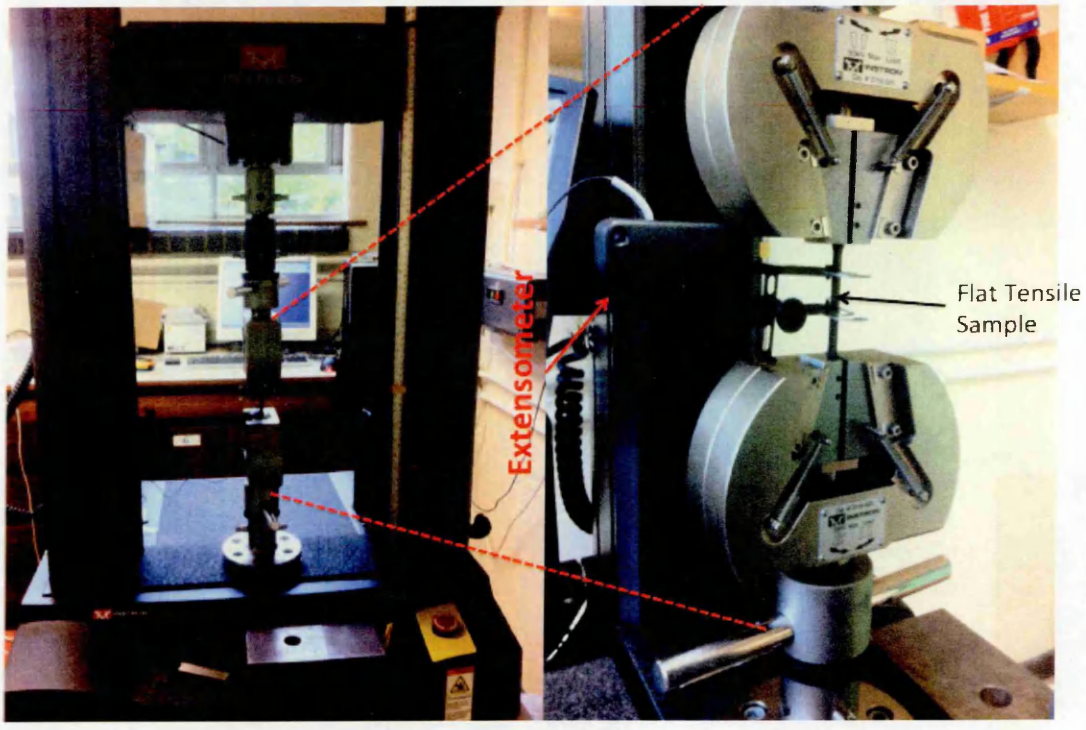

(a) (b)

Figure 6.3 (a) High temperature flat tensile test sample holders (b) Tensile sample in sample holder

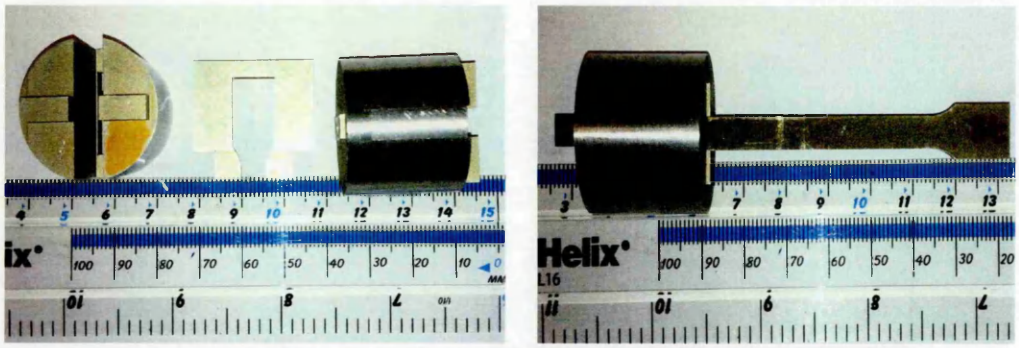

(a) (b)

Figure 6.4 High temperature flat tensile test setup (a) Instron slow strain instruments (b) thermocouples (c) high temperature extensometer

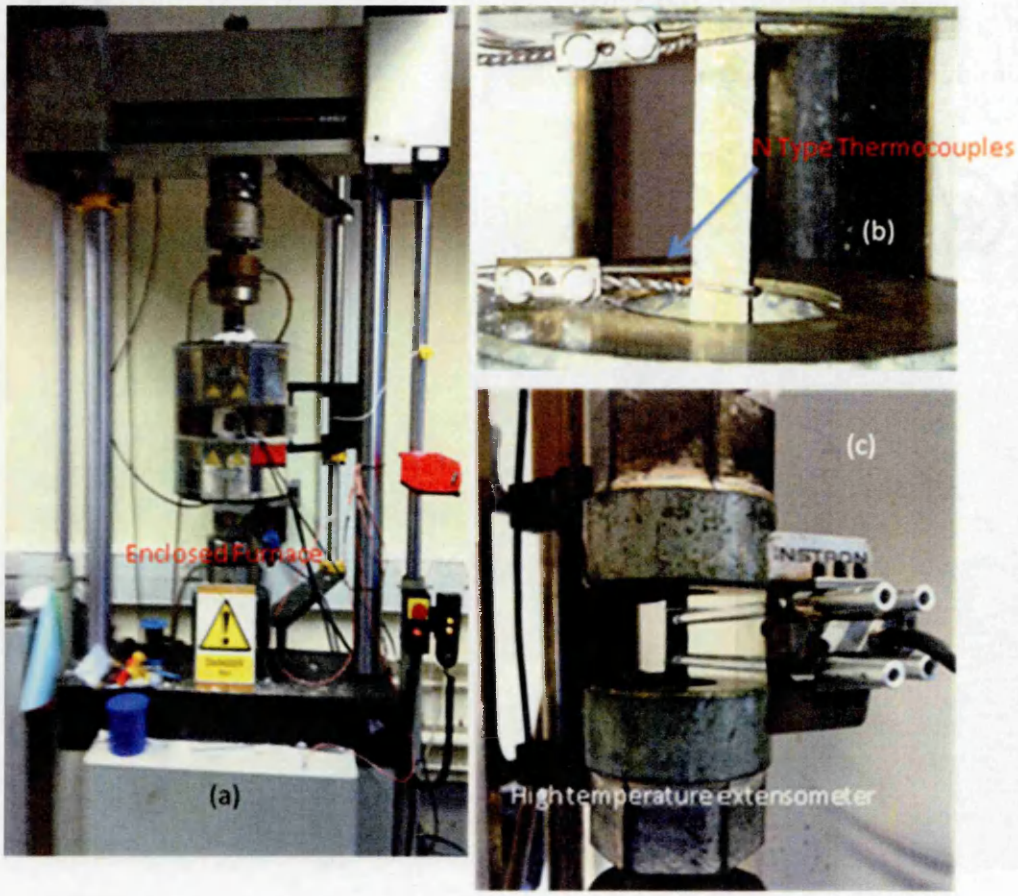

Figure 6.5 Tensile stress vs strain curves at 25°C and 550°C

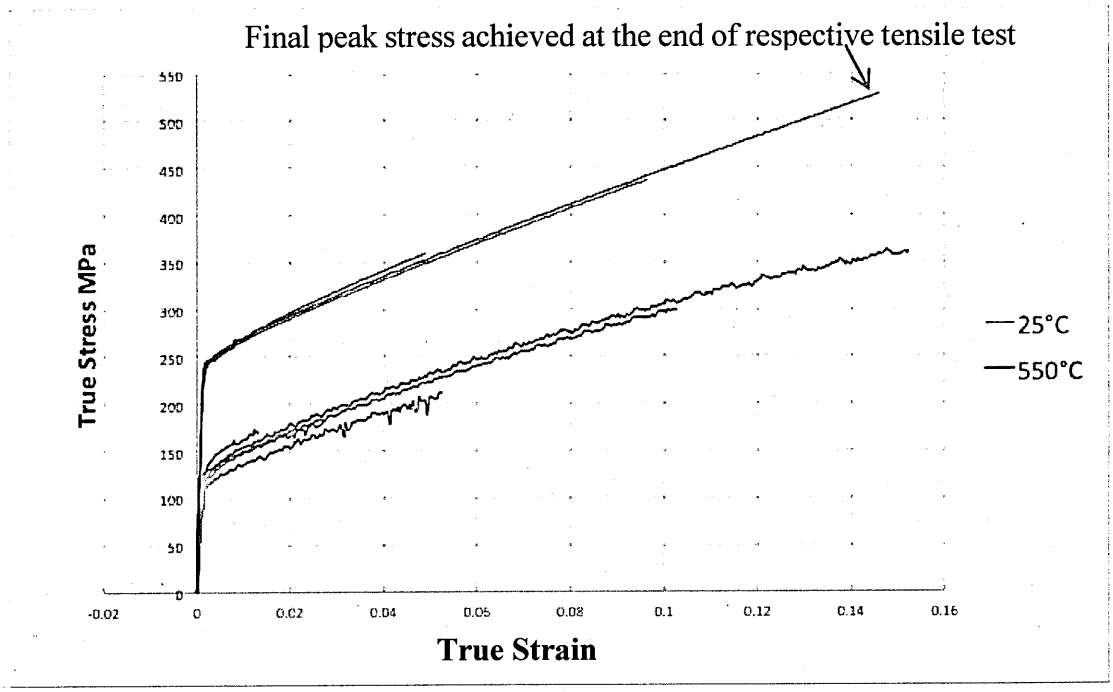

Figure 6.6 Hardness contour map for multi pass weld sample

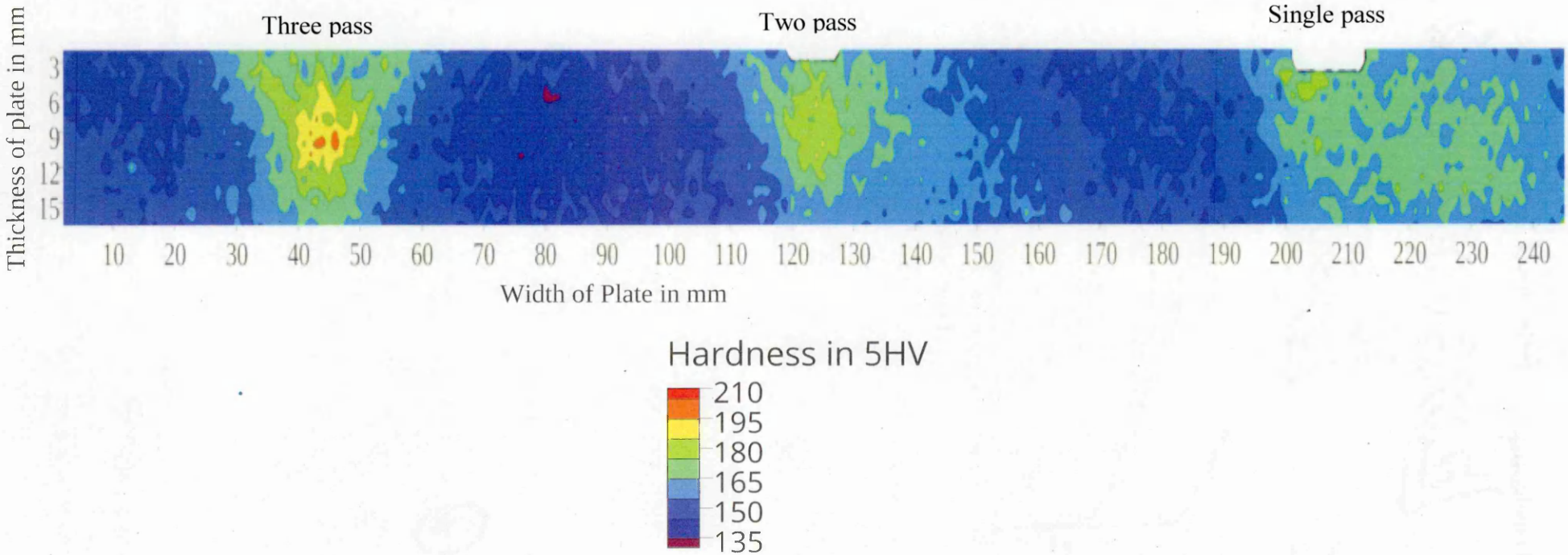

Figure 6.7 Geometry of EBSD experiment setup on welded sample

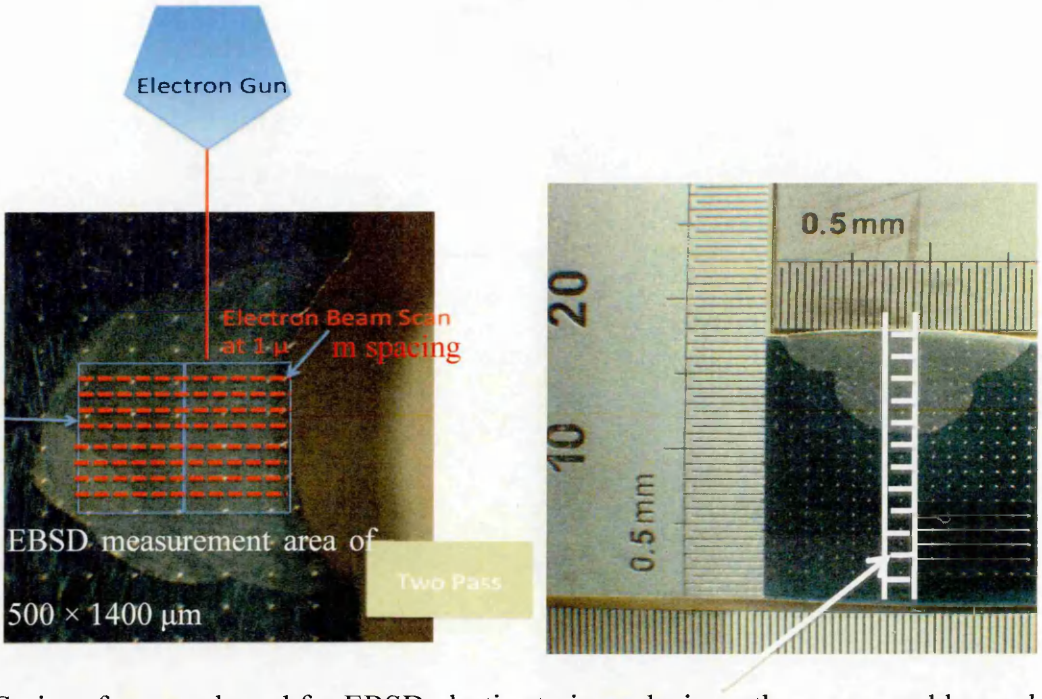

Series of areas selected for EBSD plastic strain analysis on three-pass weld sample

Figure 6.8 Kernels Average Misorientation (KAM) along line BD of welded samples

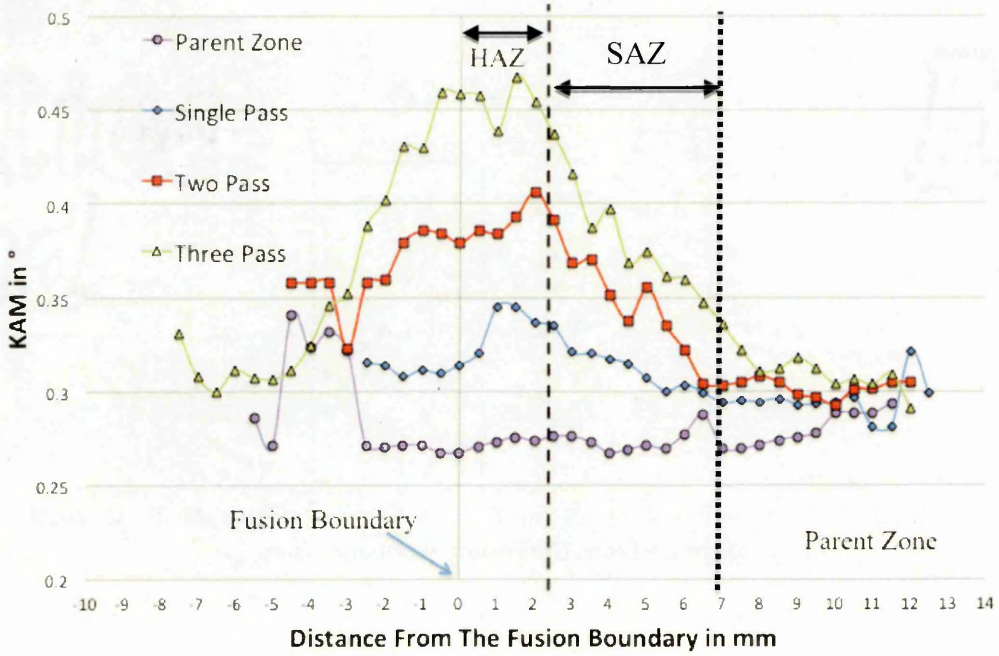

Figure 6.9 Low Angle Boundary fraction (LABf) along line BD of welded samples

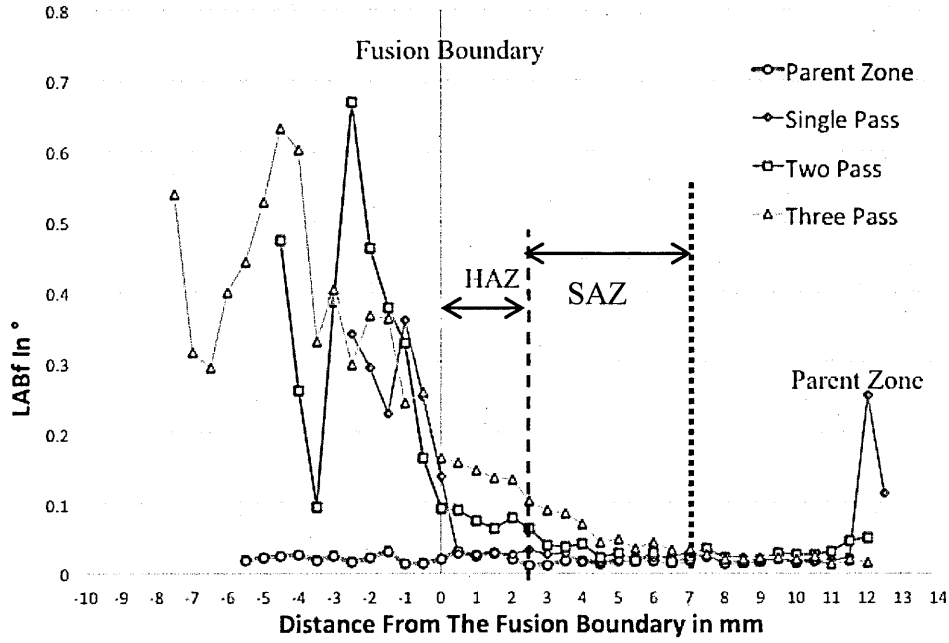

Figure 6.10 Average intergrain Misorientation along line BD of welded samples

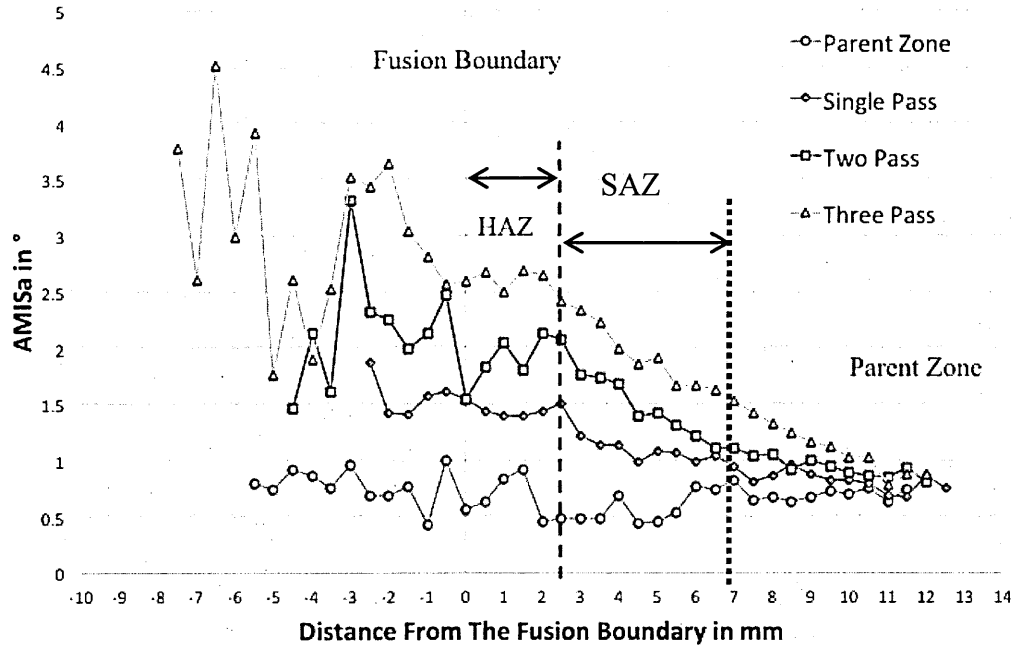

Figure 6.11 Bisected cylindrical samples, along mid plane for EBSD analysis

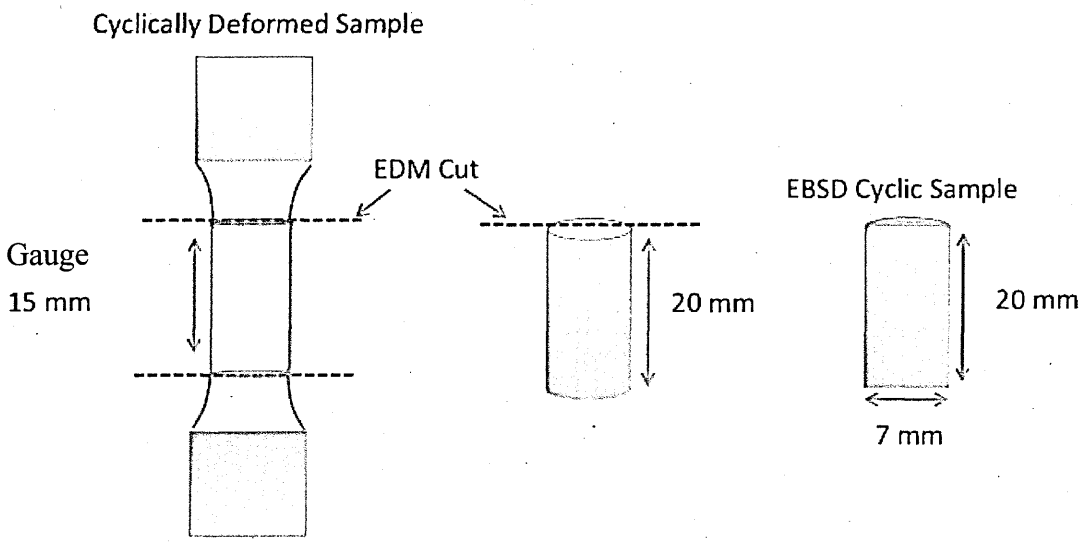

Figure 6.12 EBSD misorientation metric after symmetric cyclic deformation at 25°C and 550°C

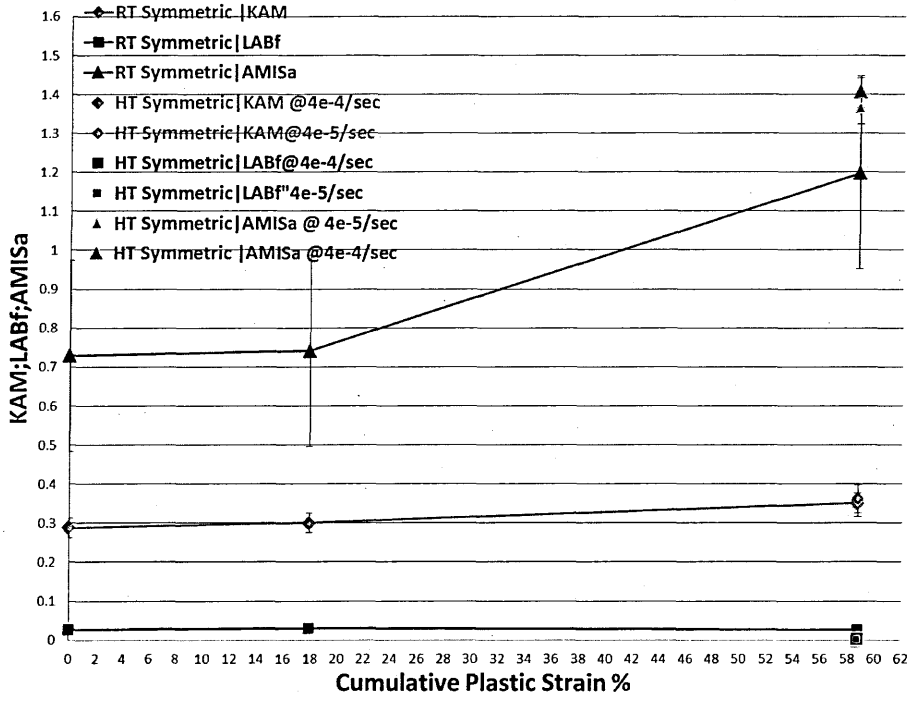

Figure 6.13 EBSD misorientation metric after asymmetric cyclic deformation at 25°C and 550°C

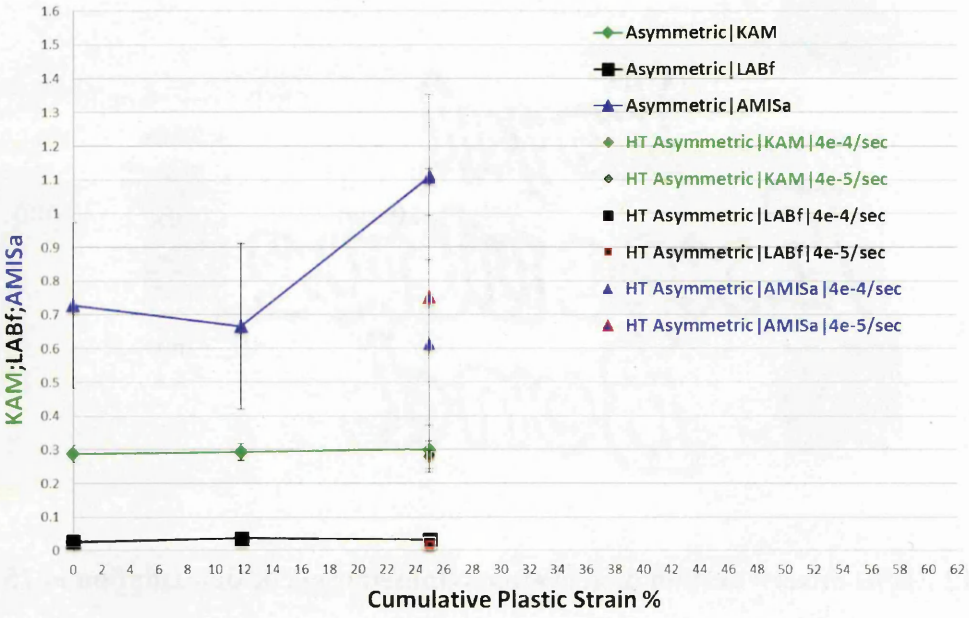

Figure 6.14 EBSD measurement location on high temperature deformed flat tensile test

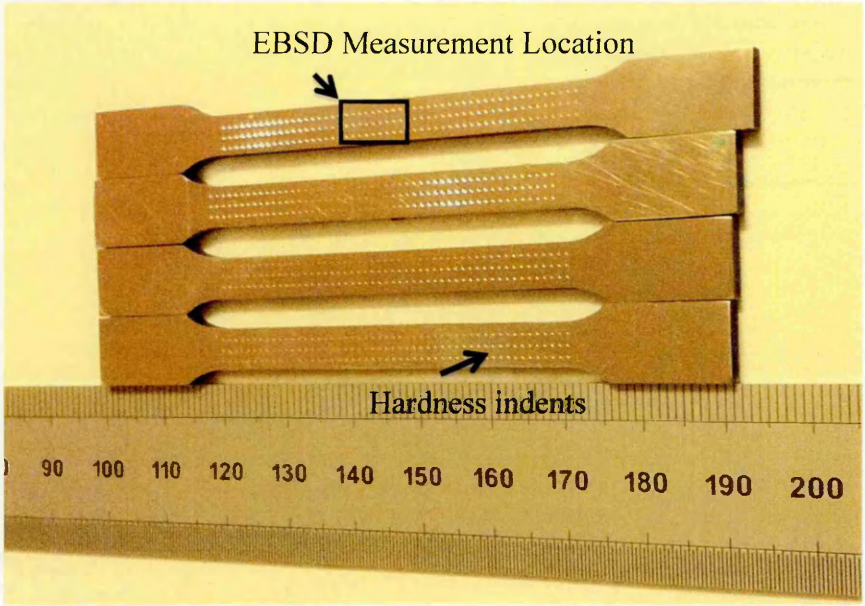

Figure 6.15 (a) Measured AMISa vs true strain and (b) AMISa vs flow stress at 25°C and 550°C

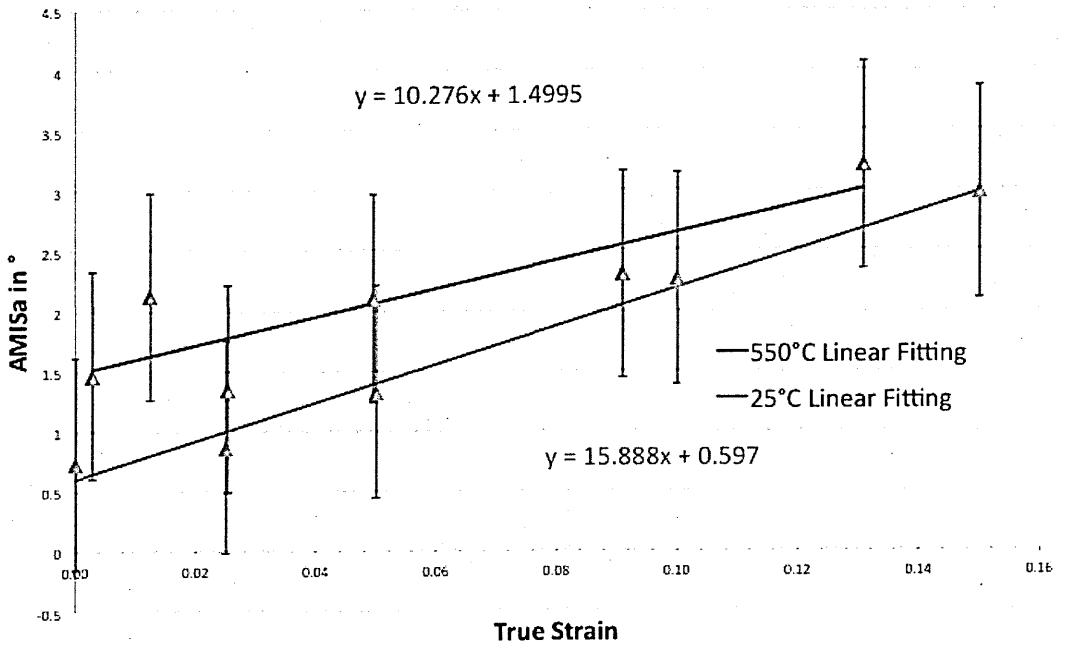

(a)

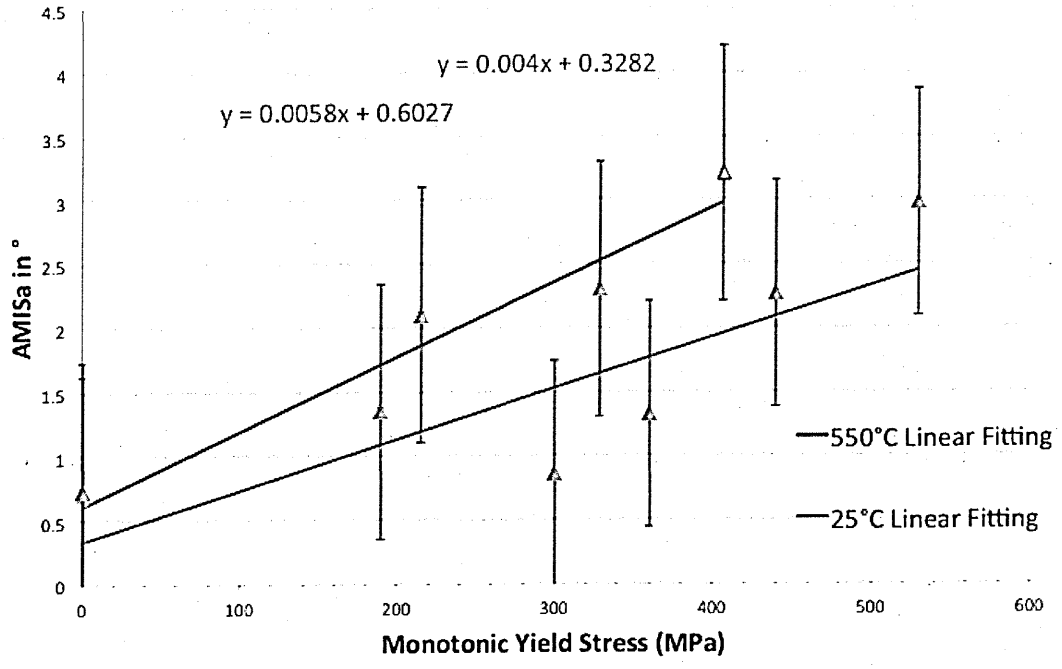

(b)

Figure 6.16 Comparison of published AMISa correlation with present studies

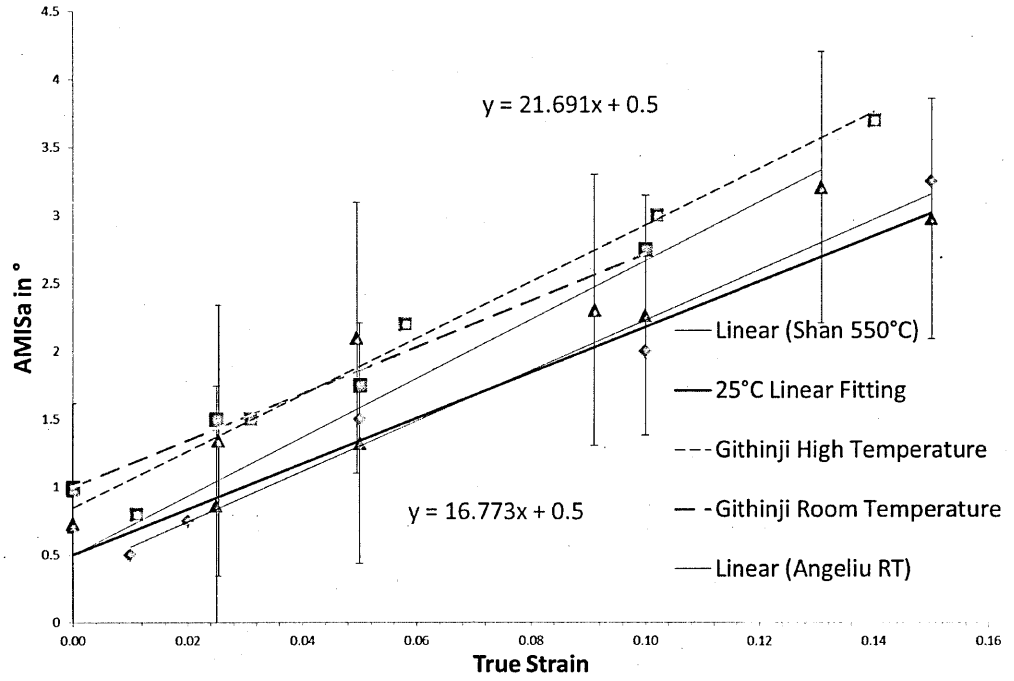

Figure 6.17 Measured hardness vs true plastic strain (b) measured hardness vs monotonic yield stress

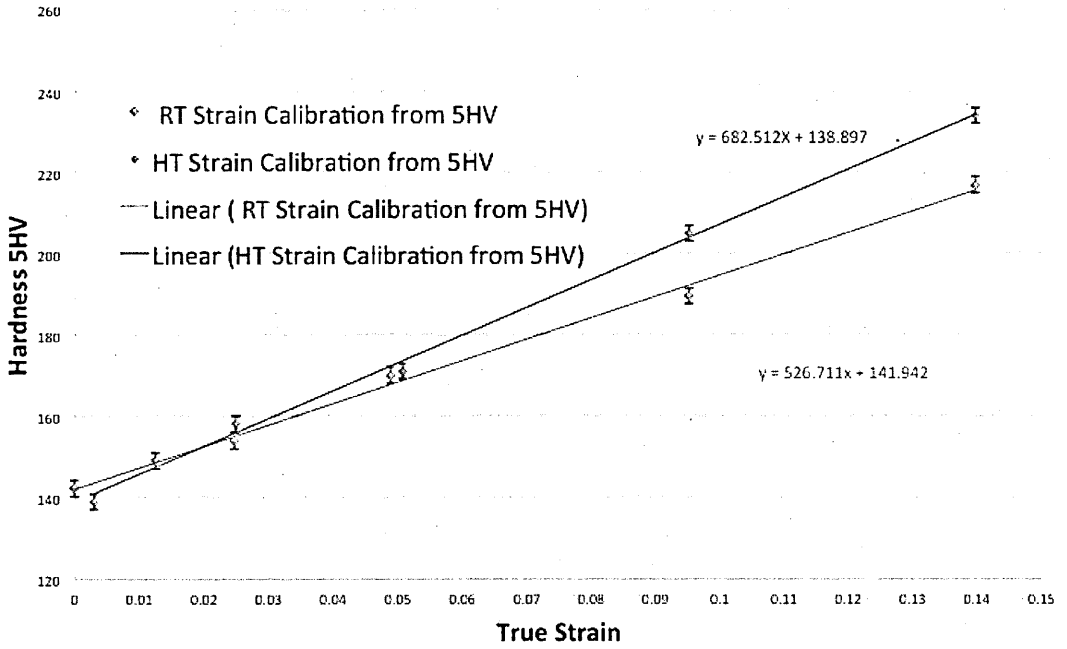

(a)

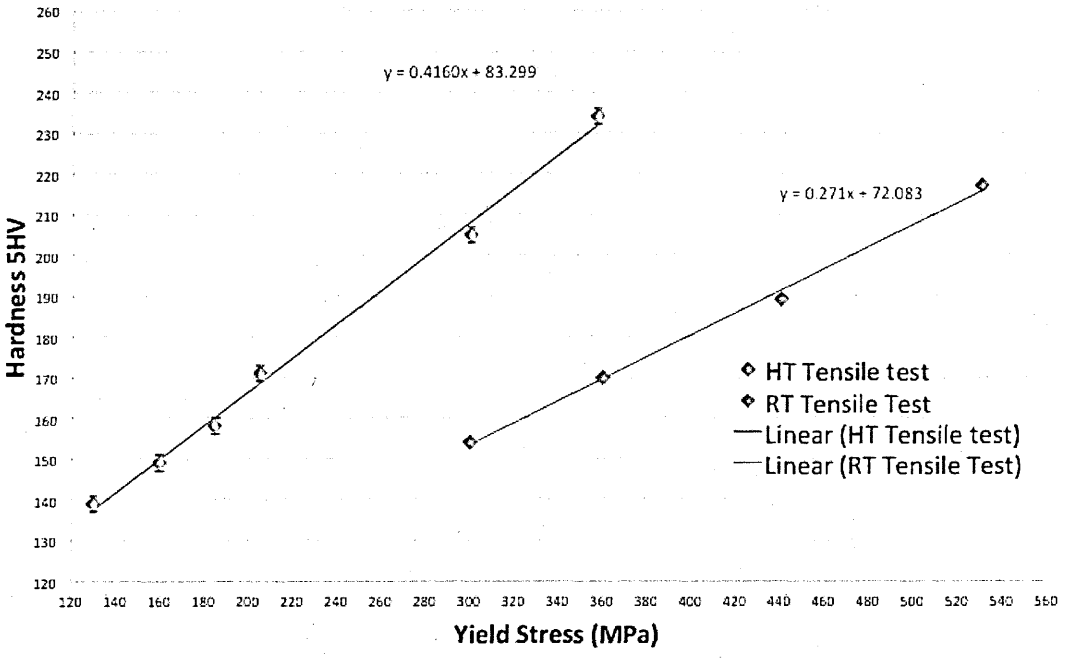

(b)

Figure 6.18 Temperature profile from the heat source through thickness (a) single pass weld (b) two pass along line BD [57]

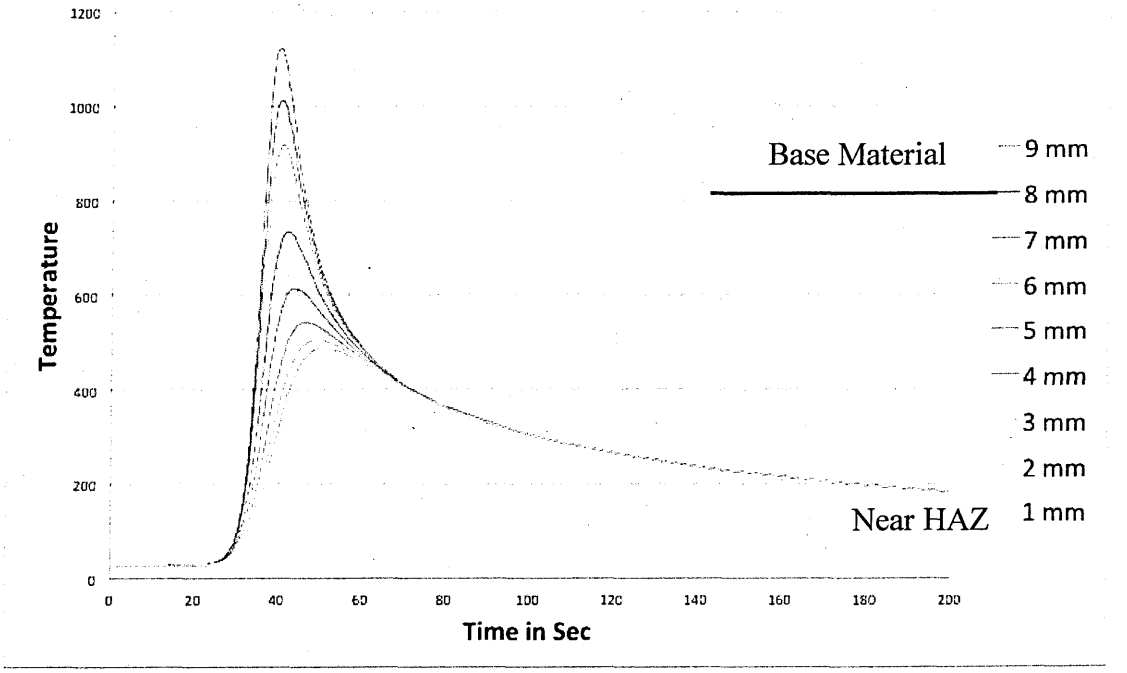

(a)

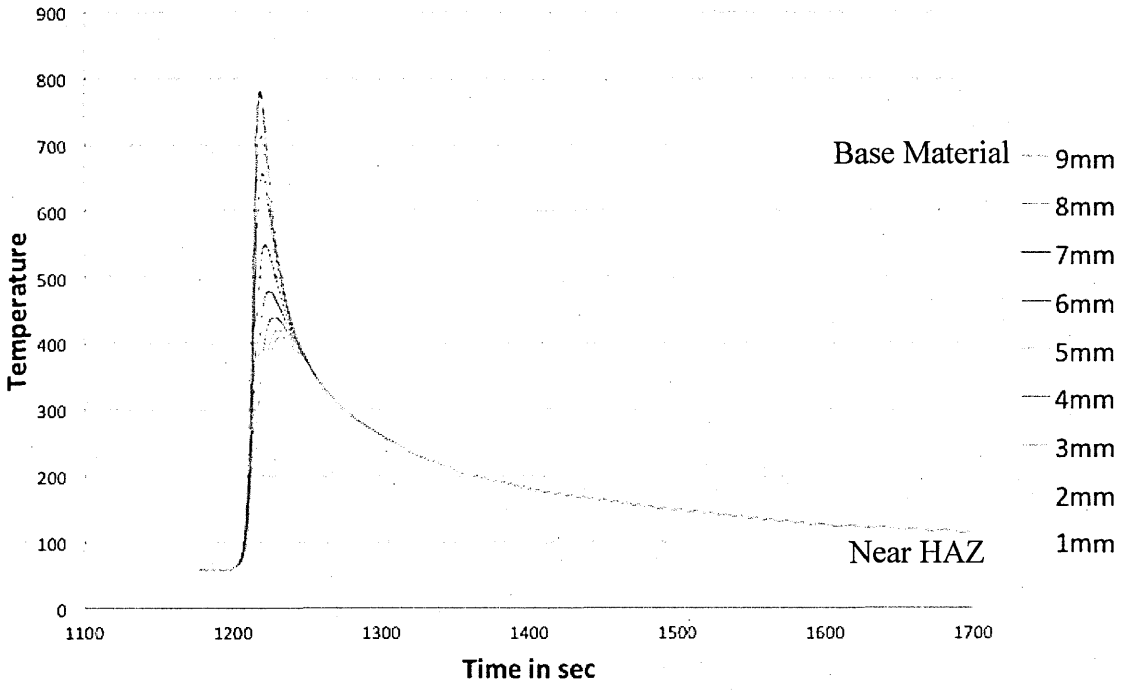
900
800
700
600
500
400
300
200
100
0
Temperature
1100
1200
1300
1400
1500
1600
1700
Time in sec
Base Material
Near HAZ
9mm
8mm
7mm
6mm
5mm
4mm
3mm
2mm
1mm

(b)

Figure 6.19 EBSD IPF colour maps: Parent Zone (PZ), HAZ, Fusion Boundary (FB) and Weld Metal

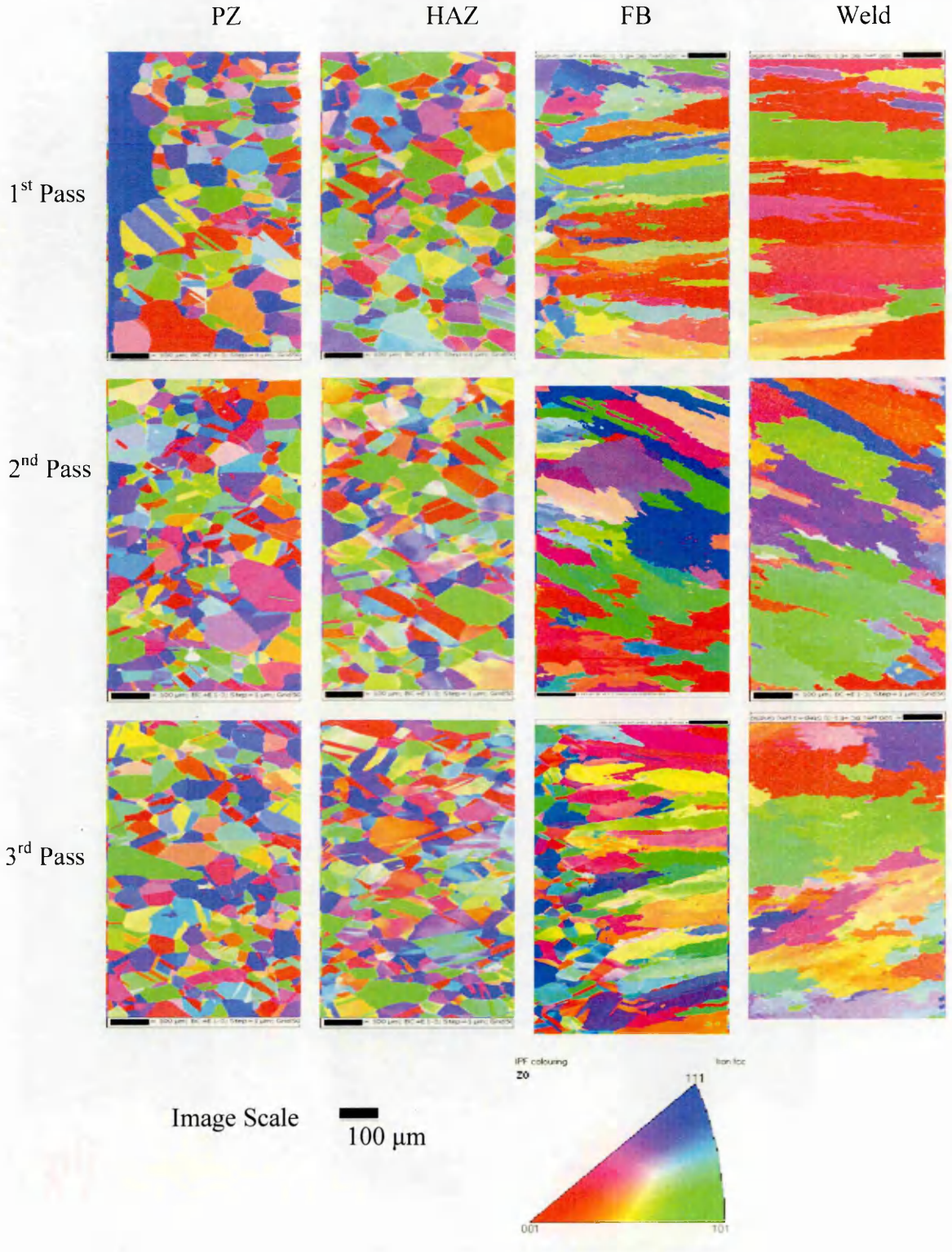

Figure 6.20 KAM maps of single pass, two pass and three pass

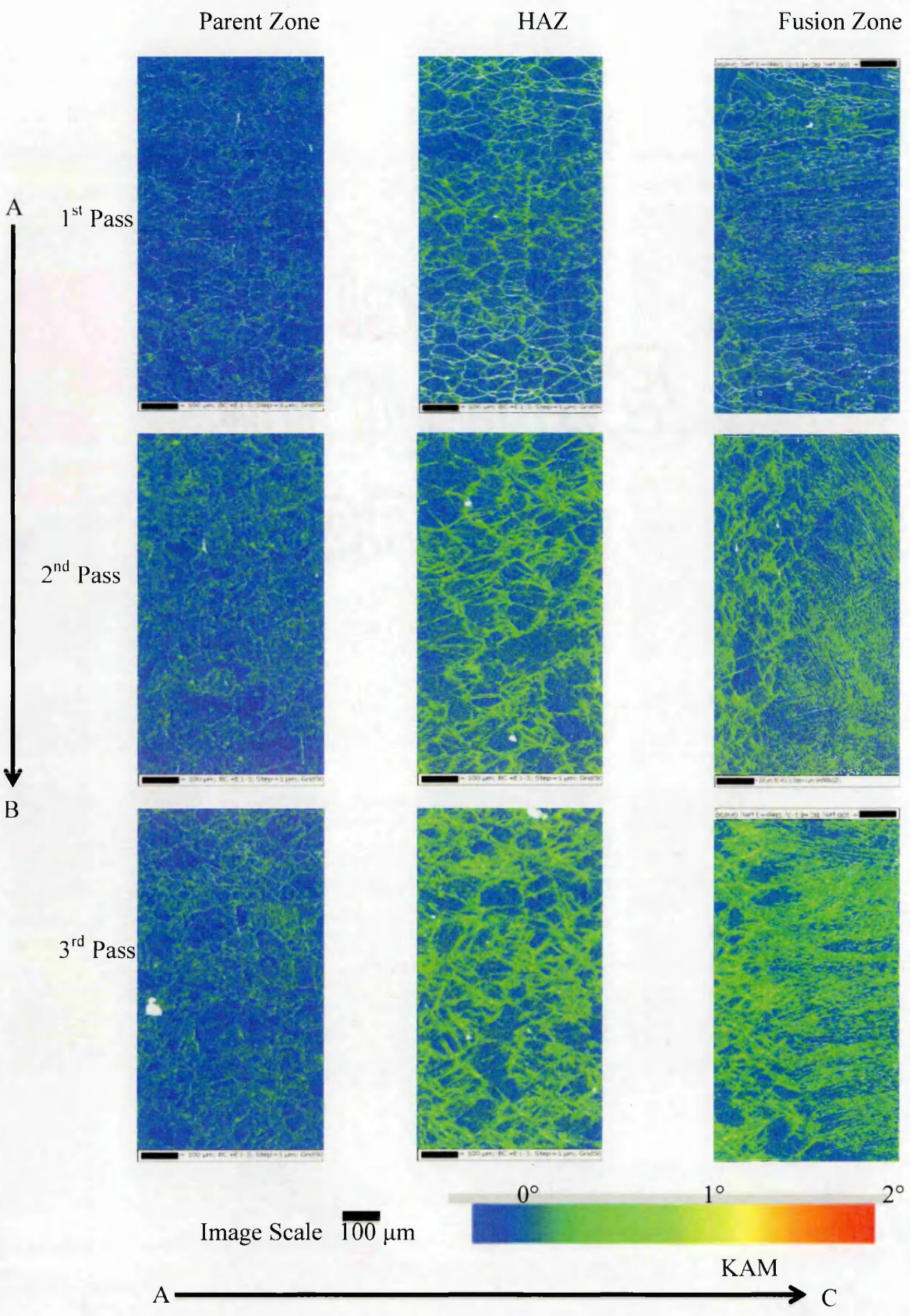

Figure 6.21 LABf of single pass, two pass and three pass

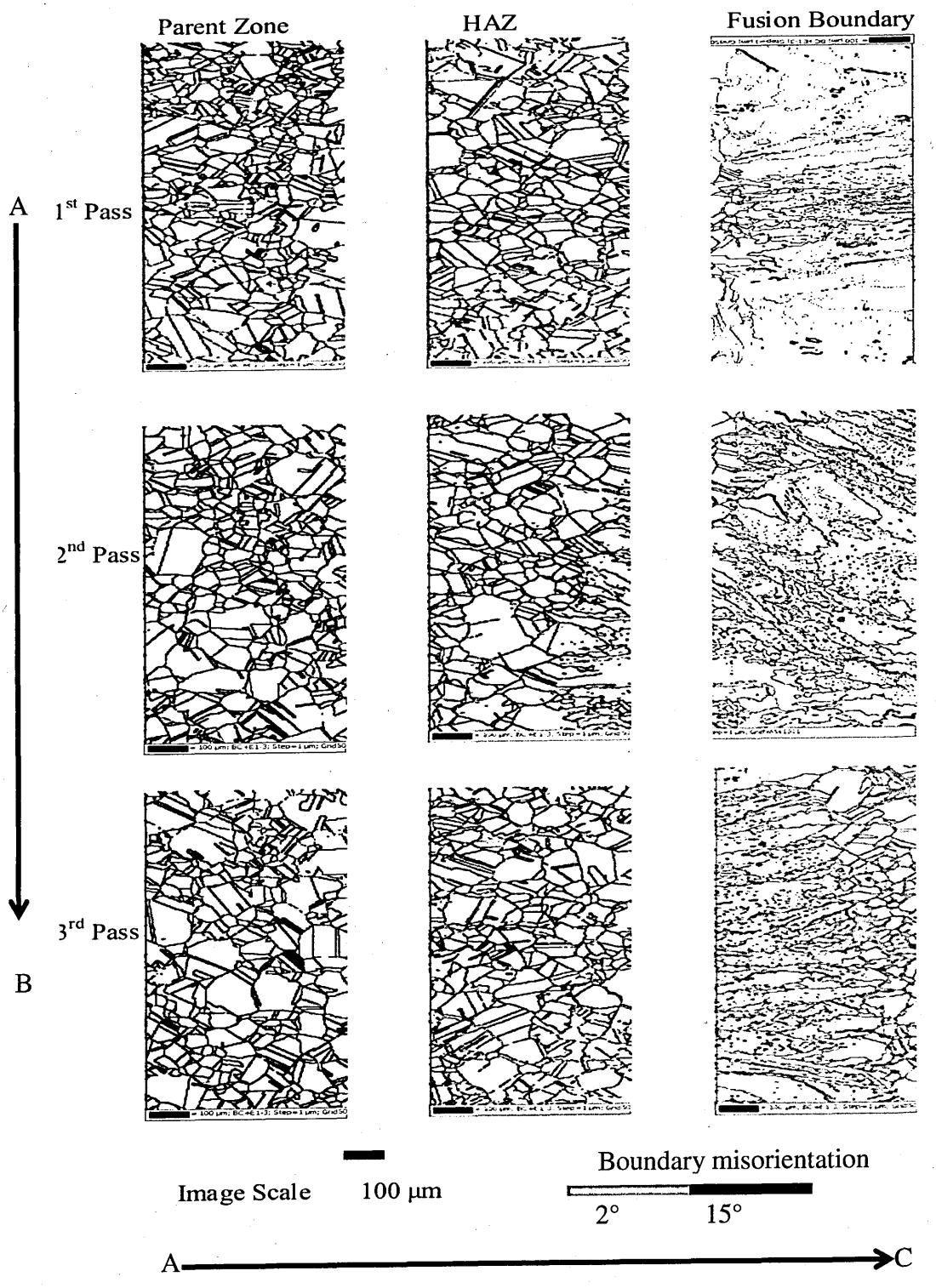

Figure 6.22 Parent material: Comparison between the different EBSD metrics misorientation and hardness result

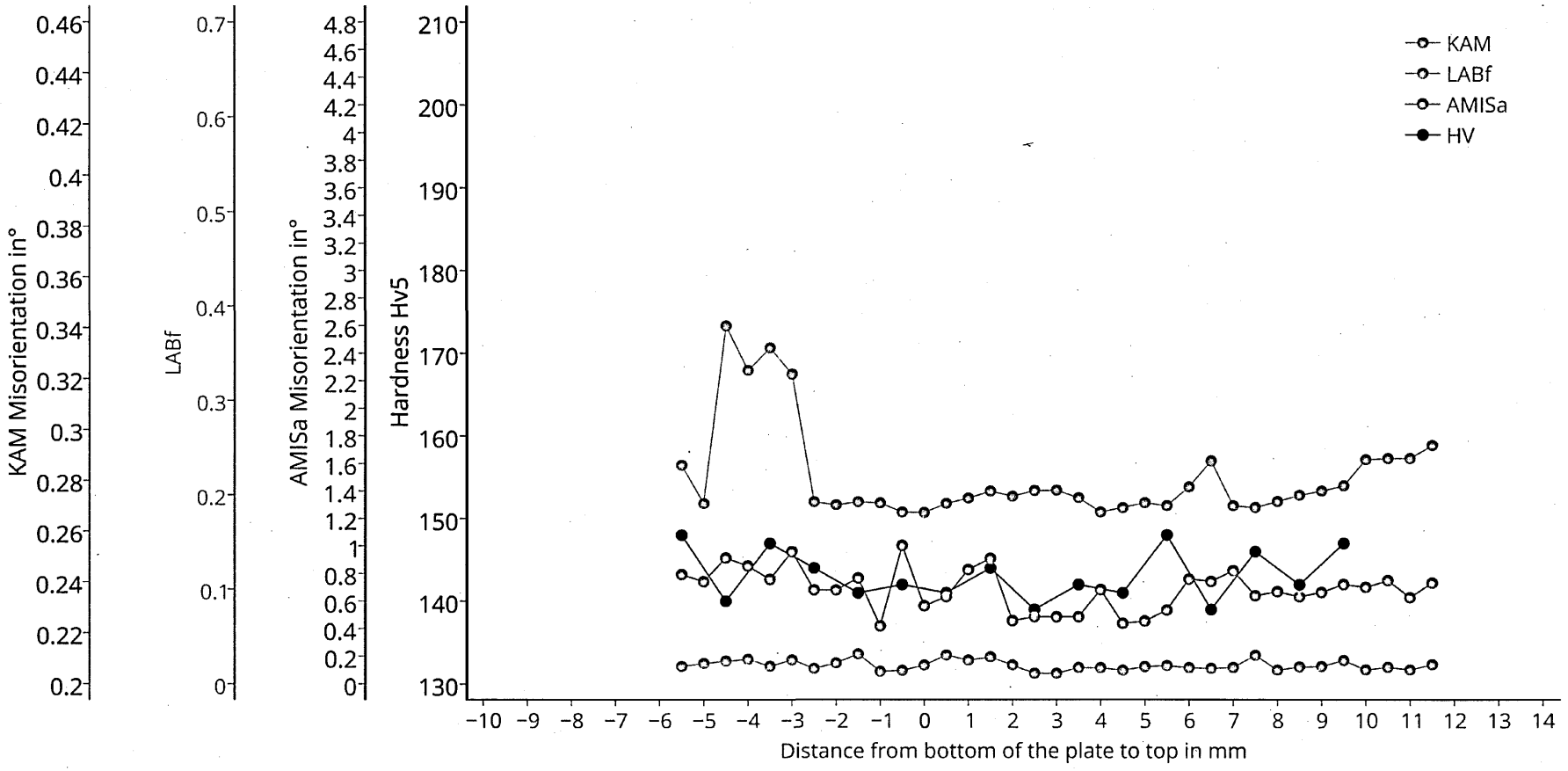

Figure 6.23 Single Pass: Comparison between the different EBSD metrics misorientation and hardness results

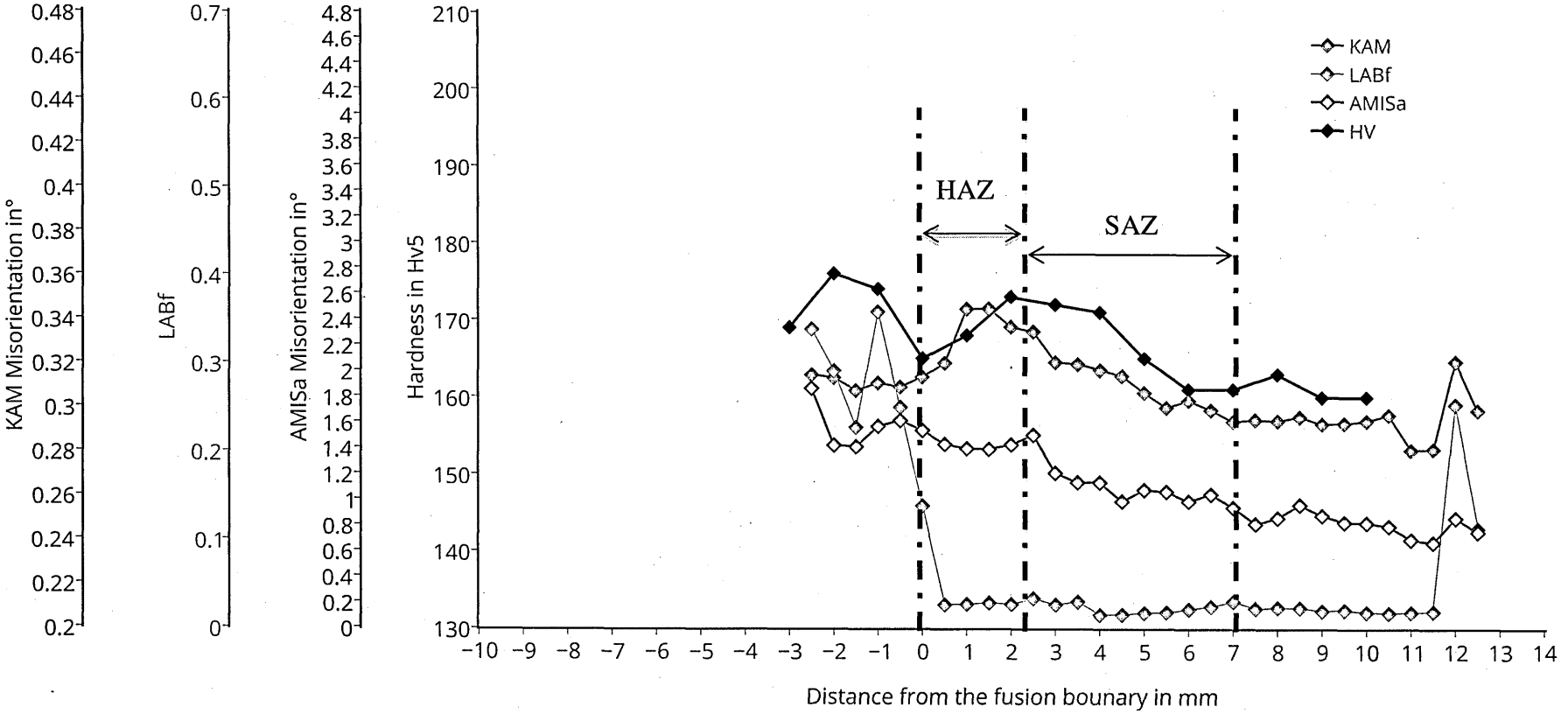

Figure 6.24 Two Pass: Comparison between the different EBSD metrics and hardness results

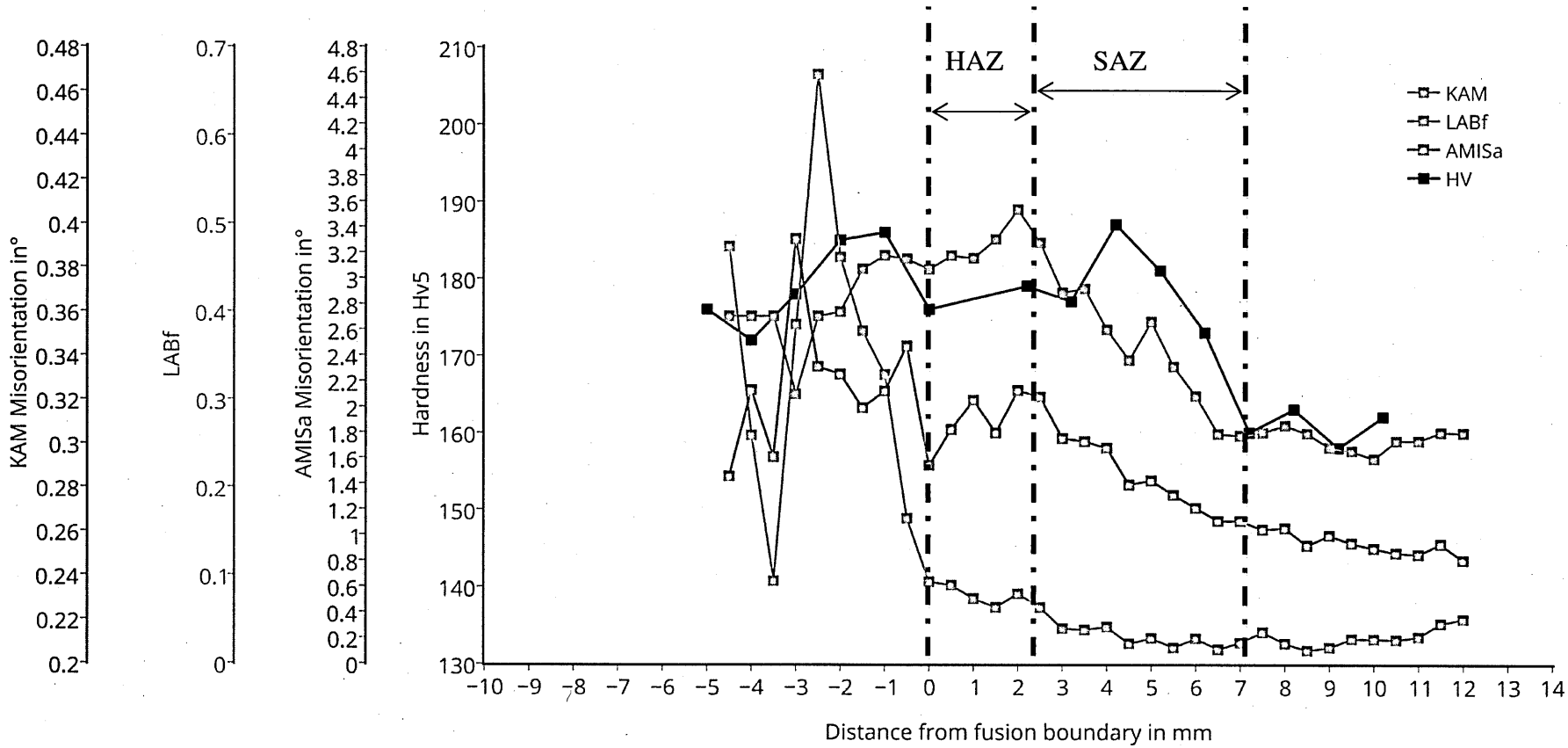

Figure 6.25 Three pass: Comparison between the different EBSD metrics and hardness results

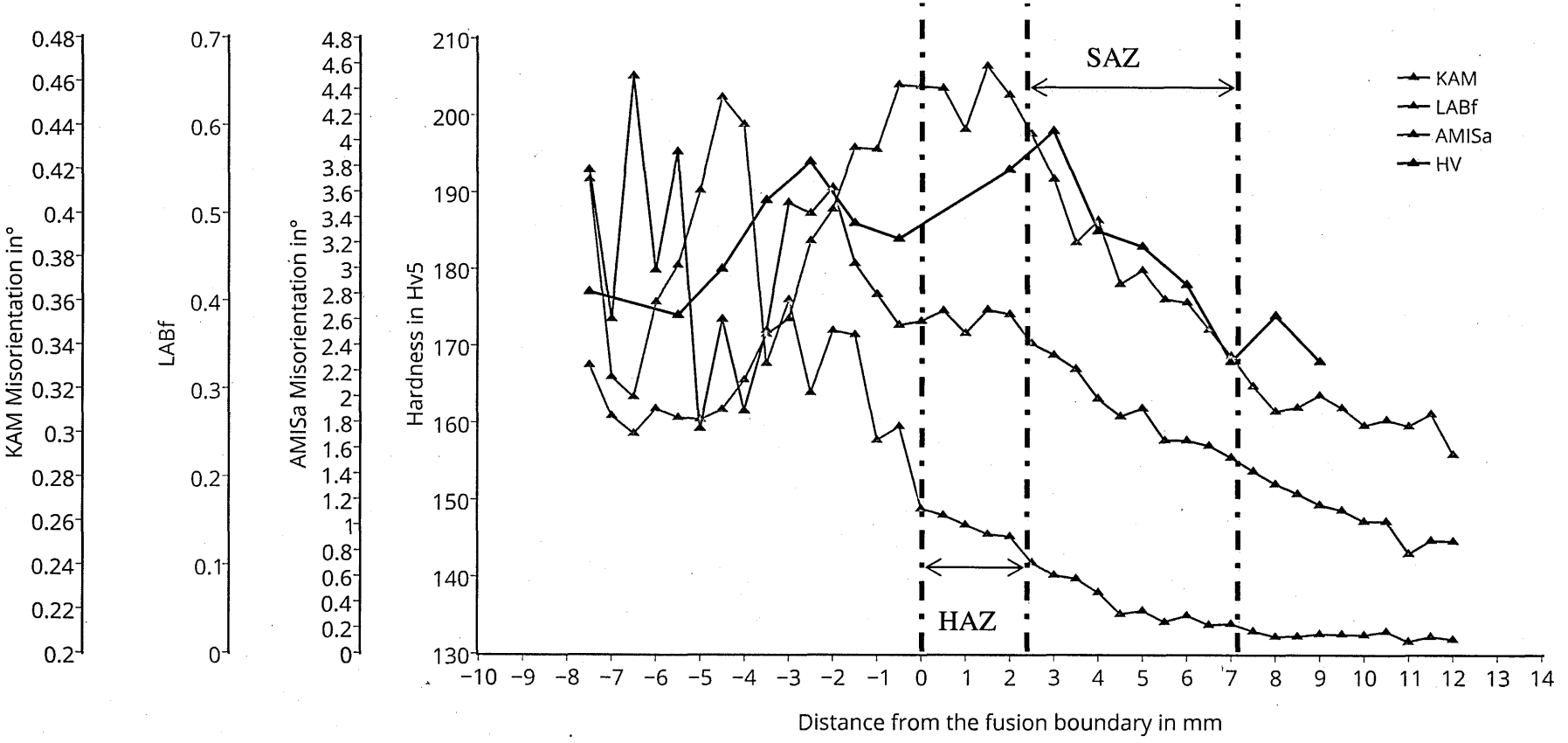

Figure 6.26 EBSD microstructure of parent zone, deformed grain near bottom plate surface

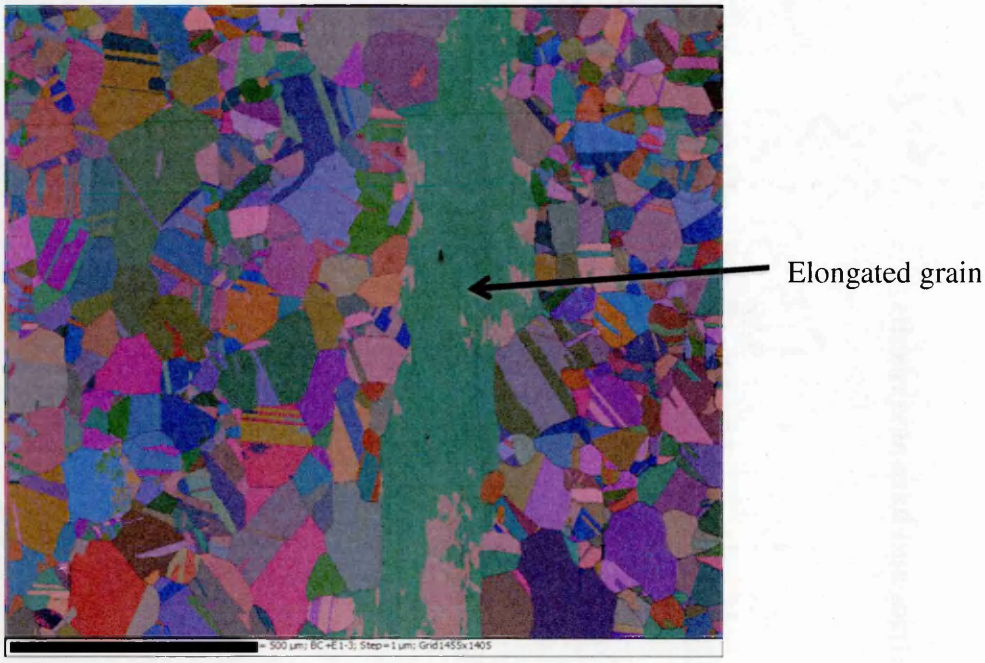

Figure 6.27 Grain size variation through thickness of single pass, two pass and three-pass samples error bar ±10μm

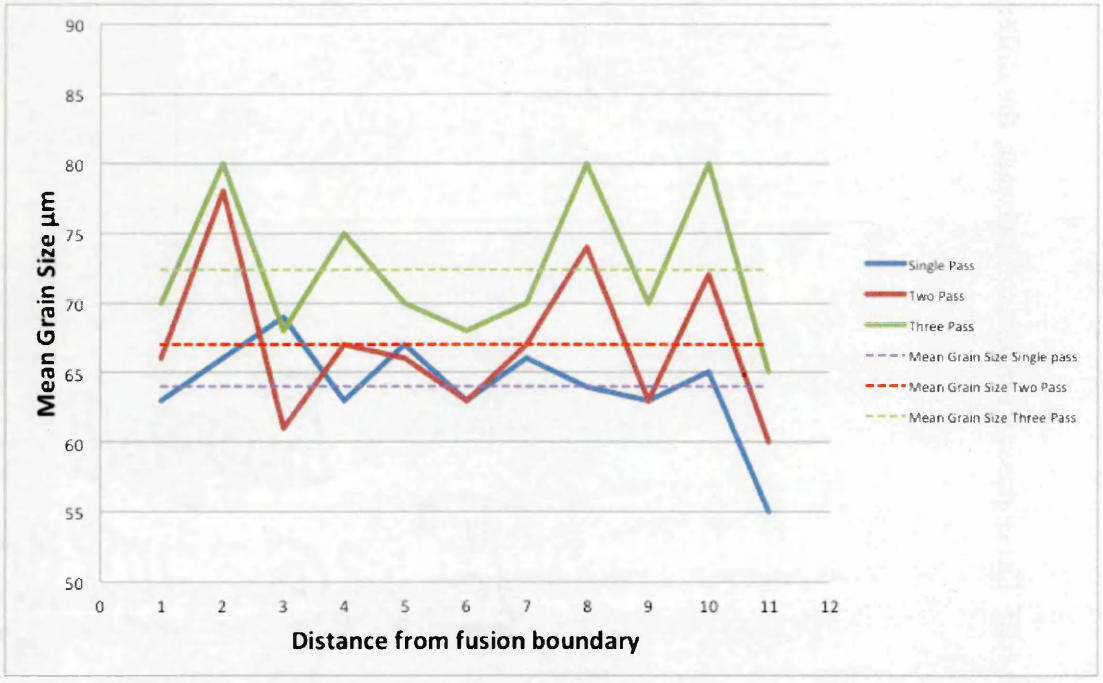

Figure 6.28 (a) Quantified plastic strain (b) Quantified equivalent yield stress

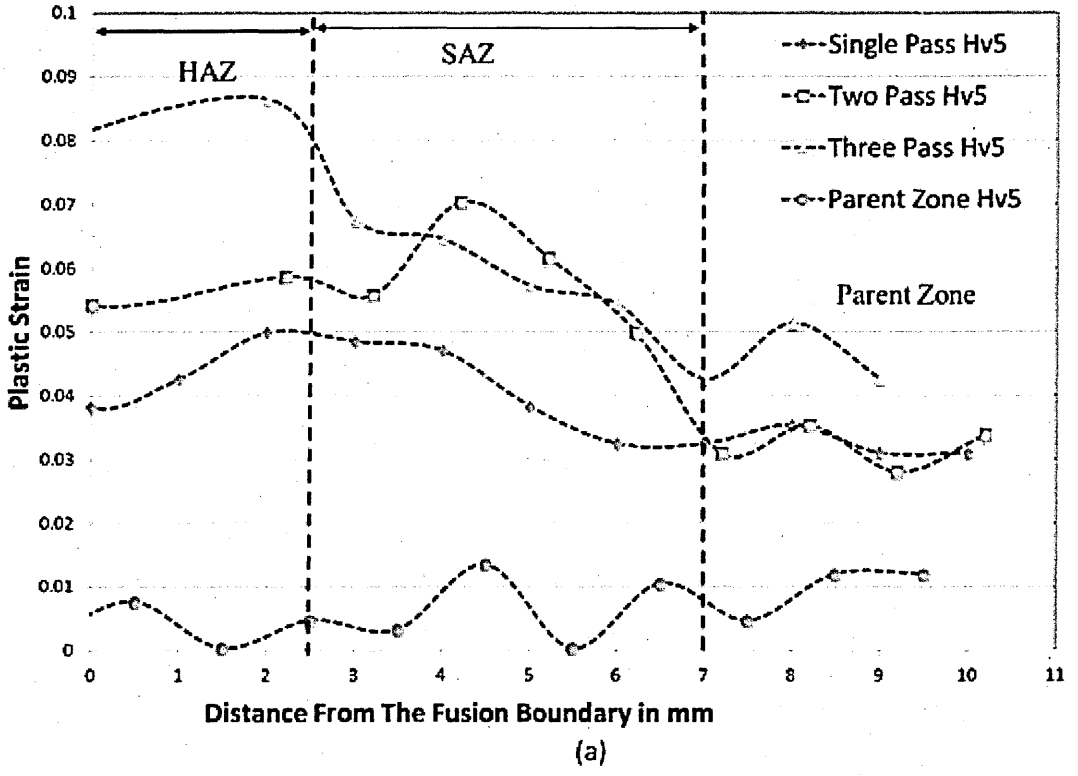

(a)

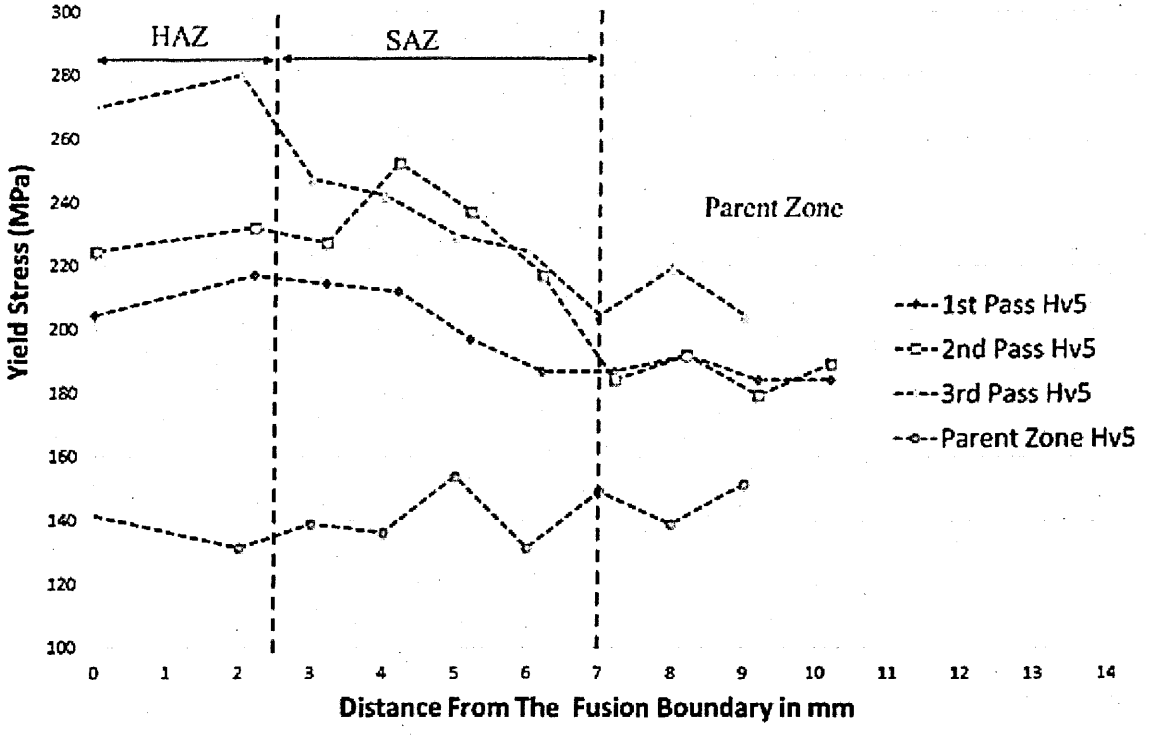

(b)

Figure 6.29 Parent material: (a) Quantified plastic strain (accuracy of ±0.015) (b) Quantified equivalent yield stress (accuracy of 20MPa)

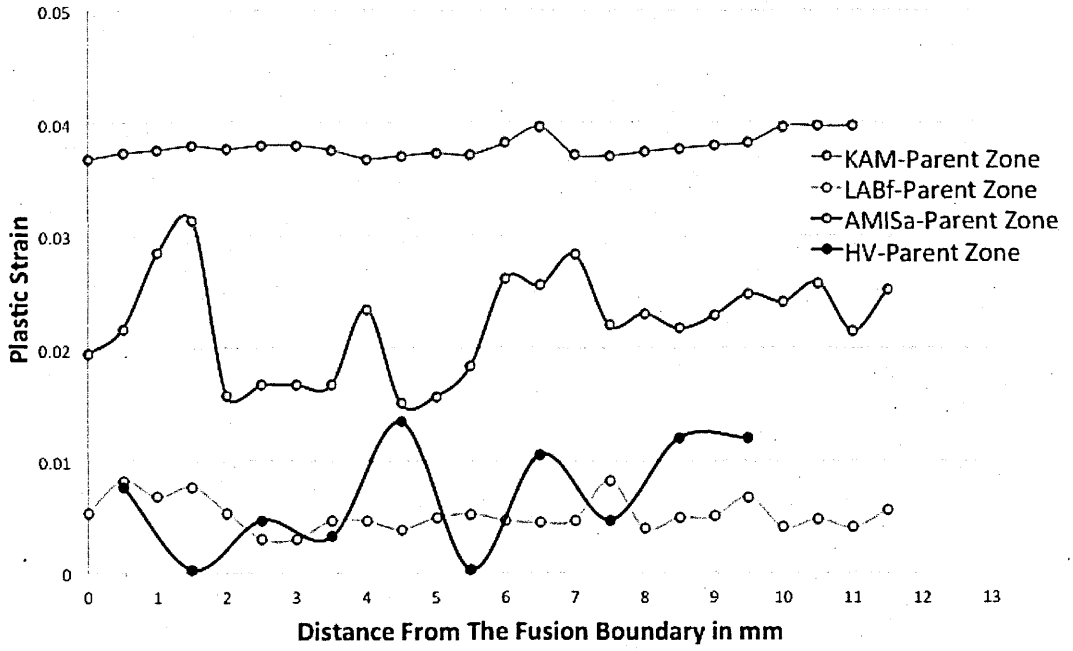

(a)

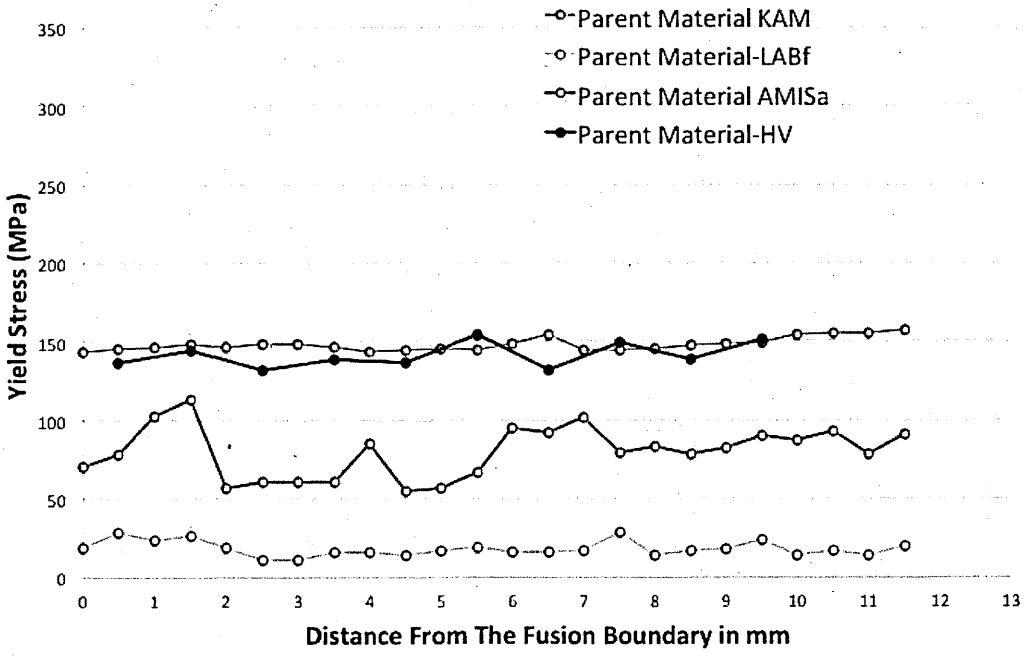

(b)

Figure 6.30 Single pass: (a) Quantified plastic strain (accuracy of ±0.015) (b) Quantified equivalent yield stress (accuracy of ±20 MPa)

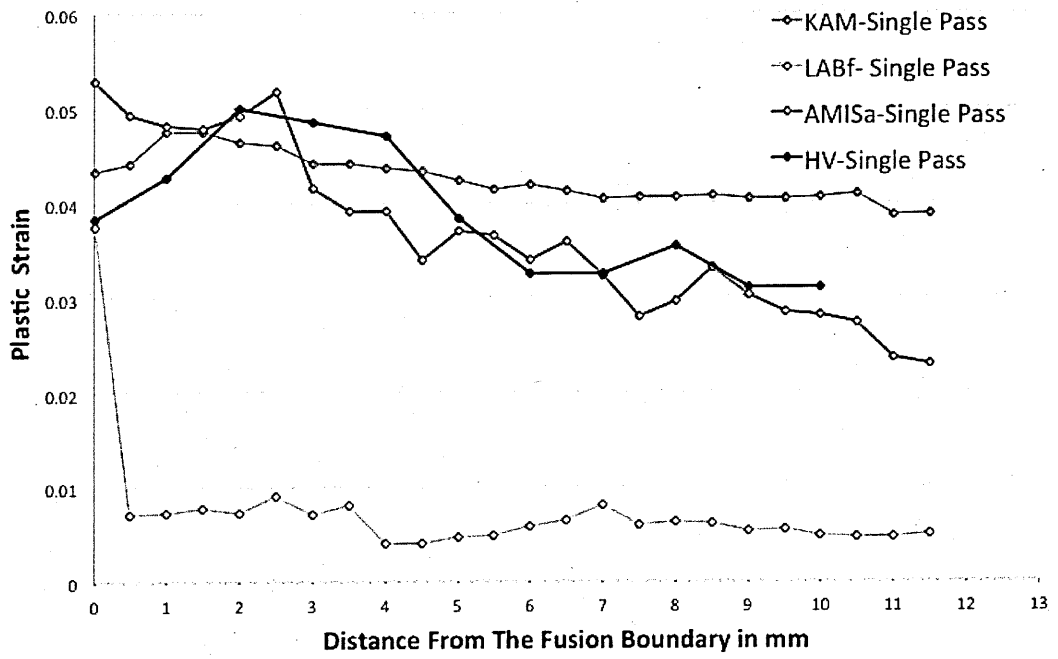

(a)

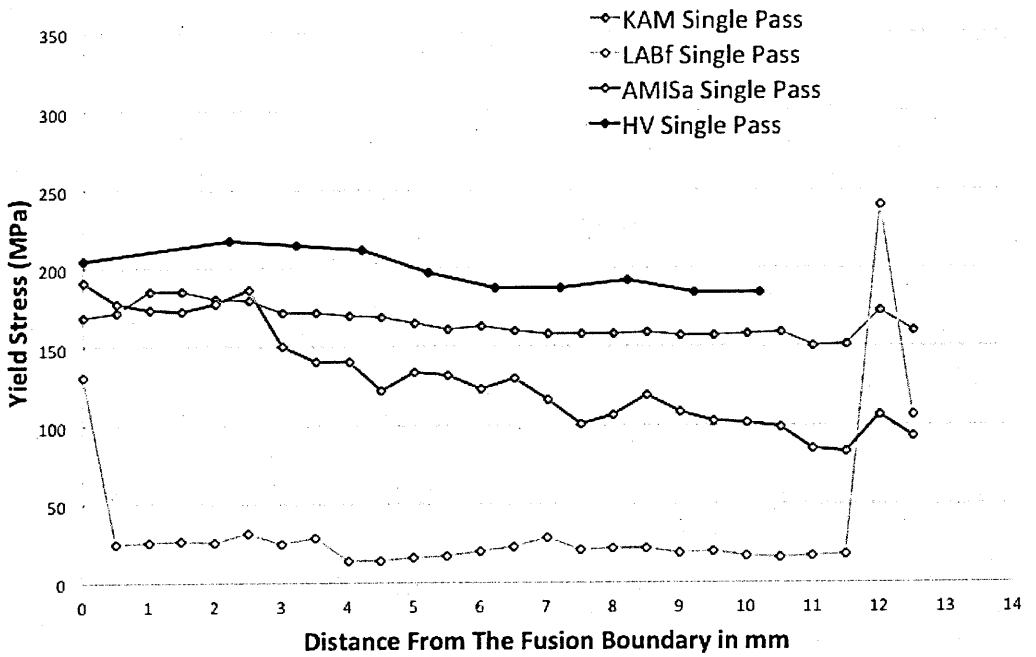

(b)

Figure 6.31 Two Pass: (a) Quantified plastic strain (accuracy of ±0.015) (b) Quantified equivalent yield stress (accuracy of 20MPa)

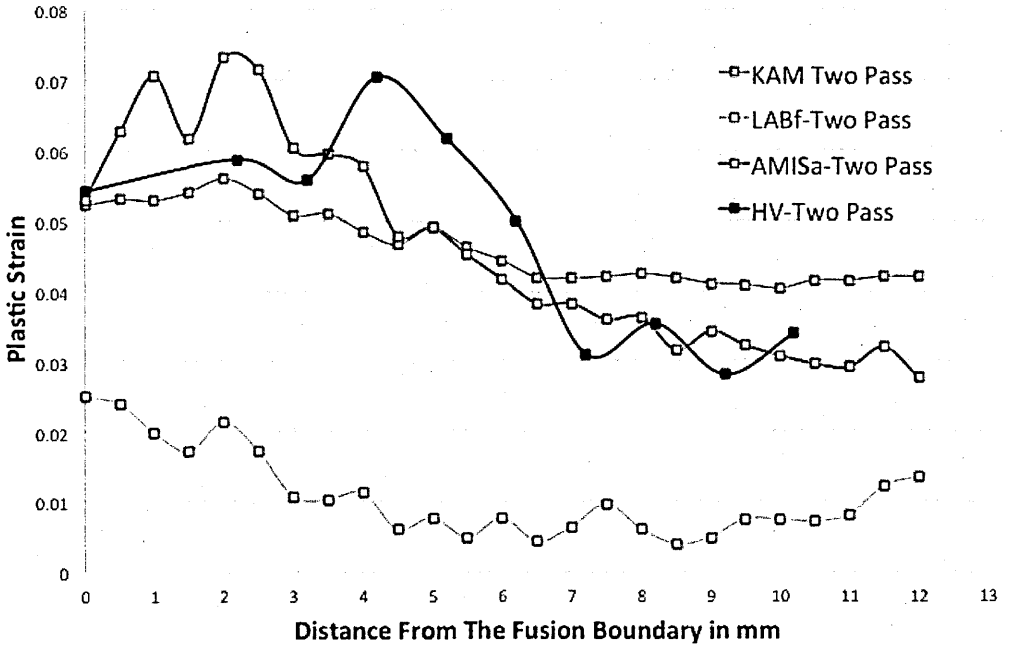

(a)

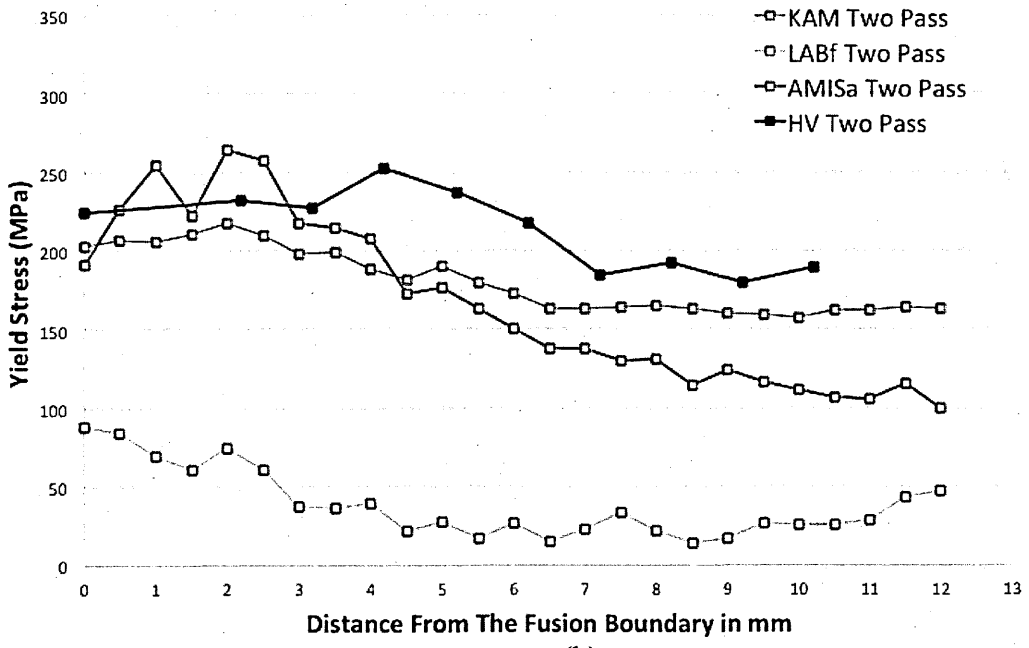

(b)

Figure 6.32 Three Pass: (a) Quantified plastic strain (accuracy of ±0.015) (b) Quantified equivalent yield stress (accuracy of 20MPa)

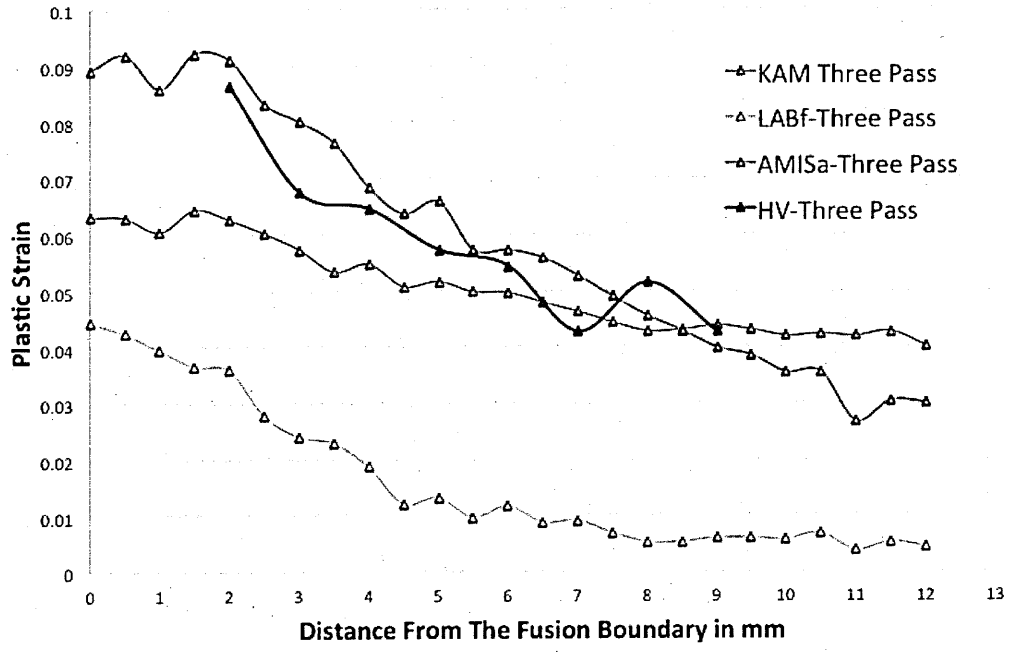

(a)

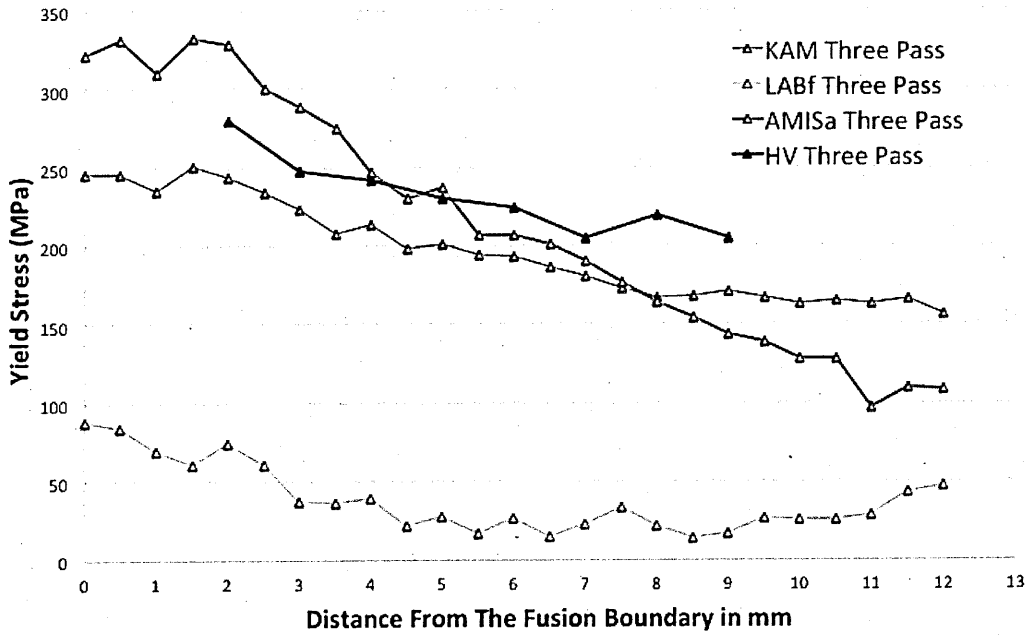

(b)

Figure 6.33 (a) Comparison of plastic strain results with those of Angeliu *et.al* [250] (b) Series of selected areas for EBSD analysis

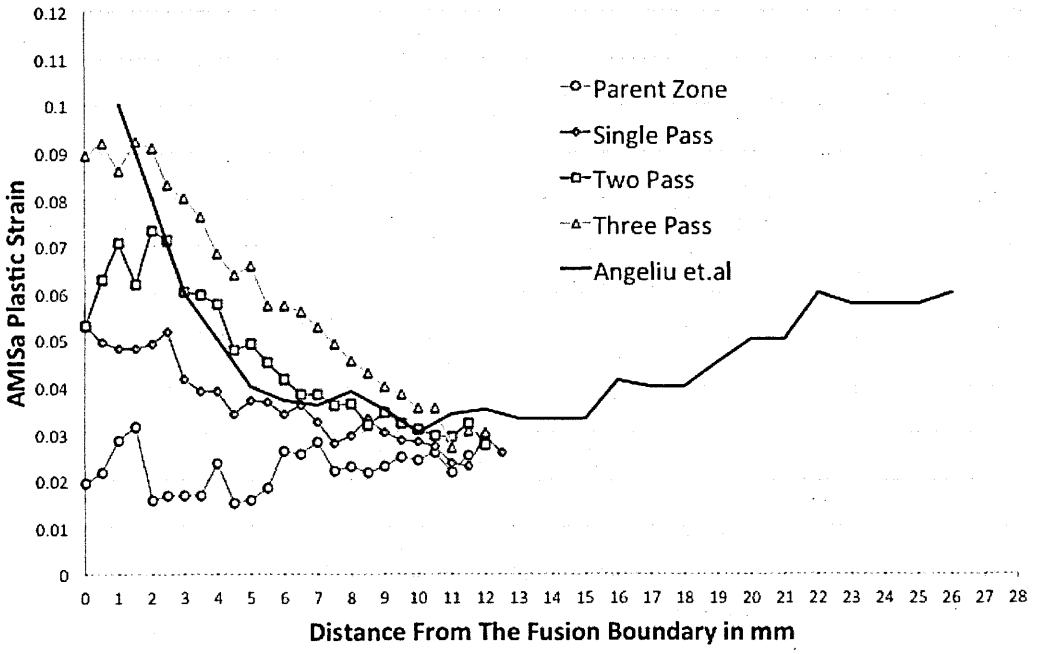

(a)

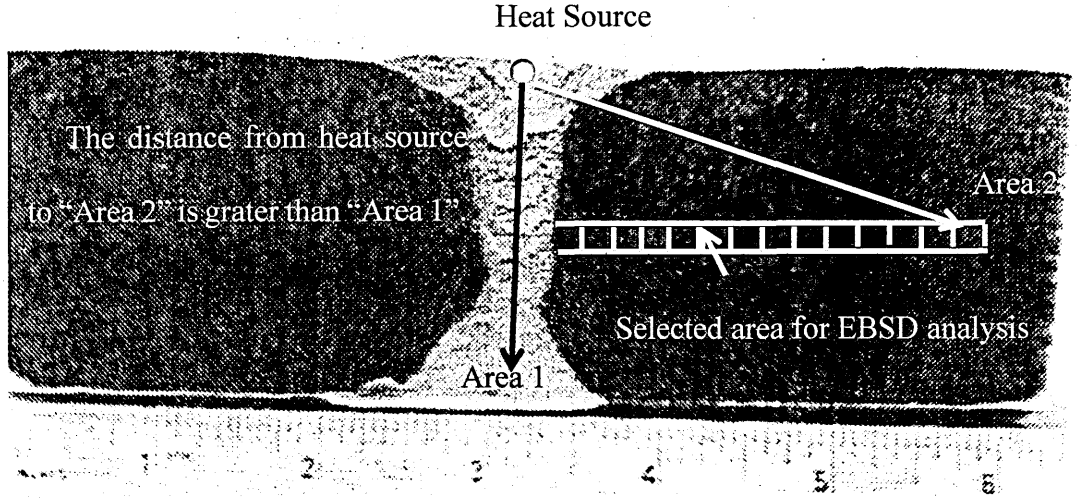

(b)

Figure 6.34 Comparison of plastic strain results with those of Saez Maderuelo et al.

197

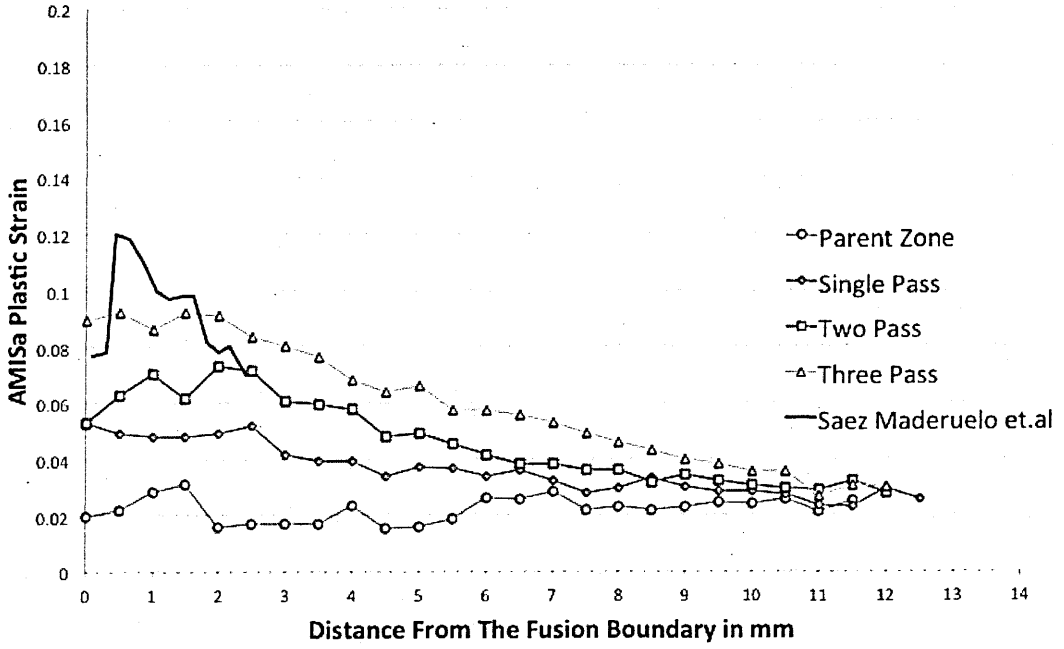

Figure 6.35 Comparison of plastic strain results with those of Hou *et al.* [198]

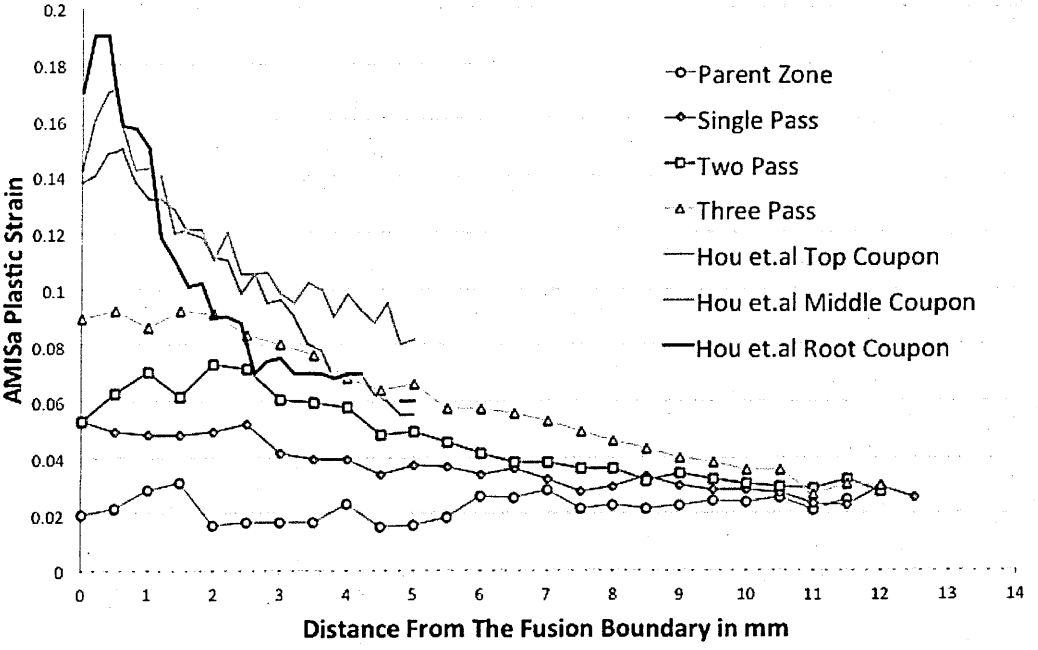

Figure 6.36 PEEQ predicted results [22]

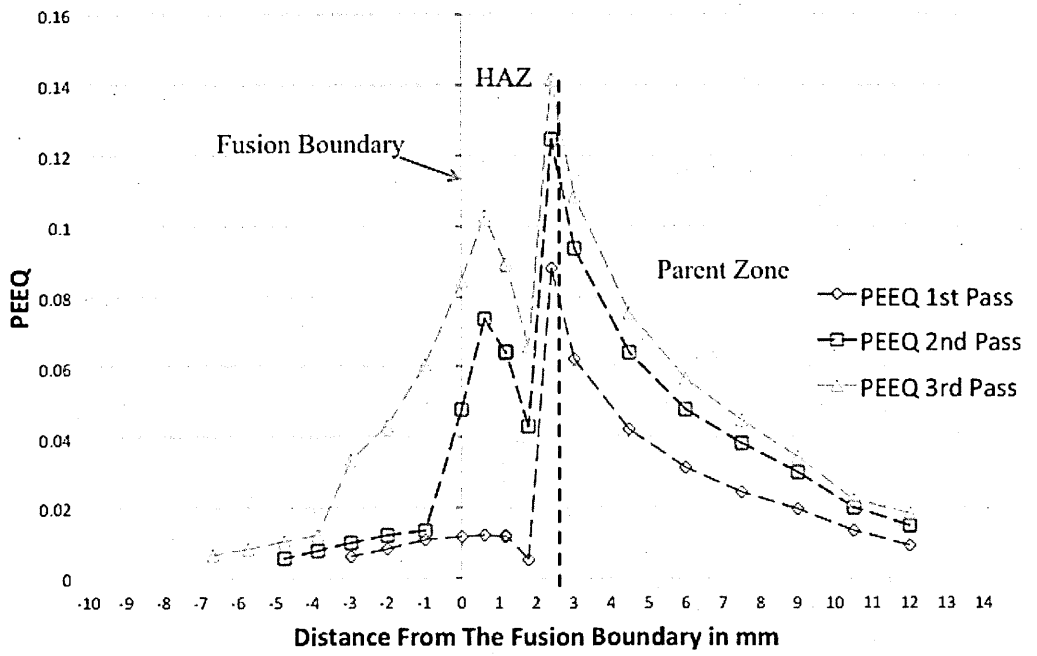

Figure 6.37 Comparison of quantified EBSD results with macro-hardness and ABAQUS prediction (a) Single pass (b) Two pass and (c) Three pass

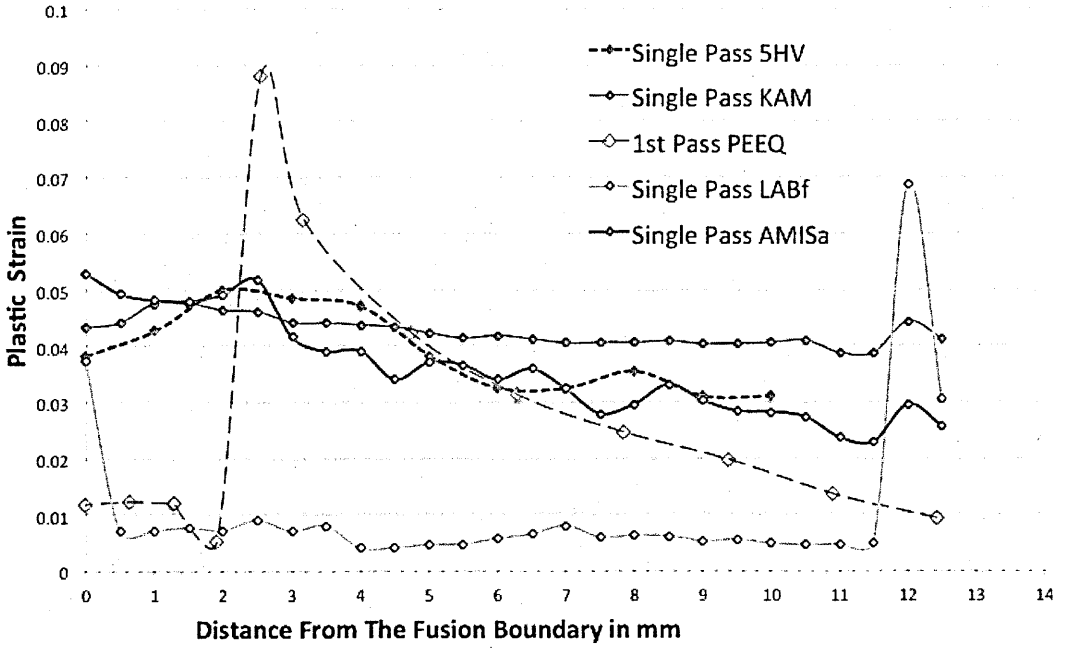

(a)

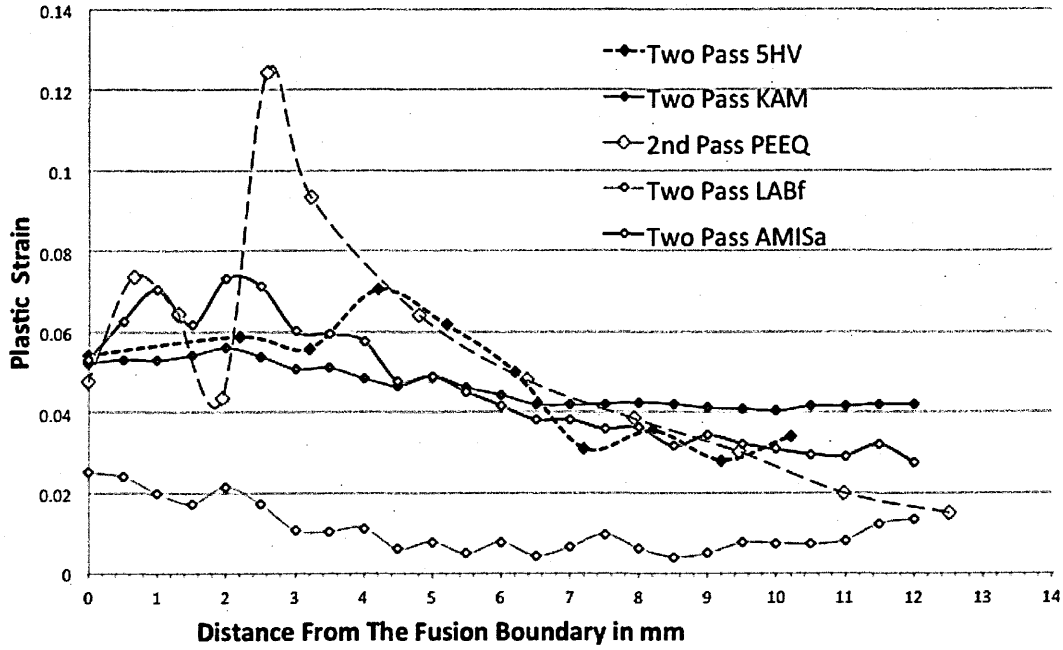
Two Pass 5HV
Two Pass KAM
2nd Pass PEEQ
Two Pass LABf
Two Pass AMISa
Plastic Strain
Distance From The Fusion Boundary in mm

(b)

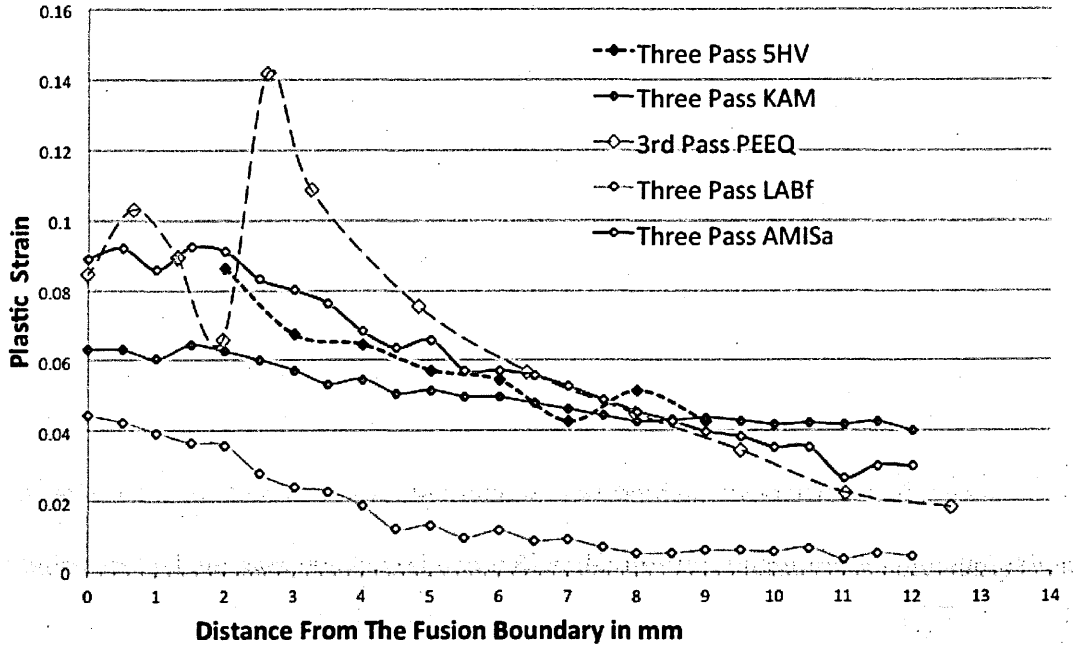
Three Pass 5HV
Three Pass KAM
3rd Pass PEEQ
Three Pass LABf
Three Pass AMISa
Plastic Strain
Distance From The Fusion Boundary in mm

(c)

CHAPTER 7. DISCUSSION

This chapter discusses the key research findings of the present work. As described earlier, this research project has analysed the residual stress distribution in a three-pass weld round robin benchmark plate and the potential origins of the measurement uncertainties. It has also investigated the contributions to possible errors in weld residual simulations of the cyclic isothermal stress-strain properties used; that is these properties sensitivities to strain rate and the type of cycle (symmetric versus asymmetric). The project has also explored the possibility of quantifying the accumulated plastic strain and stress due to the each weld bead deposit using EBSD metrics and validated the results with hardness measurements. In addition the project has investigated the limitation of various EBSD metrics in determining the accumulated plastic strain due to strain controlled cyclic loading.

7.1 Issues affecting the reliability of residual stress measurement using neutron diffraction

This thesis has analysed the distribution of residual stress in a three pass weld benchmark plate using strain diffractometers at two spallation source neutron facilities (i.e. VULCAN at SNS and ENGIN-X at the ISIS Facility). In total 76 different locations in the welded plate were measured in three orthogonal directions. In Chapter 4, VULCAN and ENGIN-X residual stress measurements have been compared independently with other measurement carried out by members of the NeT consortium at reactor neutron sources. In this section, the average of the residual stress measurements, root mean square and standard deviation along plane D (refer Figure 3.3 (a) Benchmark specimen

dimensions (b) Benchmark specimen dimensions and slot configuration (a)) evaluated from the spallation and reactor neutron sources were compared, refer Table 7.1 and Figure 7.1 to 7.4.

Figure 7.1 (b) and (c) show how the transverse and normal residual stresses measured from the spallation and reactor neutron source are in very good agreement with each other. However, the longitudinal residual stresses measured in the parent zone, i.e. from 10 to 17 mm below the top surface, differ by approximately 50 MPa, as seen in Figure 7.1(a). Figure 7.2 compares the residual stresses along a line at a depth of 5 mm beneath the surface of the single pass weld bead. The residual stress measurements in the parent zone (i.e. -90 to -40 mm and 40 to 90 mm) agree very well with each other, but differ by about 50 MPa in the region of the weld slot (i.e. -40 mm to 40 mm) in all three directions. Figure 7.3 compares the residual stress at depth of 9 mm from the top surface. The average transverse and normal residual stresses from both neutron sources are in very good agreement. However, the longitudinal residual stress results show a difference of approximately 50 MPa along the length of the scan. Figure 7.4 shows how the residual stresses at a depth of 16 mm from surface are in excellent agreement with each other.

Measurement uncertainties associated with the stress free cuboids, discussed in Chapter 4, may be contributing to systematic differences in the results from the spallation and reactor neutron sources. Perhaps more important is that at the reactor neutron sources only one diffraction peak (the 311) was analysed, while at the spallation sources more than 10 hkl peaks were analysed. Therefore far fewer grains were sampled at the reactor sources compared with the spallation sources. The grain size of the weld cuboids was very big in comparison to the parent cuboids; refer Figure 6.19 of Chapter 6. As a result of this, the number of grains diffracting in a given gauge volume in the weld cuboids was lower than the parent cuboids. At the spallation neutron source, the average of multiple

measurements of the different stress-free cuboids were used in the residual stress analysis. As a result of this, stress free cuboid issues such as the number of grains diffracting, the effects of crevices and glue were reduced or averaged out. While, at the reactor sources single value measurements of the different stress-free cuboids were used in the residual stress analysis.

Another potential origin of uncertainty (described earlier in Chapters 3 and 4) is associated with fact that the parent and weld stress free cuboids were extracted from different weldments; the weld trial plate (ID 1-2B) and the three pass welded benchmark plate (ID 2-1B). Hardness measurements for the weld trial plate (refer Figure 4.32 of Chapter 4) clearly indicated an interaction between the thermal effects of the adjacent three-pass and two pass welds.

Figure 7.5 schematically shows the cyclic deformation of material at a specific point adjacent to a three-pass weld. During heating from room temperature to above 1000°C, the material experiences compressive plastic strain from A to C as indicated in the Figure. From A to B material undergoes elastic deformation and from B to C, plastic deformation. While, in cooling from 1000°C to 0°C, the material experiences tensile plastic strain from C to E, where, C to D is elastic deformation and from D to E is plastic deformation. By the end of the cooling, the material stores tensile strain, due to constraint coming from the neighbouring material. As a result of this there will be no tensile stress unloading and the proof stress of the material has increased from its initial yield stress value. During the second weld bead deposit, the distance from the heat source of the material at the point of interest has increased, which reduces the degree of deformation (i.e. strain range) due to the lower peak temperature experienced. During heating from the second weld pass, the material undergoes a second cycle of compressive plastic strain from E to G (E to F is elastic deformation and F to G plastic). The proof stress of the material during the

reverse cycle E to G will be less than the previous weld deposit, due to the Bauchinger effect. However, during the cooling process (i.e. G to I) the material gets more strain hardened, than during the first weld pass. A similar cyclic deformation mechanism occurs during the third weld bead deposit (i.e. I to K during heating and K to M during cooling) and the material gets a bit more strain hardened in comparison to the two pass weld deposit. When a two-pass weld bead is deposited close enough to the three pass weld, the possibility of interaction of the weld thermal history with that of the adjacent three-pass weld is high. As a result of this, the original three-pass weld would have experienced two additional stress-strain cycles due to the adjacent two-pass weld deposit.

The Line B2 longitudinal and transverse residual stress results from neutron diffraction (refer Figure 4.22) and the EBSD AMISa yield stress in parent zone (refer section 6.7.4 and Figure 6.29 yield stress from parent zone to fusion boundary), indicated that the material at 30 mm away from the centre of the three pass weld bead experiences a stress about 50 to 100 MPa due to the three pass weld thermal history. In the weld trial plate (ID 1-2B, from which the 1-2B stress free cuboids are extracted) at 30 mm distance from centre of three-pass weld, the two-pass weld bead was deposited. Which means the adjacent three-pass weld bead experienced a further two loading cycles. As a result of this, the nominally stress free cuboids extracted from the weld trial plate may have had higher inter-granular stress present than the three-pass weld benchmark plate. The effect of the higher inter-granular stress is clearly visible in the Line D5 residual stress (i.e. -40mm to 40mm). However, this hypothesis would only be valid if the two-pass weld was made after the three-pass, but there is no recorded information regarding the actual welding sequence for the trial plate.

Another possible reason contributing to the difference in the residual stresses measured is that the alignment of the benchmark plate at each experimental setup would have

varied. The precise alignment of the sample allows the user to position the sample accurately. However, the facilities available to the user at different diffractometer instruments for aligning the sample vary.

The presence of crevices, the hydrogen content of the glue and the non-parallel edges of the stress-free cuboids all contribute to experimental uncertainties in the measured residual stress. In addition to experimental uncertainties, the inhomogeneity of the stress-free cuboids such as in grain size (refer Figure 6.26), and the non-uniform chemical segregation, lead to the generation of pseudo strains in a residual stress analysis.

7.2 Effect of strain rate and asymmetric cyclic deformation on weld simulation prediction

Chapter 5 has investigated the influence of strain rate and asymmetric versus symmetric cyclic loading on the stress-strain response of parent 316L (N) stainless steel, as asymmetric cyclic loading is a closer representation of real weld thermal cyclic deformation. A series of isothermal cyclic loading tests have been conducted at room temperature and 550°C for a constant total strain range and various strain rates. However, in real welding, the rate of heating and cooling is not uniform. As a result of this the material experiences a different total strain range and varying strain rates depending on the distance of the material from the heat source and the component geometry. In addition, the rate of strain hardening of the material during heating is less than that during the cooling process.

As a first approximation, the strain rate experienced by material around a weld is proportional to the rate of change of the temperature. During heating, the temperature increases very fast from room temperature to the melting point, while the rate of cooling

from 1000°C to room temperature is very slow (refer Figure 6.20 of Chapter 6). In the temperature range 300 °C to 650 °C, the material strain hardens more at a slower strain rate due to dynamic strain ageing. This is because, at slow strain rates, in the dynamic strain ageing regime, strong interactions between solute atoms and mobile dislocations reduces the number of mobile dislocations available to accommodate the required plastic deformation. As a result of this, the flow stress increases, and the material strain hardens. Most weld simulations in the published literature ignore the effect of strain rate on the strain hardening of the material at high temperature.

In welding, the material undergoes asymmetric cyclic deformation as described in section 5.3.1 of Chapter 5. The material strain hardens less during asymmetric cyclic loading than in symmetric cyclic loading both at room and high temperature. This is because when the total strain range is low, fewer dislocations are generated and the planar structure of dislocations continues to a higher number of cyclic loads. While with a higher total strain range, i.e. symmetric cyclic loading, material gets strain hardens more due to the increase in dislocations density.

The effective stress is the average of the initial yield stress and the final saturated peak stress achieved during loading. While the back stress [67] is the average difference of the saturated peak stress and initial yield stress (see Figure 7.6). The back stress is related to the collective long-range interaction of dislocations which arise during reverse cyclic loading and is due to the heterogeneous grain properties of the material. Minh-Son Pham [93] studied the relationship between microstructure and back stress in 316L stainless steel. His studies showed the rate of change of back stress and effective stress decreases with reducing total strain range at both room and high temperature.

In weld simulation the Chaboche mixed hardening model (refer section 2.3.5 of Chapter 2) has been used to predict residual stress. The mixed hardening model describes

the translation of the yield surface in the stress space using the back stress $\dot{\alpha}$, which is expressed in equation 2.8 of Chapter 2 as [24]

$$\dot{\alpha} = C_i \frac{1}{\sigma^0}(\sigma - \alpha)\dot{\varepsilon}^{pl} - \gamma_i \alpha \dot{\varepsilon}^{pl}$$

Where Ci, γi, $\dot{\varepsilon}^{pl}$, σ and σ^0 are parameters usually evaluated from symmetric (tensile-compressive) cyclic deformation testing as described in section 2.3.5 of chapter 2. However, from Pham's [93] studies, the back stress and effective stress (i.e. the size of the yield surface) increase with increasing total strain range. This means that employing a hardening model using input parameters evaluated from symmetric cyclic loading may predict higher stress values than using a model based on input parameters derived from asymmetric cyclic loading. In reality, during welding the surrounding material deforms asymmetrically in compression over a lower total strain range than usually represented in symmetric cyclic tests, see Chapter 5.

In addition, ignoring the effect of strain rate further increases the risk of predicting higher stress values during weld simulations, because increasing or decreasing the strain rate (which depend on the temperature) can lead to significant increases or decreases in the initial yield stress, back stress, rate of strain hardening of the material and area of stress-strain loops. However, in real welding the material experiences a range of strain rates throughout the thickness of the material. It would be very expensive and challenging to perform isothermal asymmetric cyclic test for each strain rate at different temperatures. The results of this study would recommended to perform representative thermo-mechanical fatigue tests to collect data to calibrate weld simulation models.

7.3 Exploring the possibilities of quantifying plastic strain using different EBSD metrics

In the published literature different EBSD metrics have been used to quantify the accumulated plastic strain due to multi-pass welding (generally with more than 10 weld passes). However, none of the papers has explained the possibility of using different EBSD metrics to quantify accumulated plastic strain weld pass by weld pass. Chapter 6 has presented results showing how plastic strain can be quantified using different EBSD metrics. The results have been validated by hardness measurements and compared with published finite element predictions. Chapter 6 also investigated the limitation of each EBSD metric in assessing accumulated plastic strain due to symmetric and asymmetric cyclic loading.

The density of the low angle misorientations (below 2°) increases linearly with increasing monotonic plastic deformation. This is due to the fact that, with increasing monotonic plastic deformation, formation of jogs and sessile dislocations increases the density of dislocations within each grain. However, above 15% strain KAM and LABf analysis tends to so saturation [196]. In addition, at high temperatures, greater than 800°C, dynamic recovery and recrystallization processes act in austenitic stainless steel to annihilate dislocations of opposite sign. On the other hand, dislocations of the same sign align themselves into walls to form low angle sub-grain boundaries. This leads to pronounced changes in the internal stresses of the material. Thus both increasing plastic strain and recovery processes at high temperature will affect KAM and LABf metrics.

In cyclic loading, the dislocation density introduced is relatively low compared with monotonic tensile deformation because plastic strain is concentrated in small clusters rather than being homogeneously distributed [201,203]. During cyclic loading, the crystal orientation fluctuates, which affects the average local misorientation significantly [74]. As

a result of this, the neighbouring points based misorientation metrics, KAM and LABf, are unable to provide reliable measures of total accumulated plastic strain. The evidence for this is presented in Chapter 6, where the KAM and LABf analyses indicated no variation of misorientation at both room and high temperature for symmetric and cyclic loading refer Figure 6.12 and 6.13. However, the fluctuation of dislocation density does not affect the AMISa, because it evaluates the misorientation from the central orientation. Due to this AMISa metric was very sensitive and consistently showed very good agreement with hardness measurement and PEEQ predictions.

Figure 7.7, presents the comparison of von Mises equivalent residual stress along line BD with EBSD AMISa metric yield stress results. Von Mises's theory is based on the distortion-energy stored in a material when it undergoes deformation [259]. According to von Mises's theory for ductile materials, the yielding of the material (during simple tension or compression test) occurs when the distortion energy per unit volume reaches or exceeds the distortion strain energy per unit volume. The von Mises's equivalent stress at which yielding of any ductile material is predicted to occur can be evaluated using the equation below [259]

$$\sigma' = \sqrt{0.5 * \{(\sigma_1 - \sigma_2)^2 + (\sigma_2 - \sigma_3)^2 + (\sigma_3 - \sigma_1)^2\}} \qquad (7.2)$$

Where σ_1, σ_2 and σ_3 are the principal stresses and the von Mises equivalent stresses are dependent on the isotropic expansion of the yield surface (i.e. amount of material hardening).

The von Mises equivalent stress was evaluated using the spallation neutron residual stress results along line BD. The EBSD quantified yield stress shows slightly lower stress results in comparison to the von Mises residual stress but they agreeing within about 50MPa. A possible reason for this difference could be due to the fact that the gauge

volume $3\times3\times3$ mm^3 used for measuring residual stress in the neutron diffraction experiment was higher than the selected area (1×0.5 mm^2) for EBSD analysis. As a result, more diffracting grains were analysed in the neutron diffraction experiment.

The EBSD AMISa results constantly showed very good agreement with hardness, PEEQ and von Mises equivalent stress. From the results (refer Figure 6.37 and Figure 7.7), it is evident that EBSD AMISa metric can quantify the accumulation of plastic strain due to each weld pass. This means EBSD analysis can supports the NeT consortium to improve the prediction of weld stresses and strains and the life time of the structural components by validating the predicted results with EBSD AMISa plastic strain and yield stress results.

7.4 Table

Table 7.1 Comparing Root Mean Square (RMS) and standard deviation of spallation and reactor neutron source residual stress measurements

Spallation Source			
line BD			
	Transverse (MPa)	Normal (MPa)	Longitudinal (MPa)
RMS	167.86	22.48	317.59
Standed deviation	81.56	17.18	60.01
Line D5			
	Transverse (MPa)	Normal (MPa)	Longitudinal (MPa)
RMS	233.45	56.71	316.05
Standed deviation	194.45	52.62	140.91
Line D9			
	Transverse (MPa)	Normal (MPa)	Longitudinal (MPa)
RMS	111.80	28.29	244.56
Standed deviation	112.53	26.64	135.16
Line D16			
	Transverse (MPa)	Normal (MPa)	Longitudinal (MPa)
RMS	46.63	16.03	111.13
Standed deviation	45.95	14.29	89.11

Reactor source			
line BD			
	Transverse (MPa)	Normal (MPa)	Longitudinal (MPa)
RMS	149.78	24.33	318.13
Standed deviation	87.79	20.68	65.97
Line D5			
	Transverse (MPa)	Normal (MPa)	Longitudinal (MPa)
RMS	202.75	20.38	289.67
Standed deviation	180.52	18.63	120.60
Line D9			
	Transverse (MPa)	Normal (MPa)	Longitudinal (MPa)
RMS	110.80	26.87	281.43
Standed deviation	111.24	20.85	140.22
Line D16			
	Transverse (MPa)	Normal (MPa)	Longitudinal (MPa)
RMS	44.37	9.24	116.05
Standed deviation	45.46	9.10	79.82

7.5 Figures

Figure 7.1 Comparison of the average residual stresses measured at spallation and reactor neutron sources along line BD (a) Longitudinal (b) Transvers and (c) Normal

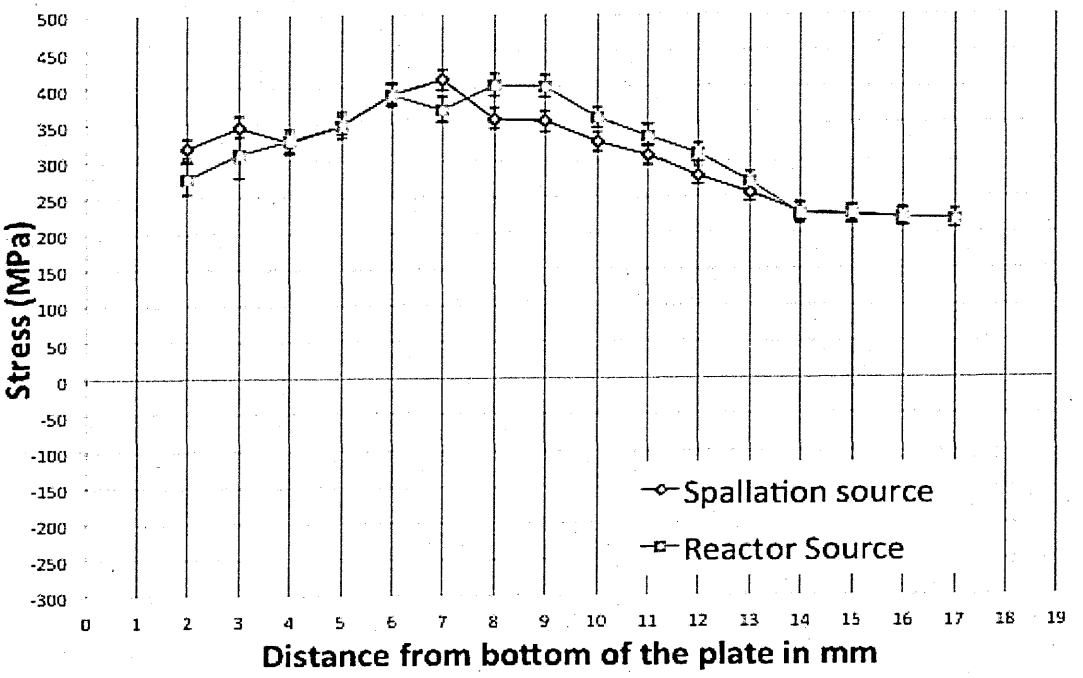

(a)

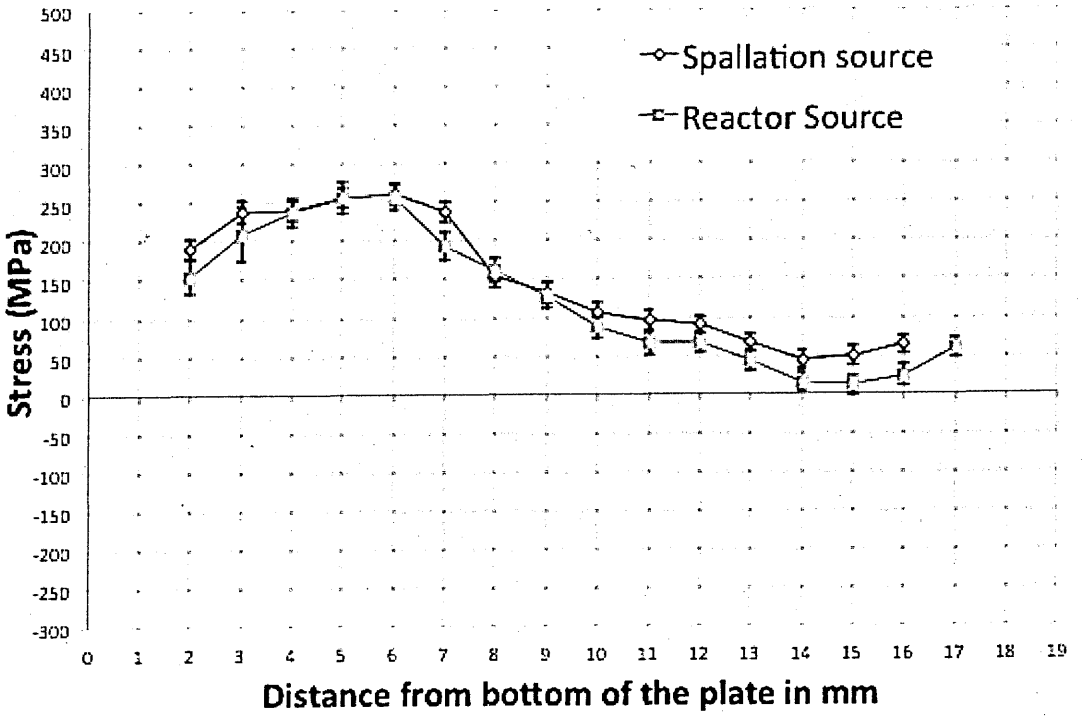

(b)

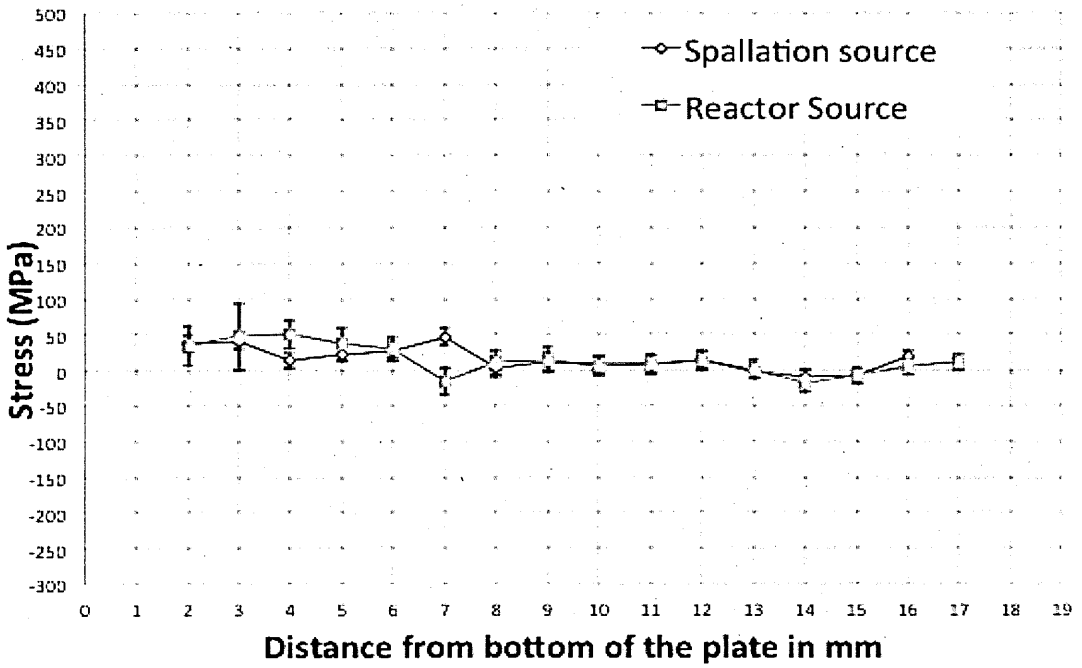

(c)

Figure 7.2 Comparison of the average residual stresses measured at spallation and reactor neutron sources along line D5 (a) Longitudinal (b) Transverse and (c) Normal

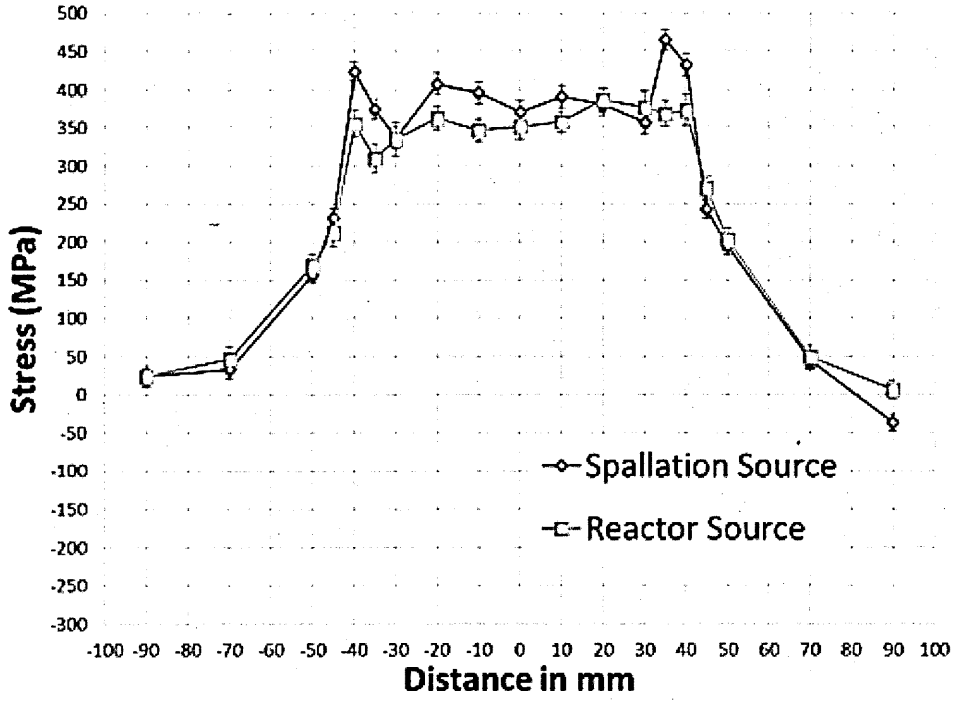

(a)

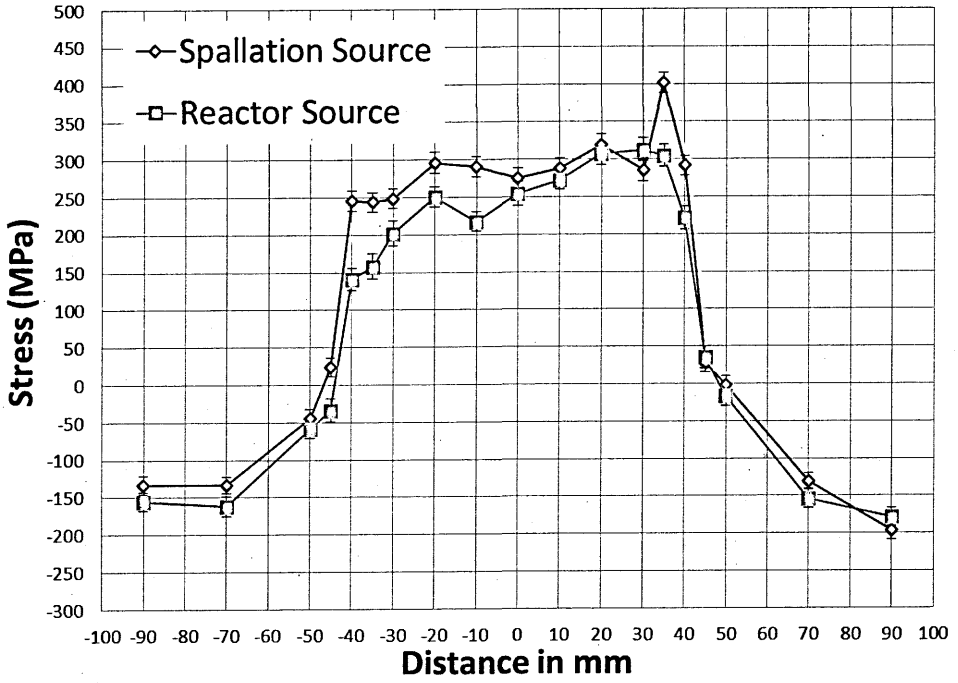
Spallation Source
Reactor Source
Stress (MPa)
Distance in mm

(b)

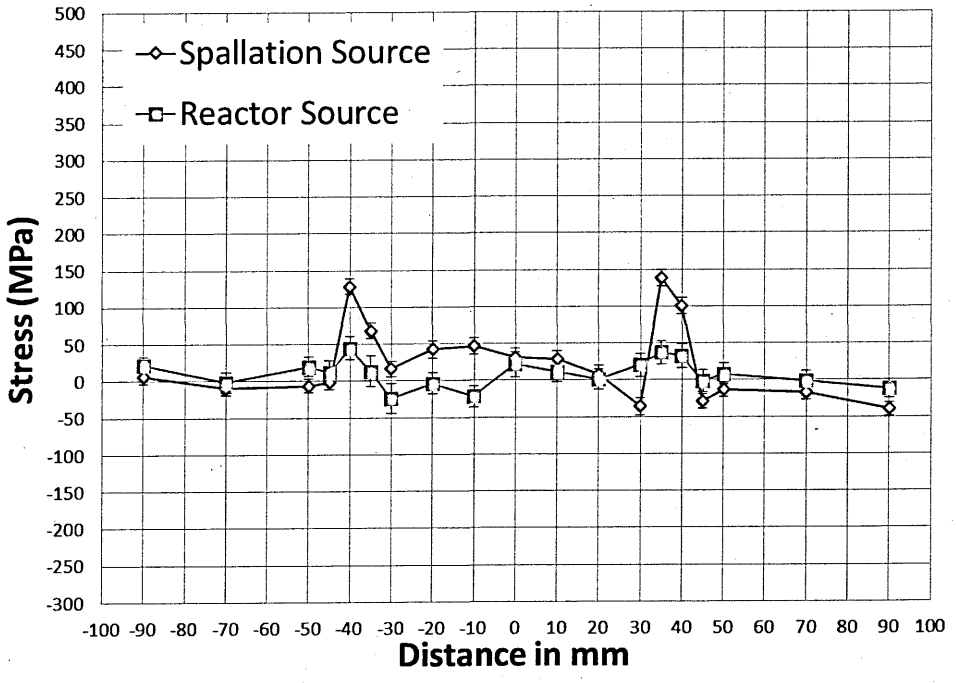
Spallation Source
Reactor Source
Stress (MPa)
Distance in mm

(c)

Figure 7.3 Comparison of the average residual stresses measured at spallation and reactor neutron sources along line D9 (a) Longitudinal (b) Transverse and (c) Normal

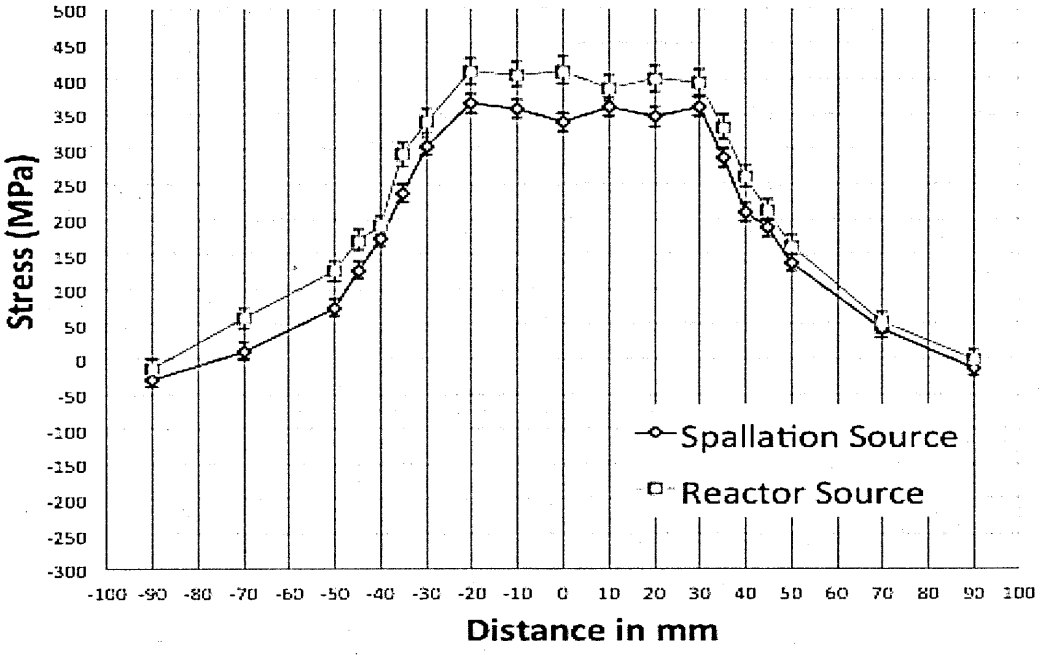

(a)

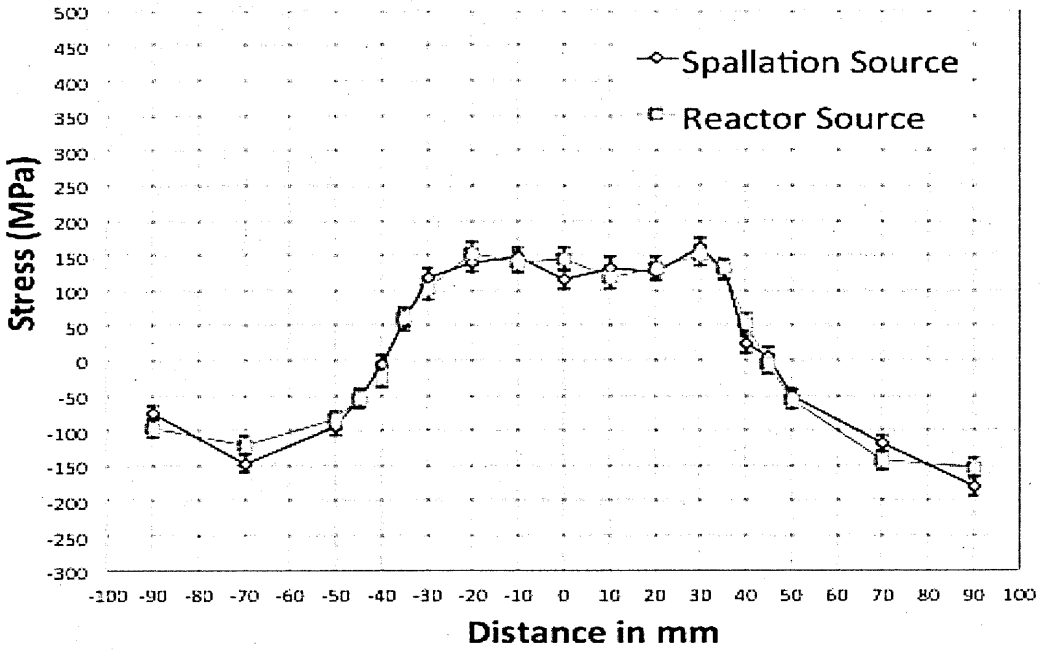

(b)

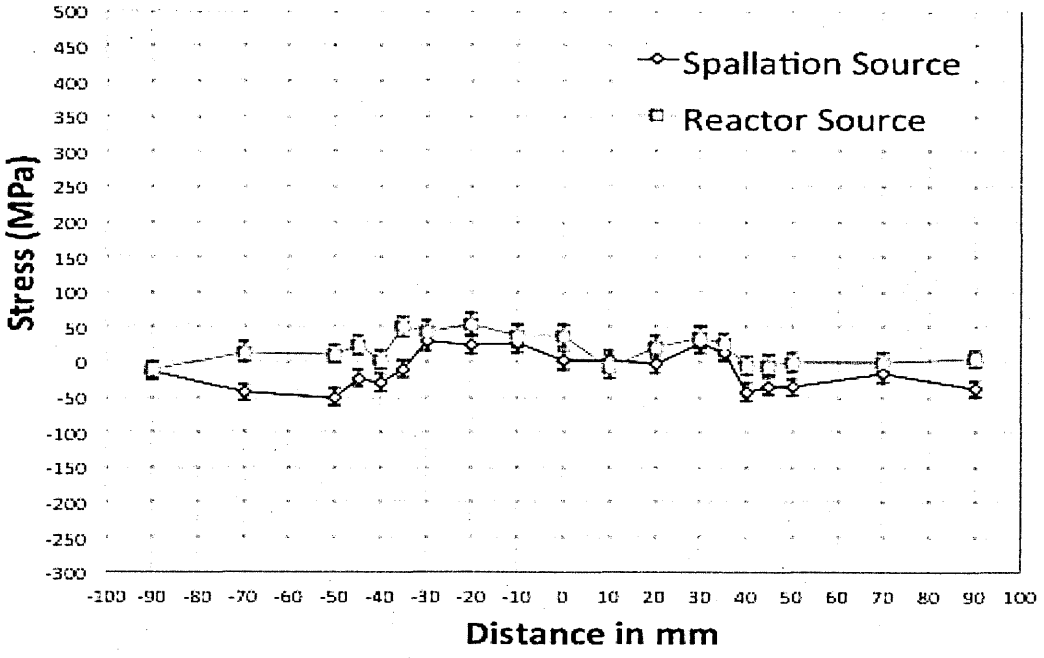

(c)

Figure 7.4 Comparison of the average residual stresses measured at spallation and reactor neutron sources along line D16 (a) Longitudinal (b) Transverse and (c) Normal

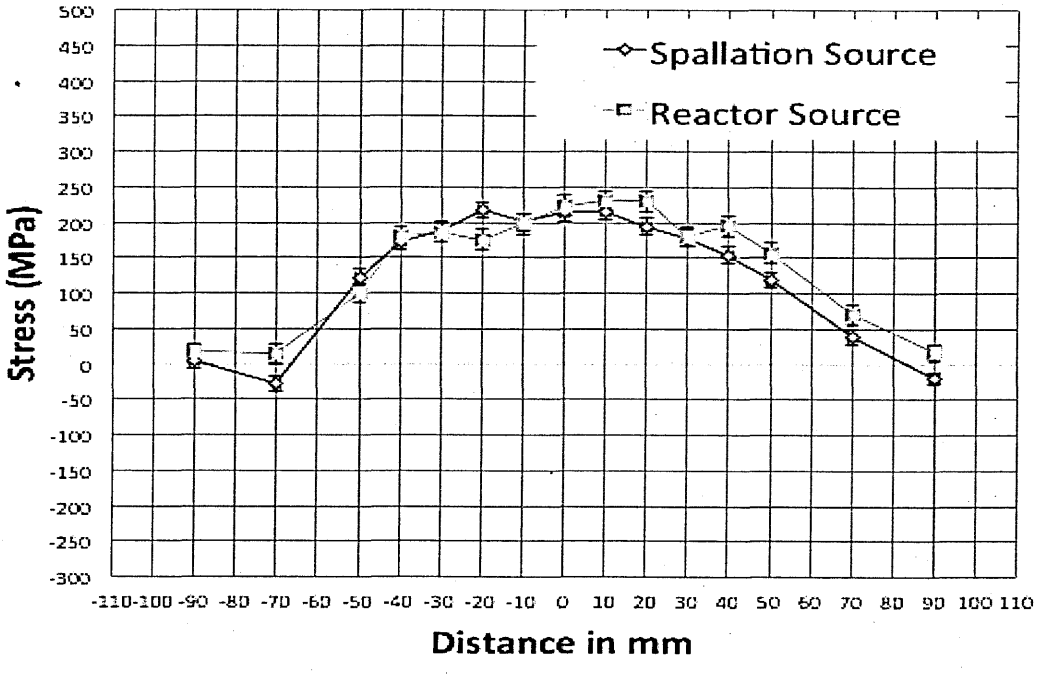

(a)

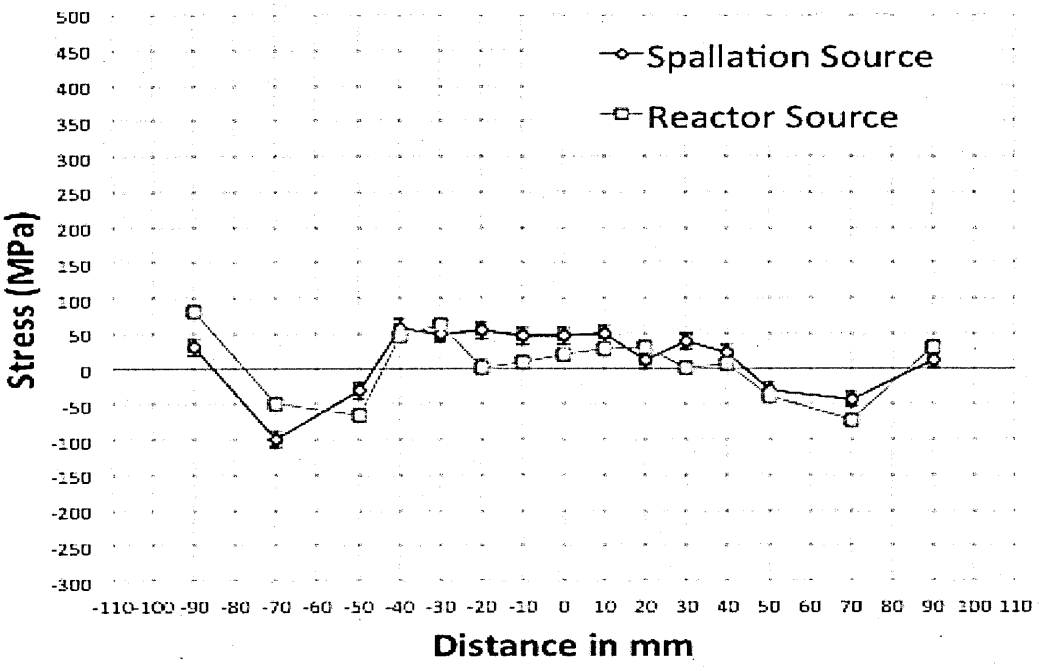
Spallation Source
Reactor Source
Stress (MPa)
Distance in mm

(b)

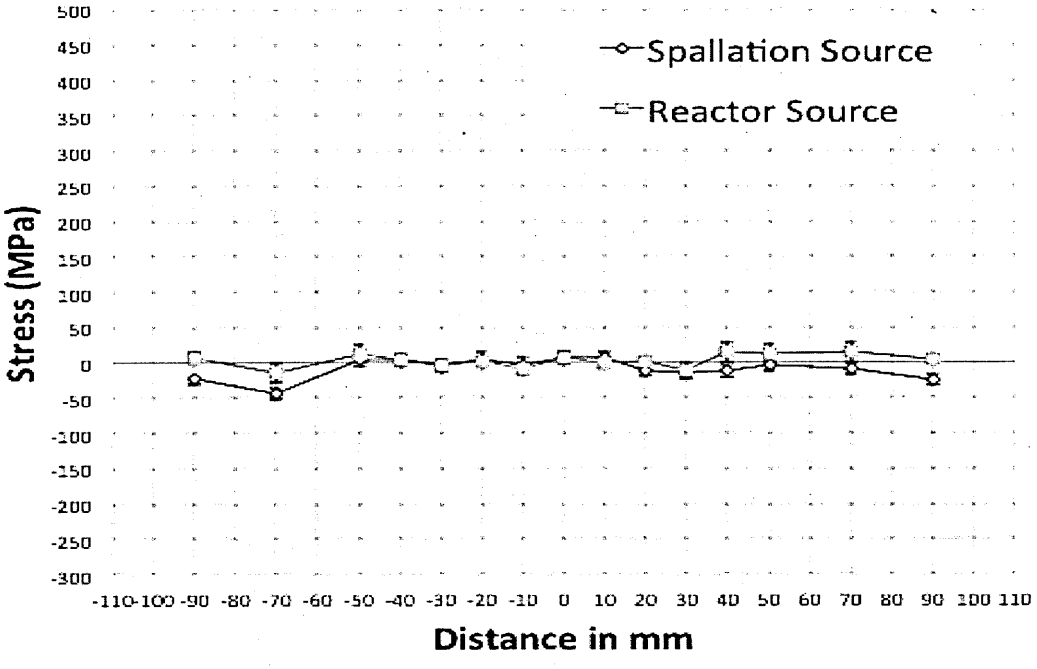
Spallation Source
Reactor Source
Stress (MPa)
Distance in mm

(c)

Figure 7.5 Schematic diagram showing stress-strain curves near HAZ of three pass weld [63]

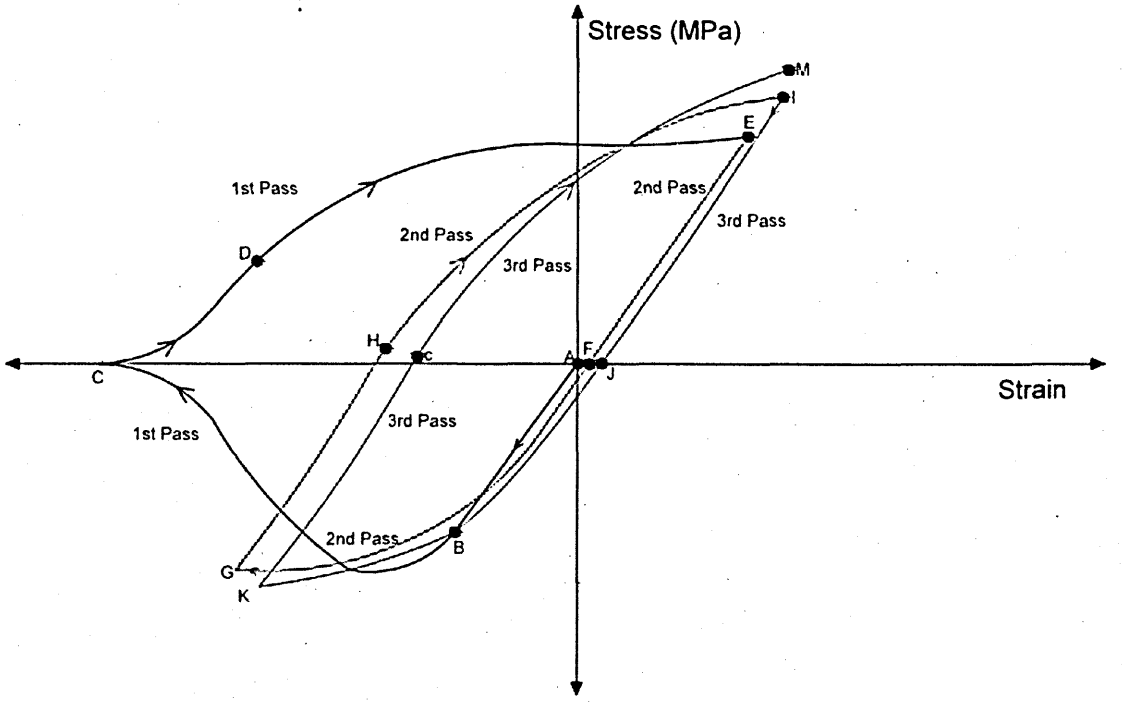

Figure 7.6 (a) Schematic diagram of effective stress and back stress [93] (b) Effective stress and back stress on cyclic stress-strain loops.

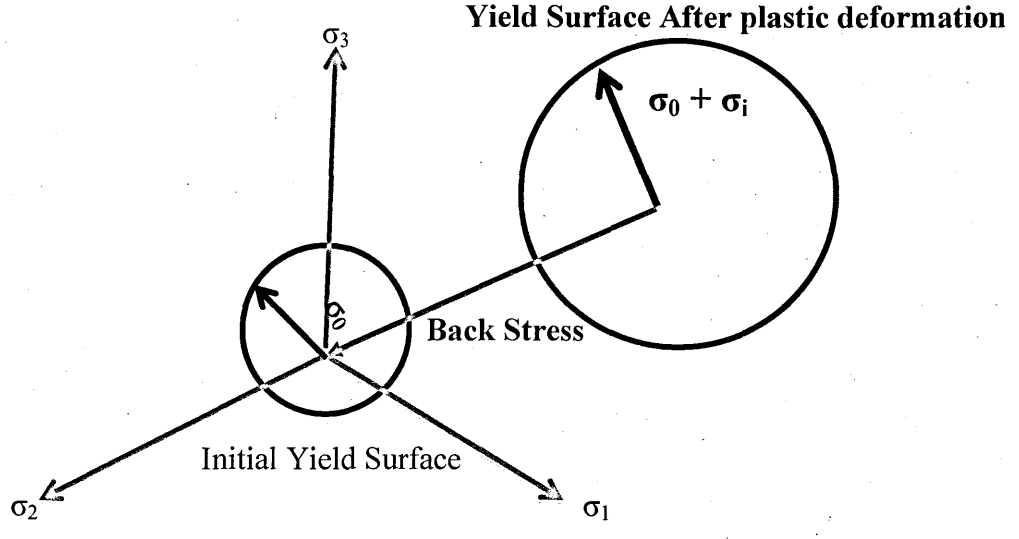

(a)

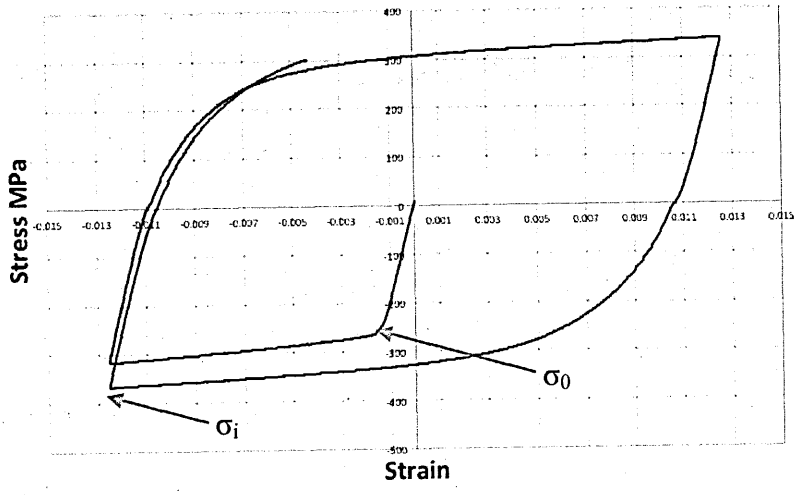

(b)

Effective stress = $(\sigma_0+\sigma_i)/2$

Back stress = $(\sigma_i- \sigma_0)/2$

Figure 7.7 Comparison of EBSD metrics yield stress (accuracy of ±20MPa) with von Misses equivalent principle stress

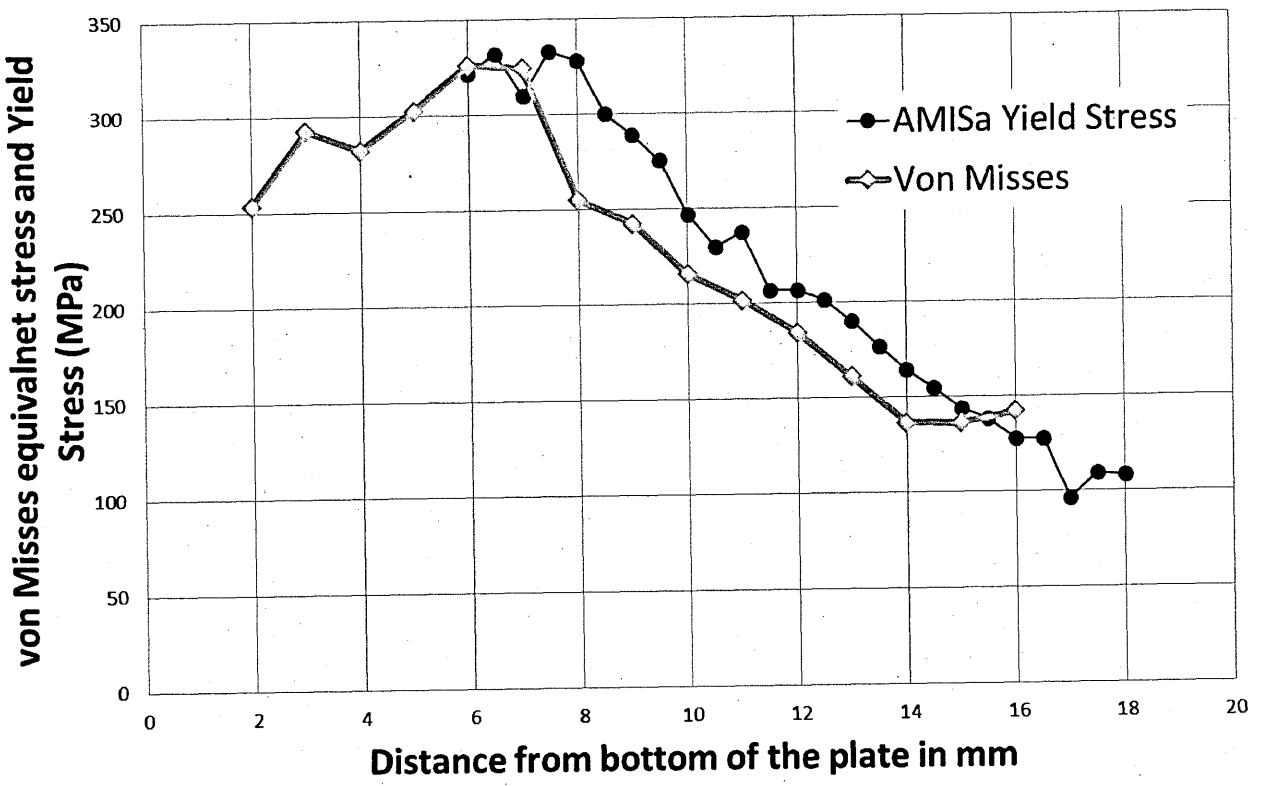

CHAPTER 8. CONCLUSIONS AND FURTHER WORK

This chapter draws conclusions from the investigations reported in this thesis and recommends further work. The project has researched the residual stress distribution and accumulated plastic strain in a benchmark welded AISI 316L(N) austenitic stainless steel plate and studied the strain hardening behaviour of the plate material under symmetric and asymmetric cyclic loading, with different strain ranges and strain rates.

8.1 Conclusions

In the first part of this study (Chapter 4), the residual stress distribution in a three-pass welded austenitic stainless steel plate was measured using neutron diffractometers at two spallation sources (VULCAN at SNS and ENGIN-X at the ISIS Facility). The objective of this work is to identify all the issues affecting the reliability of residual stress characterization in the NeT-TG4 weldment. The following conclusions were reached:

Material Issues

1. According to the neutron diffraction standards and recommendations [135] by Webster, stress free cuboids should be extracted from the original sample or an identical sample. This is to minimize additional uncertainties developing due to using the wrong stress free lattice parameter in residual stress evaluation. However, the stress cuboids extracted from the weld trial plate 2-1B may not be identical to the analysed three pass benchmark plate.

Experimental Issues

2. One of the potential issues contributing in systematic difference in measured residual stress is due to large difference in measured lattice parameter between Bank 2 of ENGIN-X and VULCAN. This differences is possibly associated with the one of the detector components. Further investigation is required to identify, whether the cause of this problem is due to some technical issues associated with instrument detector or something else.

3. In addition to the measured lattice parameter variation, another main contribution to generating pseudo strains is due to the presence of crevices, super glue and misfit between the individual elements of the stress free cuboid. This leads to significant difference in the measured residual stress.

Residual stress measurements

4. The highest tensile stresses were observed in the first pass weld metal (line D5) and the heat-affected zone (line BD) at a magnitude of 400- 450 MPa.

5. The residual stress analysis was performed at different depths of the welded benchmark plate with respect to weld bead at VULCAN and ENGIN-X neutron diffractometers. Many of the residual stress results measured at different depths in the various sets (i.e. Line BD, D2, D5, D9, D16, B2 and B16) of the welded plate were observed to differ within ±100 MPa.

6. The residual stress measurements results from ENGIN-X and VULCAN neutron diffractometers are comparable (±50 MPa) with those measurements carried out by others at FRM-II, HZB reactor source diffractometers.

In the second part of this research study (Chapter 5), the isothermal strain hardening behaviour of solution annealed 316L material, during symmetric and asymmetric cyclic loading, was measured and compared with predicted behaviour based upon a mixed

hardening model previously used for weld residual stress modelling. The objective of this part is to investigate the magnitude of the possible errors arising from ignoring the strain rate effects and input parameters which are evaluated from symmetric (tensile-compressive) cyclic deformation testing for mixed hardening model. The following conclusions were made:

7. The strain hardening of the solution annealed 316L(N) base plate material varied according to whether symmetric or asymmetric cyclic loading was applied. Asymmetric cyclic loading introduced, 50 MPa less strain hardening at room and high temperature respectively than symmetric cyclic loading. As asymmetric cyclic loading more closely represents material deformation around welds, it is recommended that the mixed hardening parameters for weld residual stress hardening models should be derived from asymmetric cyclic loading rather symmetric cyclic loading data.

8. The strain rate of cyclic tests was found to affect the yield stress and rate of hardening (50MPa at room and high temperature respectively) and therefore should be accounted for in deriving mixed hardening parameters for weld residual stress hardening models.

9. A mixed hardening model has previously been used for predicting residual stresses in the NeT TG4 benchmark weldment. In the present work (Chapter 5), the same reproduced model under predicted the measured cyclic strain-stress loops at high temperature (by 65MPa). Therefore, there is a need to develop improved models based upon more representative thermo-mechanical fatigue test data.

In the final part of this thesis (Chapter 6), the accumulation of plastic strain in parent material surrounding single pass, two pass and three pass welds was investigated using EBSD metrics and hardness mapping. In addition, the accumulated plastic strain following symmetric and asymmetric cyclic loading was studied, at different strain ranges

and strain rates, at both room and high temperature. The objective of this study is to demonstrate whether EBSD can quantify accumulated plastic strain resulting from one, two and three pass weld deposits in 316L(N) steel using different EBSD metrics. The following conclusions were reached from these experimental studies:

10. Different EBSD metrics (KAM, LABf and AMISa) showed a similar trend of increasing plastic strain from the bottom of the plate to the weld fusion boundary but of different magnitudes.

11. Results from the AMISa metric and hardness measurements were in good agreement with each other and could be used to validate finite element plastic strain predictions in weld residual stress simulations.

12. The assessment of accumulated plastic strain due to symmetric and asymmetric cyclic loading was analysed using the EBSD metrics KAM, LABf and AMISa. The results show that the KAM and LABf metrics are insensitive to the accumulated plastic strain at the end of each cycle under both room and high temperature cyclic loading. AMISa metric was unable to assess the accumulated cyclic plastic strain up to 36%. However, after 36% accumulated cyclic plastic strain, the AMISa metric showed the accumulated misorientation.

13. EBSD can quantify the accumulated plastic strain around welds using the AMISa metric but not with KAM or LABf metric.

8.2 Suggested future work

This research project has identified issues affecting the reliability of residual stress distribution results from neutron diffraction experiments. However, some key questions require further research. For example, from the literature review [140,141,151], it was clearly evident that the extraction of, and the geometry of, the 'stress free' lattice sample, has

some significant consequence in determining the reliability of residual stress measurements. Therefore, further research is required to understand the influence that the geometry of stress free samples has in determining the residual stress.

Due to limitations in the supply of material, the accumulated plastic strain in the weld itself metal was not quantified in this project. The deformation of the grains, the grain size and the texture of weld metal is different from the base metal. In order to quantify the accumulated plastic strain, a misorientation calibration curve evaluated from the weld sample, at high temperature, is required.

In the real world, most of the time austenitic stainless steel, and other metals, undergo asymmetric cyclic loading during service. For example, pipelines on the seabed undergo complex asymmetric deformation, due to changes in environmental conditions. Similarly, component materials in power plants undergo asymmetric cyclic deformation due to fluctuations in energy demands and environmental changes. For the first time, this research study has investigated material strain hardening behavior during asymmetric cyclic loading, at different strain ranges and strain rates, as well as providing an assessment of accumulated plastic strain using EBSD and hardness testing. However, dislocation structures and their role during asymmetric cyclic loading, was not analysed using TEM. TEM examination would give the enhanced knowledge of dislocation structure, fatigue life, fatigue crack propagation, etc., and will give better understanding of material behaviour at different strain ranges and strain rates.

This project has analysed strain hardening of 316L material during asymmetric cyclic loading, under strain controlled conditions. It would be interesting to extend this study to understand the behaviour of materials during strain controlled ratcheting, and include an analysis of dislocation structure, fatigue life, microstructure changes and crack propagation.

REFERENCES

1. M.McGuire. Austenitic Stainless Steel. In: *Stainless Steels For Design Engineers*. Vol Ohio: ASM International; 2008. http://www.google.com/patents?hl=en&lr=&vid=USPAT3306736&id=0pxzAAAAEBAJ&oi=fnd&dq=Austenitic+Stainless+Steels&printsec=abstract. Accessed November 1, 2013.

2. ISO 9692-1:2013. *Welding and Allied Processes -- Types of Joint Preparation -- Part 1: Manual Metal Arc Welding, Gas-Shielded Metal Arc Welding, Gas Welding, TIG Welding and Beam Welding of Steels*. http://www.iso.org/iso/home/store/catalogue_tc/catalogue_detail.htm?csnumber=62520. Accessed March 13, 2015.

3. Kou S. *Welding Metallurgy*. Vol Second Edi. Wiley Interscience; 2002.

4. Bouchard PJ. Residual Stresses in Lifetime and Structural Integrity Assessment. In: *Science and Technology*. Vol ; 2001:8134.

5. Ohms C, Neov D, Wimpory RC, Youtsos AG. Evaluation of Novel Post Weld Heat Treatment in Ferritic Steel Repair Welds Based on Neutron Diffraction. In: Gdoutos EE, ed. *PROCEEDINGS OF THE EUROPEAN CONFERENCE ON FRACTURE*. Vol European conference on fracture; Fracture of nano and engineering materials and structures. Dordrecht, Springer; 2006:1307-1308. http://libezproxy.open.ac.uk/login?url=http://search.ebscohost.com/login.aspx?direct=true&db=edsbl&AN=CN067270720&site=eds-live&scope=site.

6. Zinkle SJ, Was GS. Materials challenges in nuclear energy. *Acta Materialia*. 2013;61(3):735-758. doi:10.1016/j.actamat.2012.11.004.

7. Withers PJ. Residual stress and its role in failure. *Reports on Progress in Physics*. 2007;70:2211-2264. doi:10.1088/0034-4885/70/12/R04.

8. McGuire MF. Austenitic Stainless Steels. In: *Materials Science and Technology*. Vol 45. ; 2001:406-411.

9. Jiang W, Luo Y, Zhang G, Woo W, Tu ST. Experimental to study the effect of multiple weld-repairs on microstructure, hardness and residual stress for a stainless steel clad plate. *Materials & Design*. 2013;51(0):1052-1059. doi:http://dx.doi.org/10.1016/j.matdes.2013.05.027.

10. Li GF, Congleton J. Stress corrosion cracking of a low alloy steel to stainless steel transition weld in PWR primary waters at 292°C. *Corrosion Science*. 2000;42(6):1005-1021. doi:10.1016/S0010-938X(99)00131-6.

11. Cheng X, Prask HJ, Gnaeupel-herold T, Luzin V, Fisher JW. *Neutron Diffraction Measurements for Residual Stresses in AL-6XN Stainless Steel Welded Beams*.

12. Dong P. Recommendations for determining residual stresses in fitness-for-service applications. *Welding Research Council Bulletin*. 2002;(476):1-61.

13. Rathbun HJ, Fredette LF, Scott PM, Csontos A a, Rudland DL. NRC Welding Residual Stress Validation Program International Round Robin Program and Findings. In: *Pressure Vessels and Piping Conference*. Vol ; 2011:1-7.

14. Dong P, Hong JK. Analysis of IIW X/XV RSDP Phase I Round-Robin Residual Stress Results. *Welding Research Abroad*. 2003;49:1-8. http://libezproxy.open.ac.uk/login?url=http://search.ebscohost.com/login.aspx?direct=true&db=edsbl&AN=RN134329977&site=eds-live&scope=site.

15. Ohms C, Martins R V, Youtsos AG, et al. The Europen Network on Neutron Techniques Standardization for Structural Integrity-NET. In: *2008 ASME Pressure Vessels and Piping Division Conference*. Vol Chicago, Illinois: PVP; 2008:1-13.

16. Smith MC, Smith AC, Wimpory R, Ohms C. A review of the NeT Task Group 1 residual stress measurement and analysis round robin on a single weld bead-on-plate specimen. *International Journal of Pressure Vessels and Piping*. 2014;120-121:93-140.

17. Bouchard PJ. *Experimental Validation for Multi Pass Weld Residual Stress Predictions*. Barnwood Glasgow; 1997.

18. Bouchard PJ. Validated residual stress profiles for fracture assessments of stainless steel pipe girth welds. *International Journal of Pressure Vessels and Piping*. 2007;84(4):195-222. doi:10.1016/j.ijpvp.2006.10.006.

19. Withers PJ, Turski M, Edwards L, Bouchard PJ, Buttle DJ. Recent advances in residual stress measurement. *International Journal of Pressure Vessels and Piping*. 2008;85(3):118-127. doi:10.1016/j.ijpvp.2007.10.007.

20. Bouchard PJ, Withers PJ. The Appropriateness of Residual Stress Length Scales in Structural Integrity. *Journal of Neutron Research*. 2004;12(1):1-3.

21. Smith MC, Muransky O, Austin C, Park B, Bendeich PJ, Edwards L. Optimised Modelling of Weld Metal Constitutive Behaviour In the NeT TG4 International Weld Simulation and Measurment bechmark. In: *Pressure Vessels and Piping Conference*. Vol PVP2012-78. ; 2012:1-13.

22. Muránsky O, Hamelin CJ, Smith MC, Bendeich PJ, Edwards L. The effect of plasticity theory on predicted residual stress fields in numerical weld analyses. *Computational Materials Science*. 2012;54:125-134. doi:10.1016/j.commatsci.2011.10.026.

23. Smith MC. *Validation of Mixed Isotropic-Kinematic Material Hardening Models for Finite Element Prediction of Residual Stresses in Austenitic Steel Welds*.; 2007.

24. Smith MC, Bouchard PJ, Turski M, Edwards L, Dennis RJ. Accurate prediction of residual stress in stainless steel welds. *Computational Materials Science*. 2012;54:312-328. doi:10.1016/j.commatsci.2011.10.024.

25. Smith MC, Bate S, Bouchard PJ. SIMPLE BENCHMARK PROBLEMS FOR FINITE ELEMENT WELD RESIDUAL. In: *Pressure Vessels and Piping Conference*. Vol ; 2013:1-15.

26. Chandra SK, Shankar V, Mariappan K, Sandhya R, Chakraborty PC. Effect of Strain Rate on the Low Cycle Fatigue Behavior of 316L(N) Stainless Steel Weld Joints. *6th International Conference on Creep, Fatigue and Creep Fatigue Interaction*. 2013;55:176-180. doi:10.1016/j.proeng.2013.03.239.

27. Pham MS, Holdsworth SR. Role of microstructural condition on fatigue damage development of AISI 316L at 20 and 300°C. *International Journal of Fatigue*. 2013;51:36-48. doi:10.1016/j.ijfatigue.2013.02.005.

28. Puchi Cabrera ES. High temperature deformation of 316L stainless steel. *Materials Science and Technology*. 2001;17(February):155-161.

29. Lindgren L-E, Domkin K, Hansson S. Dislocations, vacancies and solute diffusion in physical based plasticity model for AISI 316L. *Mechanics of Materials*. 2008;40(11):907-919. doi:10.1016/j.mechmat.2008.05.005.

30. Katayama Y, Tsubota M, Saito Y. Effect of the plastic strain level quantified by EBSP method on the stress corrosion cracking of L-grade stainless steels. In: *12th International Conference on Environmental Degradation of Materials in Nuclear Power System-Water Reactors-TMS*. Vol ; 2005.

31. Lu Z, Shoji T, Meng F, et al. Characterization of microstructure and local deformation in 316NG weld heat-affected zone and stress corrosion cracking in high temperature water. *Corrosion Science*. 2011;53(5):1916-1932. doi:10.1016/j.corsci.2011.02.009.

32. Wright SI, Nowell MM, Field DP. A Review of Strain Analysis Using Electron Backscatter Diffraction. *Microscopy and Microanalysis*. 2011;17(03):316-329. href="http://dx.doi.org/10.1017/S1431927611000055.

33. Wright S. *Applications of EBSD in Materials Research for Nuclear Energy*.; 2008.

34. Easterling K. Fusion welding-process variables. In: *Introduction to the Physical Metallurgy of Welding*. Vol ; 1985:1-47.

35. Krauss G. *STEELS Processing, Structure and Performance*. ASM International; 2005.

36. Pickering FB. *Physical Metallurgy of Stainless Steel Developments*. International Materials Reviews; 1976. http://books.google.co.uk/books/about/Physical_Metallurgy_of_Stainless_Steel_D.html?id=6AcnngEACAAJ&pgis=1. Accessed March 1, 2015.

37. Kutz M. *Handbook of Materials Selection.* John Wiley & Sons; 2002. http://eu.wiley.com/WileyCDA/WileyTitle/productCd-0471359246.html. Accessed June 11, 2015.

38. Cobb HM. The History of Stainless steel. In: *ASM International.* Vol ; 2010:375. doi:10.1016/S0026-0657(10)80254-1.

39. Hull D. *Introduction to Dislocations.* Elsevier; 2011. doi:10.1016/B978-0-08-096672-4.00001-3.

40. Vitos L, Nilsson J-O, Johansson B. Alloying effects on the stacking fault energy in austenitic stainless steels from first-principles theory. *Acta Materialia.* 2006;54(14):3821-3826. doi:10.1016/j.actamat.2006.04.013.

41. Lu S, Hu Q-M, Johansson B, Vitos L. Stacking fault energies of Mn, Co and Nb alloyed austenitic stainless steels. *Acta Materialia.* 2011;59(14):5728-5734. doi:10.1016/j.actamat.2011.05.049.

42. Rosenthal D. Mathematical theory of heat distribution during welding and cutting. *Welding journal.* 1941:220 - s - 234 - s. http://scholar.google.com/scholar?hl=en&btnG=Search&q=intitle:Mathematical+theory+of+heat+distribution+during+welding+and+cutting#0.

43. Goldak J, Chakravarti A, Bibby M. A new finite element model for welding heat sources. *Metallurgical Transactions B.* 1984;15B:299-305. doi:10.1007/BF02667333.

44. Chen BQ, Adak M, Soares CG. Numerical investigations to study the effect of weld parameters on the temperature-time history in steel plates. In: *1st International Conference on Maritime Technology and Engineering.* Vol ; 2011:285-292.

45. Mahapatra MM, Datta GL, Pradhan B. Three-Dimensional Finite Element Analysis to Predict the Effects of Shielded Metal Arc Welding Process Parameters on Temperature Distributions and Weldment Zones in Butt and One-Sided Fillet Welds. In: *Proceedings of the Institution of Mechanical Engineers, Part B: Journal of Engineering Manufacture.* Vol 220. ; 2006:837-845. doi:10.1243/09544054JEM371.

46. Bouchard PJ. The NeT bead-on-plate benchmark for weld residual stress simulation. *International Journal of Pressure Vessels and Piping.* 2009;86(1):31-42. doi:10.1016/j.ijpvp.2008.11.019.

47. Lippold JC, Kotecki DJ. *Welding Metallurgy and Weldability of Stainless Steels - John C. Lippold, Damian J. Kotecki.* Wley; 2005. http://eu.wiley.com/WileyCDA/WileyTitle/productCd-0471473790.html. Accessed March 13, 2014.

48. Rajasekhar K, Harendranath CS, Raman R, Kulkarni SD. Microstructural evolution during solidification of austenitic stainless steel weld metals: A color

metallographic and electron microprobe analysis study. *Materials Characterization*. 1997;38(2):53-65. doi:10.1016/S1044-5803(97)80024-1.

49. Unnikrishnan R, Idury KSNS, Ismail TP, et al. Effect of heat input on the microstructure, residual stresses and corrosion resistance of 304L austenitic stainless steel weldments. *Materials Characterization*. 2014;93:10-23. doi:10.1016/j.matchar.2014.03.013.

50. Alipooramirabad H, Paradowska A, Ghomashchi R, Kotousov A, Reid M. Quantification of residual stresses in multi-pass welds using neutron diffraction. *Journal of Materials Processing Technology*. 2015;226:40-49. doi:10.1016/j.jmatprotec.2015.07.002.

51. Kumar S, Shahi AS. Effect of heat input on the microstructure and mechanical properties of gas tungsten arc welded AISI 304 stainless steel joints. *Materials & Design*. 2011;32(6):3617-3623. doi:10.1016/j.matdes.2011.02.017.

52. Hill H. Chloride stress corrosion cracking in austenitic stainless steel RR902 Chloride stress corrosion cracking in austenitic stainless steel. 2011:62.

53. Noyan I., Cohen J. Residual stress – measurement by diffraction and interpretation. In: *Crystal Research and Technology*. Vol 24. ; 1989:K37-K37. doi:10.1002/crat.2170240228.

54. Dong P, Hong JK, Bouchard PJ. Analysis of residual stresses at weld repairs. In: *International Journal of Pressure Vessels and Piping*. Vol 82. ; 2005:258-269. doi:10.1016/j.ijpvp.2004.08.004.

55. Elcoate CD, Dennis RJ, Bouchard PJ, Smith MC. Three dimensional multi-pass repair weld simulations. In: *International Journal of Pressure Vessels and Piping*. Vol 82. ; 2005:244-257. doi:10.1016/j.ijpvp.2004.08.003.

56. Paradowska AM, Price JWH, Ibrahim R, Finlayson TR. The effect of heat input on residual stress distribution of steel welds measured by neutron diffraction. *Journal of Achievements in materials and manufacturing engineering*. 2006;17(1-2):385-388.

57. Muránsky O, Smith M, Bendeich PJ, et al. Comprehensive numerical analysis of a three-pass bead-in-slot weld and its critical validation using neutron and synchrotron diffraction residual stress measurements. *International Journal of Solids and Structures*. 2012;49(9):1045-1062. doi:10.1016/j.ijsolstr.2011.07.006.

58. Murugan S, Rai SK, Kumar P., Jayakumar T, Raj B, Bose MS. Temperature distribution and residual stresses due to multipass welding in type 304 stainless steel and low carbon steel weld pads. In: *International Journal of Pressure Vessels and Piping*. Vol 78. ; 2001:307-317. doi:10.1016/S0308-0161(01)00047-3.

59. Woo W, An GB, Kingston EJ, DeWald a. T, Smith DJ, Hill MR. Through-thickness distributions of residual stresses in two extreme heat-input thick welds:

A neutron diffraction, contour method and deep hole drilling study. *Acta Materialia*. 2013;61(10):3564-3574. doi:10.1016/j.actamat.2013.02.034.

60. Smith MC, Smith AC. *Report Generic NeT Task Group 1 Single Weld Bead on Plate : Review of Phase 1 Weld Simulation Round Robin.*; 2006.

61. Ficquet X, Smith DJ, Truman CE, Kingston EJ, Dennis RJ. Measurement and prediction of residual stress in a bead-on-plate weld benchmark specimen. In: *International Journal of Pressure Vessels and Piping*. Vol 86. Elsevier Ltd; 2009:20-30. doi:10.1016/j.ijpvp.2008.11.008.

62. Smith MC, Smith AC. NeT bead-on-plate round robin: Comparison of residual stress predictions and measurements. *International Journal of Pressure Vessels and Piping*. 2009;86(1):79-95. doi:10.1016/j.ijpvp.2008.11.017.

63. Smith MC. *Report Hartlepool and Heysham 1 Power Stations Development of Mixed Isotropic-Kinematic Material Hardening Models for Finite Element Simulation of Austenitic Steel Welds.*; 2006.

64. Truman CE, Smith MC. The NeT residual stress measurement and modelling round robin on a single weld bead-on-plate specimen. *International Journal of Pressure Vessels and Piping*. 2009;86(1):1-2. doi:10.1016/j.ijpvp.2008.11.018.

65. Smith DJ, Bouchard PJ, George D. Measurement and prediction of residual stresses in thick-section steel welds. In: *The Journal of Strain Analysis for Engineering Design*. Vol 35. ; 2000:287-305. doi:10.1243/0309324001514422.

66. Pratihar S, Turski M, Edwards L, Bouchard PJ. Neutron diffraction residual stress measurements in a 316L stainless steel bead-on-plate weld specimen. *International Journal of Pressure Vessels and Piping*. 2009;86(1):13-19. doi:10.1016/j.ijpvp.2008.11.010.

67. Cottrell A. *Dislocations and Plastic Flow in Crystals.*; 1953. doi:10.1126/science.119.3095.551.

68. Orowan EZK. Tieftemperaturplastizitiit und Beckersche Formel. *Zeitschrift für Physik A Hadrons and Nuclei*. 1934;89:605.

69. Wei H, Wei Y. Interaction between a screw dislocation and stacking faults in FCC metals. *Materials Science and Engineering A*. 2012;541:38-44. doi:10.1016/j.msea.2012.01.115.

70. Kocks UF, Mecking H. Physics and phenomenology of strain hardening: The FCC case. *Progress in Materials Science*. 2003;48:171-273. doi:10.1016/S0079-6425(02)00003-8.

71. Cottrell AH. LX. The formation of immobile dislocations during slip. *The London, Edinburgh, and Dublin Philosophical Magazine and Journal of Science*. 2010;43(341):645-647. doi:10.1080/14786440608520220.

72. Hirth JP. On Dislocation Interactions in the fcc Lattice. *Journal of Applied Physics*. 1961;32(4):700. doi:10.1063/1.1736074.

73. Essmann U, Mughrabi H. Annihilation of dislocations during tensile and cyclic deformation and limits of dislocation densities. *Philosophical Magazine A*. 1979;40(February 2015):731-756. doi:10.1080/01418617908234871.

74. Nabarro FRN. Distribution of solute atoms round a moving dislocation. *Materials Science & Engineering A*. 2005;400-401:22-24. doi:10.1016/j.msea.2005.03.046.

75. Mesarovic SD. Dynamic Strain Aging And Plastic Instablities. *Mechanics and Physics of Solids*. 1995;43(5):671-700.

76. Aboulfadl H, Deges J, Choi P, Raabe D. Dynamic strain aging studied at the atomic scale. *Acta Materialia*. 2015;86:34-42. doi:10.1016/j.actamat.2014.12.028.

77. Leslie WC. *The Physical Metallurgy of Steels*. Hempisphere Pub. Corp.; 1981. http://books.google.co.uk/books/about/The_physical_metallurgy_of_steels.html?id=Q45TAAAAMAAJ&pgis=1. Accessed February 19, 2015.

78. Hong S-G, Lee S-B. Mechanism of dynamic strain aging and characterization of its effect on the low-cycle fatigue behavior in type 316L stainless steel. *Journal of Nuclear Materials*. 2005;340(2-3):307-314. doi:10.1016/j.jnucmat.2004.12.012.

79. Blanc D, Strudel JL. *Strength of Metals and Alloys (ICSMA 7)*. Elsevier; 1985. doi:10.1016/B978-0-08-031642-0.50065-9.

80. Samuel K., Mannan S., Rodriguez P. Serrated yielding in AISI 316 stainless steel. *Acta Metallurgica*. 1988;36(8):2323-2327. doi:10.1016/0001-6160(88)90331-8.

81. Kim DW, Ryu W-S, Hong JH, Choi S-K. Effect of nitrogen on high temperature low cycle fatigue behaviors in type 316L stainless steel. *Journal of Nuclear Materials*. 1998;254:226-233. doi:10.1016/S0022-3115(97)00360-7.

82. Smallman R., Ngan AH. *Modern Physical Metallurgy*. Vol Eighth Edi. Elsevier; 2014.

83. Asano S, Oshima K. Effect of Plastic Deformation on the Hydrogen-Induced Internal Friction Peak in Austenitic Stainless Steel. *Transactions of the Japan Institute of Metals*. 1982;23(9):530-534. http://www.jim.or.jp/journal/e/pdf3/23/09/530.pdf.

84. Snoek JL. Effect of small quantities of carbon and nitrogen on the elastic and plastic properties of iron. *Physica*. 1941;8(7):711-733. doi:http://dx.doi.org/10.1016/S0031-8914(41)90517-7.

85. Prasad Reddy GV, Sandhya R, Bhanu Sankara Rao K, Sankaran S. Influence of nitrogen alloying on dynamic strain ageing regimes in low cycle fatigue of AISI 316LN stainless steel. *Procedia Engineering*. 2010;2(1):2181-2188. doi:10.1016/j.proeng.2010.03.234.

86. Paul SK, Sivaprasad S, Dhar S, Tarafder S. Key issues in cyclic plastic deformation: Experimentation. *Mechanics of Materials*. 2011;43(11):705-720. doi:10.1016/j.mechmat.2011.07.011.

87. Li P, Li SX, Wang ZG, Zhang ZF. Fundamental factors on formation mechanism of dislocation arrangements in cyclically deformed fcc single crystals. *Progress in Materials Science*. 2011;56(December 2010):328-377. doi:10.1016/j.pmatsci.2010.12.001.

88. Feltner C., Laird C. Cyclic stress-strain response of F.C.C. metals and alloys—I Phenomenological experiments. *Acta Metallurgica*. 1967;15(10):1621-1632. doi:10.1016/0001-6160(67)90137-X.

89. Feltner C., Laird C. Cyclic stress-strain response of F.C.C. metals and alloys—II Dislocation structures and mechanisms. *Acta Metallurgica*. 1967;15(10):1633-1653. doi:10.1016/0001-6160(67)90138-1.

90. Mughrabi H. Fatigue, an everlasting materials problem - still en vogue. *Procedia Engineering*. 2010;2(1):3-26. doi:10.1016/j.proeng.2010.03.003.

91. Grosskreutz J. Fatigue mechanism in the sub-creep range. In: Manson S., ed. *Metal Fatigue Damage*. Vol ASTM; 1971:5.

92. Schramm RE, Reed RP. Stacking fault energies of seven commercial austenitic stainless steels. *Metallurgical Transactions A*. 1975;6(7):1345-1351. doi:10.1007/BF02641927.

93. Pham M. Fatigue Behaviour Of AISI316L: Mechanical response , Microstructural evolution , Fatigue crack propagation , & Physically-based constitutive modelling. 2013;(20864).

94. Mughrabi H. Dislocation in Fatigue. In: *Dislocations and Properties of Real Materials*. Vol ; 1985:244-262.

95. Kuhlmann-Wilsdorf D, Laird C. Dislocation behavior in fatigue. *Materials Science and Engineering*. 1977;27(2):137-156. doi:10.1016/0025-5416(77)90166-5.

96. Obrtlík K, Kruml T, Polák J. Dislocation structures in 316L stainless steel cycled with plastic strain amplitudes over a wide interval. *Materials Science and Engineering: A*. 1994;187(1):1-9. doi:10.1016/0921-5093(94)90325-5.

97. Li Y, Laird C. Cyclic response and dislocation structures of AISI 316L stainless steel. Part 2: polycrystals fatigued at intermediate strain amplitude. *Materials Science and Engineering: A*. 1994;186(1-2):87-103. doi:10.1016/0921-5093(94)90307-7.

98. Li Y, Laird C. Cyclic response and dislocation structures of AISI 316L stainless steel. Part 1: single crystals fatigued at intermediate strain amplitude. *Materials Science and Engineering: A*. 1994;186(1-2):65-86. doi:10.1016/0921-5093(94)90306-9.

99. Basinski ZS, Basinski SJ. Fundamental aspects of low amplitude cyclic deformation in face-centred cubic crystals. *Progress in Materials Science*. 1992;36:89-148. doi:10.1016/0079-6425(92)90006-S.

100. Hong S-G, Lee S-B. The tensile and low-cycle fatigue behavior of cold worked 316L stainless steel: influence of dynamic strain aging. *International Journal of Fatigue*. 2004;26(8):899-910. doi:10.1016/j.ijfatigue.2003.12.002.

101. Pham MS, Holdsworth SR. Dynamic strain ageing of AISI 316L during cyclic loading at 300°C: Mechanism, evolution, and its effects. *Materials Science and Engineering: A*. 2012;556:122-133. doi:10.1016/j.msea.2012.06.067.

102. Ivanchenko M. Dynamic Strain Aging of Austenitic Stainless Steels and Ni Base Alloys. 2010. http://lib.tkk.fi/Diss/2010/isbn9789526034454.

103. Calmunger M. High-Temperature Behaviour of Austenitic Alloys. 2013;(1619).

104. Gerland M, Alain R, Ait Saadi B, Mendez J. Low cycle fatigue behaviour in vacuum of a 316L-type austenitic stainless steel between 20 and 600°C—Part II: Dislocation structure evolution and correlation with cyclic behaviour. *Materials Science and Engineering: A*. 1997;229(1-2):68-86. doi:10.1016/S0921-5093(96)10560-8.

105. Gerland M, Mendez J, Violan P, Ait Saadi B. Evolution of disloction structures and cyclic behaviour of a 316L type austenitic stainless steel cycled in vacume at room temperature. *Materials Science and Engineering*. 1989;A118:83-95.

106. Hong S-G, Lee S-B, Byun T-S. Temperature effect on the low-cycle fatigue behavior of type 316L stainless steel: Cyclic non-stabilization and an invariable fatigue parameter. *Materials Science and Engineering: A*. 2007;457(1-2):139-147. doi:10.1016/j.msea.2006.12.035.

107. Srinivasan V. Comparative evaluation of strain controlled low cycle fatigue behaviour of solution annealed and prior cold worked 316L(N) stainless steel. *International Journal of Fatigue*. 2004;26(12):1295-1302. doi:10.1016/j.ijfatigue.2004.05.003.

108. Lemaitre J, Chaboche J-L. *Mechanics of Solid Materials*. Cambridge University Press; 1999.

109. Chaboche JL. A review of some plasticity and viscoplasticity constitutive theories. *International Journal of Plasticity*. 2008;24(10):1642-1693. doi:10.1016/j.ijplas.2008.03.009.

110. Abaqus 6.12. ABAQUS analysis user's manual.

111. Muransky O, Bendeich PJ, Smith MC, Kristein O, Edwards L, Holden TM. Analysis of Residual Stresses in Three-Pass Slot Weld (NeT-TG4): Finite Element Modelling and Neutron Diffraction. In: *Pressure Vessels and Piping Conference*. Vol ; 2010:1-7.

112. Withers PJ, Bhadeshia HKDH. Residual stress Part 1 – Measurement techniques. *Material Science and Technology*. 2001;17(April):355-365.

113. Sattari-Far I, Javadi Y. Influence of welding sequence on welding distortions in pipes. *International Journal of Pressure Vessels and Piping*. 2008;85(4):265-274. doi:10.1016/j.ijpvp.2007.07.003.

114. Teng T-L, Chang P-H, Tseng W-C. Effect of welding sequences on residual stresses. *Computers & Structures*. 2003;81(5):273-286. doi:10.1016/S0045-7949(02)00447-9.

115. Rossini NS, Dassisti M, Benyounis KY, Olabi a. G. Methods of measuring residual stresses in components. *Materials & Design*. 2012;35:572-588. doi:10.1016/j.matdes.2011.08.022.

116. Hutchings MT, Krawitz AD. *Measurement of Residual and Applied Stress Using Neutron Diffraction*. Vol (Hutchings MT, Krawitz AD, eds.). Oxford: Springer Science+Business Media, B.V; 1991.

117. Fitzpatrick ME, Lodini A. *Analysis of Residual Stress by Diffraction Using Neutron and Synchrotron Radiation*. Vol (Fitzpatrick ME, Lodini A, eds.). Taylor & Francis; 2003.

118. DD CEN ISO/TS 21432:2005. *Non-Destructive Testing -- Standard Test Method for Determining Residual Stresses by Neutron Diffraction.*; 2005. http://www.iso.org/iso/catalogue_detail.htm?csnumber=35868. Accessed January 6, 2015.

119. Allen AJ, Hutchings MT, Windsor CG, Andreani C. Neutron diffraction methods for the study of residual stress fields. *Advances in Physics*. 2006;34(4):445-473. doi:10.1080/00018738500101791.

120. MacEwen SR, Faber J, Turner APL. The Use of Time of Flight Neutron Diffraction to Study Grain Interaction Stresses. *Acta Materialia*. 1983;31(5):657-676.

121. Santisteban JR, Daymond MR, James JA, Edwards L. ENGIN-X: A third-generation neutron strain scanner. 2006. doi:10.1107/S0021889806042245.

122. Wang X, Holden TM, Rennich GQ, et al. VULCAN — The engineering diffractometer at the SNS. 2006;386:673-675. doi:10.1016/j.physb.2006.06.103.

123. Cooper RG. SNS detector plans. *Nuclear Instruments and Methods in Physics Research Section A: Accelerators, Spectrometers, Detectors and Associated Equipment*. 2004;529(1-3):394-398. doi:10.1016/j.nima.2004.05.018.

124. Gardner ISK. A Review of Spallation Neutorn Source Accelerators. In: *Accelerator Physics*. Vol ; 2000:98-102.

125. Wang X-L, Stoica AD. Focusing neutron guides for VULCAN—Design aspects, estimated performance, and detector deployment. *Nuclear Instruments and*

Methods in Physics Research Section A: Accelerators, Spectrometers, Detectors and Associated Equipment. 2009;600(1):309-312. doi:10.1016/j.nima.2008.11.050.

126. James JA, Santisteban JR, Edwards L, Daymond MR. A virtual laboratory for neutron and synchrotron strain scanning. *Physica B: Condensed Matter*. 2004;350(1-3):E743-E746. doi:10.1016/j.physb.2004.03.194.

127. Santisteban JR, Edwards L, Steuwer A, Withers PJ. Time-of-flight neutron transmission diffraction. 2001. doi:10.1107/S0021889801003260.

128. Krawitz AD. 25 year perspective neutron strain measurement. *Materials Science and Technology*. 2011;27(3):589.

129. Hutchings MT, Withers.P.J, Holden TM, Lorentzen T. *Introduction to Characterization of Residual Stress by Neutron Diffraction*. Vol 8. Taylor & Francis Group; 2005. doi:10.1016/S1369-7021(05)00849-7.

130. Krawitz AD, Winholtz RA. Use of position-dependent stress-free standards for diffraction stress measurements. *Materials Science and Engineering: A*. 1994;185(1-2):123-130. doi:10.1016/0921-5093(94)90935-0.

131. Paradowska A, Finlayson TR, Price JWH, Ibrahim R, Steuwer A, Ripley M. Investigation of reference samples for residual strain measurements in a welded specimen by neutron and synchrotron X-ray diffraction. *Physica B: Condensed Matter*. 2006;385-386:904-907. doi:10.1016/j.physb.2006.05.245.

132. Withers PJ, Preuss M, Steuwer A, Ang JWL. Methods for obtaining the strain-free lattice parameter when using diffraction to determine residual stress. *Journal of Applied Crystallography*. 2007;40(5):891-904. doi:10.1107/S0021889807030269.

133. Altenkirch J, Peel.M.J, Steuwer.A, Withers.P.J. Comparison of methods to determine variations in unstrained unit cell parameter across welds. *Strain Analysis*. 2011;46:651-661.

134. Babu SS. In-situ observations of lattice parameter fluctuations in austenite and transformation to bainite. *Metallurgical and Materials Transactions A*. 2005;36A:3281-3289.

135. Webster GA, Youtsos AG, Ohms C, Wimpory RC. Draft Standard for the Measurement of Residual Stresses by Neutron Diffraction. In: Daniel IM, Gdoutos EE, eds. Vol Recent advances in experimental mechanics. Kluwer Academic; 2002:467-476. http://libezproxy.open.ac.uk/login?url=http://search.ebscohost.com/login.aspx?direct=true&db=edsbl&AN=CN046480715&site=eds-live&scope=site.

136. ISO. ISO/TTA 3:2001 - Polycrystalline materials -- Determination of residual stresses by neutron diffraction. 2001. http://www.iso.org/iso/catalogue_detail?csnumber=35397. Accessed February 20, 2015.

137. Hughes DJ, Hattingh MNJDG, Webster PJ. The Use of Combs for Evaluation of Strain-free References for Residual Strain Measurements by Neutron and Synchrotron X-ray Diffraction. *Journal of Neutron Research*. 2003;11(December):289-293.

138. Daymond MR, Johnson MW. The determination of a stress-free lattice parameter within a stressed material using elastic anisotropy. *Journal of Applied Crystallography*. 2001;34(3):263-270. doi:10.1107/S0021889801002497.

139. Martins R V, Ohms C, Decroos K. Full 3D spatially resolved mapping of residual strain in a 316L austenitic stainless steel weld specimen. *Materials Science and Engineering: A*. 2010;527(18-19):4779-4787. doi:10.1016/j.msea.2010.03.110.

140. Repper J, Hofmann M, Krempaszky C, et al. Effect of macroscopic relaxation on residual stress analysis by diffraction methods. *Journal of Applied Physics*. 2012;112(6):064906. doi:10.1063/1.4752877.

141. Ganguly S, Edwards L, Fitzpatrick ME. Problems in using a comb sample as a stress-free reference for the determination of welding residual stress by diffraction. *Materials Science and Engineering: A*. 2011;528(3):1226-1232. doi:10.1016/j.msea.2010.10.039.

142. Suzuki H, Harjo S, Abe J, Xu P, Aizawa K, Akita K. Effects of gauge volume on pseudo-strain induced in strain measurement using time-of-flight neutron diffraction. *Nuclear Instruments and Methods in Physics Research Section A: Accelerators, Spectrometers, Detectors and Associated Equipment*. 2013;715:28-38. doi:10.1016/j.nima.2013.03.031.

143. Wang X-L, Wang YD, Richardson J. Experimental error caused by sample displacement in time of flight neutron diffractometry. *Applied Crystallography*. 2002;35:533-537.

144. Spooner S, Wang XL. Diffraction Peak Displacement in Residual Stress Samples Due to Partial Burial of the Sampling Volume. *Journal of Applied Crystallography*. 1997;30(4):449-455. doi:10.1107/S0021889897000174.

145. Taran YV, Balagurov a. M. Correction of a neutron diffraction peak shift due to a partial immersion of a gauge volume in an unstressed sample. *Nuclear Instruments and Methods in Physics Research Section A: Accelerators, Spectrometers, Detectors and Associated Equipment*. 2012;679:19-24. doi:10.1016/j.nima.2012.03.009.

146. Wang DQ. Strain Measurement Using Neutron Diffraction. 1996;(August).

147. Zeitelhack K, Schanzer C, Kastenmüller A, et al. Measurement of neutron flux and beam divergence at the cold neutron guide system of the new Munich research reactor FRM-II. *Nuclear Instruments and Methods in Physics Research Section A: Accelerators, Spectrometers, Detectors and Associated Equipment*. 2006;560(2):444-453. doi:10.1016/j.nima.2005.12.215.

148. Almeida GL De, Silvani MI, Furieri RC a a, Gonc MJ, Lopes RT. Evaluation of the Divergence of a Thermal Neutron Beam using a Position Sensitive Detector. *Practice*. 2005;35(3).

149. Price JWH, Ziara-Paradowska A, Joshi S, Finlayson T, Semetay C, Nied H. Comparison of experimental and theoretical residual stresses in welds: The issue of gauge volume. *International Journal of Mechanical Sciences*. 2008;50(3):513-521. doi:10.1016/j.ijmecsci.2007.08.008.

150. Johnson M., Daymond M. Neutron pulsed source instrumentation. In: *Analysis of Residual Stresses by Diffraction Using Neutron and Synchrotron Radiation*. Vol ; 2003:146.

151. Webster PJ, Mills G, Wang XD, Kang WP, Holden TM. Impediments to efficient through-surface strain scanning. *Journal of Neutron Research*. 1996;3(4):223-240. http://www.tandfonline.com/doi/abs/10.1080/10238169608200197#.VOdXSFOs VcA. Accessed February 20, 2015.

152. Wang X-L, Spooner S, Hubbard CR. Theory of the Peak Shift Anomaly due to Partial Burial of the Sampling Volume in Neutron Diffraction Residual Stress Measurements. *Journal of Applied Crystallography*. 1998;31(1):52-59. doi:10.1107/S0021889897008261.

153. HSu T., Marsiglio F, Root J., Holden T. Effects of Multiple Scattering and Wavelength-Dependent Attenuation on Strain Measurements by Neutron Scattering. *Journal of Neutron*. 1995;3(1):27. http://iospress.metapress.com/content/f673222338343816/?genre=article&volum e=3&issue=1&spage=27&issn=1023-8166. Accessed February 20, 2015.

154. Creek SR, Santisteban JR, Edwards L. *Modelling Pseudo-Strain Effects Induced in Strain Measurement Using Time-of-Flight Neutron Diffraction*. http://www.isis.stfc.ac.uk/instruments/engin-x/publications/modelling-pseudo-strain-effects-induced-in-strain-measurement6516.pdf.

155. Wang D, Santisteban JR, Edwards L. Effect of wavelength-dependent attenuation on strain measurement using pulsed neutron diffraction. *Nuclear Instruments and Methods in Physics Research Section A*. 2001;460:381-390.

156. Wimpory RC, Martins R., Hofmann.M, et al. Determmining the microstructure grain size from diffraction data and its influennce on reesidual stress dete ermination in engineering materials. *Journal of Applied Crystallography*.:1-31.

157. Wimpory RC, Ohms C, Hofmann M, Schneider R, Youtsos AG. Statistical analysis of residual stress determinations using neutron diffraction. *International Journal of Pressure Vessels and Piping*. 2009;86(1):48-62. doi:10.1016/j.ijpvp.2008.11.003.

158. Wimpory RC, Ohms C. A Step towards a Complete Uncertainty Analysis of Residual Stress Determination Using Neutron Diffraction. In: *Materials Science*

Forum. Vol 638-642. ; 2010:2487-2492. http://www.scientific.net/MSF.638-642.2487. Accessed March 16, 2015.

159. Gonzalez D, Kelleher JF, Quinta da Fonseca J, Withers PJ. Macro and intergranular stress responses of austenitic stainless steel to 90° strain path changes. *Materials Science and Engineering: A*. 2012;546:263-271. doi:10.1016/j.msea.2012.03.064.

160. Wang Y-D, Tian H, Stoica AD, Wang X-L, Liaw PK, Richardson JW. The development of grain-orientation-dependent residual stressess in a cyclically deformed alloy. *Nature materials*. 2003;2(2):101-106. doi:10.1038/nmat812.

161. Korsunsky AM, James KE, Daymond MR. Intergranular stresses in polycrystalline fatigue: diffraction measurement and self-consistent modelling. *Engineering Fracture Mechanics*. 2004;71(4-6):805-812. doi:10.1016/S0013-7944(03)00018-3.

162. Neov D, Ohms C, Wimpory RC, Youtsos AG. Residual Stress Analyses by Neutron Diffraction in Irradiated Double-V Butt Welded Steel Plates. In: *Materials Science Forum*. Vol 571-572. ; 2008:381-386. http://www.scientific.net/MSF.571-572.381. Accessed March 16, 2015.

163. Wohlfahri H, Nitschke-Pagel T, Dilger K, et al. Residual Stress Calculations and Measurements Review and Assessment of the IIW Round Robin Results. *WELDING IN THE WORLD -LONDON-*. 2012;56(9/10):120-140. http://libezproxy.open.ac.uk/login?url=http://search.ebscohost.com/login.aspx?direct=true&db=edsbl&AN=RN318382552&site=eds-live&scope=site.

164. Janosch J-J. International Institute of Welding work on residual stress and its application to industry. *International Journal of Pressure Vessels and Piping*. 2008;85(3):183-190. doi:10.1016/j.ijpvp.2007.10.008.

165. Ohms C, Wimpory RC, Katsareas DE, Youtsos a. G. NET TG1: Residual stress assessment by neutron diffraction and finite element modeling on a single bead weld on a steel plate. *International Journal of Pressure Vessels and Piping*. 2009;86(1):63-72. doi:10.1016/j.ijpvp.2008.11.009.

166. Shan X, Davies CM, Wangsdan T, O'Dowd NP, Nikbin KM. Thermo-mechanical modelling of a single-bead-on-plate weld using the finite element method. *International Journal of Pressure Vessels and Piping*. 2009;86(1):110-121. doi:10.1016/j.ijpvp.2008.11.005.

167. Ohms C, Uca O, Youtsos GA, et al. Network on Neutron Techniques Standardization for Structural Integrity. In: *ASME Pressure Vessels and Piping Conference (PVP 2008)*. Vol Chicago, Illinois: ASME; 2008:1-13. http://www.enea.it/it/enea_informa/events/net_10-11jun13/NeT_leaflet_2009.pdf.

168. Smith MC, Smith AC. NeT bead-on-plate round robin: Comparison of transient thermal predictions and measurements. *International Journal of Pressure Vessels and Piping*. 2009;86(1):96-109. doi:10.1016/j.ijpvp.2008.11.016.

169. Poorhaydari K, Patchett BM, Ivey DG. Estimation of Cooling Rate in the Welding of. *Welding journal*. 2005;(October):149-155.

170. Boumerzoug Z. Effect of Welding on Microstructure and Mechanical Properties of an Industrial Low Carbon Steel. *Engineering*. 2010;02(07):502-506. doi:10.4236/eng.2010.27066.

171. R6 III.15. Calculation of residual stress in weldments. In: *Assessment of the Integrity of Structures Containing Defects*. Vol 4. ; 2004.

172. Martins R V. *Net-Task Group4: Three Pass Slot Weld Specimen in Austenitic Stainless Steel (Protocol for the Destructive and Non Destructive)*. Vol 3.3. 2009.

173. Goldak JA, Akhlaghi M. *Computational Welding Mechanics*.; 2005. doi:10.1007/b101137.

174. Pham MS, Holdsworth SR. Change of stress-strain hysteresis loop and its links with microstructural evolution in AISI 316L during cyclic loading. *Procedia Engineering*. 2011;10:1069-1074. doi:10.1016/j.proeng.2011.04.176.

175. Kim J, Kim M, Lee J. Constitutive model for austenitic stainless steel of 316L , 321 and 347. In: *9th International Conference on Fracture and Strength of Solids*. Vol ; 2013:1-4.

176. Armas AF, Bettin OR, Alvarez-Armas I, Rubiolo GH. Strain aging effects on the cyclic behavior of austenitic stainless steels. *Journal of Nuclear Materials*. 1988;155-157:644-649. doi:10.1016/0022-3115(88)90388-1.

177. Pham MS, Holdsworth SR, Janssens KGF, Mazza E. Cyclic deformation response of AISI 316L at room temperature: Mechanical behaviour, microstructural evolution, physically-based evolutionary constitutive modelling. *International Journal of Plasticity*. 2013;47:143-164. doi:10.1016/j.ijplas.2013.01.017.

178. Joosten MM, Gallegillo MS. A Study of the Effect of Hardening Model in the Prediction of Welding Residual Stress. In: *Volume 6: Materials and Fabrication, Parts A and B*. Vol ASME; 2012:1045. doi:10.1115/PVP2012-78055.

179. Dewees DJ, Prueter PE, Kummari SR. A Continued Evaluation of The Role of Material Hardening Behavior For The NeT TG1 and TG4 Specimens. In: *Pressure Vessels and Piping Conference*. Vol PVP2014-28. ; 2014:1-12.

180. Pan B, Qian K, Xie H, Asundi A. Two-dimensional digital image correlation for in-plane displacement and strain measurement: a review. *Measurement Science and Technology*. 2009;20:062001. doi:10.1088/0957-0233/20/6/062001.

181. Moturu SR, Muyupa E, Mukerjee S, et al. *Measuring Grain Resolved Strains in Austenitic Stainless Steel Using Digital Image Correlation.*; 2014.

182. Tabor D. A Simple Theory of Static and Dynamic Hardness. In: *Royal Society A: Mathematical, Physical and Engineering Sciences.* Vol 192. ; 1948:247-274. doi:10.1098/rspa.1948.0008.

183. Hutchings IM. The contributions of David Tabor to the science of indentation hardness. *Journal of Materials Research.* 2009;24:581-589. doi:10.1557/jmr.2009.0085.

184. Pavlina EJ, Van Tyne CJ. Correlation of Yield strength and Tensile strength with hardness for steels. *Journal of Materials Engineering and Performance.* 2008;17(December):888-893. doi:10.1007/s11665-008-9225-5.

185. Lewis SJ, Truman CE. Diffraction measurements for evaluating plastic strain in A533B ferritic steel—a feasibility study. *Journal of Physics D: Applied Physics.* 2010;43:265501. doi:10.1088/0022-3727/43/26/265501.

186. Schwartz R., Field D., Adams B., Kumar M, Schwartz A. *Present State of Electron Backscatter Diffraction and Prospective Developments.* Vol LLNL-BOOK . 2nd ed.; 2008.

187. Nowell MM, Wright SI. Orientation effects on indexing of electron backscatter diffraction patterns. *Ultramicroscopy.* 2005;103(1):41-58. doi:10.1016/j.ultramic.2004.11.012.

188. Schwartz AJ, Kumar M, Adams BL, Field DP. *Electron Backscatter Diffraction in Materials Science.* Vol 40. 2001. doi:10.1002/1521-3773(20010316)40:6<9823::AID-ANIE9823>3.3.CO;2-C.

189. Baba-Kishi KZ. Review Electron backscatter Kikuchi diffraction in the scanning electron microscope for crystallographic analysis. *Journal of Materials Science.* 2002;37(9):1715-1746. doi:10.1023/A:1014964916670.

190. Oxford Instruments. *Nordlys and Fast Acquisition Software.*; 2014. doi:10.1016/S0026-0576(06)80026-7.

191. Szabo PJ, Szalai I. Effect of monotonic and cyclic deformation on the IQ-maps of austenitic stainless steel BT - 4th Hungarian Conference on Materials Science, Testing and Informatics, October 12, 2003 - October 14, 2003. In: Vol 473-474. Materials Science Forum. Budapest Univ. of Technol. and Econ., Dept. of Mat. Sci. and Engineering, Goldmann sqr. 3, H-1111 Budapest, Hungary: Trans Tech Publications Ltd; 2005:267-272.

192. Githinji DN. Characterisation of Plastic and Creep Strains From Lattice Orientation Measurements. 2013;(December).

193. Kamaya M, Quinta da Fonseca J, Li L., Preuss M. Local plastic strain measurement by EBSD. *Applied Mechanics and Materials.* 2007;7-8:173-179.

194. Githinji D, Northover S, Bouchard PJ, Rist M. An EBSD Study of the Deformation of Service-Aged 316 Austenitic Steel. *Metallurgical and Materials Transactions A*. 2013;44(9):4150-4167. doi:10.1007/s11661-013-1787-7.

195. Kamaya M, Wilkinson AJ, Titchmarsh JM. Measurement of plastic strain of polycrystalline material by electron backscatter diffraction. *Nuclear Engineering and Design*. 2005;235(6):713-725. doi:10.1016/j.nucengdes.2004.11.006.

196. Saukkonen T, Aalto M, Virkkunen I, Ehrnstén U, Hänninen H. Plastic Strain and Residual Stress Distributions in an AISI 304 Stainless Steel BWR Pipe Weld. In: *15th International Conference on Environmental Degradation of Materials in Nuclear Power Systems-Water Reactors*. Vol John Wiley & Sons, Inc.; 2012:2351-2367. doi:10.1002/9781118456835.ch244.

197. Sáez-Maderuelo a., Castro L, de Diego G. Plastic strain characterization in austenitic stainless steels and nickel alloys by electron backscatter diffraction. *Journal of Nuclear Materials*. 2011;416(1-2):75-79. doi:10.1016/j.jnucmat.2010.11.092.

198. Hou J, Shoji T, Lu ZP, et al. Residual strain measurement and grain boundary characterization in the heat-affected zone of a weld joint between Alloy 690TT and Alloy 52. *Journal of Nuclear Materials*. 2010;397(1-3):109-115. doi:10.1016/j.jnucmat.2009.12.016.

199. Ming H, Zhang Z, Wang J, Han E-H, Ke W. Microstructural characterization of an SA508-309L/308L-316L domestic dissimilar metal welded safe-end joint. *Materials Characterization*. August 2014. doi:10.1016/j.matchar.2014.08.023.

200. Lu Z, Shoji T, Yamazaki S, Ogawa K. Characterization of microstructure, local deformation and microchemistry in Alloy 600 heat-affected zone and stress corrosion cracking in high temperature water. *Corrosion Science*. 2012;58:211-228. http://ac.els-cdn.com/S0010938X12000637/1-s2.0-S0010938X12000637-main.pdf?_tid=2fd5134a-2fab-11e4-9533-00000aab0f27&acdnat=1409337481_0a4280572eb2fd3f8bc8f258749afa30. Accessed August 29, 2014.

201. Kamaya M. Characterization of microstructural damage due to low-cycle fatigue by EBSD observation. *Materials Characterization*. 2009;60(12):1454-1462. doi:10.1016/j.matchar.2009.07.003.

202. Guo J, Amira S, Gougeon P, Chen X-G. Effect of the surface preparation techniques on the EBSD analysis of a friction stir welded AA1100-B4C metal matrix composite. *Materials Characterization*. 2011;62(9):865-877. doi:10.1016/j.matchar.2011.06.007.

203. Kamaya M, Kuroda M. Fatigue Damage Evaluation Using Electron Backscatter Diffraction. *Materials Transactions*. 2011;52(6):1168-1176. doi:10.2320/matertrans.M2011014.

204. Suwas S, Ray RK. *Crystallographic Texture of Materials*. Vol (Derbey B, ed.). Springer-Verlag London; 2014.

205. J.A.Francis, Smith MC, A.C.Smith. *The Manufacture of the Three Pass Slot Weld Specimen in AISI Grade 316L Austenitic Stainless Steel*. Vol 9. 2009.

206. Smith MC, Smith A. *NeT Task Group 4: Three Pass Slot Weld Specimen in Austenitic Stainless Steel (NeT TG4 Manufacturing History)*. Vol 1.0. 2009.

207. Francis, J A, Smith MC, Smith, A C. *The Manufacture of Three Pass Slot Weld Specimen in AISI Grade 316L Austenitic Stainless Steel*.; 2009.

208. BS7270. Constant amplitude strain controlled fatigue testing. 1990.

209. Voort, G,F V. Metallography and Microstructures. In: *ASM Handbook Volume 9*. Vol ; 2012. http://www.goodreads.com/book/show/2775336-asm-handbook-volume-9.

210. Defilippi JD, Chao H-C. Effect of chromium and molybdenum segregation on the ridging behavior of type 434 stainless steel. *Metallurgical and Materials Transactions B*. 1971;2(11):3209-3216. doi:10.1007/BF02814974.

211. Gage M. Ferrite-Fissuring Relationship in Austenitic Stainless Steel Weld Metals. 1975;(August):241-246.

212. Gooch TG, Honeycomebe J. W e l d i n g Variables and Microfissuring in Austenitic Stainless Steel W e l d Metal. *Welding reserach supplement*. 1980:233-241.

213. ASTM E112-12. *ASTM E112 - 12 Standard Test Methods for Determining Average Grain Size*. Vol (Olcese E, ed.). West Conshohocken: ASTM International; 2010. doi:10.1520/E0112-10.

214. Wimpory RC. *NeT 13th Steering Commite Meetig*. Lyon, France; 2008.

215. Smith MC, Smith A. *NeT TG4 Finite Element Simulation Protocol*.; 2009.

216. Holden TM, Suzuki H, Carr DG, Ripley MI, Clausen B. Stress measurements in welds: Problem areas. *Materials Science and Engineering: A*. 2006;437(1):33-37. doi:10.1016/j.msea.2006.04.055.

217. Rietveld HM. A profile refinement method for nuclear and magnetic structures. *Journal of Applied Crystallography*. 1969;2(2):65-71. doi:10.1107/S0021889869006558.

218. Campbell SI, Akeroyd FA. *Open GENIE – Analysis and Control* .; 2002.

219. Holden TM. *Applications of Neutron Diffraction to Engineering Problems Reference Material*.; 2011.

220. Wimpory RC. NeT TG4: d0 Story. *NeT Steering Commite Meeting*. 2014.

221. Martins R V, Ohms C, Decroos K. Full Depth-Resolved Strain Mapping of a Three-Pass Slot Weld Specimen in Austenitic Stainless Steel Using the Spiral Slit Technique. In: *Materials Science Forum*. Vol 652. ; 2010:74-79. http://www.scientific.net/MSF.652.74. Accessed October 9, 2014.

222. Gilles P, El-Ahmar W, Jullien J-F. Robustness analyses of numerical simulation of fusion welding NeT-TG1 application: "Single weld-bead-on-plate." In: *International Journal of Pressure Vessels and Piping*. Vol 86. ; 2009:3-12. doi:10.1016/j.ijpvp.2008.11.012.

223. OHMS C. Residual stresses in Thick Bi-metallic Fusion Welds : a neutron diffraction study. 2013;(november).

224. Holden TM, Traore Y, James J, Kelleher J, Bouchard PJ. Determination and mitigation of the uncertainty of neutron diffraction measurements of residual strain in large-grained polycrystalline material. *Journal of Applied Crystallography*. 2015;48(2):582-584. doi:10.1107/S1600576715002757.

225. Pang JWL, Rogge RB, Donaberger RL. Effects of grain size on intergranular strain evolution in Ni. *Materials Science and Engineering: A*. 2006;437(1):21-25. doi:10.1016/j.msea.2006.04.056.

226. Turski M, Francis J a., Hurrell PR, Bate SK, Hiller S, Withers PJ. Effects of stop–start features on residual stresses in a multipass austenitic stainless steel weld. *International Journal of Pressure Vessels and Piping*. 2012;89:9-18. doi:10.1016/j.ijpvp.2011.08.006.

227. Bouchard PJ, Santisteban JR, Edwards L, et al. Residual Stress Measurements Revealing Weld Bead Start and Stop Effects in Single and Multi-Pass Weld-Runs. In: *Volume 6: Materials and Fabrication*. Vol 2005. ASME; 2005:853-860. doi:10.1115/PVP2005-71575.

228. Lindgren L-E. Numerical modelling of welding. *Computer Methods in Applied Mechanics and Engineering*. 2006;195:6710-6736. doi:10.1016/j.cma.2005.08.018.

229. Xu JJ, Gilles P, Duan YG, Yu C. Temperature and residual stress simulations of the NeT single-bead-on-plate specimen using SYSWELD. In: *International Journal of Pressure Vessels and Piping*. Vol 99-100. ; 2012:51-60. doi:10.1016/j.ijpvp.2012.08.002.

230. Duranton P, Devaux J, Robin V, Gilles P, Bergheau JM. 3D modelling of multipass welding of a 316L stainless steel pipe. *Journal of Materials Processing Technology*. 2004;153-154:457-463. doi:10.1016/j.jmatprotec.2004.04.128.

231. ASTM E1012 - 14. Standard Practice for Verification of Testing Frame and Specimen Alignment Under Tensile and Compressive Axial Force Application. 2014. http://www.astm.org/Standards/E1012.htm. Accessed December 3, 2014.

232. Instron. AlignPRO alignment system. *Instron AlignPro Manual*. 2014.

233. Smith MC, Nadri B, Smith AC, Carr DG, Bendeich PJ, Edwards LE. Optimisation of mixed hardening material constitutive models for weld residual stress simulation using the NeT task group 1 single bead on plat benchmark problem. In: *Pressure Vessels and Piping Conference*. Vol PVP2009-77. ; 2009:1-16.

234. Man J, Obrtlík K, Petrenec M, et al. Stability of austenitic 316L steel against martensite formation during cyclic straining. *Procedia Engineering*. 2011;10:1279-1284. doi:10.1016/j.proeng.2011.04.213.

235. Polak J, Obrtlik K, Hajek M. Cyclic plasticity in type 316l austenitic stainless steel.pdf. *Fatigue and Fracture of Engineering Materials and Structures*. 1994;17(7):773-782.

236. Austin C, Hayes J. *A Constitutive Model For Parent Esshete 1250 and Associated Single Bead Weld Metal*.; 2005.

237. Wilkinson a. J, Meaden G, Dingley DJ. High resolution mapping of strains and rotations using electron backscatter diffraction. *Materials Science and Technology*. 2006;22(11):1271-1278. doi:10.1179/174328406X130966.

238. Wilkinson a J, Clarke EE, Britton TB, Littlewood P, Karamched PS. High-resolution electron backscatter diffraction: an emerging tool for studying local deformation. *The Journal of Strain Analysis for Engineering Design*. 2010;45(5):365-376. doi:10.1243/03093247JSA587.

239. Mino K, Fukuoka C, Yoshizawa H. Evolution of intragranular misorientation during plastic deformation. *Nippon Kinzoku Gakkaishi*. 2000;64(1):50-55. http://cat.inist.fr/?aModele=afficheN&cpsidt=1316844. Accessed September 4, 2014.

240. Lan L, Qiu C, Zhao D. EBSD analysis of HAZ microstructure characteristics of a high strength low welding crack susceptibility steel. *Advanced Materials Research*. 2011;152-153:852-855.

241. Kell J, Tyrer JR, Higginson RL, Thomson RC. Microstructural characterization of autogenous laser welds on 316L stainless steel using EBSD and EDS. *Journal of microscopy*. 2005;217(Pt 2):167-173. doi:10.1111/j.1365-2818.2005.01447.x.

242. Claves SR, Paraventi DJ, Mills WJ. Characterization of Alloy 82H GTA Welds for SCC Studies and Structural Analyses. *Microscopy and Microanalysis*. 2012;18(S2):1348-1349. doi:10.1017/S1431927612008598.

243. Ranjbarnodeha E, Weissb S, Hankeb S, Fischerb A. EBSD Characterization of the effect of welding parameters on HAZ of AISI 409. *Journal of Mining and Metallurgy, Section B: Metallurgy*. 2012;48(1):115-121. doi:10.2298/JMMB110718015R.

244. Coelho RS, Kostka a., dos Santos J, Pyzalla a. R. EBSD Technique Visualization of Material Flow in Aluminum to Steel Friction-stir Dissimilar Welding. *Advanced Engineering Materials*. 2008;10(12):1127-1133. doi:10.1002/adem.200800227.

245. Yoda R, Yokomaku T, Tsuji N. Plastic deformation and creep damage evaluations of type 316 austenitic stainless steels by EBSD. *Materials Characterization*. 2010;61(10):913-922. doi:10.1016/j.matchar.2010.05.006.

246. Li Y, Aubin V, Rey C, Bompard P. Polycrystalline numerical simulation of variable amplitude loading effects on cyclic plasticity and microcrack initiation in austenitic steel 304L. *International Journal of Fatigue*. 2012;42:71-81. doi:10.1016/j.ijfatigue.2011.07.003.

247. BSi 6507-1. Metallic materials — Vickers hardness test —. 2005;3.

248. Kamaya M. Measurement of local plastic strain distribution of stainless steel by electron backscatter diffraction. *Materials Characterization*. 2009;60(2):125-132. doi:10.1016/j.matchar.2008.07.010.

249. Mirzadeh H, Cabrera JM, Najafizadeh a., Calvillo PR. EBSD study of a hot deformed austenitic stainless steel. *Materials Science and Engineering: A*. 2012;538:236-245. doi:10.1016/j.msea.2012.01.037.

250. Angeliu TM, Andresen P., Hall E, Sutiff J., Sitzman S, Horn R. Intergranular stress corrosion cracking of unsensitized stainless steel in BWR Environments. In: Bruemmer S, Ford P, Was G, eds. *Ninth International Symposium on Environmental Degradation of Materials in Nuclear Power Systems-Water Reactors*. Vol Hoboken, NJ, USA: John Wiley & Sons, Inc.; 1999:311-317. doi:10.1002/9781118787618.

251. Kamaya M. Assessment of local deformation using EBSD: Quantification of local damage at grain boundaries. *Materials Characterization*. 2012;66:56-67. doi:10.1016/j.matchar.2012.02.001.

252. Alain R, Violan P, Mendez J. Low cycle fatigue behavior in vacuum of a 316L type austenitic stainless steel between 20 and 600°C Part I: Fatigue resistance and cyclic behavior. *Materials Science and Engineering: A*. 1997;229(1-2):87-94. doi:10.1016/S0921-5093(96)10558-X.

253. Jiang Y, Zhang J. Benchmark experiments and characteristic cyclic plasticity deformation. *International Journal of Plasticity*. 2008;24(9):1481-1515. doi:10.1016/j.ijplas.2007.10.003.

254. Ye D, Matsuoka S, Nagashima N, Suzuki N. The low-cycle fatigue, deformation and final fracture behaviour of an austenitic stainless steel. *Materials Science and Engineering: A*. 2006;415(1-2):104-117. doi:10.1016/j.msea.2005.09.081.

255. Pham MS, Solenthaler C, Janssens KGF, Holdsworth SR. Dislocation structure evolution and its effects on cyclic deformation response of AISI 316L stainless

steel. *Materials Science and Engineering: A*. 2011;528(7-8):3261-3269. doi:10.1016/j.msea.2011.01.015.

APPENDIX

Figure A.3.1 Chemical analysis certificate for AISI 316L (N) base material

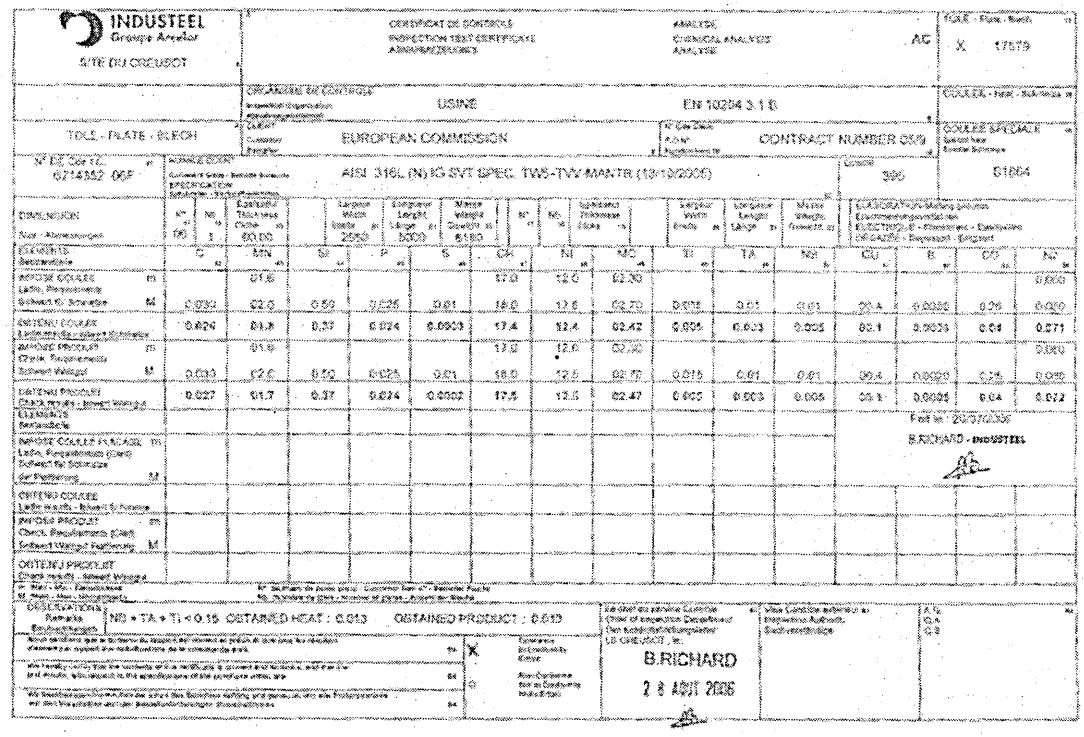

INDUSTEEL
Groupe Arcelor
SITE DU CREUSOT

CERTIFICAT DE CONTROLE
INSPECTION TEST CERTIFICATE
ABNAHMEZEUGNIS

ANALYSE
CHEMICAL ANALYSIS
ANALYSE

AC

TOLE - Plate - Blech
X 17579

ORGANISME DE CONTROLE
USINE
EN 10204 3.1 B

TOLE - PLATE - BLECH

Client
EUROPEAN COMMISSION

N° de Client
CONTRACT NUMBER 05/0

COULEE SPECIALE

N° EQ. Cont TC
0714352 06F

AISI 316L (N) IG SVT SPEC. TWE-TVV MANTR (19/10/2005)

Commande
396

01864

DIMENSION

Epaisseur / Thickness / Dicke	Largeur / Width / Breite	Longueur / Length / Länge	Masse / Weight / Gewicht
60.00	2050	3000	5180

	C	S/N	Si	P	S	Cr	Ni	Mo	Ti	TA	Nb	Cu	B	Co	N
ANALYSE COULEE		01.6				17.0	12.0	02.30							0.060
	0.030	02.0	0.59	0.025	0.001	18.0	12.6	02.70	0.010	0.01	0.01	00.4	0.0030	0.05	0.020
OBTENU COULEE	0.020	01.8	0.37	0.024	0.0003	17.4	12.4	02.42	0.005	0.003	0.005	00.1	0.0025	0.04	0.071
ANALYSE PRODUIT		01.9				17.0	12.0	02.30							0.060
	0.030	02.0	0.52	0.025	0.01	18.0	12.5	02.70	0.010	0.01	0.01	00.4	0.0020	0.05	0.080
OBTENU PRODUIT	0.027	01.7	0.37	0.024	0.0002	17.5	12.5	02.47	0.005	0.003	0.006	00.1	0.0025	0.04	0.072

Fait le : 26/07/2006
B.RICHARD - INDUSTEEL

OBSERVATIONS / Remarks / Bemerkungen

Nb + TA + Ti < 0.15 OBTAINED HEAT : 0.013 OBTAINED PRODUCT : 0.010

B.RICHARD
2 8 AOUT 2006

Figure A.3.2 Heat Treatment Certificate for AISI 316L (N) base material

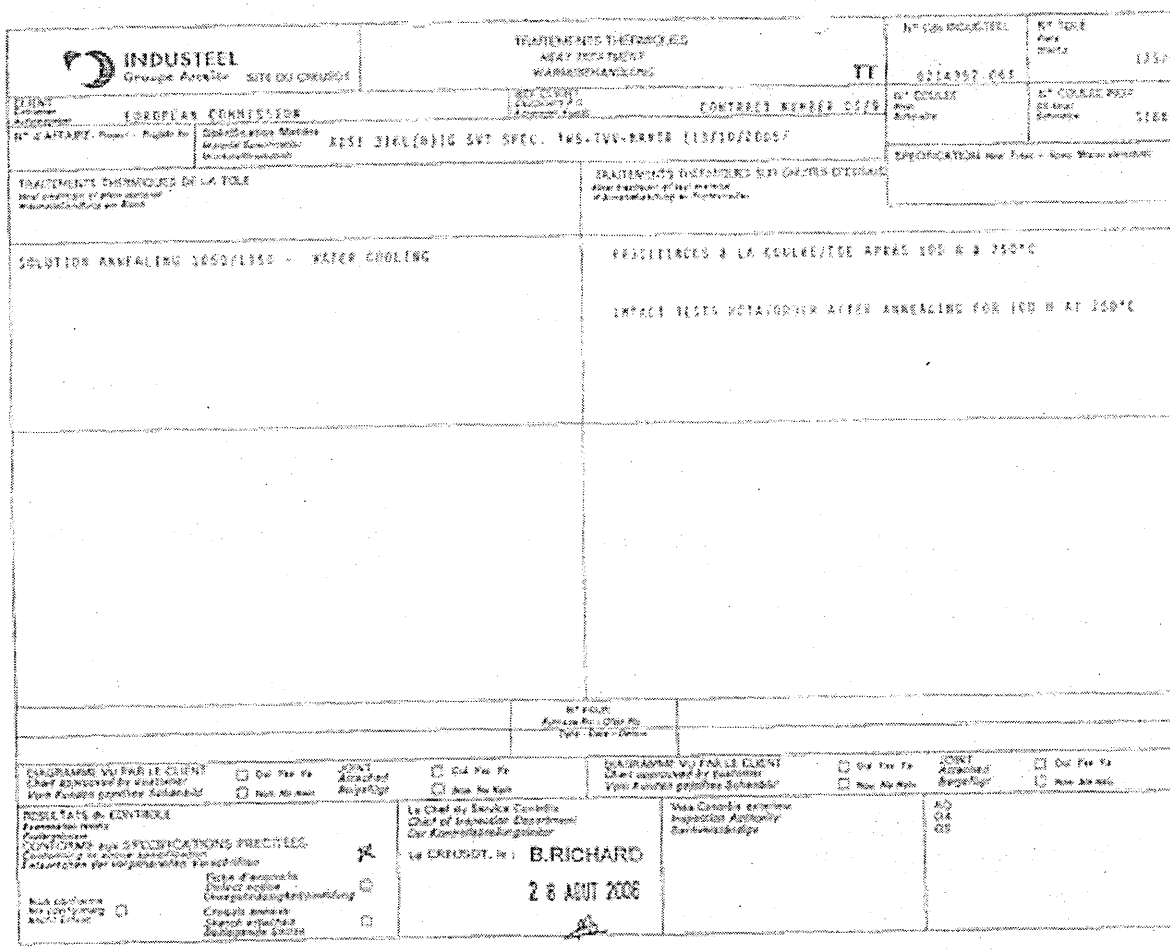

Figure A.3.3 Micrographic examination certificate for AISI 316L (N) base material

INDUSTEEL
Groupe Arcelor

EXAMEN MICROGRAPHIQUE *MICROGRAPHIC EXAMINATION*	06/M520

Client *Customer*	EUROPEAN COMMISSION	Coulée *Heat*	S 1864
Commande *Order number*	6214352	Tôle *Plate*	X 17575 T
Nuance *Grade*	AISI 316L	Epaisseur *Thickness*	60.00

Détermination de la teneur en inclusions – Champ le plus sale *Determination of Inclusion Content – Worst field*							
Suivant *In accordance with the standard*				ASTM E45 A			
Type A		Type B		Type C		Type D	
Fine *Thin*	Epaisse *Heavy*	Fine *Thin*	Epaisse *Heavy*	Fine *Thin*	Epaisse *Heavy*	Fine *Thin*	Epaisse *Heavy*
1	0	0	0	1	0	0.5	0

Détermination de la grosseur de grain apparente *Determination of Average Grain Size*	
Suivant la norme *In accordance with the standard*	ASTM E112
Réactif d'attaque *Etchant*	$HCl + H_2O_2$
Grosseur de grain *Grain size*	4

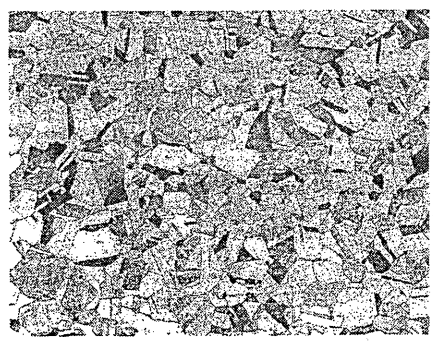

X100

Destinataires *To*	Date *Date*	Nom de l'opérateur *Operator's name*
S. RICHARD C. RENAUDIN	17-07-2006	G. RICHARD

Figure A.3.4 Mechanical test certificate for AISI 316L(N) base material

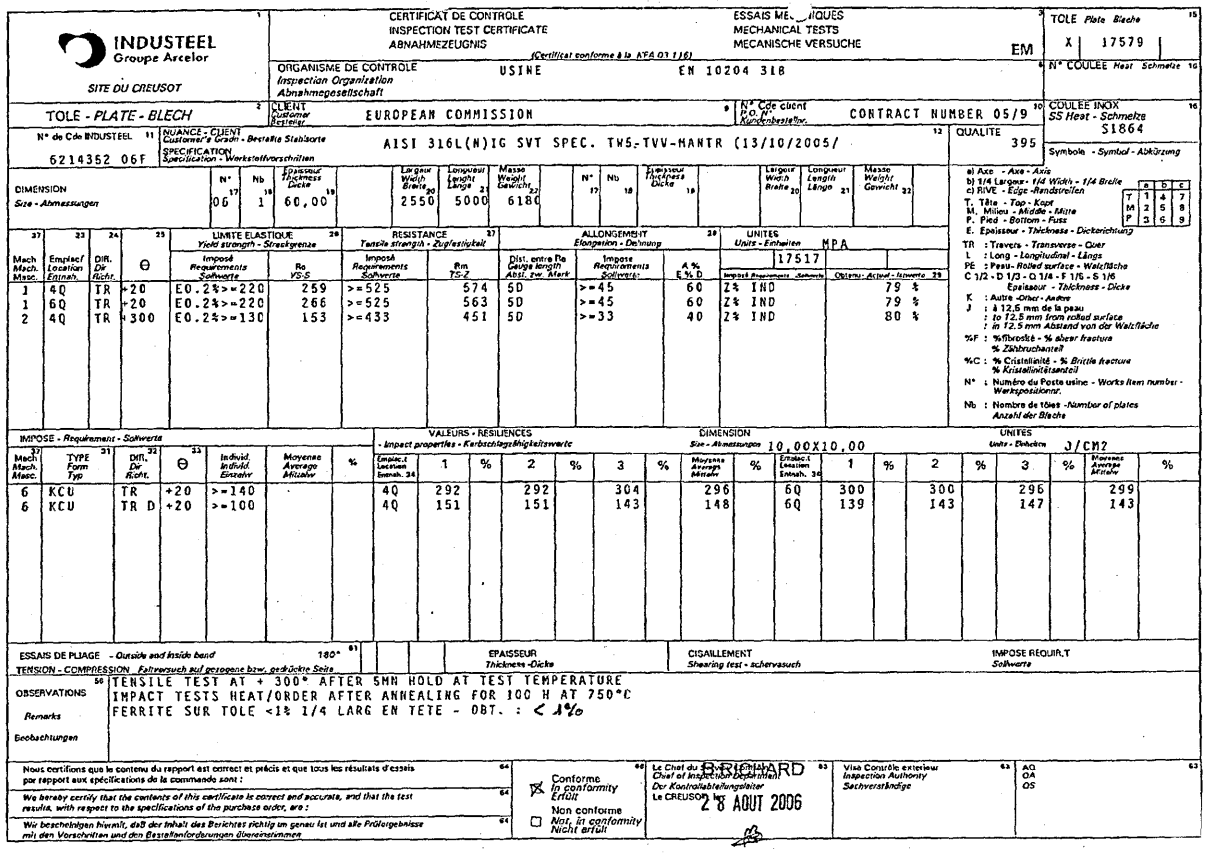

INDUSTEEL Groupe Arcelor
SITE DU CREUSOT

CERTIFICAT DE CONTROLE
INSPECTION TEST CERTIFICATE
ABNAHMEZEUGNIS
(Certificat conforme à la NFA 01 116)

ESSAIS MECANIQUES
MECHANICAL TESTS
MECANISCHE VERSUCHE

EM

TOLE Plate Blech: X | 17579

ORGANISME DE CONTROLE: Inspection Organization / Abnahmegesellschaft — USINE

EN 10204 3.1B

N° COULEE Heat Schmelze:

TOLE - PLATE - BLECH

CLIENT Customer Besteller: EUROPEAN COMMISSION

N° Cde client P.O.N. Kundenbestellnr.: CONTRACT NUMBER 05/9

COULEE INOX SS Heat - Schmelze: S1864

N° de Cde INDUSTEEL: 6214352 06F

NUANCE - CLIENT Customer's Grade - Bestellte Stahlsorte
SPECIFICATION Specification - Werkstoffvorschriften: AISI 316L(N)IG SVT SPEC. TWS-TVV-MANTR (13/10/2005/

QUALITE: 395

Symbole - Symbol - Abkürzung

DIMENSION Size - Abmessungen

N°	Nb	Epaisseur Thickness Dicke	Largeur Width Breite	Longueur Length Länge	Masse Weight Gewicht
06	1	60,00	2550	5000	6180

a) Axe - Axe - Axis
b) 1/4 Largeur - 1/4 Width - 1/4 Breite
c) RIVE - Edge - Randstreifen

a	b	c
T	1	4	7
M	2	5	8
P	3	6	9

T. Tête - Top - Kopf
M. Milieu - Middle - Mitte
P. Pied - Bottom - Fuss
E. Epaisseur - Thickness - Dickenrichtung

TR : Travers - Transverse - Quer
L : Long - Longitudinal - Längs
PE : Peau - Rolled surface - Walzfläche
C 1/2 - D 1/3 - Q 1/4 - F 1/6 - S 1/6 Epaisseur - Thickness - Dicke
K : Autre - Other - Andere
J : à 12,5 mm de la peau / to 12,5 mm from rolled surface / in 12,5 mm Abstand von der Walzfläche
%F : % fibreuse - % sheer fracture - % Zähbruchanteil
%C : % Cristallinité - % Brittle fracture - % Kristallinitsanteil
N° : Numéro du Poste usine - Works item number - Werkspositionnr.
Nb : Nombre de tôles - Number of plates - Anzahl der Bleche

Mach. Masc.	Emplac. Location Einbnah.	Dir. Dir Richt.	Θ	LIMITE ELASTIQUE Yield strength - Streckgrenze Imposé Requirements Sollwerte	Re YS-S	RESISTANCE Tensile strength - Zugfestigkeit Imposé Requirements Sollwerte	Rm TS-Z	ALLONGEMENT Elongation - Dehnung Dist. entre Re Gauge length Abst. zw. Mark.	Imposé Requirements Sollwerte	A % E % D
1	4Q	TR	+20	E0.2%>=220	259	>=525	574	5D	>=45	60
1	6Q	TR	+20	E0.2%>=220	266	>=525	563	5D	>=45	60
2	4Q	TR	+300	E0.2%>=130	153	>=433	451	5D	>=33	40

UNITES Units - Einheiten: MPA — 17517

Imposé Requirements Sollwerte	Obtenu - Achieved - Ermittelt
Z% IND	79 %
Z% IND	79 %
Z% IND	80 %

IMPOSE - Requirement - Sollwerte

VALEURS - RESILIENCES - Impact properties - Kerbschlagzähigkeitswerte

DIMENSION Size - Abmessungen: 10,00X10,00

UNITES Units - Einheiten: J/CM2

Mach. Masc.	TYPE Form Typ	Dir. Dir Richt.	Θ	Individ. Individ. Einzelnr	Moyenne Average Mittelwr	%	Emplac. Location Einbnah.	1	%	2	%	3	%	Moyenne Average Mittelwr	%	Emplac. Location Einbnah.	1	%	2	%	3	%	Moyenne Average Mittelwr	%
6	KCU	TR	+20	>=140			4Q	292		292		304		296		6Q	300		300		296		299	
6	KCU	TR D	+20	>=100			4Q	151		151		143		148		6Q	139		143		147		143	

ESSAIS DE PLIAGE - Outside and inside bend — 180°

TENSION - COMPRESSION Faltversuch auf gezogene bzw. gedrückte Seite

EPAISSEUR Thickness -Dicke

CISAILLEMENT Shearing test - schervasuch

IMPOSE REQUIRT Sollwerte

OBSERVATIONS / Remarks / Beobachtungen:
TENSILE TEST AT + 300° AFTER 5MN HOLD AT TEST TEMPERATURE
IMPACT TESTS HEAT/ORDER AFTER ANNEALING FOR 100 H AT 750°C
FERRITE SUR TOLE <1% 1/4 LARG EN TETE - OBT. : < 1%

Nous certifions que le contenu du rapport est correct et précis et que tous les résultats d'essais par rapport aux spécifications de la commande sont :
We hereby certify that the contents of this certificate is correct and accurate, and that the test results, with respect to the specifications of the purchase order, are :
Wir bescheinigen hiermit, daß der Inhalt des Berichtes richtig im genau ist und alle Prüfergebnisse mit den Vorschriften und den Bestellanforderungen übereinstimmen

☒ Conforme — In conformity — Erfüllt
☐ Non conforme — Not, in conformity — Nicht erfüllt

Le Chef du Service Contrôle — Chief of Inspection Department — Der Kontrollabteilungsleiter
Le CREUSOT, 28 AOUT 2006
RICHARD

Visa Contrôle extérieur — Inspection Authority — Sachverständige

AQ
OA
OS

Figure A.6.1 (a) Measured KAM vs true strain and (b) KAM vs flow stress at 25°C and 550°C

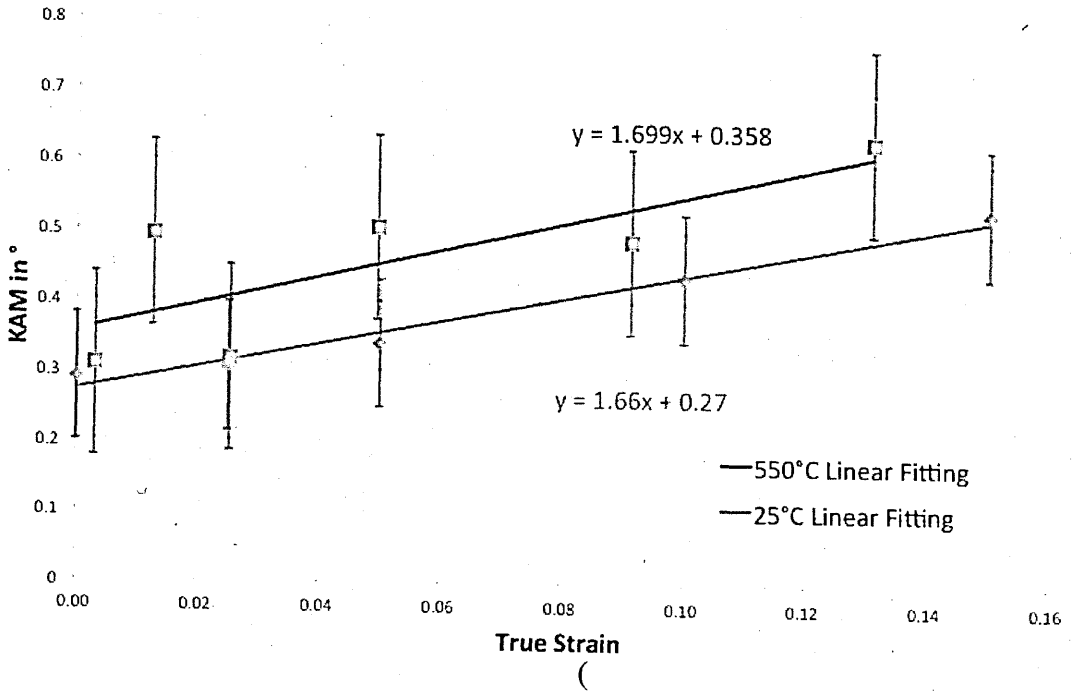

(

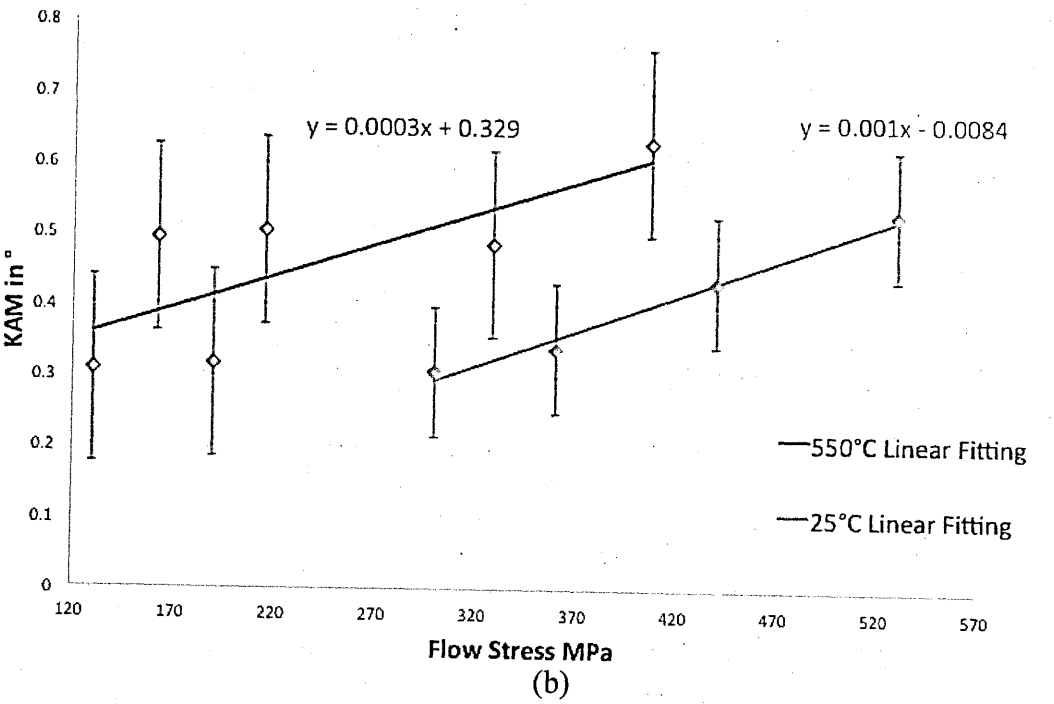

(b)

Figure A.6.2 (a) Measured LABf vs true strain and (b) LABf vs flow stress at 25°C and 550°C

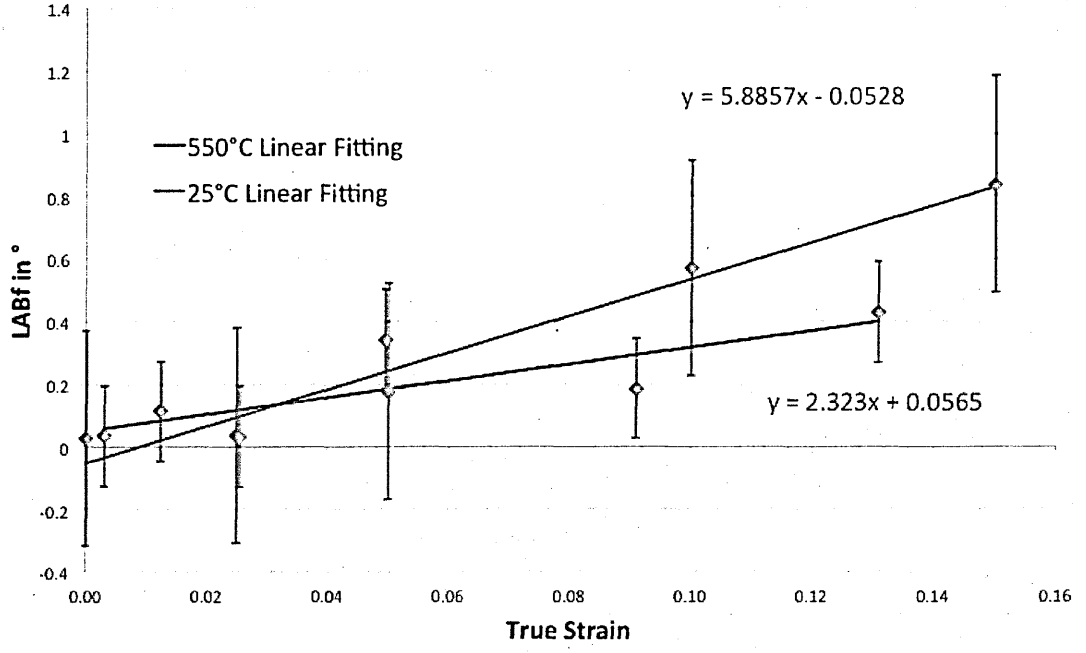

(a)

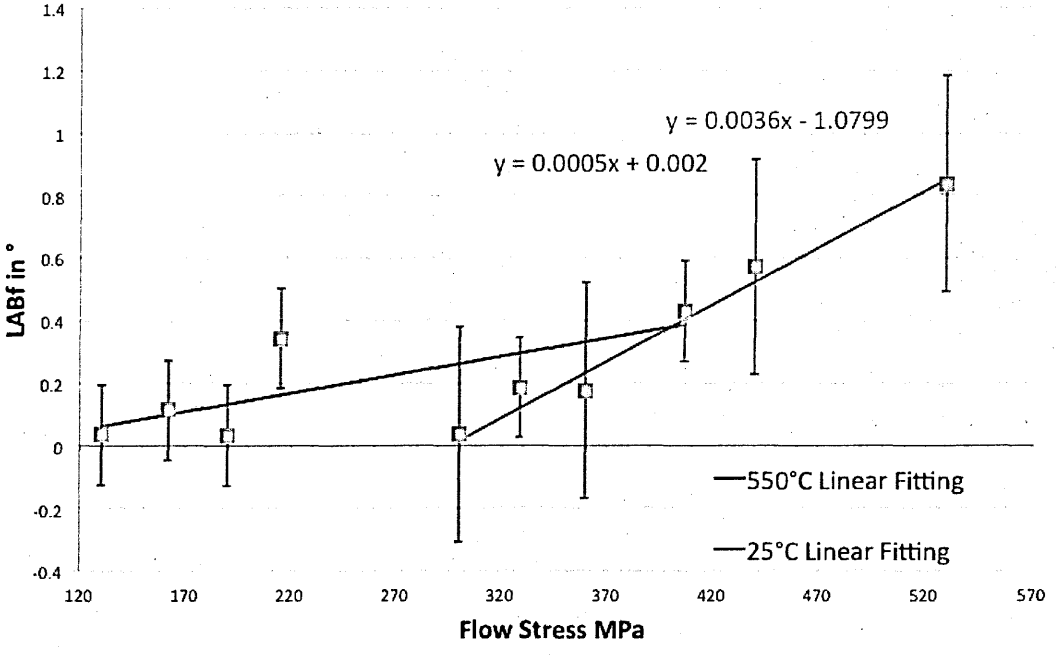

(